Low-dimensional electron systems studied by angle- and spin-resolved photoemission spectroscopy

Ji Dai

université PARIS-SACLAY

UNIVERSITÉ PARIS SUD
Comprendre le monde, construire l'avenir

NNT : 2019SACLS345

Thèse de doctorat

Low-dimensional electron systems studied by angle- and spin-resolved photoemission spectroscopy

Thèse de doctorat de l'Université Paris-Saclay
préparée à l'Université Paris-Sud

Ecole doctorale n°564 Physique en Ile de France (EDPIF)
Spécialité de doctorat : Physique

Thèse présentée et soutenue à Orsay, le 09/10/2019, par

Ji DAI

Composition du Jury :

Philippe MENDELS Professeur, Université Paris-Sud	Président
Mark S. GOLDEN Professeur, University of Amsterdam	Rapporteur
Yannick FAGOT-REVURAT Professeur, Université de Lorraine	Rapporteur
Marie D'ANGELO Maître de Conférences, Sorbonne Université	Examinatrice
Jose Enrique ORTEGA Professeur, University of the Basque Country	Examinateur
Andrés Felipe SANTANDER-SYRO Maître de Conférences, Université Paris-Sud	Directeur de thèse

"Wir müssen wissen.
Wir werden wissen."

David Hilbert

université PARIS-SACLAY
ÉCOLE DOCTORALE
Physique en Île-de-France (EDPIF)

Titre : Systèmes électroniques de basse dimensionnalité étudiés par spectroscopie de photoémission résolue en angle et en spin

Mots clés : systèmes électroniques bidimensionnels; électrons corrélés; oxydes fonctionnels; métaux topologiques; matériaux à fermions lourds; spectroscopie de photoémission résolue en angle.

Résumé : Les matériaux dans lesquels des interactions à plusieurs particules, un confinement de faible dimension et/ou un fort couplage spin-orbite sont présents témoignent d'une grande variété de phénomènes, mais sont encore mal compris. Des informations essentielles sur l'origine de tels phénomènes peuvent être obtenues en mesurant leur structure électronique. Cette thèse présente une étude expérimentale de la structure électronique de matériaux de faible dimension et/ou fortement corrélés présentant un intérêt fondamental actuel, en utilisant la spectroscopie par photoémission résolue en angle et en spin (ARPES et SARPES).
Dans la partie introductive, je présente mon travail sur deux exemples de type "livre de texte", mais innovants, montrant comment les interactions affectent la structure de bande d'un matériau : le couplage des électrons avec des phonons dans une distribution de Debye dans un système électronique à deux dimensions (2DES) dans ZnO, semi-conducteur à oxyde à bande interdite large utilisé dans les applications photovoltaïques, et le dédoublement induit par un fort couplage spin-orbite (SOC) dans la bande de valence du ZnTe, un autre semi-conducteur important utilisé dans les dispositifs optoélectroniques. Ensuite, dans la suite de cette thèse, je discute de mes résultats originaux dans trois systèmes différents de basse dimensionnalité et d'intérêt actuel en recherche :

1. La réalisation d'un 2DES à la surface (110) de SnO_2, le premier du genre dans une structure rutile. L'ajustabilité de la densité de ses porteurs au moyen de la température ou du dépôt d'Eu, et la robustesse vis-à-vis les reconstructions de surface et l'exposition aux conditions ambiantes rendent ce 2DES prometteur pour les applications. Au moyen d'un simple réaction redox à la surface, ces travaux ont prouvé que les lacunes en oxygène pouvaient doper la bande de conduction à la surface de SnO_2, résolvant ainsi un problème longtemps débattu concernant le rôle desdites lacunes dans le dopage de type n dans SnO_2.
2. L'étude des états de surface topologiques dans M_2Te_2X (avec M = Hf, Zr ou Ti ; et X = P ou As), une nouvelle famille de métaux topologiques en trois dimensions, provenant du SOC et étant protégés par la symétrie du renversement du temps. Leur structure électronique et leur texture de spin, étudiées par ARPES et SARPES, révèlent la présence de fermions de Dirac sans masse donnant naissance à des arcs de noeuds de Dirac.
3. L'étude du matériau $YbNi_4P_2$ à fermions lourds quasi unidimensionnel, qui présente une transition de phase quantique de second ordre d'une phase ferromagnétique à une phase paramagnétique de liquide de Fermi lors de la substitution partielle du phosphore par l'arséniure. Une telle transition ne devrait se produire que dans les systèmes zéro ou unidimensionnels, mais la mesure directe de la structure électronique des matériaux ferromagnétiques quantiques critiques faisait jusqu'à présent défaut. Grâce à une préparation et nettoyage méticuleux in situ de la surface des monocristaux $YbNi_4P_2$, qui sont impossibles à cliver, leur structure électronique a été mesurée avec succès au moyen de l'ARPES, dévoilant ainsi le caractère quasi-1D, nécessaire à la compréhension de la criticité quantique ferromagnétique, dans $YbNi_4P_2$. Le protocole utilisé pour rendre ce matériau accessible à l'ARPES peut être facilement généralisé à d'autres matériaux exotiques dépourvus de plan de clivage.

Université Paris-Saclay
Espace Technologique / Immeuble Discovery
Route de l'Orme aux Merisiers RD 128 / 91190 Saint-Aubin, France

université PARIS-SACLAY
ÉCOLE DOCTORALE
Physique en île-de-France (EDPIF)

Title : Low-dimensional electron systems studied by angle- and spin-resolved photoemission spectroscopy

Keywords : two-dimensional electron systems; correlated-electrons; functional oxides; topological metals; heavy-fermion materials; angle-resolved photoemission spectroscopy.

Abstract : Materials in which many-body interactions, low-dimensional confinement, and/or strong spin-orbit coupling are present show a rich variety of phenomena, but are still poorly understood. Essential information about the origin of such phenomena can be obtained by measuring their electronic structure. This thesis presents an experimental study of the electronic structure of some low-dimensional and/or strongly correlated materials of current fundamental interest, using angle- and spin-resolved photoemission spectroscopy (ARPES and SARPES).
In the introductory part, I present my work on two innovative textbook examples showing how interactions affect the band structure of a material : the coupling of electrons with phonons in a Debye distribution in a two-dimensional electron system (2DES) in ZnO, a wide-band-gap oxide semiconductor used in photovoltaic applications, and the splitting induced by strong spin-orbit coupling (SOC) in the bulk valence band of ZnTe, another important semiconductor used in optoelectronic devices. Then, in the rest of this thesis, I discuss my original results in three different low-dimensional systems of current interest :

1. The realisation of a 2DES at the (110) surface of SnO_2, the first of its kind in a rutile structure. Tunability of its carrier density by means of temperature or Eu deposition and robustness against surface reconstructions and exposure to ambient conditions make this 2DES promising for applications. By means of a simple redox reaction on the surface, this work has proven that oxygen vacancies can dope the conduction band minimum at the surface of SnO_2, solving a long-debated issue about their role in n-type doping in SnO_2.
2. The study of topological surface states in M_2Te_2X (with M = Hf, Zr, or Ti ; and X = P or As), a new family of three-dimensional topological metals, originating from SOC and being protected by time-reversal symmetry. Their electronic structure and spin texture, studied by ARPES and SARPES, reveal the presence of massless Dirac fermions giving rise to Dirac-node arcs.
3. The investigation of the quasi-one-dimensional heavy-fermion material $YbNi_4P_2$, which presents a second-order quantum phase transition from a ferromagnetic to a paramagnetic phase upon partial substitution of phosphorous by arsenide. Such a transition is expected to occur only in zero- or one-dimensional systems, but a direct measurement of the electronic structure of ferromagnetic quantum-critical materials was missing so far. By careful in-situ preparation and cleaning of the surface of $YbNi_4P_2$ single crystals, which are impossible to cleave, their electronic structure has been successfully measured by ARPES, thus effectively unveiling the quasi-one-dimensionality of $YbNi_4P_2$. Moreover, the protocol used to make this material accessible to ARPES can be readily generalised to other exotic materials lacking a cleavage plane.

Université Paris-Saclay
Espace Technologique / Immeuble Discovery
Route de l'Orme aux Merisiers RD 128 / 91190 Saint-Aubin, France

Acknowledgements

My first thanks go to my family, especially my parents and my sister who supported me throughout my studies. Next, I'd like to thank my girlfriend who offered me her company and brought so many joyful moments during the past 3 years. I also want to thank all my friends who are still chasing dreams we had when young.

Special thanks go to my thesis supervisor Andrés Felipe Santander-Syro (University of Paris Sud) who guided me to the real world of experimental physics from the "imaginary" world of theoretical physics. Thank you for being so responsible and patient during my thesis preparation.

The discussions with and help of my coworkers, especially Emmanouil Frantzeskakis, Franck Fortuna, Shamashis Sengupta, Maximilian Thees (Ph.D. student in the group), Tobias Rödel (former Ph.D student in the group), Cédric Bareille (former Ph.D. student in the group) and Ryu Yukawa (KEK, Photon Factory), made it much easier to advance my understanding in physics and to acquire practical experimental skills.

During my thesis training, I am honored to have Claire Marrache as my tutor and Olivier Plantevin as my mentor. As members of the monitoring committee, they make sure that I am mentally healthy and have no private problems with my supervisor. Thanks so much for their work!

I am also indebted to all the beamline scientists and their support which made sure that our photoemission experiments at synchrotron facilities could be conducted without major complications. In this context, I am grateful to the Synchrotron Soleil (Gif-sur-Yvette, France), BESSY (Berlin, Germany), HiSOR (Hiroshima, Japan), and Photon Factory (Tsukuba, Japan) to provide the infrastructure to conduct photoemission experiments.

I also thank the administrative staff of all the involved institutes who ensured that I could focus on my research project. Finally, I am thankful for the financial support for my thesis given by the Centre de Sciences Nucléaires et de Sciences de la Matière (CSNSM), the doctoral school (EDPIF) and the Université de Paris Sud & Université Paris-Saclay.

Contents

Overview of thesis

In the framework of this thesis, I worked in the team of "Strongly Correlated Systems and New Electronic States of Matter" at CSNSM in Orsay. During my thesis preparation, I studied several low-dimensional electronic systems, which compose of the main body of this thesis: the two-dimensional electron systems (2DESs) at the (110) surface of SnO_2, the topological surface states in a family of 3D topological metals M_2Te_2X (with M = Ti, Zr or Hf, and X = P or As), and the quasi-1D heavy Fermion system $YbNi_4P_2$ showing ferromagnetic quantum criticality. The main experimental tool I used is angle-resolved photoemission spectroscopy (ARPES). Most of the data presented in this thesis were obtained in modern synchrotrons (the high-resolution ARPES endstation of CASSIOPÉE in Synchrotron SOLEIL, the ARPES beamline BL-2A of the Photon Factory in Synchrotron KEK, the spin-resolved ARPES endstation ESPRESSO in Synchrotron HiSOR).

Following is an overview of my thesis:

1. Introductory concepts

In this chapter, I introduce the basic concepts needed for the understanding of the ensuing experimental work.

Section 1.1 briefly reviews the development of the study of two-dimensional electron systems at the surface/interface of oxides since the discovery of the 2DES at the $LaAlO_3/SrTiO_3$ heterostructure interface. During the exploration of such 2DES at the surface of transition metal oxides, especially $SrTiO_3$, new understanding and new methods have been developed in the creation and controlling of 2DESs at the surface/interface of oxides.

Section 1.2 gives a pedagogical introduction of the development of topology concepts in condensed matter physics eventually leading to the development and discovery of 3D topological materials. Basic concepts, such as Z_2 invariants $(\nu_0; \nu_1, \nu_2, \nu_3)$, time-reversal-invariant-momenta (TRIMs) and spin-momentum locking, are covered.

Section 1.3 introduces the heavy Fermion systems and the possible quantum phase transitions. The phase diagram, Kondo resonance and quantum criticality are briefly described. Additionally, because the heavy fermion material studied in this thesis $YbNi_4P_2$ is a quasi-1D system, the relation between the Fermi surface topography and the dimensionality of a given system is introduced at the end.

Section 1.4 introduces the theory of electron-phonon interaction, which is an important insight source for relevant data analysis. Eiliashberg function and Debye phonon model are the theoretical tools I used for the analysis of electron-phonon interaction in the 2DESs.

Section 1.5 presents a pedagogical introduction to spin-orbit coupling in solids. Two typical types of SOC, Dresselhaus and Rashba SOC, are discussed.

2. Experimental techniques

ARPES is the main experimental tool I used throughout my Ph.D. work. Following a brief introduction to ARPES based on the 3-step model (subsection 2.1.1), I present two original works, the study of electron-phonon interaction in the 2DES in ZnO (subsection 2.1.2) and the study of spin-orbit coupling in the valence band

of ZnTe (subsection 2.1.3), to demonstrate ARPES's power in resolving interactions within electronic systems besides its ability of probing the band dispersions directly.

Spin-resolved ARPES (SARPES) is an important complementary technique in the study of the spin textures of the topological surface states in 3D topological metals Ti_2Te_2P and Hf_2Te_2P. A brief introduction to SARPES based on the ESPRESSO machine at HiSOR synchrotron in Japan is given in Section 2.2.

Other supplementary experimental techniques, molecular beam epitaxy (MBE) and low energy electron diffraction (LEED) are introduced in Section 2.3.

3. Oxides: SnO_2 and $FeTiO_3$

In this chapter, I studied two oxides by means of ARPES mainly: SnO_2 (section 3.1) and $FeTiO_3$ (section 3.2).

For SnO_2, we discovered and characterised a two-dimensional electron system (2DES) at its bare (110) surface at $T = 16$ K utilising ARPES (subsection 3.1.2). This is the first realised 2DES in a rutile structure oxide. The carrier density of this 2DES was demonstrated to be tunable via either temperature or surface doping with oxygen vacancies created through a redox reaction with capping metals such as Al or Eu (subsection 3.1.3). The experiments with the metallic capping leading to a redox reaction also reveal that the oxygen vacancies at the surface can dope the conduction band minimum, thus help us to understand the origin of the observed 2DES and development of n-type conductivity in SnO_2 (subsection 3.1.6). Furthermore, we find this 2DES to be robust against surface reconstructions or surface impurities (subsection 3.1.4). A quantitative analysis, such as core level fit, quantum-well modelling and intensity modulation of the out-of-plane Fermi surfaces, is given in Subsection 3.1.5.

For $FeTiO_3$, we managed to measure the electronic structure (mainly the valence bands) in its paramagnetic phase at a temperature $T = 72$ K for the first time (subsection 3.2.2). Specifically, the top of the valence band at/close to the Fermi level was probed and used to characterise the magnetic phase transition from paramagnetic phase at high temperatures to antiferromagnetic phase at low temperatures (subsubsection 3.2.2). The determined Néel temperature by photoemission spectroscopy is around 52 K in good agreement with previous transport studies.

4. 3D topological-metals: (Ti, Zr, Hf)$_2$Te$_2$(P, As)

M_2Te_2X (with M = Ti, Zr or Hf, and X = P or As) is a new family of topological metals of the tetradymite family with the spin-orbit coupling (SOC) systematically tuned by element replacing Ti $\rightarrow$ Zr $\rightarrow$ Hf (increasing the strength of the SOC), and P $\rightarrow$ As (increasing the strength of the SOC).

After cleaving the samples, we measured the Fermi surfaces (both in-plane and out-of-plane) and the band dispersions along the $\bar{K} - \bar{\Gamma} - \bar{K}$ direction at $\bar{\Gamma}$ and along the $\bar{K} - \bar{M} - \bar{K}$ direction at $\bar{M}$, which confirm the existence of massless Dirac surface states and show an excellent agreement with slab DFT calculations and parity analysis (section 4.1). Further analysis of the Fermi surface data reveals the existence of a Dirac-node arc centred at the $\bar{M}$ points of the surface-projected Brillouin zone and extending along the $\bar{\Gamma} - \bar{M}$ direction (section 4.2). Focusing on the Dirac-node arc, in Section 4.3, we used spin-resolved ARPES (SARPES) to probe the spin texture of the Dirac surface states at $\bar{M}$ points in Ti_2Te_2P and Hf_2Te_2P, which are experimentally determined to be reminiscent of the well-known 3D topological insulator example

Bi_2Se_3. Furthermore, the Dirac node arc in Ti_2Te_2P is shown to be also “helical", i.e. every Dirac point forming part of such an arc corresponds to a helical surface state.

The possibility of the realisation of topological superconductivity, the possible peculiar transport property of the Dirac-node arc, the influence of different spin-orbit coupling strength, the weak and strong topological characters, and the possibly complicated spin texture, are discussed in Section 4.4.

5. One-dimensional heavy fermion material: $YbNi_4P_2$

$YbNi_4P_2$ is a quasi-one-dimensional (quasi-1D) heavy fermion material showing ferromagnetic quantum criticality. Following a brief review of several typical features of $YbNi_4P_2$ (Kondo resonance, 2nd order ferromagnetic transition, anisotropy and non-Fermi liquid behavior) observed in previous transport measurements, and recent approximative DFT calculations of its electronic structure (section 5.1), I present a systematic characterisation of its electronic structure by means of ARPES (section 5.2), which can be separated into two parts.

The first part (subsection 5.2.2), focusing on the topographies of the Fermi surfaces, explicitly demonstrates the quasi-1D character of $YbNi_4P_2$'s electronic structure, which is not only important to understand its strong anisotropic transport behavior, but also crucial for the onset of the 2nd order ferromagnetic quantum critical transition, as in clean 2D/3D metallic systems the ferromagnetic quantum criticality will be replaced by either a 1st order ferromagnetic transition, or the formation of superconducting phases or inhomogeneous magnetic phases.

The second part (subsection. 5.2.3) presents the energy-momentum dispersions measured along high symmetry directions ($Z-\Gamma-Z$, $M-\Gamma-M$ and $A-Z-A$) in the first Brillouin zone and their comparison with the corresponding DFT calculated bands. Quantitative analysis of these dispersions helps us to understand some unexpected Fermi sheets, and more importantly suggests the presence of strong spin-orbit coupling and $d-f$ hybridisation, which are important to understand the unexpected power-law exponents in thermodynamic quantities indicating the presence of strong ferromagnetic quantum critical fluctuations.

Chapter 1

Introductory concepts

1.1 Two-dimensional electron systems at the surface/interface of oxides

This introduction to the two-dimensional electron systems (2DESs) at the surface/interface of oxides is mainly based on a review paper by E. Frantzeskakis *et al*. [1] and on T. Rödel's Ph.D. thesis [2].

Two-dimensional electron gases confined at interfaces of conventional semiconductors, such as Si or GaAs, are at the basis of modern electronics, giving rise to the development of important technological devices such as the transistor, and also have played a pivotal role in fundamental science, leading to the discovery of new physical phenomena including the quantum Hall effect [3–5] and electronic states of non-trivial topology [6].

In 2004, A. Ohtomo and H. Y. Hwang discovered the high mobility 2DES at the interface between two otherwise insulating oxides, namely $LaAlO_3$ and $SrTiO_3$ [7]. This surprising discovery has attracted immense scientific interest due to new opportunities opened in the emerging field of oxide electronics [8–10]. The rich physics in the 2DES at the interface of $LaAlO_3/SrTiO_3$ includes the gate-tuneable insulator-to-superconductor transition [11] and magnetism [12] or the coexistence of superconductivity and magnetism [13–15], driving the subsequent intense scientific efforts over the last decade toward exploiting the unexpected 2DES and understanding its emergence [11, 16–19].

In early 2011, another study showed that the $LaAlO_3/SrTiO_3$ interface is not necessary to obtain a high mobility 2DES: a similar 2DES was discovered at the bare (001) surface of $SrTiO_3$ [20]. In this case, the 2DES is created by oxygen vacancies near the sample surface, which both dope with electrons the system's bulk conduction band and create a positive background of charge inducing a band bending that confines such electrons around the surface. These results, which were soon after reproduced by other research groups [23], made the 2DES accessible to surface sensitive techniques as it was no longer buried under layers of $LaAlO_3$ but could be probed right on the sample surface and subsurface layers. Since then, Angle Resolved Photoemission Spectroscopy (ARPES), a typical surface sensitive technique, became an important experimental technique in this field due to its high surface sensitivity and the possibility for a direct and high-resolution view of the electronic structure of the 2DES [1].

Further studies have subsequently generalised the mechanism of creating the 2DEG at the $SrTiO_3$(001) surface to surfaces of other transition metal oxides, such as $KTaO_3$ [24, 25] and anatase TiO_2 [22, 26], and with different orientations [21, 27, 28].

In December 2015, T. Rödel *et al*. developed a straightforward, versatile and extremely cost-effective approach to create 2DESs on surfaces of oxides: the thermal

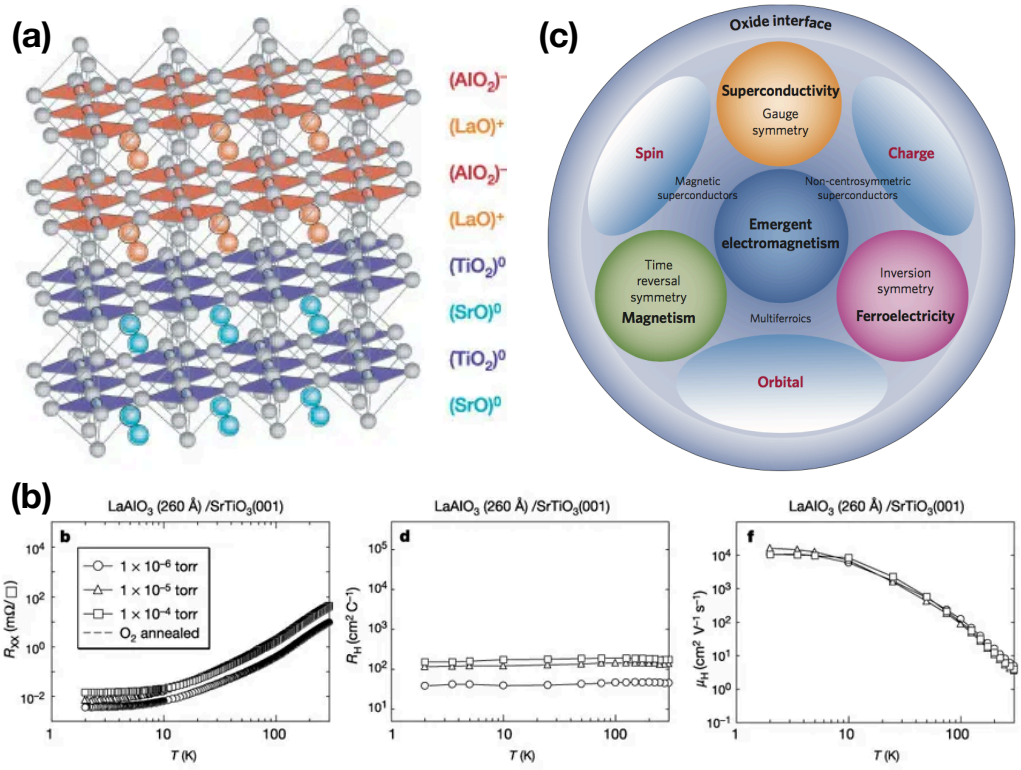

FIGURE 1.1: (a) Sketch of the $LaAlO_3/SrTiO_3$ heterostructure. (b) The temperature dependence of sheet resistance $R_{xx}(T)$, Hall coefficient $R_H(T)$ and Hall mobility $\mu_H(T)$ for the interface between 260 Å-thick $LaAlO_3$ and $SrTiO_3$. Taken from Ref. [7]. (c) Diagram showing the rich physics of oxide interface due to the interplay between spin, charge and orbital degrees of freedom and the breaking of certain symmetries. Taken from Ref. [10].

evaporation of pure aluminum (Al) at room temperature [1, 2, 30]. As illustrated in Fig. 1.3(a), aluminium, an elementary reducing agent, pumps oxygen from the oxide substrate thereby oxidising into insulating AlO_x, and and releasing into the oxide substrate the electrons of the remaining vacancies. These electrons may become mobile carriers confined at the surface leading to the formation of a 2DES. Furthermore, the insulating AlO_x capping layer can also serve as a passivation layer for the emerging 2DES, making it possible to conduct transport experiments in ambient conditions [29], as shown in Fig. 1.3(b). These transport experiments at the $AlO_x/SrTiO_3$ interface (Fig. 1.3(d-f)) suggests that this 2DES as imaged in Fig. 1.3(c) by ARPES is identical to the one at the $LaAlO_3/SrTiO_3$ interface. Later on, the reducing metal capping idea was generalised to other functional metals, such as europium (Eu), adding new functionalities to the 2DES, as the resulting EuO capping layer becomes magnetic at low temperatures [31].

The first part of my thesis work (see Section 3.1) is a direct application of this approach to the transparent binary oxide SnO_2 in the rutile structure. Both Al and Eu capping are shown to be valid for the creation and control of the 2DES at the (110) surface of SnO_2.

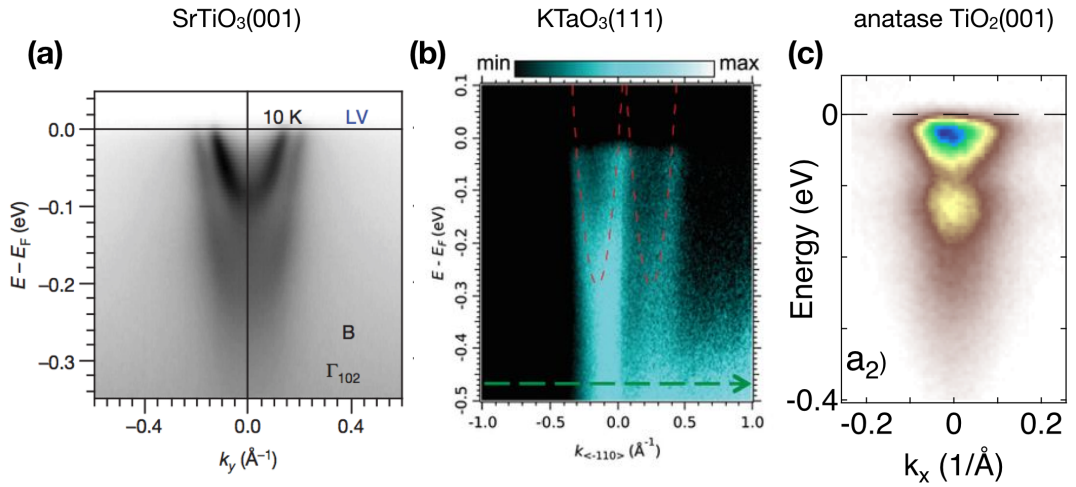

FIGURE 1.2: (a) $E-k$ dispersion intensity map of the 2DES at the (001) surface of $SrTiO_3$ measured by ARPES. One observes two parabolic bands of free electrons corresponding to two quantum-well states of carriers confined near the material surface. Taken from [20]. (b) E-k dispersion intensity map of the 2DES at the (111) surface of $KTaO_3$ measured by ARPES. One observes two parabolic bands fitted with the red dashed parabolic curves. Taken from [21]. (c) E-k dispersion intensity map of the 2DES at the (001) surface of TiO_2 measured by ARPES. One observes replica polaronic 2D electron gas state. Taken from [22].

1.2 Topological surface states and 3D topological materials

This pedagogical introduction to the basic concepts of topological surface states and topological materials is based on a review paper of X. L. Qi and S. C. Zhang [32], and the pioneering works on 3D TIs by L. Fu *et al*. [33, 34].

The topology concept stimulates a still on-going revolution in condensed matter physics. Starting from the quantum Hall state discovered in 1980 [3], to nowadays Dirac and Weyl semimetals, researchers continue exploring new exotic topological quantum states. Being different from the quantum Hall state where the time-reversal symmetry (TRS) is broken, for example, by an external magnetic field, many new quantum states where the TRS is conserved and the spin-orbit coupling plays an essential role, have been theoretically predicted and experimentally observed in recent years [35–38]. Soon after the proposal of the 2D topological insulator i.e. the quantum spin Hall (QSH) insulator, the 3D topological insulators together with topological surface states were predicted in 2007 [33, 34, 39–42].

Three-dimensional topological insulators include bulk insulator properties with metallic surface states. As shown in Fig. 1.4(a), though these materials do not conduct electricity in the bulk, electrons are able to move freely on the surface of the material in a manner that is protected from defect scattering. Moreover, these topological surface states show spin-momentum locking. All electrons traveling in a given direction must have their spins pointing the same way, or conversely, all electrons with the same spin component must be moving in the same direction. Transformed to k space, helical spin texture develops, as shown in Fig. 1.4(b). As will be discussed later, the spin-momentum helical locking is originated from the spin-orbit coupling.

For all these systems conserving TRS, the key theory behind is the Z_2 topological

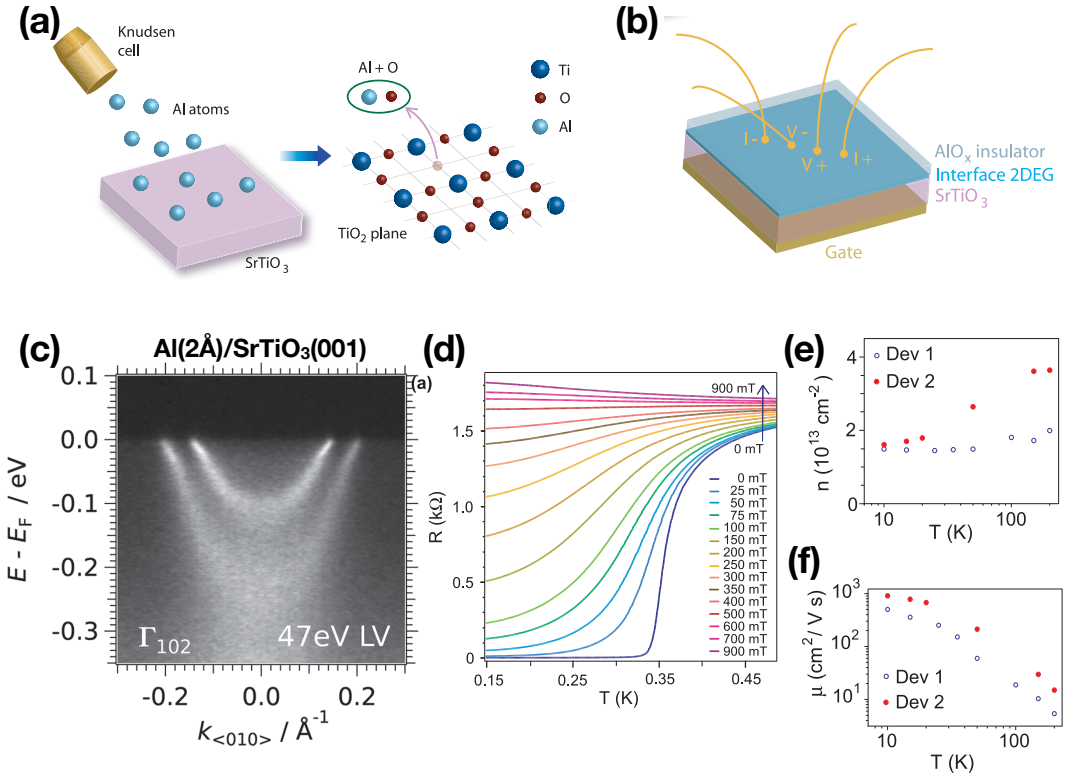

FIGURE 1.3: (a) Schematic representationof the thermal evaporation of pure Al on the surface of TiO_2-terminated $SrTiO_3(001)$. (b) A sketch of the four-probe transport measurement on $AlO_x/SrTiO_3$. (c) $E-k$ dispersion intensity map of the 2DES at the interface of $AlO_x/SrTiO_3$ measured by ARPES. The evaporated Al was 2 Å thick. One observes the two quasi-parabolic quantum well states, together with clear kinks at around $E-E_F = 30$ meV, due to electron-phonon coupling. (d) Temperature and magnetic field dependence of the sheet resistance measurements showing the superconductivity at low temperatures and small magnetic fields. (e) Temperature dependence of carrier densities calibrated in transport measurements on two samples. (f) Temperature dependence of mobilities measured on 2 samples. (a, b, d, e, f) Adapted from Ref. [29]. (c) Taken from Ref. [30].

invariants and the topological band theory. In 3D, four of such Z_2 topological invariants $(\nu_0;\nu_1,\nu_2,\nu_3)$ are needed to classify the 16 topologically distinct surface states belonging to two general classes: weak (WTI) and strong (STI) topological insulators depending on ν_0 being 0 or 1 [33, 34]. The WTI can be considered as adiabatically stacked 2D QSH insulators where the interlayer interaction is weak, thus becomes equivalent to a band insulator with disorder present. While the STI is genuinely 3D and remains robust against disorder [33, 34]. These Z_2 invariants can be calculated thought the parity analysis at the time reversal invariant momenta (TRIMs). Examples are given in Fig. 1.4(c). The parity indicated as + and - at the 8 (2^3, for 3D systems) TRIMs can be calculated from tight binding model or more rigorously from the DFT calculated band structure. (ν_1,ν_2,ν_3) are then determined by the parity products in the yz, zx, and xy plane respectively, while ν_0 is the overall product of the parity at the 8 TRIMs.

The surface states with a single Dirac cone due to SOC have been experimentally observed with ARPES in 3D topological insulators Bi_2Se_3, Bi_2Te_3 and Sb_2Te_3 [44],

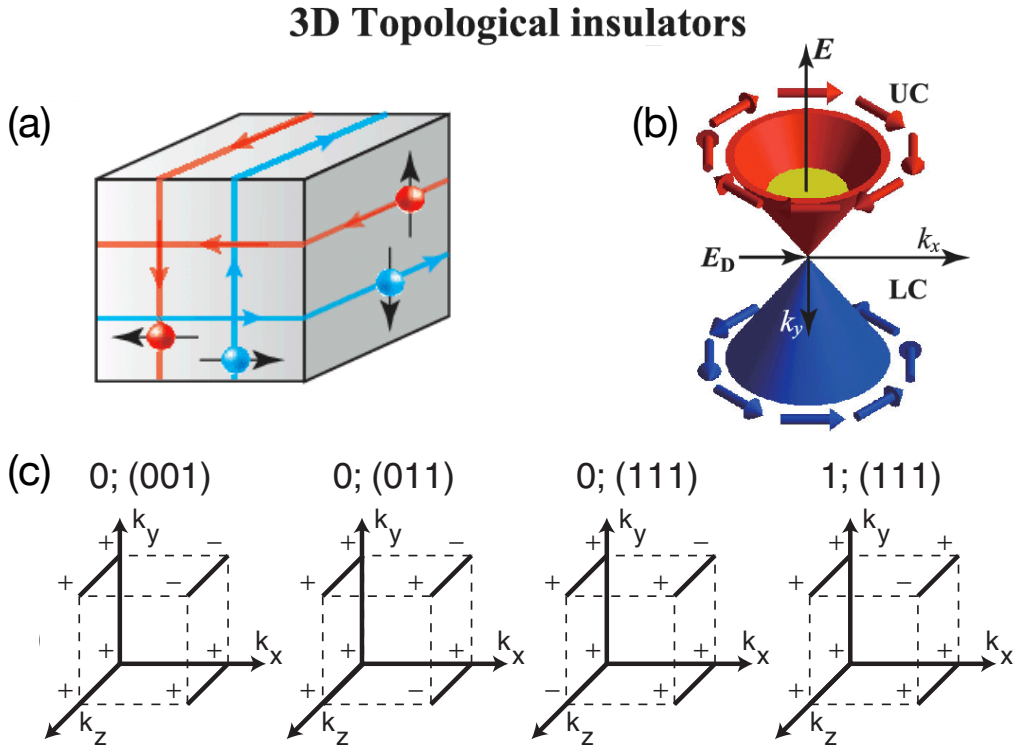

FIGURE 1.4: (a) Spin current flow at surface state of three dimensional (3D) topological insulator (TI). (b) A single Dirac cone with helical spin texture showing the spin-momentum helical locking. Spin directions are denoted with arrows. The upper Dirac cone (UC) above the Dirac point (E_D) has a left-handed helicity, while the lower Dirac cone (LC) below E_D has a right-handed helicity, when looking from above the surface. Adapted from Ref. [43]. (c) Diagrams representing four different phases indexed by $(\nu_0; \nu_1, \nu_2, \nu_3)$. The parity are indicated as + and - at the 8 TRIM points. Adapted from Ref. [33, 34]

and can be effectively described as [44, 45]:

$$H_{surf}(k_x, k_y) = C + A_2(\sigma^x k_y - \sigma^y k_x) \tag{1.1}$$

where C and A_2 are two material dependent constants. The corresponding eigenvalues can be easily calculated

$$\varepsilon^{\pm}(k_{//}) = C \pm A_2 k_{//} \tag{1.2}$$

where $k_{//} = \sqrt{k_x^2 + k_y^2}$. Related to the physical quantities, C determines the Dirac crossing point's energy position, and $A_2/\hbar$ gives the velocity $v = \frac{1}{\hbar}\frac{\partial \varepsilon}{\partial k}$ of the surface states. An important property emerging from this Hamiltonian is the so-called "spin-momentum locking". It can be demonstrated that the Pauli matrix vector $\vec{\sigma}$ in Equation 1.1 is proportional to the physical spin [32], and perpendicular to $k_{//}$. The spin direction depends on material properties such as the atomic SOC. For example, in the Bi_2Se_3 family of materials, the upper Dirac cone has a left-handed helicity when looking from above the surface [44], as shown in Fig. 1.4(b).

Similar massless (i. e. linearly dispersing) Dirac states can also be found in other

systems, such as graphene or any 2D Dirac system. In theory, the number of Dirac cones are different for 2D (even due to spin and valley degeneracy) and 3D (odd) systems. A single (or odd number) 2D Dirac cone without time-reversal symmetry breaking can exist only on the surface of a 3D topological insulator. In practice, using spin-integrated ARPES, we can not distinguish the helical surface states in 3D topological insulators and the massless Dirac states in a 2D Dirac system, like graphene. In order to resolve the spin texture of the helical surface states, spin-resolved ARPES (SARPES) is needed.

In recent years, the concept of 3D topology has been generalised from insulators to semi-metals and metals. As long as there are gaps in the bulk band structure, the parity analysis can be applied to the system. With the presence of strong enough SOC, parity inversion can be induced and new topological surface states emerge at the band gaps. Then depending on the number of such surface states, the system can be classified to be a strong or weak topological material. Chapter 4 will present a study of such topological metals, showing multiple Dirac cones and helical Dirac-node arcs.

1.3 Heavy fermion systems

Heavy fermion systems Heavy fermion systems belong to the class of strongly correlated electron systems, where the electronic localisation and delocalisation strongly compete with each other [46, 47].

In heavy fermion systems, the electronic localisation comes from the magnetic f electrons, while the electronic delocalisation comes from the highly conducting bands, usually of d character, crossing the Fermi level. Thus, a heavy fermion system can be viewed as a lattice of localised f electrons acting as magnetic scattering centers immersed in a quantum sea of mobile conduction electrons. Between two f electrons, the Ruderman-Kittel-Kasuya-Yosida (RKKY) exchange interaction [48–50] via the surrounding conduction electrons can drive the system into a magnetically ordered ground state at low temperatures. In most of the cases, it forms an antiferromagnetic phase. Here in our studied system $YbNi_4P_2$, it is a ferromagnetic phase [51, 52].

At absolute zero temperature T = 0 K, this magnetically ordered phase can be tuned to a paramagnetic and Fermi liquid regime via an adjustable parameter, such as pressure, magnetic field, or chemical doping, as shown in Fig. 1.5. A phase transition occurring at $T = 0$ K is called a **quantum phase transition**, as in this case, it is the quantum (not the thermal) fluctuations which drive the transition process, inducing an abrupt change in the ground state of the many-body system as an external parameter is varied.

Another interaction, the so-called Kondo effect, can compete with the RKKY interaction at low temperatures. In the Kondo effect, a free magnetic ion becomes screened by the spins of the conduction electron sea, and forms a spinless scattering center at low temperatures and low magnetic fields. This screening process is continuous, and takes place once the magnetic field, or the temperature drops below a characteristic energy scale called the Kondo temperature T_K, as shown in Fig. 1.6(a). If there is only one single magnetic scattering center (like a magnetic impurity), such a “quenched" magnetic moment acts as a strong elastic scattering potential for electrons, giving rise to an increase in resistivity, as illustrated in Fig. 1.6(b). This process is called “Kondo resonance" and its signature is the development of a sharp peak in the density of states at the Fermi level.

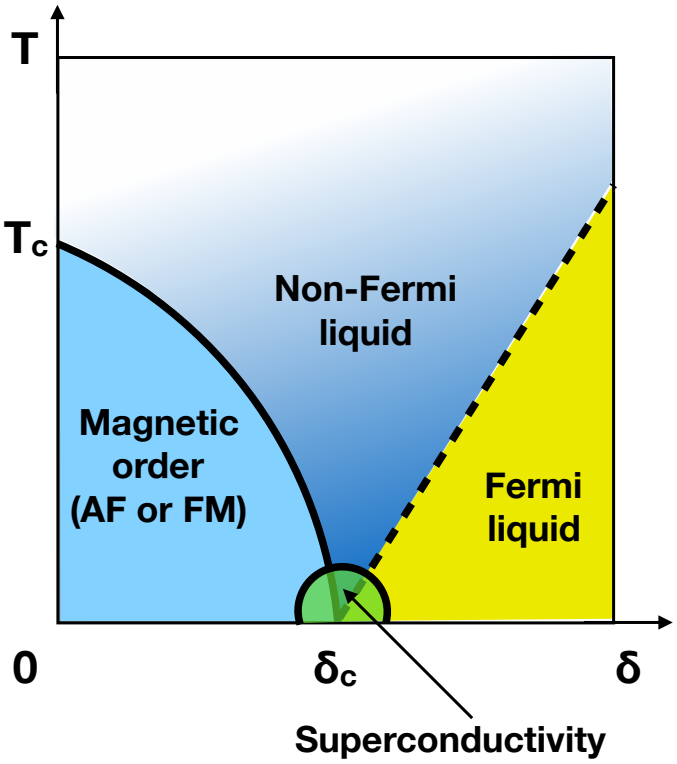

FIGURE 1.5: A sketch of the phase diagram of heavy fermion systems. Depending on the parameter δ (pressure, magnetic fields, or chemical doping), a quantum phase transition goes on at T = 0 K from a magnetically ordered phase to the Fermi liquid phase. In the neighbouring of the quantum critical point δ_c, spectacular phenomena, such as the so-called "non-Fermi liquid regime" [53] or the development of a superconducting pocket [54] are observed.

However, when the same process takes place at every site of the f electron lattice (see Fig. 1.6(c)), the Kondo resonance develops coherence. In this regime, also called the "Anderson lattice", the screened f electrons become itinerant quasiparticles with profoundly increased effective masses, thus need to be counted and increase the Fermi surface volume v_{FS} suddenly according to Luttinger theorem, as shown in Fig. 1.6(c). Experimentally, this coherence resonance will lead to a sudden drop of resistivity at very low temperatures [55].

The huge effective mass of the f electron quasiparticles results in fact from the hybridisation between f electron localised bands close to E_F and the mobile electron conducting bands, as shown in Fig. 1.7.

Quantum critical point When a system undergoes a quantum phase transition, the associated transition point is called a quantum critical point. Around this quantum critical point at finite temperature, the competition between the thermal fluctuations with an energy scale k_BT and the quantum fluctuations with an energy scale $\hbar\omega$, where ω is the characteristic quantum oscillation frequency, defines the quantum critical region where $\hbar\omega > k_BT$ and thus the quantum fluctuations dominate. In heavy fermion systems, the magnetic and electronic orders can become correlated in the quantum critical region, leading to the formation of exotic phases of electronic matter, such as non-Fermi liquids, which cannot be described in the framework of

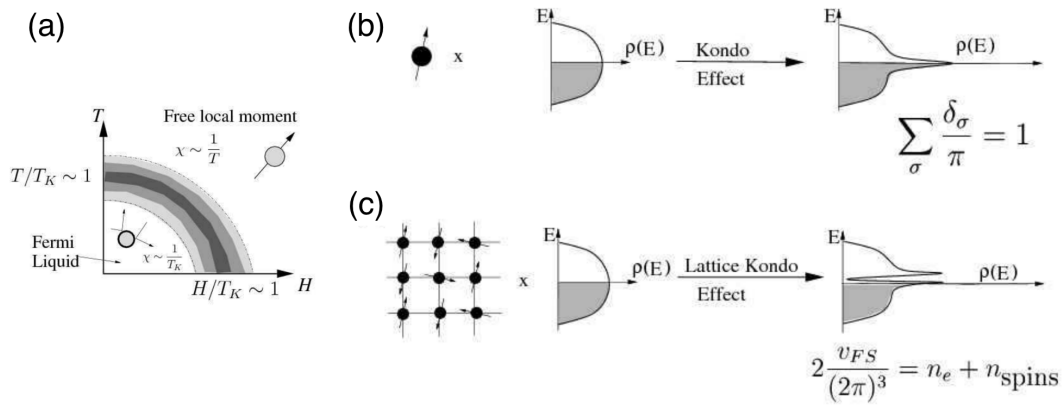

FIGURE 1.6: (a) In the Kondo effect, local magnetic moments are free at high temperatures and high magnetic fields, but become "screened" at temperatures and magnetic fields that are small compared with the "Kondo temperature" T_K forming resonant scattering centers for the electron fluid. The magnetic susceptibility χ changes from a Curie law $\chi \sim 1/T$ at high temperatures and saturates at a constant paramagnetic value $\chi \sim 1/T_K$ at low temperatures and fields. (b) The single-impurity Kondo effect leads to the development of a single fermionic level into the conduction sea, giving rise to a resonance in the conduction electron density of states. For this single magnetic site, the total density of the single fermionic level counts to be 1. (c) The lattice Kondo effect leads to the development of a fermionic resonance in the conduction sea in each unit cell. The elastic scattering off this lattice of resonances leads to the formation of a heavy electron band, of width T_K. Due to the emergence of itinerant quasiparticles from f electrons, whose density is counted as n_{spins}, the volume of the Fermi surface v_{FS} is increased suddenly.

Landau's theory of renormalised quasi-particles, or superconductivity, as aforementioned and illustrated in Fig. 1.5.

Specifically, the heavy-fermion compound $YbNi_4P_2$ shows a second-order quantum critical transition from a ferromagnetic phase to a paramagnetic phase upon partial substitution of P by about 10% As [52]. Theoretically, it is expected that such a ferromagnetic quantum critical point cannot exist in a clean metallic systems with dimensions larger than one. Instead, a ferrimagnetic phase transition of first order is supposed to happen in 2D or 3D clean metallic systems [57–61].

Thus, probing the dimensionality of the electronic structure of $YbNi_4P_2$ is essential to understand, from an experimental standpoint, the fundamental microscopic aspects of ferromagnetic quantum criticality. As shown in Fig. 1.8, the topography of the Fermi surface can serve as direct evidence of the dimensionality of the studied system. On one hand, the Fermi surface can be calculated in theory even if these calculations are not always valid in heavy fermion systems. On the other hand, the topography of Fermi surfaces can be measured, for instance, using de Haas-van Alphen (dHvA) quantum oscillations or ARPES. However, dHvA can only detect closed Fermi contours, i.e. only the 2D and 3D Fermi sheets. In order to probe open quasi-1D Fermi sheets, ARPES is the only experimental technique available today.

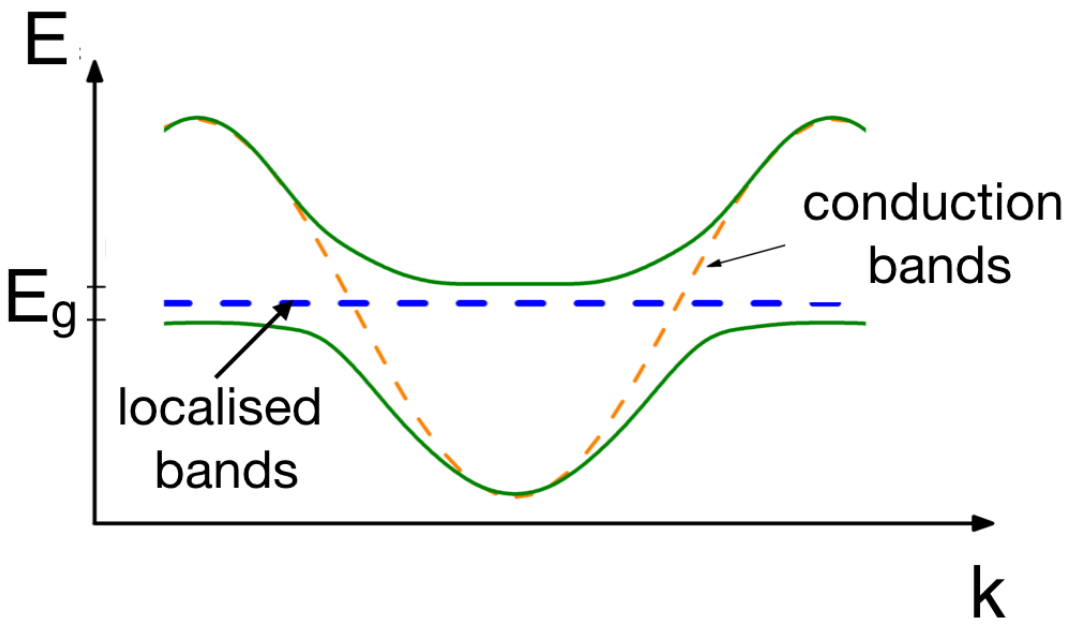

FIGURE 1.7: A sketch of the lattice Kondo effect. The blue and orange dashed lines are the original localised and conduction bands, respectively. After a hybridisation due to the coherent Kondo screening of the local moments by the sea of conduction electrons, an indirect energy (hybridisation) gap E_g forms. Adapted from Ref. [56].

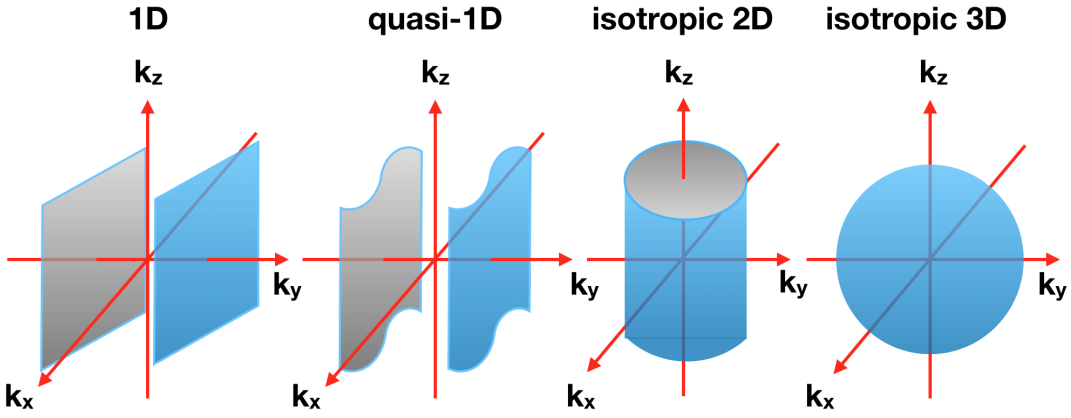

FIGURE 1.8: Sketch of the Fermi surface topographies in 1D, quasi-1D, 2D and 3D electron systems. A simple free-electron gas is used to illustrate the 2D and 3D cases. For the 1D and quasi-1D cases, the 1D chains are set along the y axis. In a quasi-1D system, the Fermi surface presents small dispersions in the directions perpendicular to the chains, induced by weak inter-chain coupling.

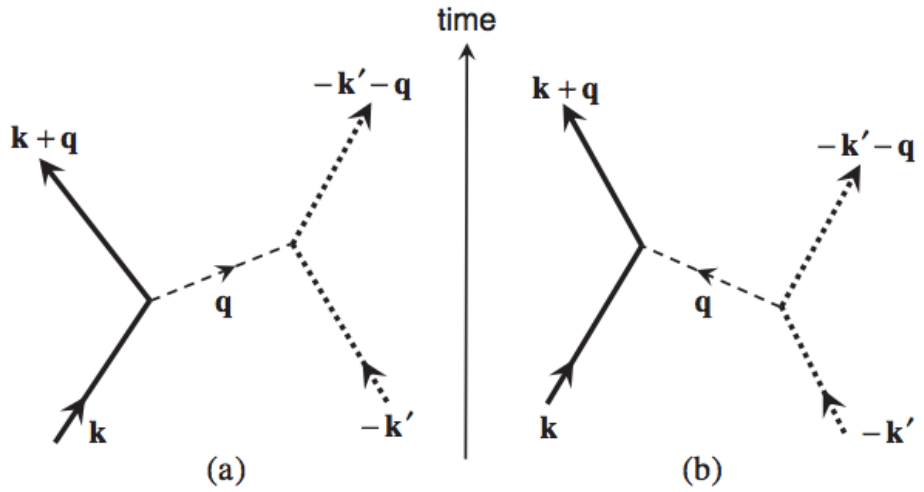

FIGURE 1.9: the diagrams of electron-phonon interaction:(a) the phonon emission process; (b) the phonon absorption process.

1.4 Electron-phonon interaction

The electron-phonon interaction is basic for the understanding of the electronic properties of matter, like renormalisation of the band structures, and many special phenomena in condensed matter physics, such as superconductivity and polarons.

The exchange of phonons between electrons can induce an attractive interaction, which is responsible for the forming of Cooper pairs in BCS theory. In recent years, there have been several reports showing that superconductivity can be realised in oxide-based 2DEGs [29, 62]. Moreover, there has been a recent revival of interests in polarons [22, 63–66], which are excited on the surface of transition metal oxides (TMOs). Thus, the study of this electron-phonon interaction in experimental data is meaningful and important for future research on 2DEGs.

The most common Hamiltonian including the electron-phonon interaction in a second quantisation form is [67]

$$H = \sum_{\mathbf{k},\sigma} \varepsilon_{\mathbf{k}} c^{\dagger}_{\mathbf{k}\sigma} c_{\mathbf{k}\sigma} + \sum_{\mathbf{q}} \hbar\omega_{\mathbf{q}} b^{\dagger}_{\mathbf{q}} b_{\mathbf{q}} + \frac{1}{\sqrt{N}} \sum_{\mathbf{k},\mathbf{q},\sigma} g(\mathbf{k},\mathbf{q})(b_{\mathbf{q}} + b^{\dagger}_{-\mathbf{q}}) c^{\dagger}_{\mathbf{k}+\mathbf{q}\sigma} c_{\mathbf{k}\sigma}, \tag{1.3}$$

where $c_{\mathbf{k}\sigma}$ is the annihilation operator of electrons with energy $\varepsilon_{\mathbf{k}}$ and spin σ, $b_{\mathbf{q}}$ is the annihilation operator of phonons with energy $\hbar\omega_{\mathbf{q}}$, and $g(\mathbf{k},\mathbf{q})$ is the coupling function. Here we consider only one phonon mode.

The theoretical tool to deal with this Hamiltonian is the Eliashberg theory and the associated equations, at the center of which is the Eliashberg coupling function, $\alpha^2F(\omega)$. Given the initial electron state with energy ε_i and momentum $\mathbf{k}$ and the emitted or absorbed phonon with energy $\omega(\mathbf{q})$, the Eliashberg function, which gives the electron-phonon coupling between the initial state and all other possible final states, can be written in the quasi-elastic approximation (the energy of phonons is neglected) as [68, 69]:

$$\alpha^2F(\omega) = \sum_{\mathbf{q},f} = \mid g^{i,f}(\mathbf{k},\mathbf{q}) \mid^2 \delta(\omega - \omega(\mathbf{q}))\delta(\varepsilon_i - \varepsilon_f). \tag{1.4}$$

From equation (1.4), one could interpret $\alpha^2F(\omega)$ as the phonon density of states weighted by the electron-phonon coupling matrix element.

The electron-phonon mass enhancement parameter λ, can be calculated with $\alpha^2F(\omega)$ and understood as the dimensionless coupling strength:

$$\lambda(\varepsilon_i, \mathbf{k}) = 2\int_0^{\omega_{max}} \frac{\alpha^2F(\omega)}{\omega} d\omega. \tag{1.5}$$

The ω_{max} is the maximum phonon frequency, and usually takes the value of Debye frequency ω_D. The factor 2 appears as both the absorption and emission processes are counted in.

The Eliashberg coupling function can also be related to the electron-phonon self-energy:

$$\begin{cases} \Im\Sigma(\omega, \mathbf{k}; T) = \pi \int_0^{\omega_{max}} \alpha^2F(\omega')[1 + 2n(\omega', T) + f(\omega + \omega', T) - f(\omega - \omega', T)]d\omega', \\ \lambda = -\frac{\partial \Re\Sigma}{\partial \omega} \mid_{\omega=0, T=0}, \end{cases} \tag{1.6}$$

where $n(\omega, T)$ is the Bose- Einstein distribution, $f(\omega, T)$ is the Fermi-Dirac distribution, and the mass enhancement parameter λ is calculated at the Fermi surface. In the limit $T \to 0$ that we will use, $\Im\Sigma$ can be simplified:

$$\Im\Sigma(\omega, \mathbf{k}; T = 0) = \pi \int_0^{min(\omega, \omega_{max})} \alpha^2F(\omega')d\omega'. \tag{1.7}$$

In principle, once the dispersion relation of the scattering phonon is given, the Eliashberg coupling function and the electron-phonon coupling strength can be calculated by applying some assumptions and approximations. In some simple models, such as the Einstein model and the Debye model, analytical results can be derived. In the analysis of the 2DES in ZnO that will be discussed later, we chose the 2D Debye model to analyse and understand our measured data, in which $\alpha^2F(\omega)$ can be calculated [70]:

$$\alpha^2F(\omega) = \begin{cases} \frac{\lambda}{\pi} \frac{\omega}{(\omega_D^2 - \omega^2)^{1/2}}, & \mid \omega \mid < \omega_D \\ 0, & \mid \omega \mid > \omega_D \end{cases} \tag{1.8}$$

Thus, from equation 1.7, we have

$$\Im\Sigma^{Debye-2D} = \begin{cases} \lambda\omega_D(1 - \sqrt{1 - (\frac{\omega}{\omega_D})^2}), & \mid \omega \mid < \omega_D \\ \lambda\omega_D, & \mid \omega \mid > \omega_D \end{cases} \tag{1.9}$$

with λ the mass enhancement parameter or the minus slope of $\Re\Sigma$ at $E - E_F = 0$. Fig. 1.10 is a schematic diagram showing the behavior of $\Re\Sigma$ and $\Im\Sigma$ based on the 2D Debye phonon model.

Since ARPES measures the spectral function, from which the self-energy can be extracted with some approximations and assumptions, the Eliashberg coupling function can be determined experimentally by applying some basic models. From this point of view, the ARPES technique is a suitable and powerful tool for the understanding of electron-phonon interaction in two-dimensional electron systems.

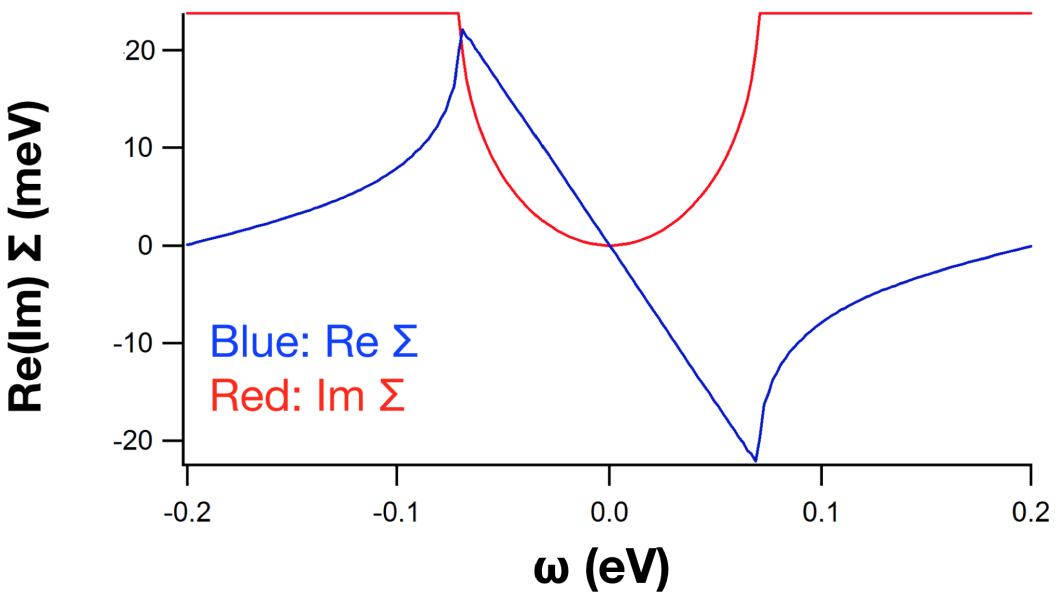

FIGURE 1.10: An example of the self-energy of electron-phonon coupling based on the 2D Debye phonon model.

1.5 Spin-orbit coupling

The spin-orbit coupling (SOC) is a relativistic interaction between a particle's spin and its motion inside an electronic potential via the associated magnetic field in the electron rest frame. In crystalline solids, this interaction is described by the Hamiltonian [71]

$$H_{SO} = \frac{\hbar}{4m_e^2c^2}\vec{\sigma}\cdot(\nabla V \times \vec{p}), \tag{1.10}$$

where m_e is the electron mass, c is the light speed in a vacuum, V is the periodic electric potential in crystal, and $\vec{\sigma}$ is the spin vector in the Pauli matrices basis.

If rewriting H_{SO} in a similar form as the Zeeman term in an external magnetic field $H_{Zeeman} = -\mu_B\vec{\sigma}\cdot\vec{B}_{ext}$, we have

$$H_{SO} = -\mu_B\vec{\sigma}\cdot\vec{B}_{eff} \tag{1.11}$$

with μ_B the Bohr magneton and $\vec{B}_{eff} = \frac{\vec{E}\times\vec{p}}{2m_ec^2}$ the effective magnetic field due to orbital motion.

Depending on the type of inversion asymmetry in the system, there are two kinds of such effective magnetic field:

1. Dresselhaus contribution due to the bulk inversion asymmetry (BIA):

$$\vec{B}_D \propto \gamma\begin{pmatrix} k_x \\ -k_y \end{pmatrix}$$

with eigenvalues $\pm\gamma\sqrt{k_x^2+k_y^2} = \pm\gamma k_{//}$.

2. Rashba contribution due to the structure inversion asymmetry (SIA) caused by macroscopic confining potential, e.g. at the surface:

$$\vec{B}_R \propto \alpha \begin{pmatrix} k_y \\ -k_x \end{pmatrix}$$

with eigenvalues $\pm\alpha\sqrt{k_x^2 + k_y^2} = \pm\alpha k_{//}$.

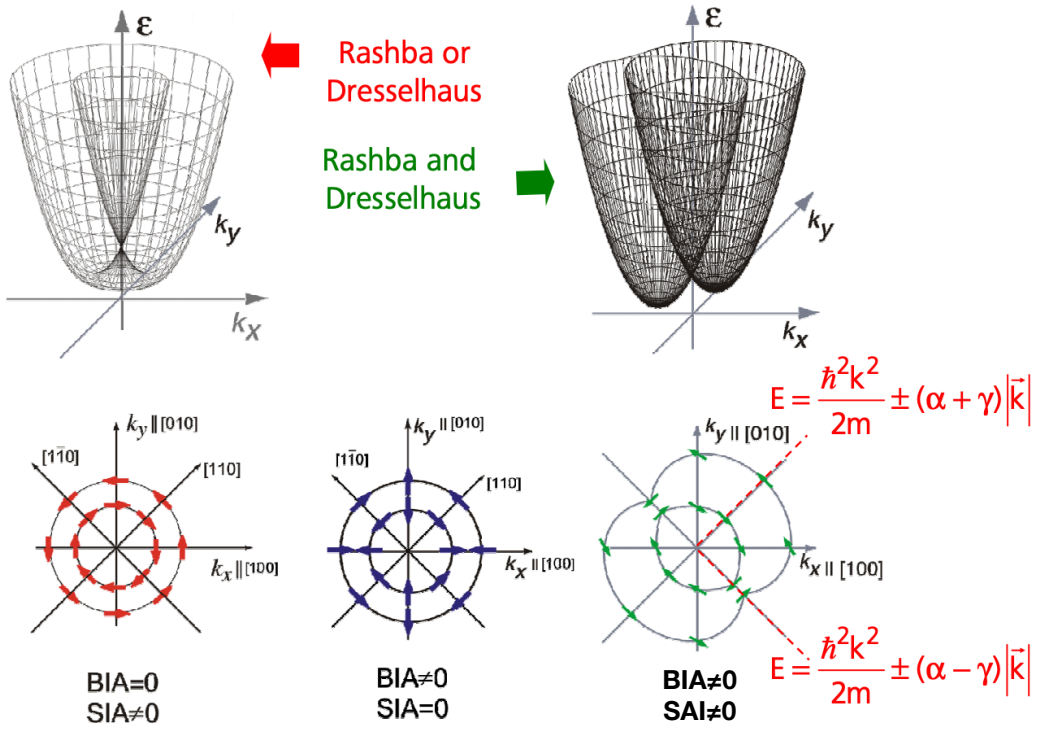

FIGURE 1.11: Left: the band structure (dispersions above and spin textures below) of a nearly free electron system with only the Dresselhaus or Rashba spin-orbit coupling (SOC). Though the energy-momentum dispersions behave the same, the spin textures are fully different between these two kinds of SOC contributions. Right: the band structure (dispersions above and spin textures below) of a nearly free electron system with both the Dresselhaus and Rashba SOC present. Taken from Ref. [72].

Fig. 1.11 demonstrates diagrammatically the change of the band structure and spin texture of a nearly free electron system due to the spin-orbit coupling.

Chapter 2

Experimental techniques

This thesis presents an experimental exploration of low-dimensional electronic systems. The main experimental technique used throughout this work is the angle-resolved photoemission spectroscopy (ARPES). The first section will introduce the fundamental and practical aspects of ARPES, and will illustrate its use with two original study cases from my work. A related technique, spin-resolved ARPES (SARPES) used for the study of topological surface states in Chapter 4, will be introduced in the second section. Another two supplementary techniques, MBE and LEED, mainly used during the sample surface preparation processes, will be discussed in the third section.

2.1 ARPES

2.1.1 Standard ARPES: setup

This brief introduction to ARPES setups and the working mechanism is based on T. RÖdel's doctoral thesis [2], C. Bareille's doctoral thesis [73] and A. F. Santander-Syro's habilitation à diriger des recherches [74].

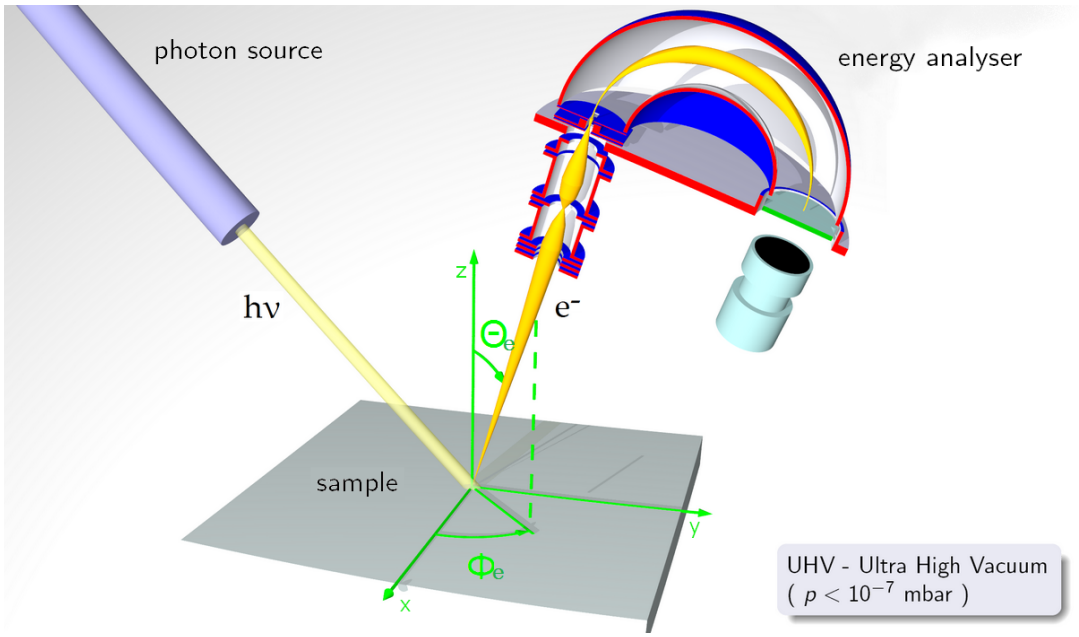

FIGURE 2.1: Schematic representation of an ARPES experiment. Taken from Ref. [75].

Fig. 2.1 is a sketch of the usual ARPES experimental setup. The incident light beam with energy $h\nu$ excites the electrons in the occupied states to the vacuum states.

Some of these photo-excited electrons can escape the surface and enter into the analyser to be measured. By applying some assumptions and approximations, information about the band structure and interactions, can be inferred from the measured energies and momenta of the photo-emitted electrons.

Basically speaking, the ARPES setup is composed of three parts [74]:

1. a monochromatic light source, which can be the synchrotron radiation, gas-discharge lamps, or frequency-multiplied UV lasers working in quasi-continuous mode (pulsed lasers will be good for time-resolved photoemission, but their energy resolution will be bad). The usual energy range is $10 - 100$ eV. These three kinds of light sources have their own advantages and limitations. For example, the most commonly used synchrotron radiation can provide a continuous energy range while the latter two can only produce photons with some specific energies but have better energy resolutions than the synchrotron radiation.

2. a cryo-manipulator system, where the sample can be cooled down to low temperatures (typically < 20 K). By adjusting the sample's spatial position (x, y, z), the experimentalist can find the focal position of the light beam and select the area on the sample surface for measurement. By rotating around the local $x/y/z$ axes, the experimentalist can reorient the sample with respect to the detector and explore the momentum space.

3. an electron detector or the so-called "analyser". The most widely used detector in ARPES experiments is the hemispherical angle-resolved electron analyser, which consists of the electron lens related to the angular resolution or momentum resolution, the deflector giving the energy resolution, and the detector recording the impacts per second of electrons as a function of their kinetic energy and of their angle along the perpendicular direction defined by the analyser entrance slit.

Additionally, the ARPES experiments should be carried out in an ultra-high vacuum lower than 10^{-10} Torr to protect the surface of the sample from unwanted contamination (which would scatter the outgoing electrons) and increase the mean free path of the photo-emitted electrons.

Supposing the detector receives an electron with energy E_{kin} from an emission angle θ_e excited from an occupied state at binding energy E_{bind} by a photon with energy $h\nu$, we have (see Fig. 2.1 and Fig. 2.2(b)):

$$\begin{cases} E_{kin} = h\nu - |E_{bind}| - \Phi \\ k_{\parallel}^{out} = \sqrt{\frac{2m_e}{\hbar^2}} E_{kin}^{1/2} \sin(\theta_e) \\ k_{\perp}^{out} = \sqrt{\frac{2m_e}{\hbar^2}} E_{kin}^{1/2} \cos(\theta_e) \end{cases} , \tag{2.1}$$

where Φ is the "work function" of the sample, *i.e.*, the energy of the vacuum level with respect to the Fermi level E_F, m_e is the free electron mass. As the photoemission process is invariant under translations parallel to the sample surface, the projection of the electron momentum in this plane is conserved (within a reciprocal lattice vector) if neglecting the photon momentum [1], thus being the same outside and inside the sample: $k_{\parallel} = k_{\parallel}^{in} = k_{\parallel}^{out}$.

[1] Typical photon energies for an ARPES experiment are $E = 10 - 100$ eV. The momentum $k = E/\hbar c$ of a 100 eV photon is 0.05 Å^{-1}. The typical size of the Brillouin zone of a solid (lattice parameter 1-10 Å) is one to two orders of magnitude larger.

Assume the final state E_f of the photoelectron inside of the sample is a free electron state, as shown in Fig. 2.2(a):

$$E_f = \frac{\hbar^2}{2m_e}k^2 - |E_0|, \text{ with } k^2 = k_\perp^2 + k_\parallel^2, \tag{2.2}$$

where E_0 is the bottom of the last occupied band (Fig. 2.3(a)). Since final state energy $E_f = h\nu - |E_{bind}| = E_{kin} + \Phi$, we can calculate the perpendicular momentum inside the sample:

$$k_\perp^{in} = \sqrt{\frac{2m_e}{\hbar^2}(E_{kin} + \Phi + |E_0|) - k_\parallel^2} = \sqrt{\frac{2m_e}{\hbar^2}(E_{kin}\cos^2\theta_e + V_0)}, \tag{2.3}$$

where $V_0 = \Phi + |E_0|$ is defined as the inner potential (see Fig. 2.3(a)) - the energy from the bottom of the last occupied band to the vacuum level. As illustrated in Fig. 2.2(a), with the free-electron final state approximation, the photoelectron passes through the surface as if penetrating a V_0 step-like potential.

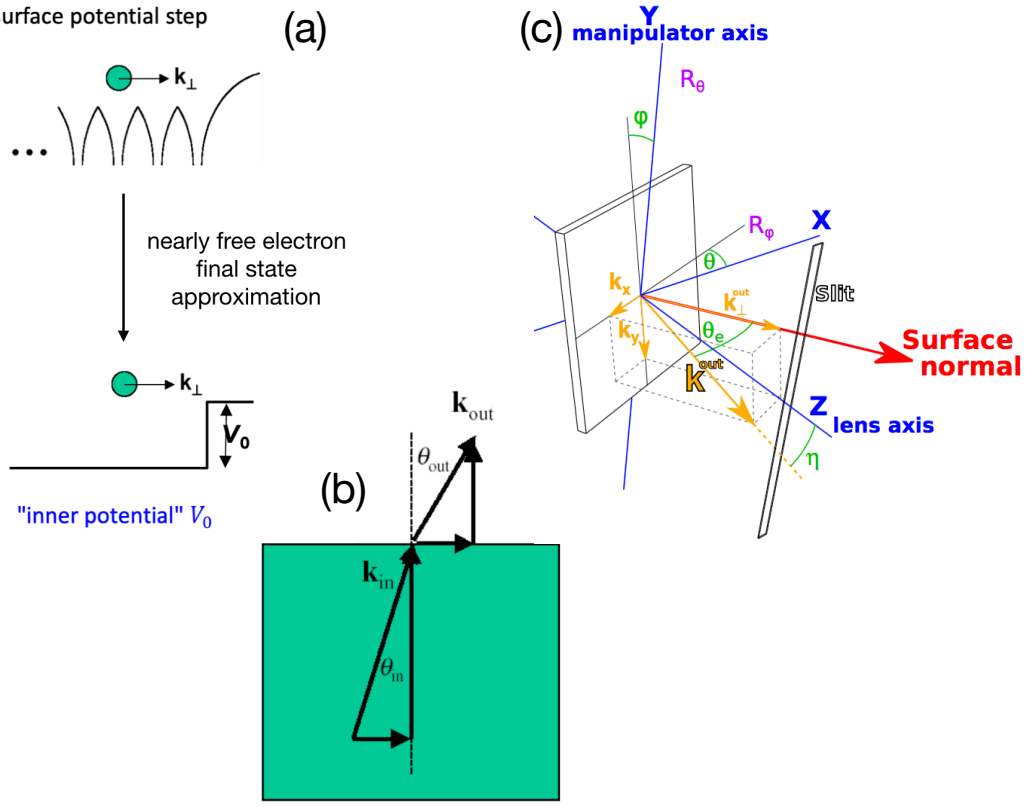

FIGURE 2.2: (a) A diagrammatic sketch of the transmission through the surface via an inner potential V_0 with the nearly free electron final state approximation. (b) A diagrammatic sketch of the surface diffraction process conserving the in-plane momentum $\vec{k}_{//}$ while altering the out-of-plane momentum $\vec{k}_\perp$. Adapted from Ref. [76]. (c) Related angles to control the sample orientation and calculate the momenta. η is the angle of electron impact along the detector slits. θ_e is the angle of electron emission from the surface normal. θ and φ are rotation angles of the sample in the laboratory reference frame. Adapted from Ref. [73].

Transformed to the laboratory reference frame as shown in Fig. 2.2(c), the momentum of the electron in its initial state in the solid, before being photo-emitted, can be expressed as:

$$\begin{cases} k_x = -\sqrt{\frac{2m_e}{\hbar^2}} E_{kin}^{1/2} \sin\theta \ \cos\eta, \\ k_y = \sqrt{\frac{2m_e}{\hbar^2}} E_{kin}^{1/2} (\sin\eta \ \cos\varphi + \cos\theta \ \cos\eta \ \sin\varphi), \\ k_z = \sqrt{\frac{2m_e}{\hbar^2}} [E_{kin}(\cos\theta \ \cos\eta \ \cos\varphi - \sin\eta \ \sin\varphi)^2 + V_0]^{1/2}. \end{cases} \tag{2.4}$$

Usually in practical experiments, the angle φ is fixed and set to zero most of the times for simplicity. The measurement result is an electron intensity map $I(E_{kin}, \eta)$ with a given θ and a given photon energy $h\nu$. It is easy to transform η to $k_{\parallel} = \sqrt{k_x^2 + k_y^2}$ by using equation 2.4. The out-of-plane momentum $k_{\perp}$ can also be explored through the variation of E_{kin} by changing the photon energy $h\nu$ (see equation 2.3).

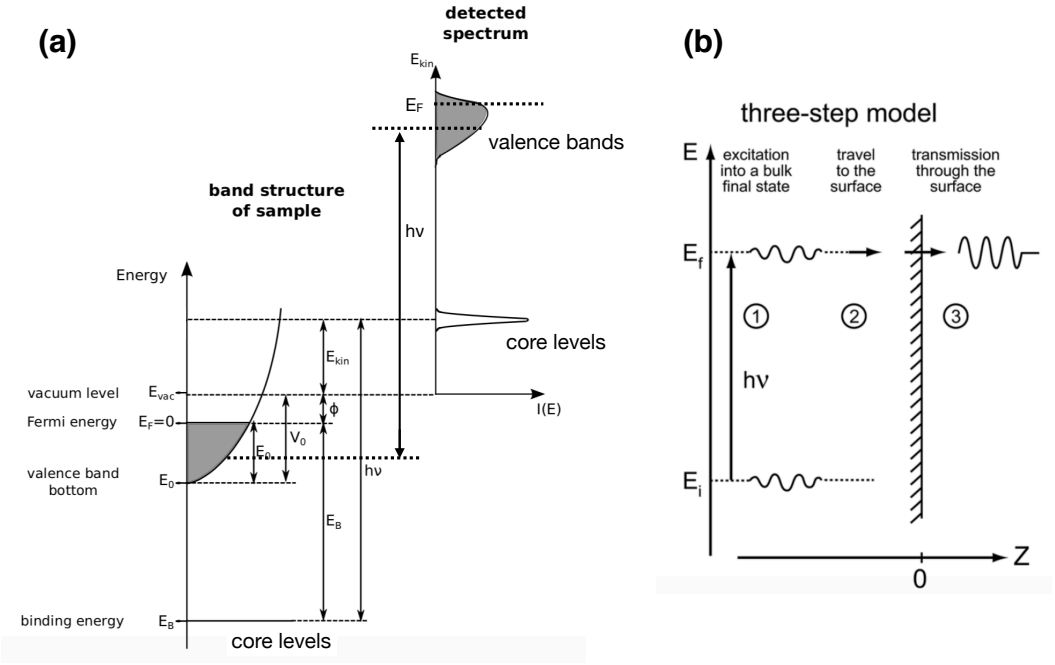

FIGURE 2.3: (a) A schematic view of the photoemission process. On the left side, a simplified band structure (core levels and valence bands) of a sample is shown. The electron states are occupied up to the Fermi level E_F which is defined as the zero energy. The kinetic energy E_{kin} of those electrons in a vacuum is directly measured by the analyser. The work function Φ is the energy between the E_F and the vacuum level E_{vac}. E_0 the valence band bottom, together with E_{vac}, defines the inner potential V_0. On the right side, the detected spectrum of the band structure is shown. Taken from Reinert and Hüfner [77]. (b) A schematic view of the three-step model [76].

Three-step model

In order to understand the measured photo-emitted electron intensity I, the so-called "three-step model" was proposed first in by Berglund and Spicer [78]. In order to fill the gap between the spectrum obtained from first-principle calculations and the experimental one, a many body theory of photoemission, the one-step model, which was first proposed by Pendry and co-workers [79–81], is needed. The one-step model treats the three steps in the Three-step model into a single quantum-mechanically coherent process including all multiple-scattering events. As a pedagogical introduction to the working mechanism of ARPES, the three-step model is discussed below.

The process of the excitation of an electron by a photon to the propagation of the electron in a vacuum is modelled into the following 3 steps (see Fig. 2.3(b)), which are assumed to be independent of each other:

1. optical excitation of the initial electron (Bloch) state into a bulk final state
2. propagation to the surface
3. transmission through the surface into vacuum by overcoming a potential barrier

1st step: optical excitation In the first step, one electron is excited due to the perturbation from the incoming light field. Under the dipole approximation (the electromagnetic field of the perturbation light is homogeneous over atomic dimensions, *i.e.* $\vec{A}(r) = \vec{A}$, where $\vec{A}$ is the vector potential of the electromagnetic field) and by neglecting non-linear terms in $\vec{A}$, the light-matter interaction Hamiltonian can be approximated to be

$$H_{int} \approx -\frac{e}{mc}\vec{A}\cdot\vec{p} \tag{2.5}$$

where c is the speed of light in a vacuum, and $\vec{p}$ is the momentum operator.

According to Fermi's golden rule, the probability of this optical excitation process is:

$$w_{fi} = \frac{2\pi}{\hbar}|<\Phi_f^N|-\frac{e}{mc}\vec{A}\cdot\vec{p}|\Phi_i^N>|^2\delta(E_f^N - E_i^N - h\nu) \tag{2.6}$$

with $\Phi_{i(f)}^N$ the initial (final) wave function of the N electron system, $E_{i(f)}$ the energy of the initial (final) state and $h\nu$ the photon energy. Note that the momentum conservation term is neglected as the photon momentum in the UV (where our ARPES experiments were done) is small compared to the momentum of the excited electron (*i.e.*, compared to the typical magnitude of reciprocal-lattice vectors) thus $\vec{k}_f = \vec{k}_i$ in a reduced Brillouin zone.

The N-body wave function $\Phi_{i(f)}^N$ can be separated into a 1-electron wave function $\phi_{i(f)}^k$ and a $(N-1)$-electron wave function except an asymmetry factor due to the indistinguishability of Fermions. Under the sudden approximation, the photoelectron has "no time" to interact with the system left behind, thus being decoupled from the remaining $(N-1)$-electron system. The final state wave function of the $(N-1)$-electron system left behind can then be approximated as an eigenstate of the unperturbed $(N-1)$-electron Hamiltonian with eigenfunction $|\Phi_m^{N-1}>$ and energy E_m^{N-1}. As a result, w_{fi} can be further written as

$$w_{fi} = \frac{2\pi}{\hbar}|M_{fi}^k|^2|<\Phi_m^{N-1}|\Phi_i^{N-1}>|^2\delta(E_{kin} + E_m^{N-1} - E_i^N - h\nu) \tag{2.7}$$

with $M_{fi}^{k} =< \phi_f^k| - \frac{e}{mc}\vec{A}\cdot\vec{p}|\phi_i^k >$ called matrix elements, $\Phi_{i(m)}^{N-1}$ the (N-1)-electron wave function of the originally unperturbed (afterward excited) system, and E_{kin} the kinetic energy of the exited electron.

By summing over the indexes, we have the total electron flux after this first step:

$$I(E_{kin},\vec{k}) = I_0 \sum_{f,i} |M_{fi}^{k}|^2 \sum_{m} | < \Phi_m^{N-1}|\Phi_i^{N-1} > |^2 \delta(E_{kin} + E_m^{N-1} - E_i^N - h\nu) \tag{2.8}$$

with I_0 the originally incoming photon flux.

2nd step: propagation to the surface During the second step, the electron flux will be reduced due to the inelastic scattering, which leads to a continuous background in the spectra recorded in an experiment. This flux decay is described in an exponential way by the inelastic mean free path $\lambda(E)$ of an electron in a solid:

$$I(d) = I * e^{-d/\lambda(E)} \tag{2.9}$$

The behaviour of λ(E) in energy is universal for most of the materials. For ARPES measurements, the energy of the photons is around $20-100$ eV, thus the corresponding inelastic mean free path is around $5-10$ Å. This explains why ARPES is a surface sensitive technique.

3rd step: transmission through the surface In the third step, the electron needs minimum energy to overcome the potential barrier of the surface (inner potential V_0). During this process, the in-plane momentum $\vec{k}_{//}$ is conserved while the out-of-plane momentum $\vec{k}_{\perp}$ is changed due to the diffraction at the surface barrier, as shown in Fig. 2.2(a).

Relation to the single particle spectral function

In Equation 2.8, the latter two terms together define the so-called single particle spectral function

$$A(\omega,\vec{k}) = \sum_{m} | < \Phi_m^{N-1}|\hat{c}_{\vec{k}}|\Phi_i^N > |^2 \delta(\omega + E_m^{N-1} - E_i^N) \tag{2.10}$$

with $\omega = E_{kin} - h\nu$ and $\hat{c}_{\vec{k}}$ the annihilation operator describing the process in which an electron with momentum $\vec{k}$ and energy ω is removed from an N-electron system in the ground state Φ_i^N. The spectral function quantifies the probability that an electron of energy ω and momentum $\vec{k}$ be removed (direct photoemission) or added (inverse photoemission) to the system.

Thus, including the Fermi-Dirac distribution of electrons $f(\omega,T)$ at a finite temperature T, the final detected electron intensity can be expressed as

$$I(\omega,\vec{k}) \propto \sum_{f,i} |M_{fi}^{k}|^2 \times A(\omega,\vec{k}) \times f(\omega,T) \tag{2.11}$$

A typically measured photoemission intensity map is shown in FIG. 2.4(a)

The removal spectral function is theoretically defined as the imaginary part of the retarded Green function $A = -\frac{1}{\pi}\Im G^R$. In turn, the retarded single particle Green

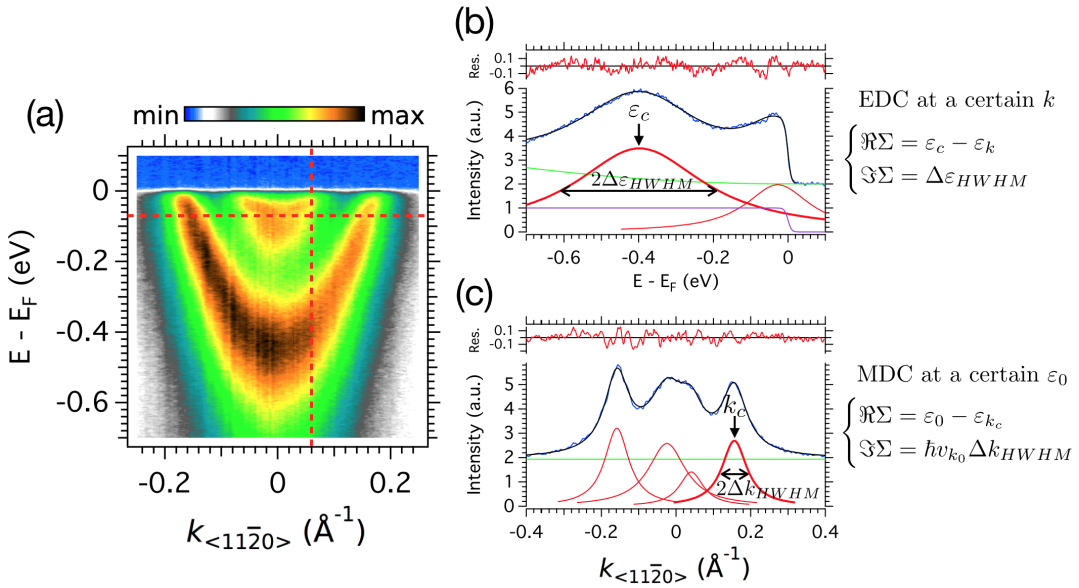

FIGURE 2.4: (a) ARPES intensity map showing in color scale the number of photoelectrons detected *vs* binding energy and momentum parallel to the surface for the 2-dimensional-electron-gas (2DEG) at the AlO_x/ZnO interface [82]. (b) A typical energy-distribution curve (EDC) which is proportional to $f(\omega) \times A(\omega, k)$ with $k = 0.06 Å^{-1}$ corresponding to the vertical dashed red line in panel (a). From the Lorentzian peak fit, the peak position ε_c and the corresponding half width at half maximum (HWHM) can be extracted and further used to determine the self-energy. (c) An example of a momentum-distribution curve (MDC) which is proportional to $A(\omega, k)$ with binding energy $E_{bind} = -\omega = 70$ meV corresponding to the horizontal dashed red line in panel (a). From the Lorentzian peak fit, the peak position k_c and the corresponding half width at half maximum (HWHM) can be extracted and further used to determine the self-energy. Blue: experimental data; black: overall fit; red: Lorentzian peaks used; green: quadratic or constant background; purple: the Fermi-Dirac distribution with an effective temperature 50 K.

function of an N-body system can be expressed as

$$G^R(\omega, \vec{k}) = \frac{1}{\omega^+ - \varepsilon_{\vec{k}} - \Sigma(\omega, \vec{k})} \tag{2.12}$$

with $\Sigma(\omega, \vec{k})$ the so-called self-energy and $\varepsilon_{\vec{k}}$ the unrenormalized dispersion relation.

Thus, we have

$$A(\omega, \vec{k}) = -\frac{1}{\pi} \frac{\Im\Sigma(\omega, \vec{k})}{(\omega - \varepsilon_{\vec{k}} - \Re\Sigma(\omega, \vec{k}))^2 + (\Im\Sigma(\omega, \vec{k}))^2}. \tag{2.13}$$

In general, the self-energy Σ is a function of both the energy ω and the wave vector $\vec{k}$, making it complicated to extract Σ from the photo-emitted electron intensity. The methods that have been applied to do so are closely related to the traditional measuring modes of ARPES, energy distribution curves (EDCs) and momentum distribution curves (MDCs). An EDC is the photoemission intensity as a function of electron energy with a fixed wave vector $\vec{k}$, while an MDC is the photoemission

intensity as a function of $\vec{k}$ at certain electron energy. A typical EDC and MDC are demonstrated in FIG. 2.4(b) and (c).

In the EDC case, if Σ is independent or weakly dependent of ω, the spectral function becomes quite simple, just a Lorentzian function with $\Im\Sigma$ its half-width at half maximum(HWHM). In practice, the product of a Lorentzian function and a Fermi-Dirac distribution function is used to fit the EDC photoemission profile lines to extract the information of the self-energy Σ as shown in the inset of Fig. 2.4(b).

In the MDC case, if $\Im\Sigma$ is independent of $\vec{k}$, with a locally linearised bare band dispersion $\varepsilon_{\vec{k}} = \varepsilon_0 + \hbar v_0(k - k_0)$, where $v_0 = \frac{1}{\hbar}\frac{\partial\varepsilon}{\partial k}\,|_{k_0}$ is the local bare band velocity, the photoemission intensity

$$I \propto \frac{1}{(k - k_0 + \frac{\Re\Sigma}{\hbar v_0})^2 + (\frac{\Im\Sigma}{\hbar v_0})^2} \tag{2.14}$$

behaves as a Lorentzian function with a peak position $k_c = k_0 - \frac{\Re\Sigma}{\hbar v_0}$ and a HWHM $\Delta k = \frac{\Im\Sigma}{\hbar v_0}$, both of which can be determined by fitting the photoemission profile peaks with a Lorentzian function. This allows thus, in principle, a complete determination of the self-energy, as shown in the inset Fig. 2.4(c).

In both cases, a knowledge of the bare dispersion is needed, but as interactions cannot be turned off in a material, such bare band dispersion cannot be measured independently and sometimes guessing it is not obvious. Moreover, a slight modification of the bare dispersion will change the final result of the self-energy greatly when the concerned interaction is small. Nevertheless, by applying the Kramers-Kronig relation obeyed by Σ [83]

$$\begin{cases} \Re\Sigma(\omega) = \frac{1}{\pi} P \int_{-\infty}^{+\infty} \frac{\Im\Sigma(\omega')}{\omega' - \omega} d\omega' \\ \Im\Sigma(\omega) = -\frac{1}{\pi} P \int_{-\infty}^{+\infty} \frac{\Re\Sigma(\omega')}{\omega' - \omega} d\omega' \end{cases}, \tag{2.15}$$

the obtained result of the self-energy can be evaluated in a self-consistent way. One can thus always adjust the model, the bare dispersion and the parameters until the self-consistency of the extracted self-energy is reached.

To perform such self-energy analysis, both the EDCs and MDCs are used in practice but in different energy regimes and for different aims. More details are discussed below.

2.1.2 Standard ARPES - original study case 1: electron-phonon interaction in a 2DES at the surface of ZnO

As introduced above, the ARPES measured spectrum is a direct fingerprint of the spectral function $A(\omega, \vec{k})$, through which the many-body interactions, *i.e.* the self-energy Σ of a many-body system can be extracted. In the following part of this subsection, I am going to show how the electron-phonon interaction is extracted and analysed in our ARPES data of a two-dimensional electron system (2DES) at the interface of Al(2Å)/ZnO($000\bar{1}$). I performed this analysis work right after joining the team, using ARPES data obtained by Tobias Rödel, the preceding Ph.D. student in our group. The results were published in Ref. [82].

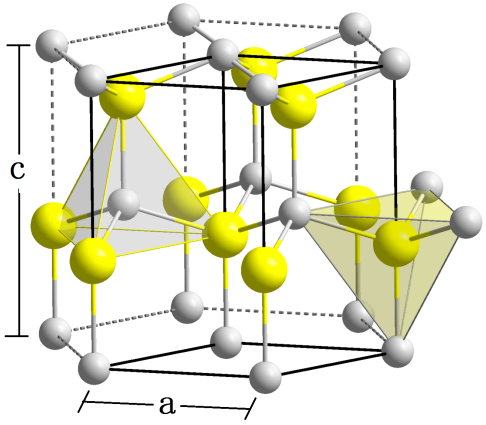

FIGURE 2.5: The crystal structure of hexagonal wurtzite ZnO with lattice parameters $a = 3.25$ Å, $c = 5.2$ Å. Adapted from Ref. [84].

ZnO

ZnO, whose crystal structure is shown in Fig. 2.5, is a direct bandgap semiconductor intensively studied for its many special properties, like large bandgap at room temperature and strong near-band-gap excitonic absorption [85], and its possible novel applications, such as transparent conducting electrodes for flat panel displays and solar cells, field emitters and spintronic devices [86]. In the case of the experiments I analyzed, the O-terminated $(000\bar{1})$ surface of ZnO is covered, by means of MBE, with 2 Å of Al, which introduces oxygen vacancies into the surface after oxidising into AlO_x once in contact with the ZnO. Each oxygen vacancy leaves behind 2 electrons, which can partially dope the empty 4*s* states of Zn, forming a 2D electron gas on the surface due to a confining potential exerted by the positive background of the formed oxygen vacancies in the normal direction. Since the data was measured along the *c*-direction and no surface reconstruction was observed experimentally, the in-plane lattice parameter concerned here is $a = 3.25$ Å.

ARPES spectrum of the 2DES

FIG. 2.6(a) presents the electron intensity map $I(E - E_F, k)$ obtained in a high-statistics measurement at the Γ point of the first Brillion zone along the in-plane $k_{<11\bar{2}0>}$ direction with these conditions: $\Delta E = 2$ meV, $h\nu = 25$ eV, $T = 7$ K.

There are two electronic bands measured, which will be called the inner band and the outer band. These two bands correspond to two quantum well states in a simplified physical picture as discussed later. The inner band is quite shallow and strongly renormalised, which makes it difficult to use this band to perform the self-energy analysis. So we focus on the outer band and carry out the self-energy analysis first. Afterward, by assuming that the two bands have the same bare dispersion except for a constant energy shift, which is the energy difference between two consecutive quantum-well states, and the same self-energy renormalisation assuming that they are subject to the same electron-phonon interaction, we reconstruct the inner band to compare with the experimental result.

Before doing the self-energy analysis, one must take care of the energy scales. As shown in FIG. 2.6(a), the energy range of the outer band is about $0 - 500$ meV, while for the inner band it is about $0 - 100$ meV. On the other hand, the typical energy

of phonons in any material, and certainly in ZnO, is usually smaller than 100 meV. So for the outer band near the bottom, the renormalisation due to electron-phonon interaction can be neglected. For the low energy part close to the Fermi level, a renormalisation of both bands can be clearly observed in the form of a “kink" or deformation of the spectrum at binding energy around 70 meV.

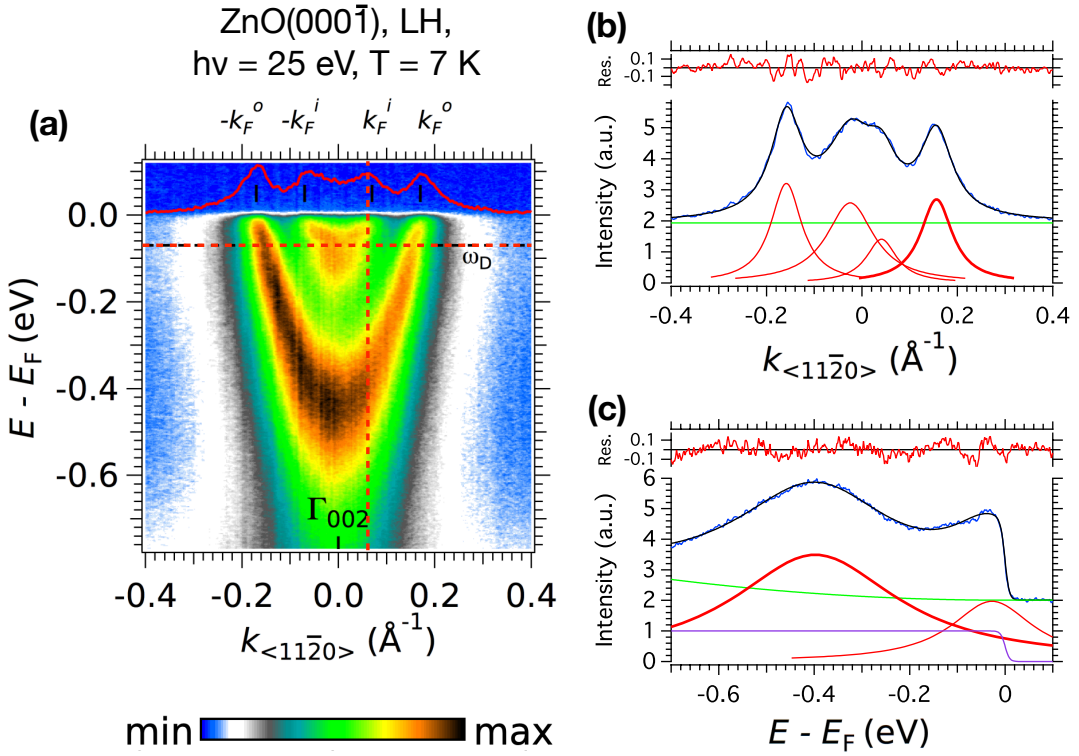

FIGURE 2.6: (a) Energy-momentum ARPES intensity map around the bulk Γ_{002} point along the in-plane $k_{<11\bar{2}0>}$ direction, measured with linear-horizontal light polarization at $h\nu = 25$ eV and $T = 7$ K [82]. The red curve is the MDC over $E_F \pm 5$ meV. The black vertical bars show the Fermi momenta k_F^i and k_F^o of the inner and outer subbands. The Fermi liquid is coupled to phonons with a characteristic Debye energy $\omega_D \approx 70$ meV shown by the horizontal, dashed red line. (b) An example of a momentum-distribution curve (MDC) taken at binding energy $E_{bind} = -\omega = (70 \pm 2)$ meV indicated with the horizontal dashed red line in panel (a). (c) A typical energy-distribution curve (EDC) taken at $k = (0.06 \pm 0.002)$ Å^{-1} corresponding to the vertical dashed red line in panel (a). From the Lorentzian peak fit, the peak positions and the corresponding half widths at half maximum (HWHM) can be extracted and further used to determine the self-energy. Blue: experimental data; black: overall fit; red: Lorentzian peaks used; green: quadratic or constant background; purple: the Fermi-Dirac distribution with an effective temperature 50 K.

Self-energy analysis

Determination of $\Im\Sigma$ and $\Re\Sigma$ The first step of the self-energy analysis is to use the EDC and MDC methods described previously to fit the peak positions and widths (see Fig. 2.6(b) and (c)). In the case of ZnO, due to the energy scales discussed above

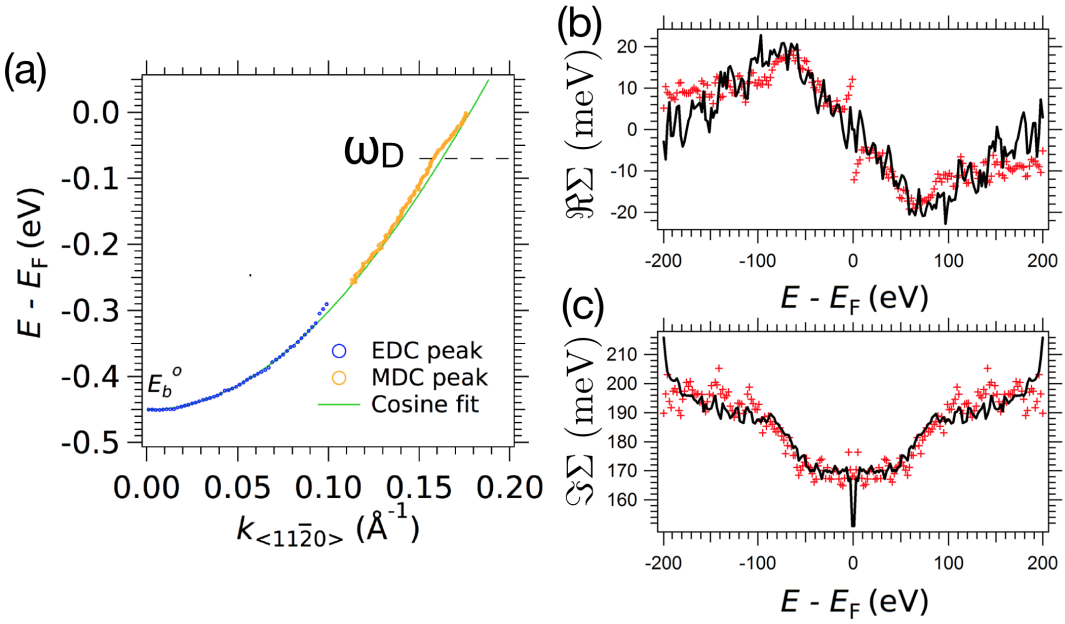

FIGURE 2.7: (a) Maxima of the EDC (blue circles) and MDC (orange circles) peaks for the outer subband of the 2DES at the Al(2Å)/ZnO(000$\bar{1}$) interface [82]. Only data for the right branch (positive momentum region) are shown. The continuous green curve is a cosine fit to the data representing the non-interacting electron dispersion of this subband. (b, c) The self-energy extracted from the left branch. The red markers are the results of $\Re\Sigma$ ($\Im\Sigma$) determined directly from the experimental data, and the black lines are the results of Kramers-Kronig transform from the corresponding $\Im\Sigma$ ($\Re\Sigma$).

and the broadening due to experimental resolution, the EDC method is applied only to the bottom of the outer band to extract its bare dispersion, while for the part close to the Fermi level, we use the MDC method to extract the self-energy information. The fitted peak positions are shown as blue markers for EDCs and yellow markers for MDCs in Fig. 2.7(a).

As the electron-phonon interaction is negligible at the bottom of the outer band, the EDC peak positions at the bottom of the outer band can be used to obtain a good approximation for the bare band dispersion, which is crucial to determine the final self-energy. The form of the bare band we choose is a tight binding cosine band

$$\varepsilon(k) = A + B\cos(Ck) \tag{2.16}$$

where $C = \sqrt{3}a = 5.63$ Å^{-1} is fixed in ZnO. The fit result $\varepsilon(k) = 0.539 - 0.989\cos(5.63k)$ is shown as the green line in FIG. 2.7(a). Thus, the binding energy of the band bottom is $E_b^o = 450$ meV. The effective mass at the bottom $k = 0$ Å^{-1} can be calculated with our fitted bare band:

$$\frac{m^*}{m_e} = \frac{\hbar^2}{2m_e}\frac{k}{\partial\varepsilon/\partial k}\,|_{k=0} = 0.243, \tag{2.17}$$

which agrees well with the theoretical estimation of the effective mass in ZnO perpendicular to $\vec{c}$ axis (for example, $m_{e\perp} = 0.24m_e$ [87] and $m_{e\perp} = 0.25m_e$ [88]).

Self-consistency of $\Im\Sigma$ and $\Re\Sigma$ In ARPES measurements, only the occupied states can be observed. Due to causality, $\Re\Sigma$ is an odd function and $\Im\Sigma$ is an even function of energy. We make a symmetrisation (anti-symmetrisation) of the negative energy parts of $\Im\Sigma$ ($\Re\Sigma$) to get the positive energy parts shown in FIG. 2.7(b) and (c). Afterward, we calculate $\Re\Sigma$ ($\Im\Sigma$) from the Kramers-Kronig transformation of the so-symmetrized $\Im\Sigma$ ($\Re\Sigma$).

The satisfying result is that the self-consistency between $\Re\Sigma$ and $\Im\Sigma$ is immediately fulfilled without any adjustment of the parameters of the bare dispersion, A, B. This supports the correctness of the bare dispersion function we use. In fact, if we choose a parabolic dispersion, which is a simpler and naive guess, a tedious and complicated adjustment of the parameters is needed to obtain a self-consistent self-energy.

Eliashberg coupling function In FIG. 2.7(b) and (c), two features about the self-energy can be observed. One is that $\Re\Sigma$ behaves almost linearly around $E - E_F = 0$, then shows a peak, followed by a slow drop at higher energies; the other is that $\Im\Sigma$ reaches a plateau when $|E - E_F|$ exceeds a certain energy range comparable to the peak position in $\Re\Sigma$. In fact, these are two typical features of self-energy derived from the Debye model for electron-phonon coupling (see Fig. 1.10). As we are studying the two-dimensional electron systems, the 2D Debye model for electron-phonon coupling is chosen to calculate the Eliashberg coupling function [70]:

$$\Im\Sigma^{Debye-2D} = \begin{cases} \lambda\omega_D(1 - \sqrt{1 - (\frac{\omega}{\omega_D})^2}), & |\,\omega\,| < \omega_D \\ \lambda\omega_D, & |\,\omega\,| > \omega_D \end{cases} \tag{2.18}$$

with λ the mass enhancement parameter or the minus slope of $\Re\Sigma$ at $E - E_F = 0$. So the Debye frequency ω_D and the dimensionless coupling strength λ can be fitted from the experimental data. Note that the ARPES determined self-energy is a sum over all possible interactions. Another important contribution is the self-energy due to electron-electron interaction in a 2D Fermi liquid [89]:

$$\Im\Sigma^{FL-2D}(\varepsilon) = C_{2D}\frac{\varepsilon^2}{4\pi\epsilon_F}\ln|\frac{4\epsilon_F}{\varepsilon}|, \tag{2.19}$$

where C_{2D} is a constant, $\epsilon_F = 2\pi n_{2D}\frac{\hbar^2}{2m_e}$, and n_{2D} is the density of electron carriers.

Combining $\Im\Sigma^{Debye-2D}$ and $\Im\Sigma^{FL-2D}$, we fit the self-energy extracted from APRES data with 3 parameters, ω_D, λ, and n_{2D}, as shown in Fig. 2.8. The fit gives a Debye frequency $\omega_D = (68 \pm 2)$ meV, in excellent agreement with our data and the phonon energy (the longitude optical phonon mode E_1) measured by other techniques [90, 91], and a dimensionless coupling constant $\lambda = 0.3 \pm 0.05$. The isotropic Fermi liquid of the fit is characterised by a carrier density of $(6.7 \pm 0.4) \times 10^{13}$ cm^{-2}, close to the experimental value $(5.4 \pm 0.3) \times 10^{13}$ cm^{-2} determined from the area enclosed by the in-plane Fermi circle contours according to the Luttinger theorem.

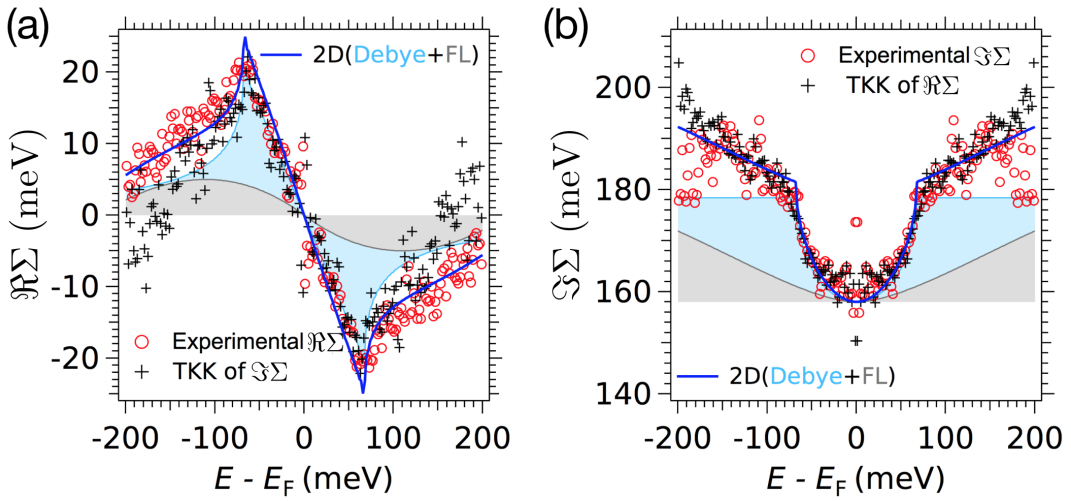

FIGURE 2.8: Experimental (a) real and (b) imaginary parts of the electron self-energy (red circles), and their Kramers-Kronig transforms (black crosses), for the right branch of the outer subband [82]. The dark blue curves are simultaneous fits to $\Re\Sigma$ and $\Im\Sigma$ using a 2D Fermi-liquid + 2D Debye model. The 2D Fermi liquid and 2D Debye components of the fit are shown by the filled light blue and grey curves. Data were symmetrised with respect to E_F, as required by the Kramers-Kronig relation.

2.1.3 Standard ARPES - original study case 2: spin-orbit coupling in bulk valence bands of ZnTe

With a given photon energy $h\nu$, a certain out-of-plane momentum $k_\perp$ is selected in the bulk Brillouin zone with an uncertainty inversely proportional to $\sqrt{h\nu}$. Thus, in fact, the bands measured with ARPES result from an average over a certain range of $k_\perp$, and this range of $k_\perp$ becomes wider at low photon energy. This is not a problem for 2D or 1D systems, but indeed will make it complicated and difficult to resolve and understand the bulk bands through ARPES in 3D systems, especially in the low photon energy range and for materials with a small Brillouin zone extension along $k_\perp$. Nevertheless, the following case of the study shows that ARPES can still be used to resolve and characterise the dispersing 3D valence bands of single crystalline samples of current interest in optoelectronics.

ZnTe

ZnTe is a face-centred cubic (see Fig. 2.9(a)) p-type II-VI semiconductor with a direct bandgap of 2.26 eV [94] and a wide range of applications, such as green light-emitting diodes [95], THz light generators and detectors [96, 97], and substrates for CdTe self-assembled quantum dots [98]. Despite its great importance in modern electronic applications, there is not enough experimental data (especially modern ARPES data) to support a complete understanding of its electronic band structure.

Here we used high-resolution APRES to measure the electronic structure of ZnTe and explore the spin-orbit coupling (SOC) within ZnTe by comparing the experimental data with the results of DFT calculation. The calculations were performed and kindly provided by Dr. Rubén Weht from CNEA (Argentina), with whom our group has had a long collaboration. Our results show that SOC is crucial to understand

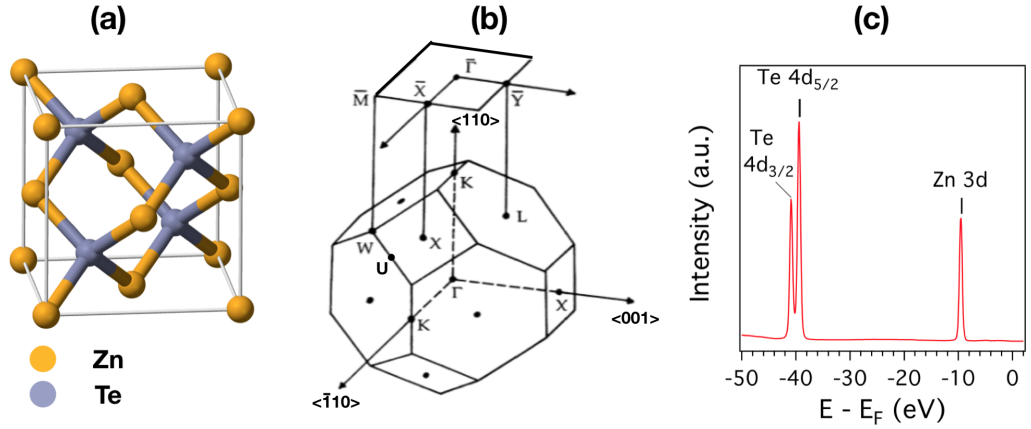

FIGURE 2.9: (a) The face-centred-cubic (fcc) lattice structure of ZnTe with a lattice parameter $a = 6.1$ Å. Taken from Ref. [92]. (b) Relation between bulk and surface Brillouin zones for a (110) surface of the fcc lattice. Taken from Ref. [93]. (c) XPS profile presenting the Zn $3d$ core level and the Te $4d$ doublet core levels measured on a cleaved crystal along the (110) direction at photon energy $h\nu = 110$ eV and a temperature $T = 196$ K.

the band structure of ZnTe, and that these bands are bulk states following the bulk symmetry, while surface states were not observed.

ARPES results

As ZnTe is a semiconductor with a bandgap 2.26 eV, there is no well defined Fermi level. Instead, we will use the top of the measured valence band as an effective energy reference denoted as E_v. The actual Fermi level was determined to be ≈ 0.4 eV above E_v, from the gold reference in the ARPES measurement chamber. Moreover, we found that due to this bandgap, the photoemission process induces a strong charging effect at low temperatures, hindering the obtention of meaningful ARPES data. Therefore, we performed the measurements at ≈ 200 K in order to reduce this undesired charging effect and managed to measure the electronic bands of ZnTe with acceptable momentum and energy resolutions. Fig. 2.9(c) shows the Zn $3d$ and Te $4d$ core levels measured on the cleaved (110) surface of ZnTe, indicating that the surface was clean after cleaved *in situ* in UHV.

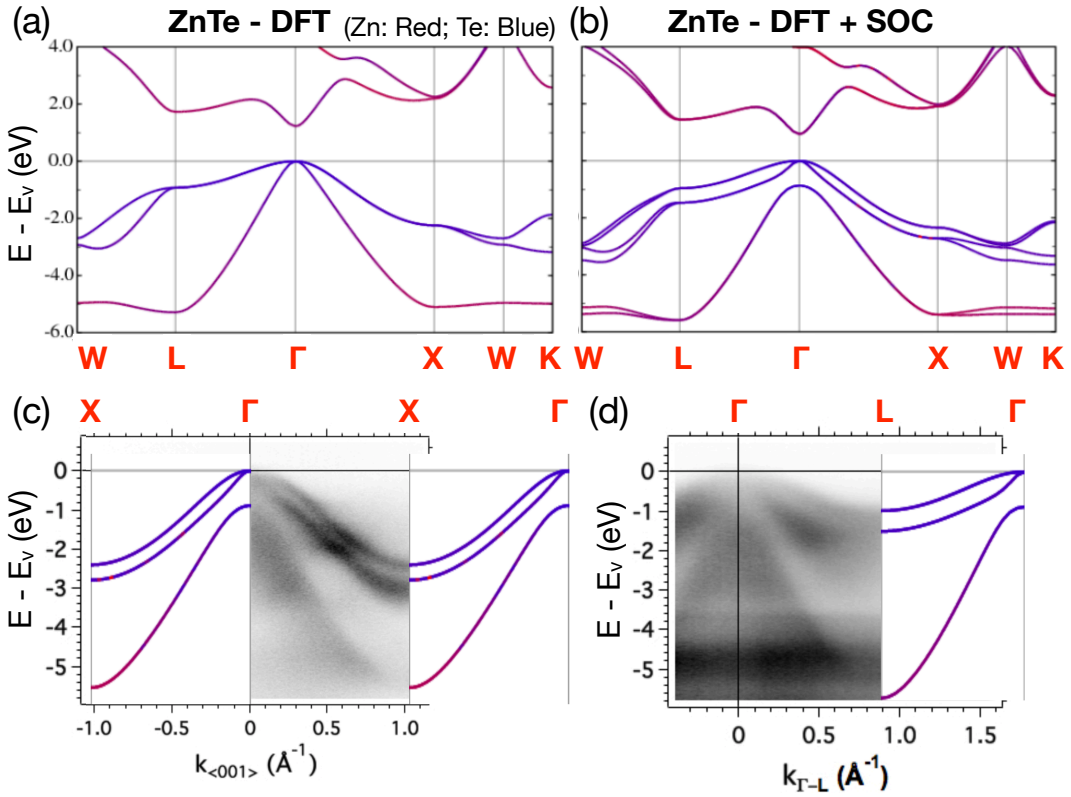

FIGURE 2.10: (a-b) DFT calculated valence bands without (a) and with (b) spin-orbit coupling (SOC). (c) ARPES measured energy-momentum dispersion along $\Gamma - X$ of the valence bands in comparison with the DFT calculated dispersions including SOC. (d) ARPES measured energy-momentum dispersion along $\Gamma - L$ of the valence bands in comparison with the DFT calculated dispersions including SOC. ARPES data were obtained with LH polarised $h\nu = 66$ eV photons at a temperature $T = 195$ K.

Band splitting due to SOC Fig. 2.10(a) and (b) show that the DFT calculated valence bands of ZnTe disperse quite differently depending on whether the SOC is included or not. Due to the presence of SOC, the top valence band (mainly from Te) splits into two bands opening gaps at L and X but remaining degenerate at Γ, while the lower valence band (mainly from Zn) is pushed down to larger binding energy remaining degenerate from L to Γ and from Γ to X.

Fig. 2.10(c) and (d) show the ARPES measured valence bands along $\Gamma - X$ and $\Gamma - L$ in comparison with the DFT calculated bands including SOC. The excellent agreement between the ARPES measurement and the DFT calculation with SOC proves and confirms experimentally that relatively strong SOC exists in the bulk electronic structure of ZnTe, and causes sizeable energy splitting of the valence bands, thus being crucial for understanding the bulk band structure of ZnTe.

Constant energy maps In our measurement of ZnTe, the in-plane constant energy maps (CEMs) were measured at two photon energies $h\nu = 66$ eV and $h\nu = 120$ eV as indicated with the blue dashed curves in Fig. 2.11(a). $h\nu = 66$ eV crosses the X point in bulk BZ and the Γ points in neighbouring BZs, while $h\nu = 120$ eV crosses the bulk Γ point at normal emission. Fig. 2.11(b) and (c) show the constant energy (the valence band top E_v and 0.5 eV below E_v) contours centred at Γ. The

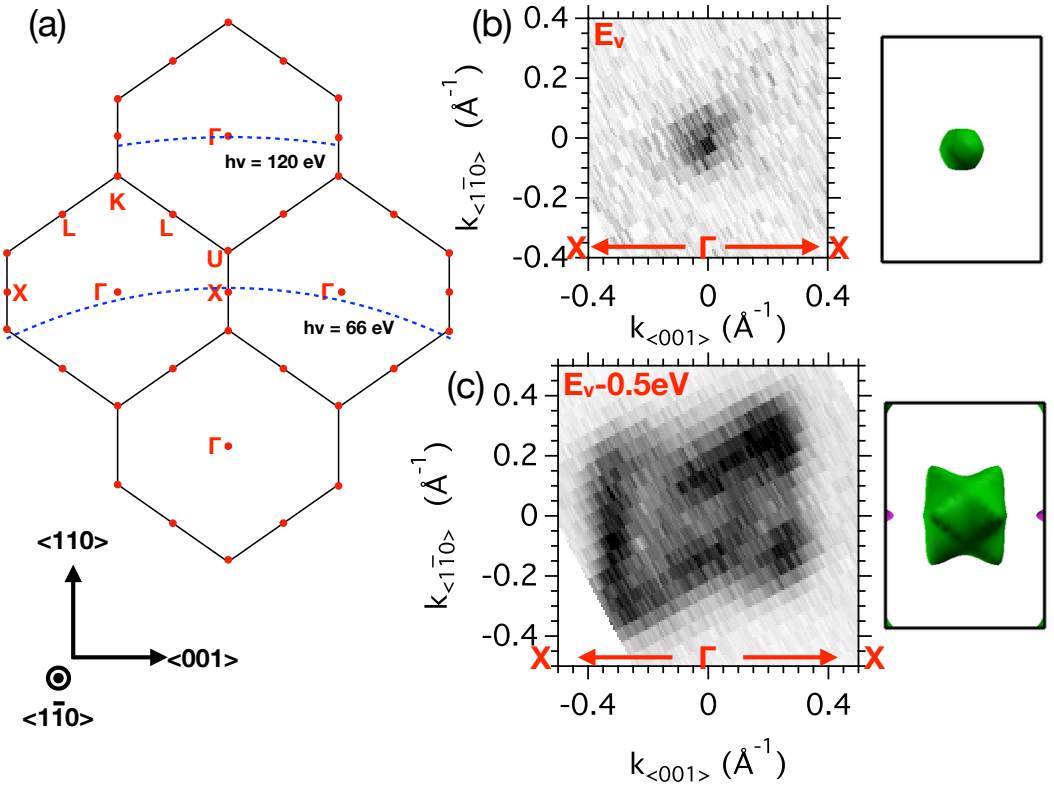

FIGURE 2.11: (a) A schematic view of the bulk Brillouin zone (BZ) shown in Fig. 2.9(b) from the $<1\bar{1}0>$ direction. The blue dashed curves indicate where the constant energy $h\nu = 66$ eV and $h\nu = 120$ eV locate in the bulk BZ. (b, c) Constant energy (E_v and $E_v - 0.5$ eV) maps centred at Γ measured with linear horizontal polarised $h\nu = 120$ eV photons at a temperature $T = 200$ K, in comparison with the DFT calculated constant energy maps including SOC.

comparison with the DFT calculated (including SOC) constant energy maps (right insets of Fig. 2.11(b) and (c)) shows a good agreement. However, the "knot" like constant energy ($E_v - 0.5$ eV) map shows a lack of mirror symmetry.

The out-of-plane CEMs shown in Fig. 2.12 form closed contours indicating these states are bulk states. If they are indeed bulk states, the directions $< 110 >$ and $< 1\bar{1}0 >$ should be equivalent. And indeed, the patterns (the knot-like contours) in these out-of-plane CEMs are very similar to the pattern at Γ in Fig. 2.11(c).

Cuts of CEM Fig. 2.13(a) shows the in-plane constant energy ($E_v - 2.5$ eV) map measured with linear horizontal polarised photons with energy $h\nu$ = 66 eV at T = 195 K. As aforementioned (see Fig. 2.11(a)), with this photon energy, the normal emission corresponds to the bulk X point. Once the bulk Brillouin zone is projected properly, cuts on the constant energy map along high symmetry directions, can be done, as shown in Fig. 2.13(b-d). Dispersions along $\Gamma - L$ and $\Gamma - X$ (see Fig. 2.13(c) and (d)) are quite similar to those in Fig. 2.10(c) and (d), indicating again the existence of relatively strong SOC in ZnTe. The dispersion along $U - X$ shown in Fig. 2.13(b) shows some discrepancy if compared to the DFT calculation with spin-orbit coupling. The bottom band locates around $E - E_v = -5.5$ eV, being 0.5 eV lower than the calculated band position, and the small gaps at U were also not observed. Notably, the observed CEM (2.5 eV below E_v, Fig. 2.13(a)) centred at X shows

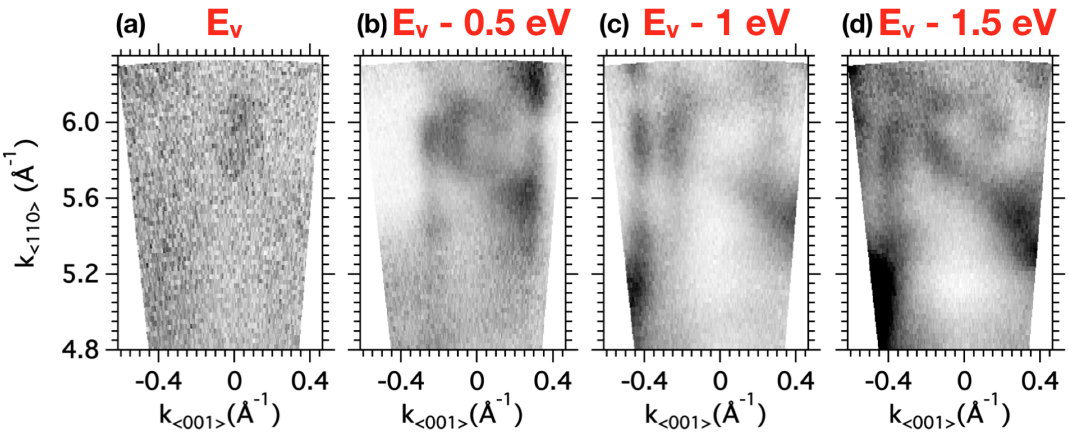

FIGURE 2.12: (a-d) Out-of-plane constant energy maps at various binding energies measured with LH polarised photons with energy ranging from 80 eV to 145 eV in an energy step of 1 eV at T = 195 K. E_v is set to the top of valence bands.

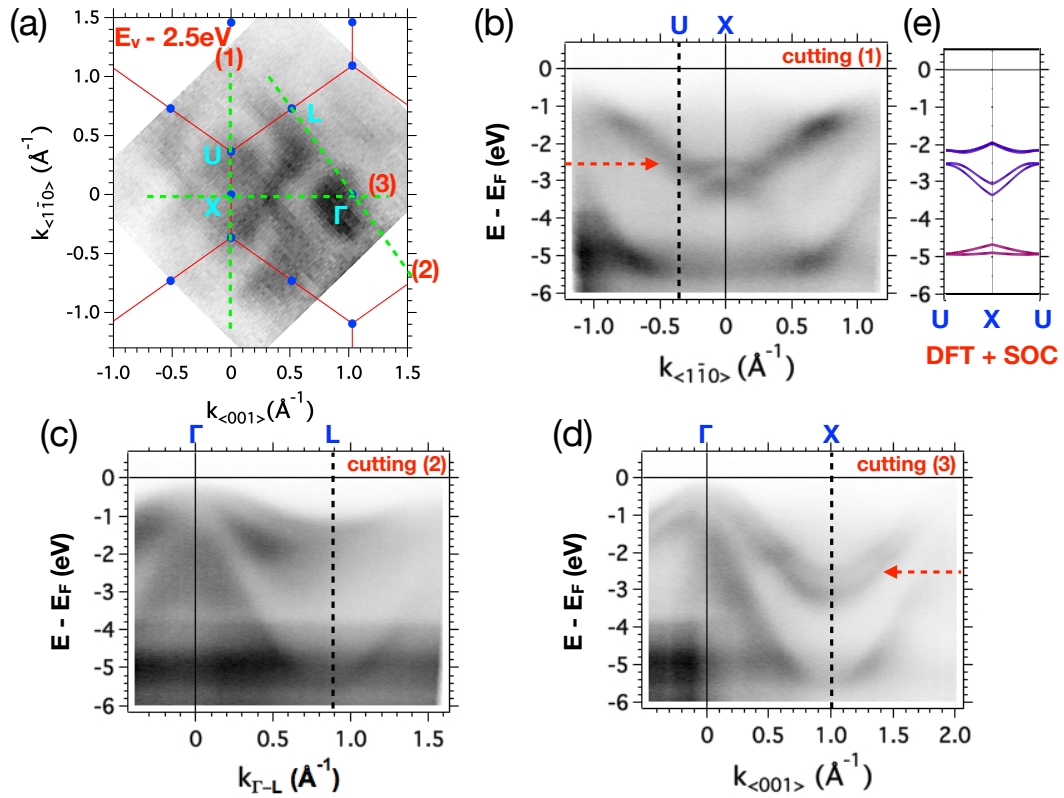

FIGURE 2.13: (a) Constant energy map at binding energy $E - E_v = -2.5$ eV together with the borders of the bulk Brillouin zone as shown in Fig. 2.9(b). (b-d) Energy-momentum dispersions along the high symmetry cutting lines (1)-(3) respectively indicated with green dashed lines in panel (a). These ARPES data were obtained by using LH polarised photons with energy $h\nu$ = 66 eV at T = 195 K. E_v is set to the top of valence band. The red dashed arrows point the position of $E_v - 2.5$ eV around X points. (e) DFT calculated bands dispersing along $U - X$ with SOC considered.

a peculiar pattern, which mimics the constant energy contours in the presence of both Dresselhaus and Rashba SOC (see Fig. 1.11 in Section 1.5).

The Dresselhaus SOC is due to the lack of bulk inversion symmetry. The spin-orbit splitting due to Dresselhaus SOC is quite typical in zine-blende structure (fcc) semiconductors, such as GaAs and InAs [71,99,100]. So it is reasonable that Dresselhaus SOC contributes to our observed energy splitting of the valence band.

The Rashba SOC needs the structure inversion asymmetry caused by macroscopic confining potential, e.g. at the surface [71]. The (110) surface of ZnTe is not polarised, thus there is no spontaneous net out-of-plane electric field. The bands we measured are bulk valence bands instead of surface states. However, with ARPES we are always measuring states lying in the vicinity of the surface even though these states are bulk states.

Recall that the band dispersion around X along $X - U$ shows some discrepancy with the DFT calculation including SOC. This suggests that DFT bulk calculation (including SOC) alone is not enough to understand all aspects of ZnTe's electronic structure. The lack of mirror symmetry in the in-plane constant energy contour around Γ may also be due to the fact that these measured states are located near the surface.

Thus, as an interesting perspective for future work, further slab calculations and spin-resolved ARPES experiments can help to understand the origin behind the special shapes of the constant energy contours around Γ and X.

2.2 SARPES

In the study of the topological surface states of 3D topological metals Ti_2Te_2P and Hf_2Te_2P (see Chapter 4, Section 4.3), I used the spin- and angle-resolved photoemission spectroscopy (SARPES) set-up ESPRESSO at HiSOR synchrotron in Japan. The following introduction to SARPES will be based on papers introducing the ESPRESSO setup [101,102].

Besides energy, momentum and charge degrees of freedom, the spin of an electron is an inner degree of freedom, which is usually degenerated in materials without an external magnetic field. However, in some materials with strong spin-orbit interaction, surface states with peculiar spin texture, such as Rashba spin-split states and spin polarised helical states in non-trivial topological materials, have been discovered in recent years. This development in fundamental physics, as well as the increasing demand for spintronics applications, has driven researchers to develop high-resolution SARPES, which enables a direct measurement of the spin-resolved band dispersions of materials.

In SARPES, instead of using an external magnetic field which will alter the electron trajectory and smear the information about the momenta of the emitted electrons, one uses only spin-dependent electron scattering processes to separate electrons with different spins.

One widely used type of such spin polarimeter is the Mott detector, which is based on the spin dependent scattering of electrons of high kinetic energy (≤ 25 kV) off nuclei of heavy atoms such as gold and thorium. Since gold is relatively inert and the kinetic energy of injected electrons is quite high, the target does not have to be cleaned during spin detection, thus leading to high stability in operation, which in the end has become one of the reasons why Mott detectors are the most widely used. However, the efficiency of the Mott detector is extremely low because the scattering probability, number of scattered electrons/number of incident electrons, is as low as

10^{-2} in typical Mott detector [101]. Because of such low efficiency, spin-polarised photoemission measurements are time consuming and one has to sacrifice energy resolution to get reasonable data acquisition time.

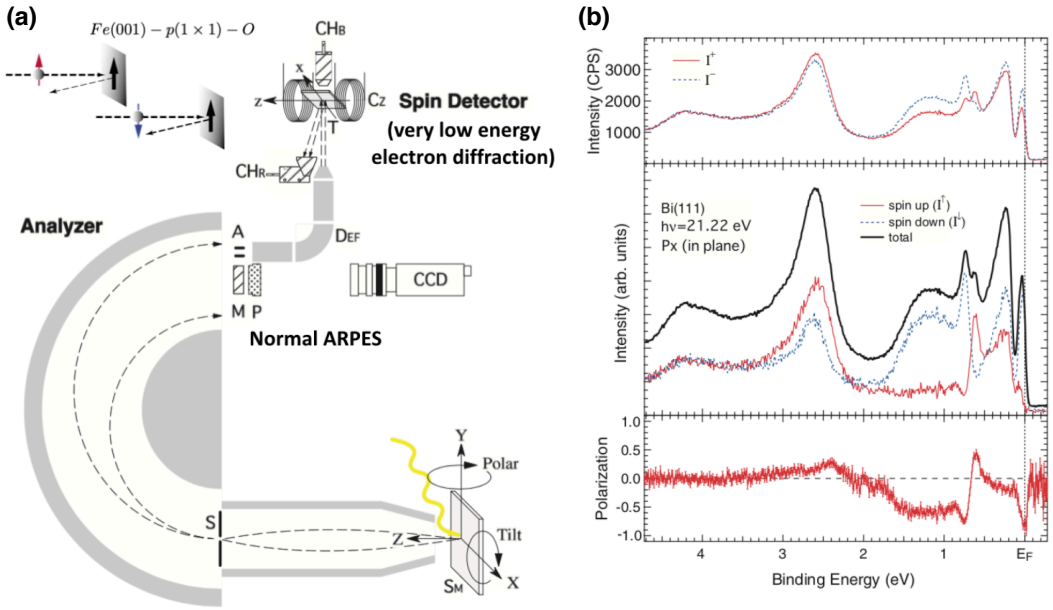

FIGURE 2.14: (a) Schematic diagram of ESPRESSO machine. The highly efficient VLEED spin detector is connected to a high-energy resolution hemispherical analyser (VG-SCIENTA R4000) via 90° electron deflector (D_{EF}). The ferromagnetic target (T) can be magnetised by electric coils along z (Cz) and x (Cx; not shown in the figure) directions. The electrons reflected by the target are detected by the channeltron (CH_R) beside the exit of the deflector. By using the electron deflector both in-plane (x direction) and out-of-plane (z direction) spin components can be observed. Spin-integrated ARPES measurement is also available by observing the portion of photoelectron with the two-dimensional electron detector, multi-channel plate (MCP: (M)), and phosphor screen (P), through a CCD camera. Since the size of the aperture (A) for the spin-resolved measurement channel and the entrance slit (S) is variable, one can select the optimum energy resolution and angular resolution for the SARPES measurement. (b) An example of how the data is measured and analysed to extract the necessary spin texture information of electronic bands. First, a pair of reflected electron intensities by the reversibly magnetised FeO target plate are recorded. Then depending on the calculated reflectivity asymmetry A from the first step and the pre-calibrated effective Sherman function S_{eff}, the spin polarisation P is determined. In the meantime, the electron populations of spin up and down are also extracted. Adapted from Ref. [102].

In order to overcome the very low-efficiency problem of Mott detectors, researchers developed the very low energy electron diffraction (VLEED) spin detector, where the spin-exchange interaction of electrons is applied. The ESPRESSO machine in HiSOR

synchrotron adopts such VLEED technique (see Fig. 2.14(a)). It measures the spin-dependent electron reflectivity of very low energy (a few eV to a few tens of eV) electrons at a Fe(001)-p(1×1)-O film grown on a MgO(001) substrate, a magnetised ferromagnetic target which lasts longer than 1 day and can be prepared or refreshed quickly in a UHV chamber. The spin asymmetry A of the electron beam is detected after switching the magnetisation direction of the ferromagnetic target:

$$A = \frac{I^+ - I^-}{I^+ + I^-} \tag{2.20}$$

where I^+ and I^- are the intensities measured at the channeltron using reversely magnetised FeO film target.

Supposing that the spin-parallel scattering rate is a and spin-antiparallel scattering rate is b, we have:

$$\begin{cases} I^+ = aI^\uparrow + bI^\downarrow \\ I^- = bI^\uparrow + aI^\downarrow \end{cases} \tag{2.21}$$

where $I^\uparrow$ and $I^\downarrow$ are the spin populations of opposing spin in the photoelectrons.

Thus,

$$A = S_{eff}P, \text{ with } S_{eff} = \frac{a-b}{a+b} \text{ and } P = \frac{I^\uparrow - I^\downarrow}{I^\uparrow + I^\downarrow} \tag{2.22}$$

where S_{eff} is the energy-dependent effective Sherman function and P is the spin polarisation of the photoelectrons. The Sherman function S_{eff} can be calibrated with a standard material (Bi(111) is normally used in the ESPRESSO machine) at a given photon energy. In our case specifically, it was calibrated to be 0.18 during the beam time in HiSOR in 2017 and 0.25 during the beam time in HiSOR in 2018, for photon energy $h\nu$ = 55 eV.

Once S_{eff} is calibrated, the spin polarisation P is determined through the measured reflectivity asymmetry A. In the end, the spin up and down populations can be obtained

$$\begin{cases} I^\uparrow = \frac{1+P}{2} I \\ I^\downarrow = \frac{1-P}{2} I \end{cases} \tag{2.23}$$

where $I = I^\uparrow + I^\downarrow$ is the total amount of photoelectrons. By magnetising the target film in three orthogonal directions, the full information of the spin polarisation vector $\vec{P} = (P_x, P_y, P_z)$ is obtained.

2.3 Supplementary techniques

During my thesis work, two important supplementary experimental techniques of surface science have been extensively used: molecular beam epitaxy (MBE) and low energy electron diffraction (LEED). A basic introduction will be given to them in the following.

2.3.1 MBE

Originally developed in the late 1960s at Bell Telephone Laboratories by J. R. Arthur and Alfred Y. Cho [103], MBE has become a widely used epitaxy method for thin-film deposition of single crystals.

We used mostly the MBE system at CASSIOPÉE beamline, which is connected in UHV, *via* an exchange carrousel, to the high-resolution ARPES endstation. To enable

sample preparation and thin film deposition, the MBE chamber is equipped amongst others with:

- a heating stage using electron bombardment from the back of the sample holders up to approximately 1000°C. The temperature is monitored with pyrometers. For some of our ARPES measurements, the uncleavable samples are annealed in this way to clean the surfaces. In some cases, a high-temperature annealing is applied for a better crystallised surface.
- an ion gun for Ar^+ sputtering. In many cases, annealing alone is not enough to obtain a clean surface. Then Ar^+ sputtering at grazing incidence (20 - 30°) with respect to sample surfaces) is needed to remove the impurities and contaminants at the surface.
- electron diffraction (ED) techniques: low energy ED (LEED) and reflective high energy ED (RHEED). We used LEED mainly and it will be introduced below.
- an Auger spectroscopy setup to check for surface contaminants, like carbon.
- various ports to mount evaporators (e.g. Al in Knudsen cell or alkali metals dispensers).
- a 10-crucible electron gun for material evaporation.
- a quartz microbalance to calibrate the evaporation rate.

2.3.2 LEED

LEED is a surface sensitive technique used to determine the surface structure of single-crystalline materials [104]. Electrons emitted from a wire by thermionic effect are accelerated in a homogeneous electric field to 20 - 200 eV, then hit the sample surface. Part of these electrons are diffracted due to elastic scattering and observed as spots on a fluorescent screen.

Upon penetrating the crystal, some electrons of the primary injection beam will lose kinetic energy due to inelastic scattering processes such as plasmon and phonon excitations. Usually, exponential decay of the primary electron beam intensity, I_0, in the direction of propagation is assumed:

$$I(d) = I_0 e^{-d/\lambda(E)} \tag{2.24}$$

where d is the penetration depth and $\lambda(E)$ denotes the inelastic mean free path. The inelastic scattering processes depend on energy. Consequently, the electronic mean free path also depends on the energy, and relatively independent of the material. This mean free path turns out to be minimal (5-10 Å) in the energy range of low-energy electrons (20-200 eV). So in LEED measurements, only a few atomic layers are detected by the electron beam making LEED a very surface sensitive technique.

Generally, LEED can be used in one of two ways:

- Qualitatively, where the diffraction pattern is recorded and analysis of the spot positions gives information on the symmetry of the surface structure.
- Quantitatively, where the intensities of diffracted beams are recorded as a function of incident electron beam energy to generate the so-called I-V curves. By comparison with theoretical curves, these may provide accurate information on atomic positions on the surface at hand.

During my thesis work, we only used LEED to obtain qualitative informations about the symmetry and orientation of the studied surfaces.

Chapter 3

Oxides: SnO_2 and $FeTiO_3$

In recent decades, oxide surfaces and interfaces have attracted a lot of research interest due to their importance in both fundamental physics and practical applications [8–10].

One major research area is the creation of two dimensional electron systems (2DESs) at the surfaces or interfaces of oxides. There are several fundamental challenges on this topic:

1. How to realise such 2DESs?
2. What is the origin of these 2DESs?
3. How could one control their basic properties, such as carrier density, mobility, and magnetic properties?
4. Is there many-body physics involved in these 2DESs?

In the last years, our group has established a practical method to create 2DES at the surface of oxides [1, 2, 30], such as $SrTiO_3$, $KTaO_3$, anatase TiO_2, $CaTiO_3$ [105], and ZnO [82]. The key physics involves the creation of oxygen vacancies at the oxide surface by means of annealing in ultra-high-vacuum (UHV), photon irradiation or redox reactions.

In this chapter, I am going to present two oxide case studies: SnO_2 and $FeTiO_3$. For each oxide, I will discuss the main physics and whether the creation of a 2DES was possible or not.

3.1 SnO_2(110): two-dimensional electron system

Tin oxide is a technologically important compound with a wide range of applications. Its exceptional properties stem from its ability to exhibit variable oxygen stoichiometries –a consequence of the variable valence of Sn– accompanied by substantial changes, up to two orders of magnitude, in its conductivity. This remarkable combination of reducibility and changes in conductivity is crucial in the field of gas sensing [106–113]. The ability of SnO_2 to readily release oxygen in the presence of reactants makes it also an important material in the field of heterogeneous catalysis. SnO_2 can either directly promote the oxidation of hydrocarbons or enhance the activity of noble metal catalysts [108, 113–120]. Moreover, the unique association of high conductivity due to intrinsic defects, transparency to visible light, and high resistance to chemical attack at ambient conditions, opens up a whole new class of technological applications for SnO_2, including solar cells, liquid crystal displays, and transparent electrodes, conductive coatings and windows [110, 113, 114, 121, 122].

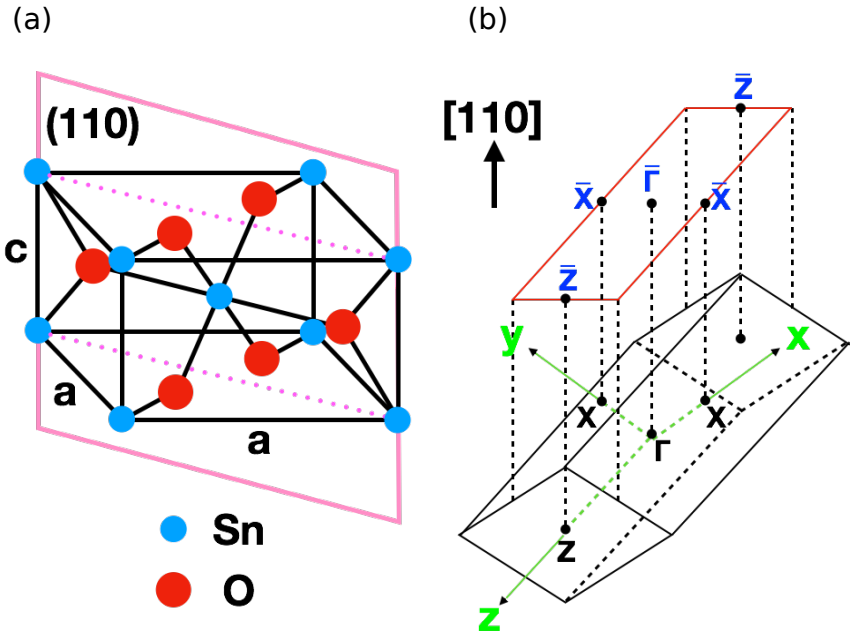

FIGURE 3.1: (a) 3D unit cell of SnO_2 with $a = 4.737$ Å and $c = 3.185$ Å; (b) Corresponding 3D Brillouin zone of rutile SnO_2 (black parallelepiped) together with the surface Brillouin zone projected on the (110) plane (red rectangle).

Being the key for its numerous applications, the origin of *n*-type conductivity in SnO_2 has attracted a large scientific interest. Bulk SnO_2 stabilizes in the rutile structure, see Fig. 3.1 (a). It is a wide gap insulator with a bandgap of 3.6 eV [123–126], but the presence of a surface modifies this simple picture. Calculations on the thermodynamically most stable termination, the (110) surface, have proposed O 2*p*-derived defect states within the bandgap [126]. Early photoemission studies on oxygen deficient SnO_2 after annealing in UHV have experimentally confirmed the existence of such defect states near the valence band maximum [127–133]. Other experiments suggested that, on further reduction, such defect states fill the bandgap gradually by moving towards the conduction band [115, 127, 134, 135]. It is however surprising that they extend up from the top of the valence band, rather than being pulled down from the conduction band minimum. This is in contrast with the metallic states experimentally observed in similar transparent conducting oxides and gas sensing materials, where *n*-type doping from surface defects leads to an occupied conduction band. Prime examples are the metallic two-dimensional electron systems (2DESs) resulting from the doping and near-surface confinement of the conduction band electrons in In_2O_3 [136], CdO [137], ZnO [82, 138] and TiO_2 [22, 26, 30].

By means of Angle Resolved PhotoEmission Spectroscopy (ARPES), here we measure the electronic band structure of SnO_2 experimentally and show that there exists a 2DES at its (110) surface. Similar to its counterparts in $SrTiO_3$ [20, 28] and $KTaO_3$ [21], the 2DES in SnO_2 is related to the presence of oxygen vacancies and is robust with respect to various surface reconstructions. Most intriguingly, the 2DES in SnO_2 is not affected by exposure to ambient air, and can be readily retrieved in the ARPES measurements without further surface treatment, making it the most easily created 2DES so far among all oxides. Moreover, its carrier density can be tuned by external parameters such as temperature or deposition of reducing agents at its surface such as Al and Eu, which have been reported to be effective methods to create

oxygen vacancies at oxide surfaces [1, 30, 31]. These results open exciting possibilities of using and controlling the surface conductivity of SnO_2 in view of novel types of technological applications.

3.1.1 Surface preparation

As stated in the Section 2.1.1 Chapter 2, ARPES is sensitive to surface impurities. Thus before an ARPES measurement, a clean surface has to be obtained by means of one of the following methods.

- in situ cleavage to expose a pristine surface: this method is widely used for compounds with a layered structure, for example, many topological materials [139]. In some special cases, it could also be applied to non-layered structures, such as $SrTiO_3$ [20, 140] and some high T_c superconducting cuprates [141], as long as they can be fractured along a well-defined plane.

- annealing in an ultra-high vacuum to desorb surface impurities: this method is usually used for rigid bulk samples, for example many transition metal oxides. This method is often preceded by ion bombardment in order to remove impurities that might not be easily desorbed during high-temperature annealing. Annealing temperature, annealing time and vacuum pressure are all crucial for the final surface quality. Typically, a surface quality check by means of LEED is followed right after the preparation.

Here, our SnO_2 samples are rutile structure (see Fig. 3.1) bulk single crystals and not suitable for *in situ* cleaving. Therefore, we have followed the method of annealing in order to create a clean surface for ARPES experiments.

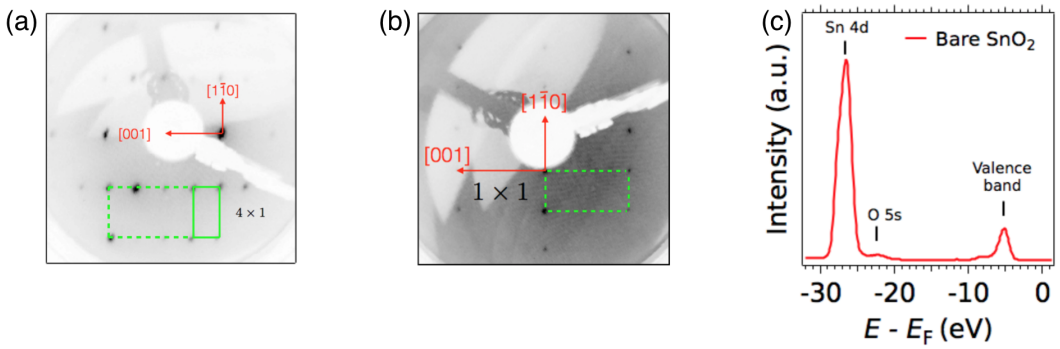

FIGURE 3.2: (a) LEED pattern of the bare (110) surface of SnO_2 showing a 4×1 surface reconstruction after annealing up to 600°C in UHV (electron energy: 58 eV). (b) LEED pattern of the bare (110) surface of SnO_2 showing a 1×1 surface reconstruction after annealing up to 730°C in UHV (electron energy: 116 eV). (c) Angle-integrated spectrum of the 4×1 reconstructed bare (110) surface of SnO_2 showing the profiles of the Sn 4*d* core-level peak and the valence band. The photon energy was 110 eV and the polarisation was linear horizontal.

Low-energy electron diffraction (LEED) and core-level photoemission spectroscopy were employed to verify the long-range crystallinity and cleanliness of our surfaces after preparation. As shown in Fig. 3.2 (a) and (b), depending on the annealing temperature, the clean surfaces showed either a 1×1 bulk-like periodicity or a weak 4×1 surface reconstruction [107, 113, 114]. As discussed later, these two surface reconstructions do not give observable differences in the ARPES spectra. The energy

position and lineshape of photoemission peaks, as seen in Fig. 3.2(c), match well with previous experimental results [114].

3.1.2 Bare SnO_2: observation of the 2DES

Valence bands

The energy-momentum dispersion of the valence band of $Sn_2(110)$ is shown in Fig. 3.3.

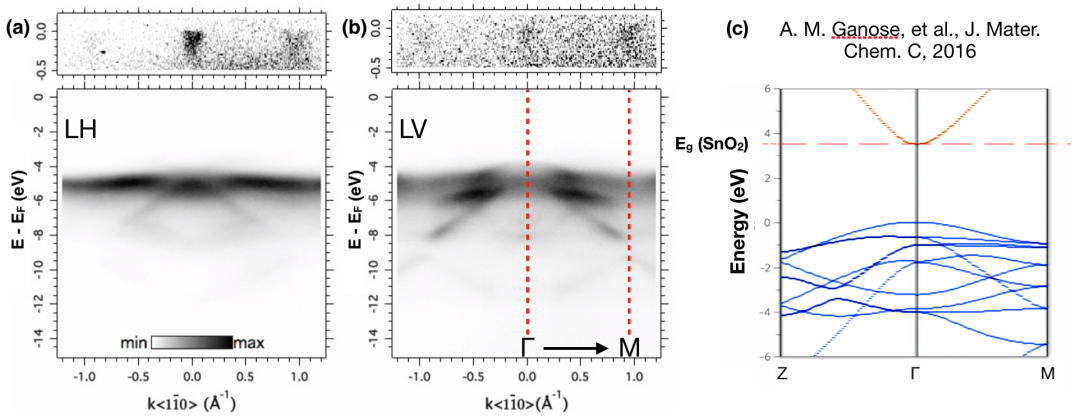

FIGURE 3.3: (a-b) ARPES energy-momentum map of the valence bands on the bare (110) surface of SnO_2 measured with photons of energy 111 eV using the linear horizontal (a) and linear vertical (b) polarizations. The top panels show a shallow metallic state, made visible after changing the contrast of the color scale. (c) The numerically calculated valence bands of SnO_2 along $Z - \Gamma - M$ direction in the BZ extracted from [142].

In striking contrast with the bulk insulating character of SnO_2, there is a clear metallic state in the vicinity of the Fermi level with a band bottom at binding energy of ≈ 0.2 eV. The energy difference with the valence band maximum (VBM) matches well with the energy gap of SnO_2 (3.6 eV) as determined by previous experimental and theoretical studies [123–126]. We therefore attribute the metallic state to the conduction band of SnO_2 that has been pulled below the Fermi energy (E_F) due to band bending, as observed in surfaces of other bulk insulating oxides [1, 20, 23–28, 30, 82, 105, 143, 144]. However, in contrast to the *d*-orbital character of the conduction band in transition metal oxides, the conduction band bottom in SnO_2 originates mainly from the 5*s* states of Sn [125].

Metallic state at E_F

Fig. 3.4 presents a high resolution image of the energy-momentum dispersion of this metallic state. The dispersion is quasi-parabolic, with a kink at an energy of about 80 meV (red arrows) and an intensity built-up at the bottom of the band. Such a kink and strong renormalisation of the band are characteristic signatures of electron-phonon interaction, as previously observed in other oxides such as $SrTiO_3$ [23,63,64], TiO_2 [30] and ZnO [82]. The Fermi momentum (k_F) of the metallic state, determined from the maxima of the momentum distribution curve (MDC) integrated over ($E_F \pm 2$) meV, is $k_F = (0.077 \pm 0.001)$ Å^{-1}.

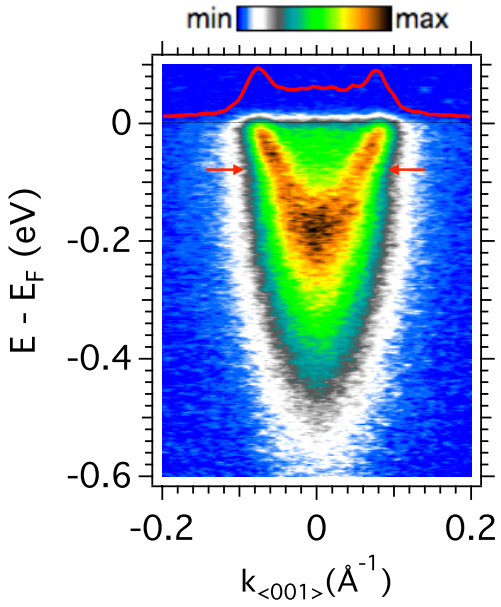

FIGURE 3.4: The energy-momentum dispersion of the 2DES measured at the SnO_2(110) surface with LH polarised photons at $h\nu = 88$ eV and $T = 16$ K. Electron-phonon interaction induces the observed deviations (red arrows) from a simple parabolic shape. The red curve above E_F is an MDC integrated over $E_F \pm 10$ meV.

Fermi surface contours

As a basic characterisation of this metallic state, we measured its in-plane and out-of-plane Fermi surface contours, as shown in Fig. 3.5.

Fig. 3.5 (a) shows the in-plane ARPES intensity map at E_F measured over several neighbouring Brillouin zones. The aforementioned metallic state gives rise to a circular Fermi contour around the center of, and with the same reciprocal-space periodicity as, the reduced 2D Brillouin zone of the bulk rutile structure of SnO_2 (inset of Fig. 3.5). Moreover, the isotropic shape of the Fermi contours is in line with the expected *s*-like orbital character at the bottom of the SnO_2 conduction band, as discussed above.

Fig. 3.5 (b) shows the out-of-plane Fermi contour of the metallic state. The absence of dispersion along the <110> direction throughout the complete bulk Brillouin zone demonstrates the near-surface confinement of the conduction band, hence forming a 2DES. Recalling that the in-plane Fermi surface is a circle, the corresponding Fermi surface in 3D *k*-space would be a cylinder. Our combined findings prove thus the realisation of an s-derived 2DES on a rutile structure oxide. Following the Luttinger theorem, the corresponding 2D carrier density (n_{2D}) can be extracted from the area (A_F) of the in-plane contour as $n_{2D} = A_F/(2\pi^2) = (9.4 \pm 0.2) \times 10^{12}$ cm^{-2}. This is about 5 times smaller than the carrier density found in analogous 2DESs created by oxygen vacancies at the surface of other binary oxides, such as TiO_2(001)-anatase [26] or ZnO(000$\bar{1}$) [82], and up to 20 times smaller than the density of the 2DES at the $SrTiO_3$(001) surface [20, 23, 30].

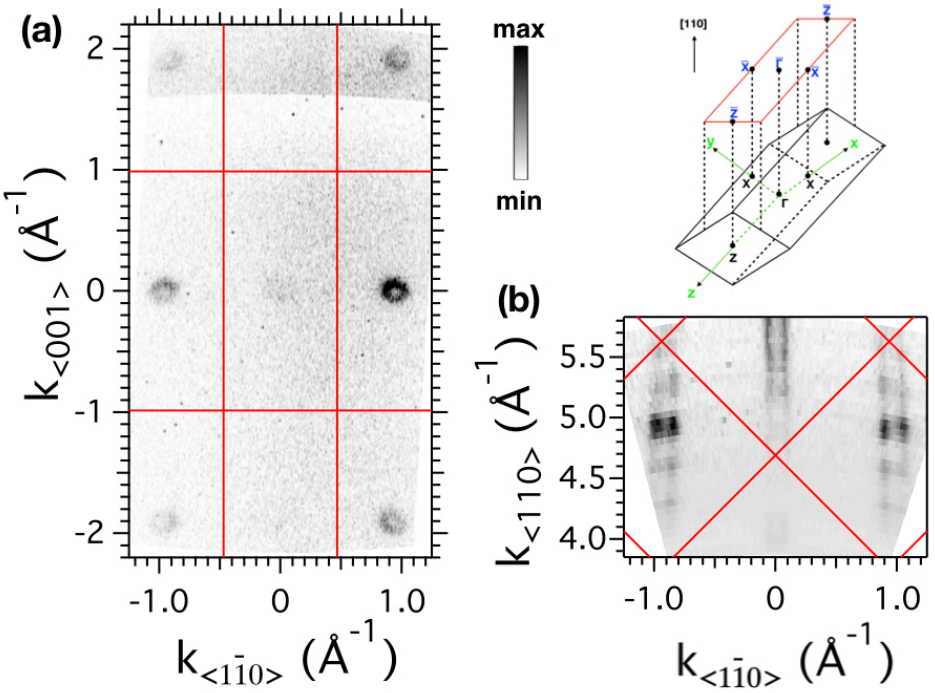

FIGURE 3.5: (a) In-plane Fermi surface map of SnO_2(110) measured with LH photons at $h\nu = 88$ eV. (b) Out-of-plane Fermi surface map of SnO_2(110) acquired by a stepwise change ($\Delta h\nu = 2$ eV) of the photon energy between 50 and 120 eV using LH polarisation. An inner potential of 10 eV was used in the calculation of the out-of-plane momentum. Red lines mark the borders of the reduced 2D Brillouin zone (in-set) in (a) and of the bulk Brillouin zones in (b). All data in this figure were acquired at 16 K.

LV polarisation For the sake of completion we present here the main results obtained on the bare (110) surface of SnO_2 using photons with linear vertical (LV) polarisation. Fig. 3.6 shows the out-of-plane Fermi surface contours, the in-plane Fermi surface contours, and the energy dispersion of the metallic 2DES in panels (a), (b) and (c), respectively. A comparison of Figs. 3.6 (a) and Fig. 3.5 (b) reveals a clear polarisation selection at normal emission (i.e. $k_{||} = 0$) where there is almost no photoemission intensity with LV photons. Moreover, there is a strong suppression of spectral weight along the <001> directions. These intensity variations are can be qualitatively explained with the parity analysis of the matrix element for *s* orbit. The parity of *s* orbit is always even with respect to any mirror planes. The parity of the final state of the photoelectron is also required to be even with respect to the detected emitting electron plane (*xz* plane in Fig. 5.25 in Chapter 5). But the parity of LV polarisation is odd with respect to *xz* mirror plane. Thus, the overall parity of the photoemission matrix element is odd leading to a strongly suppressed intensity on the observed spectrum. A more rigorous explanation can be found in a matrix element simulation work by S. Moser [145].

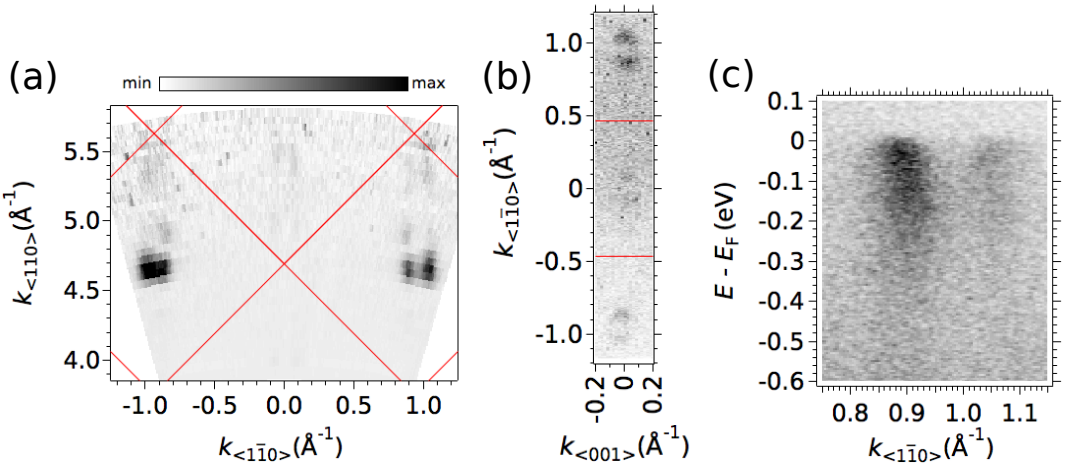

FIGURE 3.6: (a) Out-of-plane Fermi surface map of SnO_2(110) measured by a stepwise change ($\Delta h\nu = 2$ eV) of the photon energy between 50 and 120 eV. (b) In-plane Fermi surface of SnO_2(110) measured with $h\nu = 88$ eV. Red lines mark the borders of the projected surface Brillouin zone. (c) Energy-momentum dispersion of the 2DES measured with $h\nu = 88$ eV, corresponding to an out-of-plane momentum in the upper Brillouin zone of (b). All data in this figure were acquired at 16 K using linear vertical polarization. An inner potential of 10 eV was used in the calculation of the out-of-plane momentum.

3.1.3 Tunability of the carrier density of this 2DES

Having successfully created a 2DES at the bare surface of SnO_2(110), we may be tempted to control its basic properties, for example, tuning the carrier density. We now show two simple methods for tuning the carrier density of the 2DES in SnO_2:

- controlled temperature variations: temperature may affect several properties of the sample. For example, it determines the value of the dielectric constant which plays an important role in the formation of the confining potential well. It may also affect the distribution of the oxygen vacancies as it promotes their diffusion from the surface to the bulk.

- surface deposition of reducing metals (Eu and Al): as introduced in the experimental technique part, we use MBE to evaporate elemental reducing agents at the surface of target samples in order to create oxygen vacancies due to the redox reaction between the capping metal and the sample. In our experiment, we used two kinds of reducing metals, Al and Eu. In previous studies, Al deposition has been demonstrated to be a valid method to create 2DESs at the surface of many oxides [1,30], such as $SrTiO_3$, $CaTiO_3$, anatase TiO_2 and ZnO [82]. On the other hand, Eu deposition has been shown to creates a 2DES at the surface of $SrTiO_3$ [31].

Temperature dependence

Figs. 3.7 (a-g) show the energy-momentum dispersion of the 2DES as the temperature gradually increases from 20 K to 300 K. The succession of images reveals that the metallic state continuously shifts upwards in energy upon increasing T. The corresponding decrease of the Fermi momenta translates into a reduction of the 2D carrier

density. A quantitative analysis of the k_F values obtained from the MDCs, presented in the Tab. 3.1 shows a 50% reduction of the carrier density at 150 K with respect to 20 K. We highlight the clear 2DES fingerprint at room temperature, but we note that there is an uncertainty whether the electronic band lies above or below E_F at such high temperatures because the band bottom is masked by the thermal broadening. Temperature-dependent transport measurements may shed light on this issue. Nevertheless, the robustness of the 2DES at high temperatures is of obvious importance for technological applications.

After heating the sample from 16K to 300K, we decreased the temperature back to 15K in order to check the reversibility of the phenomenon. Figs. 3.7 (g-j) and Tab. 3.1 show indeed that the 2D carrier density increases as T decreases. After a full thermal cycle, the final k_F value is close to the original one, although the recovery is incomplete, similar to our previous observations for $SrTiO_3$. The reason behind the incomplete recovery might be the diffusion, while the sample is heated, of some oxygen atoms from the bulk to the surface that irreversibly replenish the oxygen vacancies.

This temperature dependent behavior of the carrier density is probably related to the variation of the dielectric constant, which plays an important role in the formation of the self-sustained confining potential well [146].

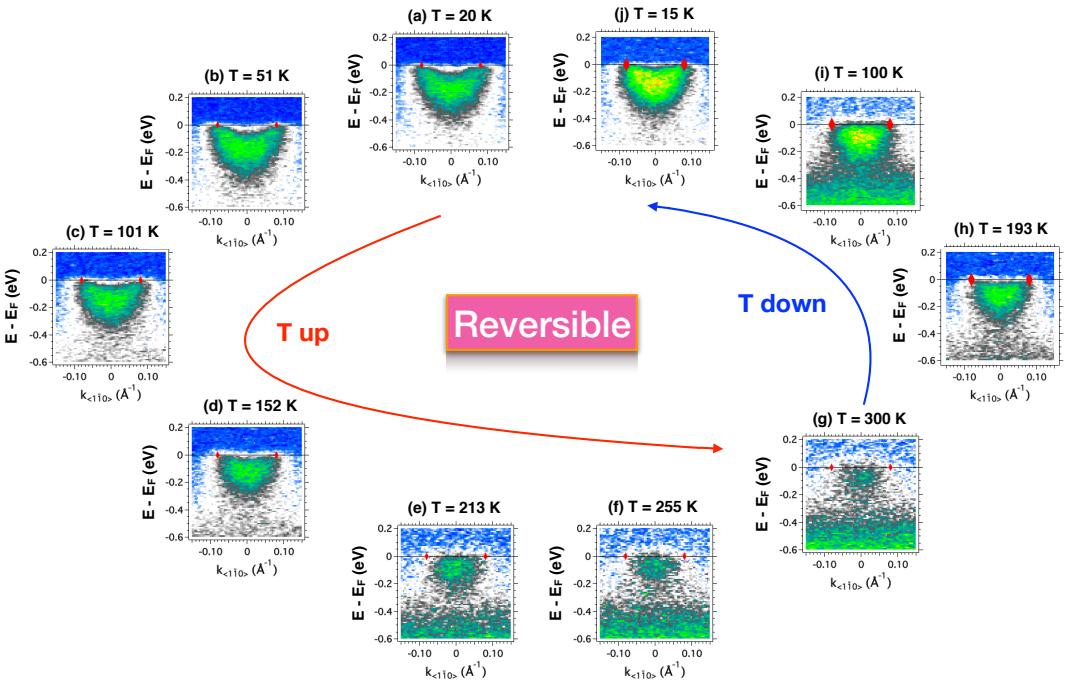

FIGURE 3.7: Energy-momentum dispersion of the 2DES on SnO_2(110) during a gradual temperature increase from 20 K (a) to 300 K (g), and a subsequent decrease from 300 K (g) to 15 K (j). Red markers indicate the Fermi momenta at 20K inferred from the MDC at the Fermi level. Data were acquired with $h\nu = 88$ eV and LH polarisation.

T(K)	20	50	100	152	100*	15*
$k_F(10^{-3}$ Å$^{-1})$	85 ± 1	80 ± 1	71 ± 1	60 ± 2	51 ± 2	63 ± 1
$n_{2D}(10^{12}$ cm$^{-2})$	11.5 ± 0.3	10.2 ± 0.3	8.0 ± 0.2	5.7 ± 0.4	4.1 ± 0.3	6.3 ± 0.2

TABLE 3.1: Fermi wave vectors of the 2DES in SnO_2(110) at different temperatures. The corresponding carrier densities are calculated using the Luttinger theorem. A star denotes that the corresponding temperature has been reached starting from a higher value (i.e cooling process). The temperature uncertainty is ±2K.

Eu capping

Elemental Eu is a very active reducing metal, and has several oxidation states available, most notably Eu^{2+} and Eu^{3+}. From a standard database of enthalpies and free energies [147–149], one can find the Gibbs free energies of the redox reactions needed to form SnO_2 and EuO at room temperature:

$$\begin{cases} Sn + O_2 = SnO_2 + 519.65\ KJ/mol \\ Eu + (1/2)O_2 = EuO + 556.89\ KJ/mol \end{cases} . \tag{3.1}$$

Thus,

$$SnO_2 + 2Eu = Sn + 2EuO + 594.13\ KJ/mol. \tag{3.2}$$

Having a positive energy balance, this exothermic redox reaction should happen spontaneously once Eu is deposited at the surface of SnO_2.

Before deposition, the Eu source needs to be degassed and calibrated by means of a quartz microbalance. The deposition was set at $T = 435°C$ and the evaporation rate at 0.0051Å/s.

In the following experiments, we evaporated 1 monolayer (ML) - i.e. 3.6 Å- and 2 ML - i.e. 7.2 Å- of Eu on the bare (110) surfaces of two SnO_2 samples which had been cleaned by UHV annealing.

1 ML Eu Fig. 3.8 summarises all the pertinent spectral changes after the deposition of 1 ML of Eu. The Sn 4*d* core levels are drastically modified and develop two new peaks at the low binding energy side [Fig. 3.8(a)]. Their energy is in fair agreement with the 4*d* spin-orbit-split doublet of metallic Sn, an indication that near-surface Sn atoms have been deprived of their oxygen neighbours. A detailed quantitate analysis of these peaks by numerical fitting will be presented later. The spectral fingerprint of Eu^{2+} states is now clearly seen in the energy gap between the valence band and the conduction band [Fig 3.8(b)]. The presence of Sn atoms with a lower oxidation number than in the pure surface is an indication that Eu has been effective in removing the near-surface oxygen by a redox reaction, hence driving the emergence of a 2DES, similar to the $AlO_x/SrTiO_3$ and $EuO/SrTiO_3$ systems [30, 31]. Nevertheless, the EuO/SnO_2 interface shows a peculiar behavior that has no counterpart in the 2DES observed in the related $EuO/SrTiO_3$ system. As shown in Figs. 3.8(c-e), the band bottom and Fermi momenta of the 2DES at the EuO/SnO_2 interface are larger than the ones observed at the bare SnO_2 surface. The corresponding 2D carrier density in Eu(1 ML)/SnO_2, deduced from the observed Fermi momenta $k_F = (0.116 \pm 0.001)$ Å^{-1}, is now $(2.15 \pm 0.04) \times 10^{13}$ cm^{-2}, implying a twofold increase with respect to the bare surface of SnO_2. This enhancement of n_{2D} beyond the saturation limit presented by the bare surface under UV irradiation has not been observed in other 2DES created by redox reactions at metal-oxide interfaces [30, 31],

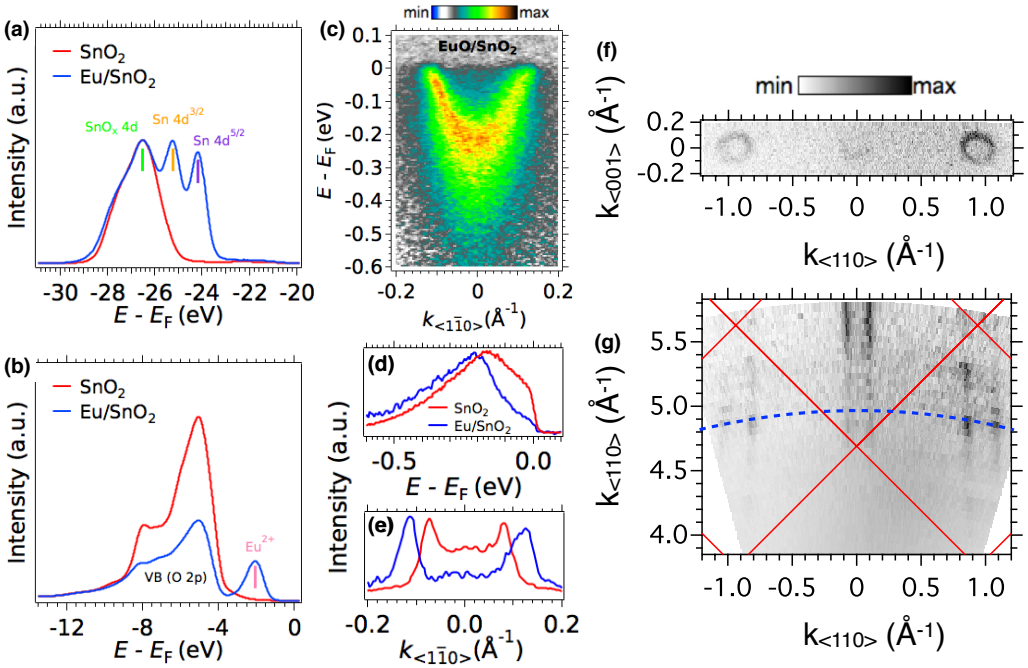

FIGURE 3.8: (a, b) Sn 4*d* core-levels peaks (a) and valence band (b) before (red) and after (blue) the deposition of 1 ML of Eu on SnO_2(110). (c) Energy-momentum dispersion of the 2DES measured at the EuO/SnO_2(110) interface obtained after deposition of 1 ML of elemental Eu. (d, e) Comparison of the energy distribution curves (EDCs) at $k_{<1\bar{1}0>} = 0$ (integrated over ± 0.05 Å^{-1}) and the MDCs at E_F (integrated over ± 10 meV) of the 2DESs at the bare (red) and Eu-capped (blue) SnO_2 surfaces. (f) In-plane Fermi surface of Eu(1 ML)/SnO_2(110) measured with $h\nu = 88$ eV. (g) Out-of-plane Fermi surface map of Eu(1 ML)/SnO_2(110) measured by a stepwise change ($\Delta h\nu = 2$ eV) of the photon energy between 50 and 100 eV. An inner potential of 10 eV was used in the calculation of the out-of-plane momentum. Red lines mark the borders of the bulk Brillouin zones. Blue dashed lines mark where $h\nu = 88$ eV is along the out-of-plane momentum. All data in this figure were measured at 16 K with LH photons. The photon energy was 110 eV for panel (a) and 88 eV for panels (b-e).

and implies that the carrier density of the 2DES in SnO_2 can be tuned via adatom deposition. As shown in Fig. 3.8 (f) and (g), the topography of the FS of Eu(1 ML)/SnO_2 remains the same as a cylinder proving again the 2D character of this interface metallic system.

2 ML Eu Previous work in the EuO/$SrTiO_3$ system [31] showed that the capping layer in EuO(1 ML)/$SrTiO_3$ is paramagnetic. On the other hand, EuO(2 ML)/$SrTiO_3$ shows a ferromagnetic behavior, even though the carrier density of the resulting interfacial 2DES remains the same, indicating a saturation for creating itinerant electrons from oxygen vacancies at the surface of $SrTiO_3$. Following this observation, we deposited 2 ML of pure Eu on SnO_2(110) to check whether the resulting capping

layer would be also fully oxidized, and to explore potential changes in the concomitant 2DES.

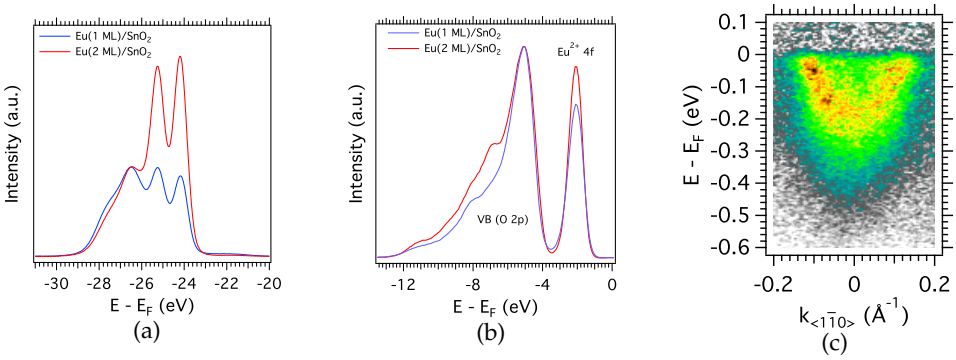

FIGURE 3.9: (a, b) Sn 4*d* core-level peaks (a) and valence bands (b) after the deposition of 1 ML (blue) and 2 ML (red) Eu on SnO_2(110). The photon energy used was 110 eV. (c) Energy-momentum dispersion of the 2DES at the Eu/SnO2(110) interface obtained after deposition of 2 ML of elemental Eu measured with LH photons at hν = 88 eV and $T = 15$ K.

As seen in Fig. 3.9, an intensity increase in the metallic Sn 4*d* core level doublet (panel a) and in the Eu^{2+} 4f peak (panel b) suggest that more oxygen vacancies have been created when the amount of deposited Eu increases from 1 ML to 2 ML. Furthermore, the line shapes of the XPS peaks remain similar, without additional peaks appearing, indicating that, after 2 ML deposition, Eu is still mainly oxidized into Eu^{2+}. Fig. 3.9(c) shows the metallic state close to the Fermi level measured under the same experimental conditions as in the 1 ML Eu case. This state has the same carrier density and effective mass as the 2DES at Eu(1 ML)/SnO_2 interface, indicating that the 2DES carrier density has already reached a saturation value, as with the previously reported EuO/$SrTiO_3$ system [31]. The insensitivity of the carrier density to Eu deposition beyond 1 ML Eu also implies that it is the oxidation of Eu (hence the formation of oxygen vacancies), rather than its ionization or the formation of residual metallic Eu, which is behind the electron doping of SnO_2 conduction band.

Al capping

Al is a well known reducing metal that has previously generated 2DESs in many oxide systems [1,30,82]. The resulting Al_2O_3 forms a capping layer, thus making it possible to conduct transport experiments on the same surfaces measured by ARPES. The redox reactions in the case of Al deposition on SnO_2 can be written as [147–149]:

$$\begin{cases} Sn + O_2 = SnO_2 + 519.65\ KJ/mol \\ 2Al + (3/2)O_2 = Al_2O_3 + 1581.97\ KJ/mol \end{cases} . \tag{3.3}$$

Thus,

$$3SnO_2 + 4Al = 3Sn + 2Al_2O_3 + 1604.99\ KJ/mol \tag{3.4}$$

Once again, the redox reaction between Al and SnO_2 is exothermic and therefore spontaneous.

Before depositing Al, the Knudsen cell needs to be degassed and its Al contents need to be molten ($> 900\ ^{\circ}C$ for 20 - 30 minutes). The deposition temperature was set at $T = 980^{\circ}C$ and the evaporation rate at 0.48 Å/min.

We deposited 2 Å of pure Al on the bare SnO_2(110) surface. The corresponding angle-integrated photoemission profiles, compared to those of the Eu-capped surface, are shown in Fig. 3.10(a-c). Along with the clear oxidation of Al as indicated in Fig. 3.10(a), a pair of peaks at binding energies of 24.2 eV and 25.2 eV, similar to those observed after Eu deposition, are also clearly visible, as shown by the green spectrum in Fig. 3.10(b). Furthermore, as shown in Fig. 3.10(c), the additional peak above the valence band after Eu deposition, which we assigned to Eu^{+2} $4f$, is not present after Al deposition, in line with our identification.

All these results combined imply that:

1. the new double peaks after Eu (or Al) deposition correspond to metallic Sn $4d$ rather than Eu core levels;

2. the additional peak above the valence band after Eu deposition is not an in-gap state due to oxygen vacancies, but rather the Eu^{+2} $4f$ core level (note that the Eu-$5p$ atomic levels have binding energy of $\approx$ 20 eV and $\approx$ 25 eV, close to the value of the Sn-$4d$ peaks).

Based on the above, we can firmly conclude that the redox reaction between Eu (Al) and SnO_2 happened, and thus oxygen vacancies were created after evaporating Eu (Al) at the surface of SnO_2.

Further ARPES measurements were also carried out to characterise the 2DES after Al deposition. Fig. 3.10(d) shows the energy-momentum dispersion of the 2DES. The Fermi momentum of this 2DES, extracted from the MDC at E_F as shown in Fig. 3.10(e), is $k_F = (0.091 \pm 0.001)^{-1}$, larger than the one at the bare surface but smaller than the one at the Eu capped surface. According to the Luttinger theorem, the corresponding 2D carrier density is $n_{2D} = (1.32 \pm 0.03) \times 10^{13} cm^{-1}$, which is 40% larger than the carrier density at the bare surface. So, even though Al is more efficient than Eu in taking away oxygen atoms, as shown by the chemical reaction formulae and indicated by Fig. 3.10(b), Al is less efficient than Eu in increasing the carrier density of the 2DES, suggesting that in this case more electrons remain localised around the oxygen vacancies.

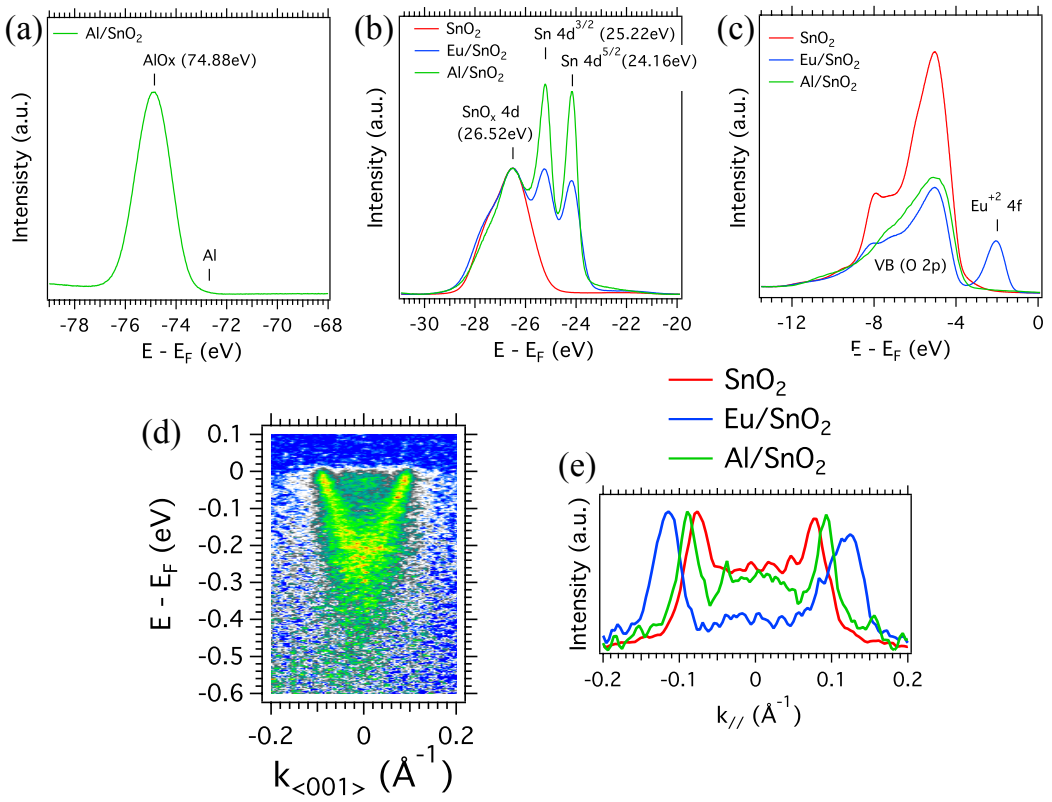

FIGURE 3.10: (a-c) XPS profiles of (a) Al $2p$ core level after Al deposition; (b) Sn $4d$ core levels at bare, Al capped and Eu capped surface of SnO_2; (c) valence bands of SnO_2 and Eu^{2+} $4f$ core level. (d) Energy-momentum dispersion of the 2DES at the Al/SnO2(110) interface obtained after deposition of 2 Å Al, measured with LH photons at $h\nu = 88$ eV. (e) Comparison of the MDCs at E_F (integrated over ± 10 meV) of the 2DESs at the bare (red), Eu-capped (blue) and Al-capped (green) SnO_2 surface. All the measurements were carried out at $T = 16$ K.

3.1.4 Robustness

Our results suggest that the 2DES generated on SnO_2(110) is robust against surface reconstructions and surface impurities. In the following, we explain these findings in detail.

Surface reconstructions

As stated previously, we observed two different LEED patterns indicating a 1×1 or a 4×1 atomic arrangement on the clean surface of SnO_2(110) (Fig. 3.11(a) and (b)). In principle, this change in surface periodicity may also be reflected in the periodicity of corresponding Fermi surfaces. However, the following ARPES measurements over two samples with different surface reconstructions show that the Fermi surface of the metallic 2DES remains the same. This may suggest that the 2DES resides in the subsurface region (1-2 unit cells below the surface as analyzed later) without being affected by the electric field periodicity of the atomic potential at the top-surface, in agreement with previous conclusions on the (111)-oriented surfaces of SrTiO3 [28] and KTaO3 [21].

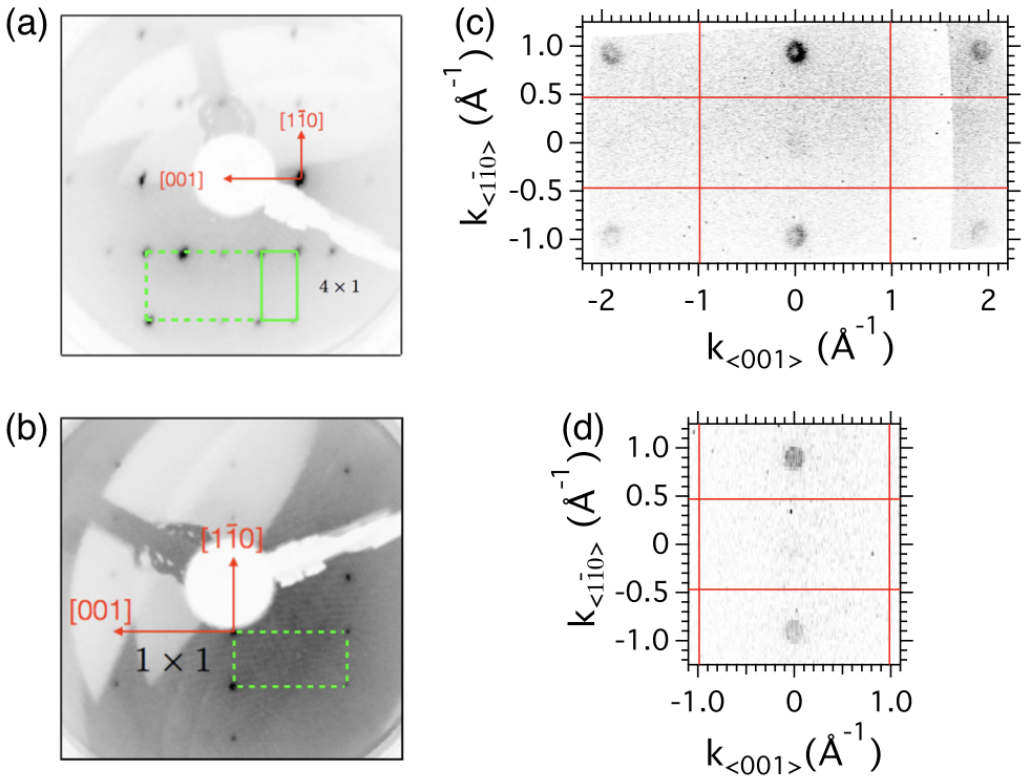

FIGURE 3.11: (a) LEED pattern of the bare (110) surface of SnO_2 showing a 4×1 surface reconstruction after annealing up to 600°C in UHV (electron energy: 58 eV). (b) LEED pattern of the bare (110) surface of SnO_2 showing a 1×1 surface reconstruction after annealing up to 730°C in UHV (electron energy: 116 eV). (c) In-plane Fermi surface of SnO_2(110) corresponding to (a) measured at $T = 16$ K using linear horizontal polarization at $h\nu = 88$ eV. (d) In-plane Fermi surface of SnO_2(110) corresponding to (b) measured at $T = 16$ K using linear horizontal polarization at $h\nu = 88$ eV.

Surface impurities

The 2DES at the surface of SnO_2 survives exposure to ambient pressure. In fact, being an excellent material for heterogeneous catalysis, the surface of SnO_2 is expected to easily adsorb and desorb gas molecules, which might help protecting the 2DES. Thus, we studied the electronic structure of the SnO_2(110) surface without prior preparation or cleaning in UHV. To this end, we used the UV beam at beamline 2A of KEK-PF, whose low brilliance ($5 \times 10^7\ s^{-1}\ \mu m^{-2}$), about 100 times smaller than other photoemission beamlines in third generation synchrotrons, has been previously shown to strongly reduce or even inhibit the photo-induced creation of oxygen vacancies in other oxides [150], thus, to make sure that any observed 2DES is not due to vacancies created by UV irradiation. As demonstrated in Fig. 3.12, the characteristic parabolic dispersion and circular Fermi surface of the 2DES can be observed even under these adverse measurement conditions. It should be noted that even the slightest exposure to moderate vacuum would normally make the surface unsuitable for ARPES measurements, due to the strong surface sensitivity of the technique. It is also noteworthy that the 2DES was observed immediately after illumination with the low-brilliance UV beam, and no evolution of its carrier density was evident even after several hours of measurements.

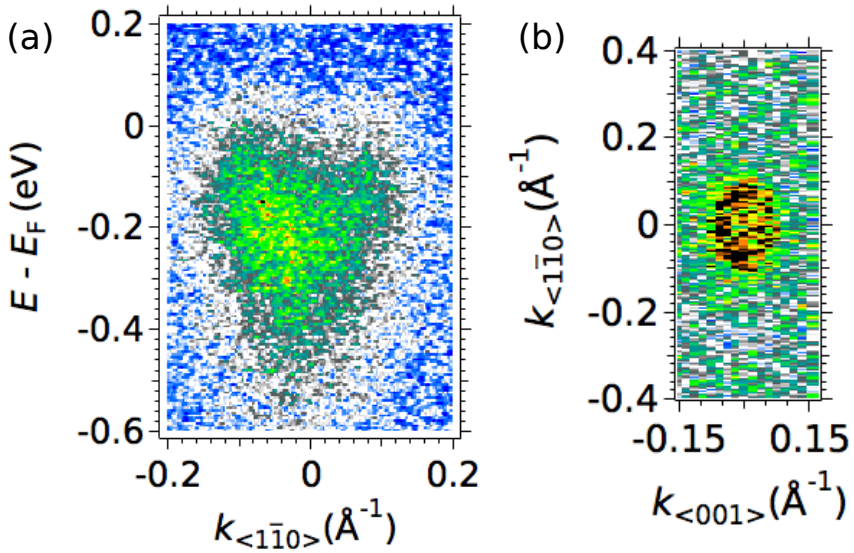

FIGURE 3.12: (a) Energy-momentum dispersion of the 2DES measured at the surface of an as-received crystal, i.e., never prepared or cleaned in UHV. (b) Corresponding Fermi surface contour around the center of the reduced 2D Brillouin zone. Data in this figure were acquired at 20 K using LH photons of energy 120 eV

The Fermi momentum of such a 2DES intrinsically present at the SnO_2 surface, determined from the MDC peaks at E_F, is $k_F = (0.077 \pm 0.003)$ Å^{-1}, which is comparable to the Fermi momentum of the UHV-prepared surface shown in Fig. 3.4. A 2DES in SnO_2 can be readily observed even under very unfavorable conditions: absence of surface treatment and exposure to low-brilliance light. This observation suggests that the catalytic properties of this material protect, or might even induce, such a 2DES, thus making SnO_2 a unique candidate for future technological applications.

3.1.5 Quantitative analysis

Sn 4d core levels

We further analyzed the Sn 4*d* core levels measured after 1 ML of Eu deposition at SnO_2(110) surface by numerical fitting with Lorentzian peaks and a Shirley background as shown in Fig. 3.13. From the fitting result, we find that for the newly emerged double peaks, the splitting energy is 1.08 eV which matches well with the energy splitting of the Sn 4*d* doublet [151], and the intensity ratio is around 11 : 13 which is in fair agreement with the theoretical value 2 : 3 for d double core levels. It should be noted that only if the final states corresponding to the two transitions are pure $j = 3/2$ and $j = 5/2$ sates, this ratio would be 2 : 3. Otherwise, especially when the spin-orbit interaction is not very strong, j is not anymore a good quantum number, the final states are not pure j states and the intensity ratio could be different.

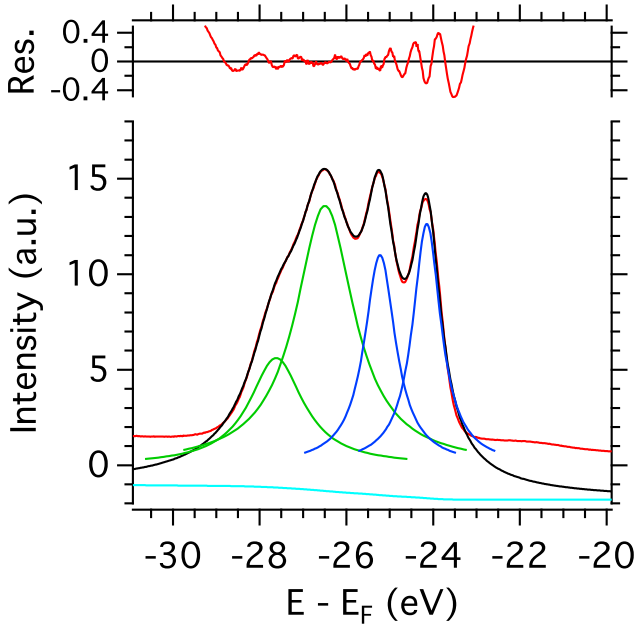

FIGURE 3.13: Numerical fit of the Sn 4*d* core levels in the binding energy range from 23 eV to 29 eV. Red: the experimental line-shape measured after 1 ML of Eu deposition at SnO_2(110) surface. Black: the final fitting result. Green: SnO_x 4*d* peaks. Blue: metallic Sn 4*d* peaks. Sky blue: the Shirley background. The red line in the inset above is the fitting residual.

Parameters of the quantum well

In this subsection, I present further analysis of the 2DES dispersion after the deposition of 1 ML of Eu in order to extract the parameters of the confining potential. Fig. 3.14(a) presents the 2D curvature [152] of the spectral intensity previously shown in Fig. 3.8(c). A parabolic fit of the energy dispersion, in the form $E = (\hbar^2/2m^\star)k^2 + E_b$, yields a band bottom $E_b = -225$ meV and an effective mass $m^\star = 0.29m_e$ [125, 142]. We assume that the first excited state ($n = 1$) of the confining quantum well, not directly observed in our data, lies just above E_F. This will provide an upper bound for the width of the quantum well. Taking, for simplicity, a wedge-shaped potential well, the values (in eV) of the discrete energy levels E_n are given by [1, 20]:

$$E_n = V_0 + 9 \times 10^{-7}(\frac{m_e}{m^\star})^{1/3}(n + \frac{3}{4})^{2/3}F^{2/3},$$

with V_0 the energy depth of the quantum well (eV), $m^\star$ the effective mass of the confined electrons, and F the strength of the electric field generating the confining potential (V/m). With the $n = 0$ subband (ground state) at 225 meV below E_F, and the $n = 1$ subband (first excited state) at the Fermi level, the electric field strength can be calculated to be $F = 122$ MV/m. This yields $V_0 \approx 500$ meV, $L \approx 18$ Å (i.e. 3 unit cells) for the spatial extension (mean value of the position operator) of the wavefunction in the ground state of the 2DES the main part of which thus lies between the 1st and 2nd unit cell below the surface, and a maximum width of the confining potential $L_z = 42$ Å (6 unit cells). These parameters are similar to the characteristics of the textbook 2DES observed at the (001) surface of $SrTiO_3$ [1, 20, 23].

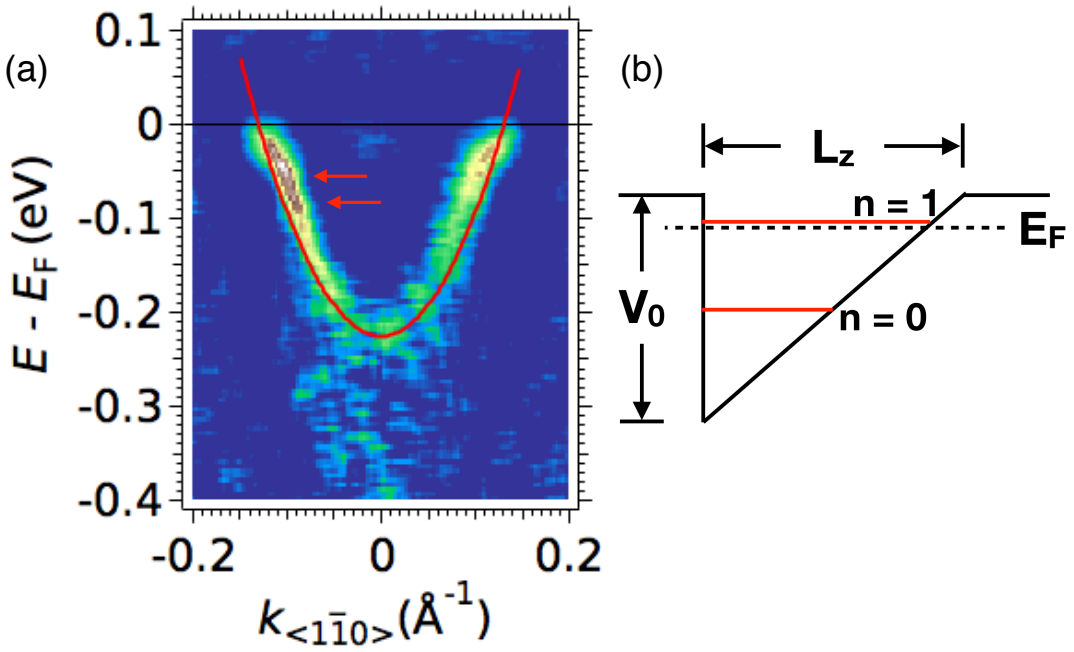

FIGURE 3.14: (a) 2D Curvature of the experimental intensity corresponding to the energy-momentum dispersion shown in Fig. 3.8(c) together with a parabolic fit of the form $E = (\hbar^2/2m^\star)k^2 + E_b$, with $E_b = -225$ meV and $m^\star = 0.29m_e$. Two kinks at 59 meV and 79 meV indicated with red arrows are the spectroscopic fingerprints of electron-phonon interaction. (b) Sketch of a wedge-like quantum-well potential with a potential depth V_0 and a maximum confining width L_z. The observed 2DES is confined as the $n = 0$ ground state, while the $n = 1$ quantum-well substate is supposed to be in the vicinity of the Fermi level E_F.

Intensity modulations along k_z in Fig. 3.5(b)

The ARPES intensity modulations as a function of out-of-plane momentum, also observed in many other 2DESs [26, 28, 30, 82, 105], are a consequence of dipole-transition selection rules from the confined electronic states at the surface of the material [26, 28, 153]. The periodicity of the modulations is related to the width of the spatial confinement of the $n = 0$ state ($L \approx 18$ Å). This confinement width would be reflected in momentum space as $2\pi/L \approx 0.35$ Å, in good agreement with the value inferred from Fig. 3.5(b).

Electron-phonon interaction

The spectroscopic fingerprint of the electron-phonon interaction is a kink in the experimental dispersion that corresponds to the characteristic Debye energy (ω_D) of the phonon, as described for instance in the case of the 2DES at the surface of ZnO in the second chapter of this manuscript. After the deposition of Eu, two such kinks are observed in the energy dispersion of the 2DES at the (110) surface of SnO_2

(Fig. 3.14(a)). The corresponding Debye energies of the phonons are 59 meV (E_g mode) and 79 meV (A_{1g} mode) [154–156].

In the presence of electron-phonon coupling, the predominant interactions vary as a function of the carrier density, giving rise to two different regimes: the polaronic regime at low carrier densities, where the long-range Fröhlich interaction prevails, and the Fermi liquid regime at high carrier densities, where the long range interaction is suppressed by strong electronic screening [63, 64].

The critical carrier density between these two regimes can be estimated by balancing the relevant phonon energy and the surface plasma frequency ω_s given by the carrier density n [65]:

$$\omega_s = \sqrt{\frac{ne^2}{\varepsilon_0(\varepsilon_\infty + 1)m^\star}},$$

where ε_0 is the vacuum permittivity, ε_∞ is the dielectric constant in high frequency limit, and $m^\star$ is the carriers' effective mass.

Given that $\varepsilon_\infty = 5$ and $m^\star = (0.24 \pm 0.02)m_e$ for SnO_2, and a phonon energy cutoff of 80 meV as observed experimentally, the critical carrier density per unit volume would be $n \approx 6.7 \times 10^{18}$ cm^{-3}. Using the aforementioned spatial extension of the confining potential ($L_{\max} = 42$ Å), this yields a critical surface carrier density $n_c^s = nL_{\max} \approx 2.81 \times 10^{12}\ cm^{-2}$.

This rather low critical carrier density is mainly due to the small dielectric constant ε_∞ of SnO_2, and means that the 2DESs both at the bare SnO_2 surface and at the EuO/SnO_2 interface lie in the Fermi liquid regime -as their corresponding carrier concentrations are up to one order of magnitude larger than the critical one. This is confirmed in the experimental data by the absence of the spectroscopic fingerprint of Fröhlich polarons: replica bands at higher binding energies [22, 63, 64]. This is in stark contrast with the 2DESs on $SrTiO_3$ and TiO_2 surfaces where clear band satellites were observed at similar carrier densities owing to the large dielectric constant of the corresponding materials [22, 63, 64].

3.1.6 Origin and nature of the 2DES in SnO_2

The origin of the 2DES on SnO_2(110) We now turn to the origin of the 2DES on SnO_2. The widely-accepted mechanism of formation of 2DESs at the surface of transition metal oxides, such as $SrTiO_3$, TiO_2, $KTaO_3$, $CaTiO_3$ and ZnO, is the creation of oxygen vacancies in the near-surface region, induced either by UV/X incoming photons, or by a redox reaction between the oxide substrate and a reducing metallic agent evaporated at its surface [20, 23–28, 30, 31, 82, 105, 143, 144, 157] Nevertheless, in some oxides, other microscopic phenomena, such as intrinsic electron accumulation and doping with hydrogen impurities may also have an important role for the onset of conductivity [158]. In fact, recent numerical calculations for SnO_2 have suggested that even though the (110) surface, which is characterized by an ordered arrangement of Sn_3O_3 clusters, contains a deficiency of oxygen atoms, it remains insulating with a small bandgap open [108]. Our work shows that the deposition of a reducing metal agent changes dramatically the chemical environment of Sn atoms as some of the latter pass into a lower oxidation state [Fig. 3.8(a)]. Therefore, the structural model based on Sn interstitials cannot account for the 2D conductivity. On the other hand, a structural model based on the presence of surface oxygen vacancies as suggested in Refs. [115] and [159] might explain the absence of bonding counterparts to the Sn atoms and the enhancement of the 2DES.

s electrons *vs* **d electrons** The 2DES observed at the (110) surface of SnO_2 is, to our knowledge, the first of its kind on a rutile structure. In fact, a previous comparison of the near-E_F electronic structure of TiO_2-rutile and TiO_2-anatase has led to the conclusion that surface oxygen vacancies on a rutile structure create excess electrons that remain localized at Ti sites rather than forming a 2DES [22, 26]. The present work shows that such a conclusion cannot be generalized to all rutile lattices, and other factors, such as the orbital character of the confined states (d for TiO_2 *vs* s for SnO_2), have to be taken into account to understand the emergence of a 2DES.

3.1.7 Conclusion

In conclusion, we observed a metallic 2DES at the (110) surface of SnO_2 by means of ARPES. Its carrier density can be enhanced by the deposition of elemental Eu or Al, and reduced by a controlled temperature increase, while the 2DES remains robust against different surface reconstructions, high temperatures and exposure to ambient pressure. The spectral fingerprints of the 2DES show an appreciable electron-phonon interaction, with the system always lying in the Fermi liquid regime due to the small dielectric constant of SnO_2. The strong effect of a reducing metal agent such as Eu and Al on the emergence and enhancement of the 2DES proves that surface oxygen vacancies are at the origin of the 2DES in SnO_2. Our results provide new important insights on the long-withstanding debate on the origin of the n-type conductivity of SnO_2, and prove that both the crystal structure and the orbital origin of the conduction electrons are decisive for the emergence of a 2DES in oxides.

3.2 $FeTiO_3$: ferromagnetic phase transition

Traditionally, ilmenite $FeTiO_3$ is the most important ore source of titanium widely used in the industry [160, 161]. In the past few years, ilmenite has attracted a lot of academic interest due to its potential applications in spintronics, optoelectronics and photo-catalysis [162–166]. There are many experiments in crystal synthesis and characterisations of its magnetic, structural and optical properties [167–169]. Bulk $FeTiO_3$ is an antiferromagnetic p-type semiconductor with a wide bandgap around 2.8 eV [162,168,170,171], and has a rhombohedral structure (see Fig. 3.15) with trigonal space group $R\bar{3}$, in which Fe^{2+} ($3d^6$) and Ti^{4+} ($3p^6$) layers are arranged alternately with an antiferromagnetic coupling between Fe interlayers below the Néel temperature around 55 K [167,172,173] (see Fig. 3.16(a)). If synthesised as a thin film, $FeTiO_3$ is reported to be ferrimagnetic at low temperatures [174], while if synthesised as nanoparticles, it shows weak ferromagnetism at and below room temperature and has an indirect optical bandgap 2.8 eV determined from the Tauc plot, making it possible to design ferromagnetic semiconductor devices operating at room temperature [168].

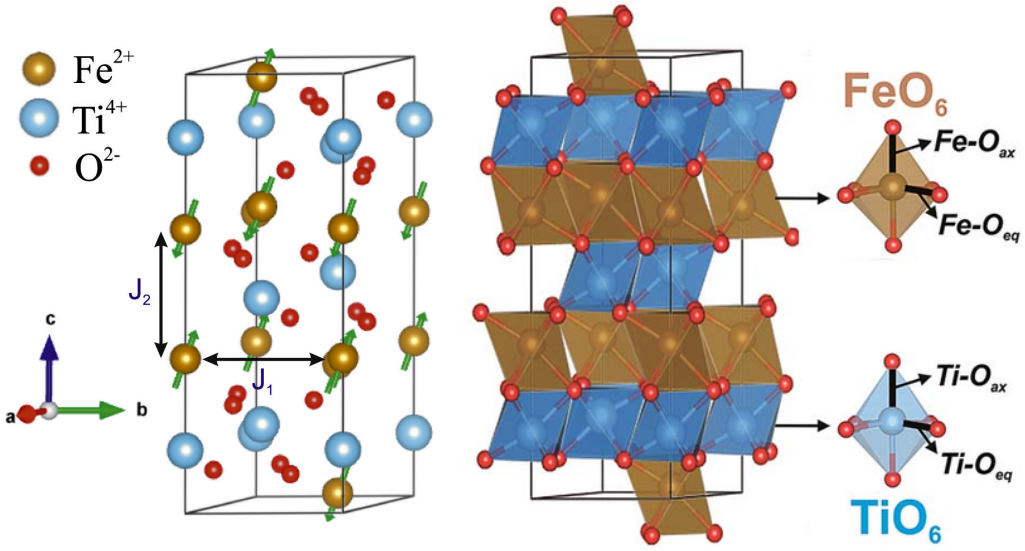

FIGURE 3.15: Sketch of the bulk structure of ilmenite $FeTiO_3$ with lattice parameters $a = b = 5.087$ Å and $c = 14.083$ Å. Each Fe and Ti site is surrounded by 6 oxygen atoms, and Fe^{2+} ($3d^6$) and Ti^{4+} ($3p^6$) layers are arranged alternately. The positive $J_1 = 28.5$ K and the negative $J_2 = -6.67$ K refer respectively to the intra-layer and inter-layer magnetic interactions between Fe^{2+} ions [172, 173]. Thus, the intralayer coupling is ferromagnetic while the interlayer coupling is antiferromagnetic with a Néel temperature $T_N \approx 55$ K. The magnetisation direction is mainly along c axis with a small off-set angle. Taken from Ref. [172, 175]

Fig. 3.16(a) presents the zero-field-cooled (ZFC) and field-cooled (FC) magnetisation curves of $FeTiO_3$ nanoparticles measured with applied magnetic fields 100 Oe,

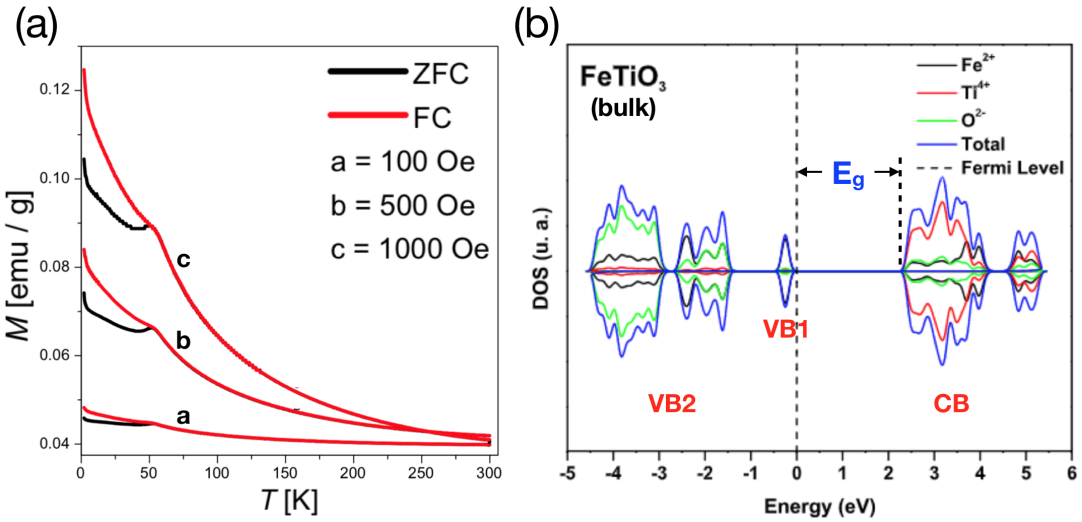

FIGURE 3.16: (a) Temperature dependent magnetisation of nano-ilmenite $FeTiO_3$ in an external magnetic field with three different strengths 100, 500, and 1000 Oe respectively. The black curve was measured in zero field cooling (ZFC) process and the red curve was measured with the magnetic field always present. Taken from Ref. [168]. (b) Atom-resolved and spin-resolved (above and below the central line) density of state of bulk $FeTiO_3$ in the ground state calculated by means of the Becke's three-parameter hybrid density functional (B3LYP). The top of the valence band is set to zero acting as the Fermi level. The valence band (VB) can be separated into two parts: VB1 (the top of the valence band) and VB2 (the rest of the valence band). The conduction band (CB) locates E_g = 2.6 eV above VB1. Taken from Ref. [172].

500 Oe and 1000 Oe from 2 K to 300 K. These two curves diverge at their common peak position T $\approx$ 52 K, which is assigned to be the Néel temperature [168, 176].

Fig. 3.16(b) [172] shows the atom-resolved and spin-resolved density of states (DOS) of bulk $FeTiO_3$ in the ground state at $T = 0$, calculated in the framework of Density Functional Theory (DFT) with the Becke's three-parameter hybrid density functional (B3LYP) used to treat the electron exchange and correlation in the calculations [177]. These calculations suggested that $FeTiO_3$ has a semiconducting behavior with an indirect band-gap of 2.60 eV in accordance with the experimental results (2.5 - 2.9 eV) [162, 164, 168, 178]. The zero net spin behavior is also in line with $FeTiO_3$'s antiferromagnetism at low temperatures.

Theoretically, $FeTiO_3$ has several possible terminations for its (0001) surface as shown in Fig. 3.17(a) [173]. Experimentally, Fellows *et al*. indeed found different surface terminations by LEED [179] and STM [180]. By applying the hybrid density functional B3LYP method to the unreconstructed (1×1) (0001) surface of $FeTiO_3$, the surface energy of a certain termination can be calculated at $T = 0$ K as a function of the oxygen chemical potential. Fig. 3.17(b) shows the results for two selected terminations (Fe-O_3-Ti- and Ti-O_3-Fe-) and their corresponding oxidised configurations. Note that the oxygen chemical potential $\Delta\mu_O(T, p_{O_2})$ at 0 K can be converted into pressure scales at fixed temperatures, through an approximation approach outlined by K. Reuter and M. Scheffler [181], as shown in the top of Fig. 3.17(b). These results suggest that the Fe-O_3-Ti– surface is the most stable surface at low oxygen partial pressures, thus being most likely to form under high vacuum [173].

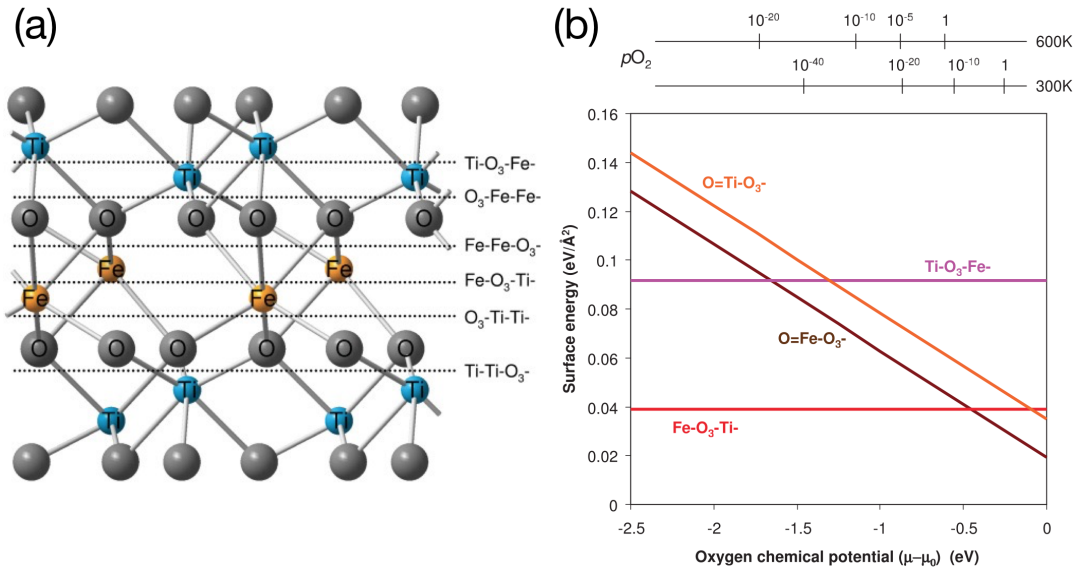

FIGURE 3.17: (a) Sketch of possible terminations of the ilmenite ($FeTiO_3$) (0001) surface. (b) Surface energy of selected surface terminations (Fe-O_3-Ti- and Ti-O_3-Fe-, and their oxidised versions) plotted as a function of oxygen chemical potential. O_2 is used as the chemical reservoir for O, and $FeTiO_3$ is used for Ti and Fe. In the top x axis, the chemical potential $\Delta\mu_O(T, p_{O_2})$ has been converted into pressure scales at fixed temperatures of $T = 300$ and 600 K. Taken from Ref. [173].

Within the same framework of DFT, the hybrid density functional B3LYP, a 24-layer slab was used to compute the surface relaxation and perform further DFT calculations, as at this thickness the cleavage energy converged to the bulk value [173]. Fig. 3.18(a) shows the relaxed geometry of the Fe-O_3-Ti- surface with the top Fe atom moving inwards (0.72 Å) to the O_3 layer [173]. Fig. 3.18(c) and (d) show the atom-resolved DOS contributed from the surface layer and the other left layers. As previously mentioned, the intralayer magnetic interaction between Fe^{2+} ions is ferromagnetic ($J_1 > 0$), thus the single Fe^{2+} layer has a net spin polarisation of $3.76|e|$ in the bulk [182]. So it is not surprising to find a net spin state close to the Fermi level in the slab calculation. Besides the small change of the net spin of the surface Fe ($3.68|e|$ [173]) with respect to the bulk value, the Fe state at the top of the valence band splits into two parts, with the surface Fe contributing a state 0.5 eV lower in energy than the bulk Fe state, which is close to the Fermi level in line with the bulk calculation shown in Fig. 3.16(b) indicating a p-type semiconducting behavior. Though the results of these calculations are obtained for the ground state at 0 K, they could still be helpful to understand the experimentally measured electronic structure in the paramagnetic phase at temperatures higher than the Néel temperature (≈ 55 K).

In this section, I present my ARPES results across the magnetic phase transition. The goal was not only to monitor the electronic structure of $FeTiO_3$ across the transition but also to study whether a 2DES could be fabricated at its surface and how the magnetic transition would affect it.

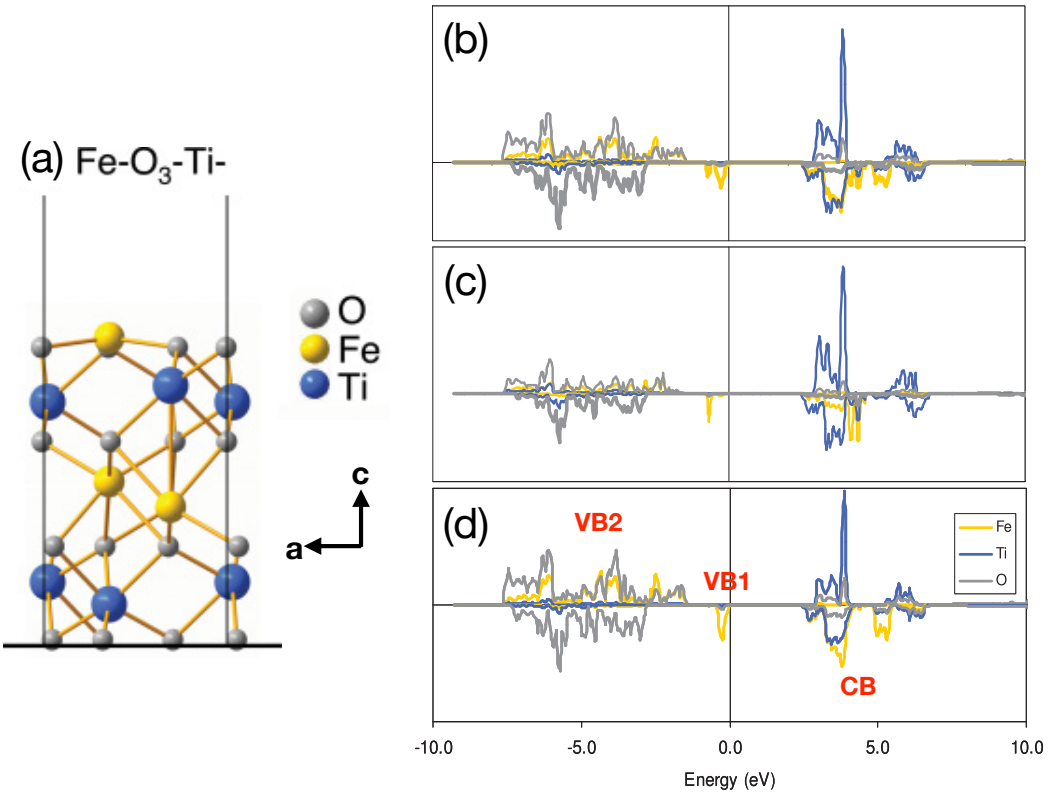

FIGURE 3.18: (a) Relaxed geometry of the Fe-O_3-Ti- terminated surface. (b-d) Electron DOS for the Fe-O3-Ti- surface at ground state, calculated by using the hybrid density functional B3LYP. Total DOS decomposed to Fe (yellow), Ti (blue), and O (grey) is shown in panel (b), while panel (c) shows a decomposition of just the surface Fe, Ti, and O, and panel (d) shows the decomposition of the other layers. The top of the valence band is set to zero in energy. Taken from Ref. [173]

3.2.1 Sample preparation and characterisation

Our experiment was carried out at the beamline CASSIOPÉE of synchrotron Soleil in France. Two $FeTiO_3$ single crystal samples (from Surfacenet) were annealed up to 600°C and 850°C respectively, with a vacuum pressure up to $P = 2.5 \times 10^{-8}$ mbar. The LEED pattern shown in the inset of Fig. 3.19 suggests that our treatment to the $FeTiO_3$(0001) sample did not cause any surface reconstruction. Core level spectroscopy (see Fig. 3.19) was employed to confirm the presence of Ti and Fe elements by identifying their $3p$ peaks. Note that a small peak at binding energy around 17.5 eV could not be unequivocally identified. Its intensity became larger after a longer time of annealing. Thus, it may be due to bulk impurities that segregate at the surface after anealling, for example, potassium (K) whose $3p$ core level energy is a good match according to the NIST database [183].

Close to the Fermi level, a small intensity shoulder can be clearly observed in the zoom-in inset of Fig. 3.19. Our ARPES data (see later) show that this state close to the Fermi level, although weak in intensity, has strongly dispersing behavior and forms well-resolved constant energy contours in k-space at/close to the Fermi level at $T = 72$ K. The pressure during ARPES measurements did not exceed $P = 1.0 \times 10^{-10}$ mbar.

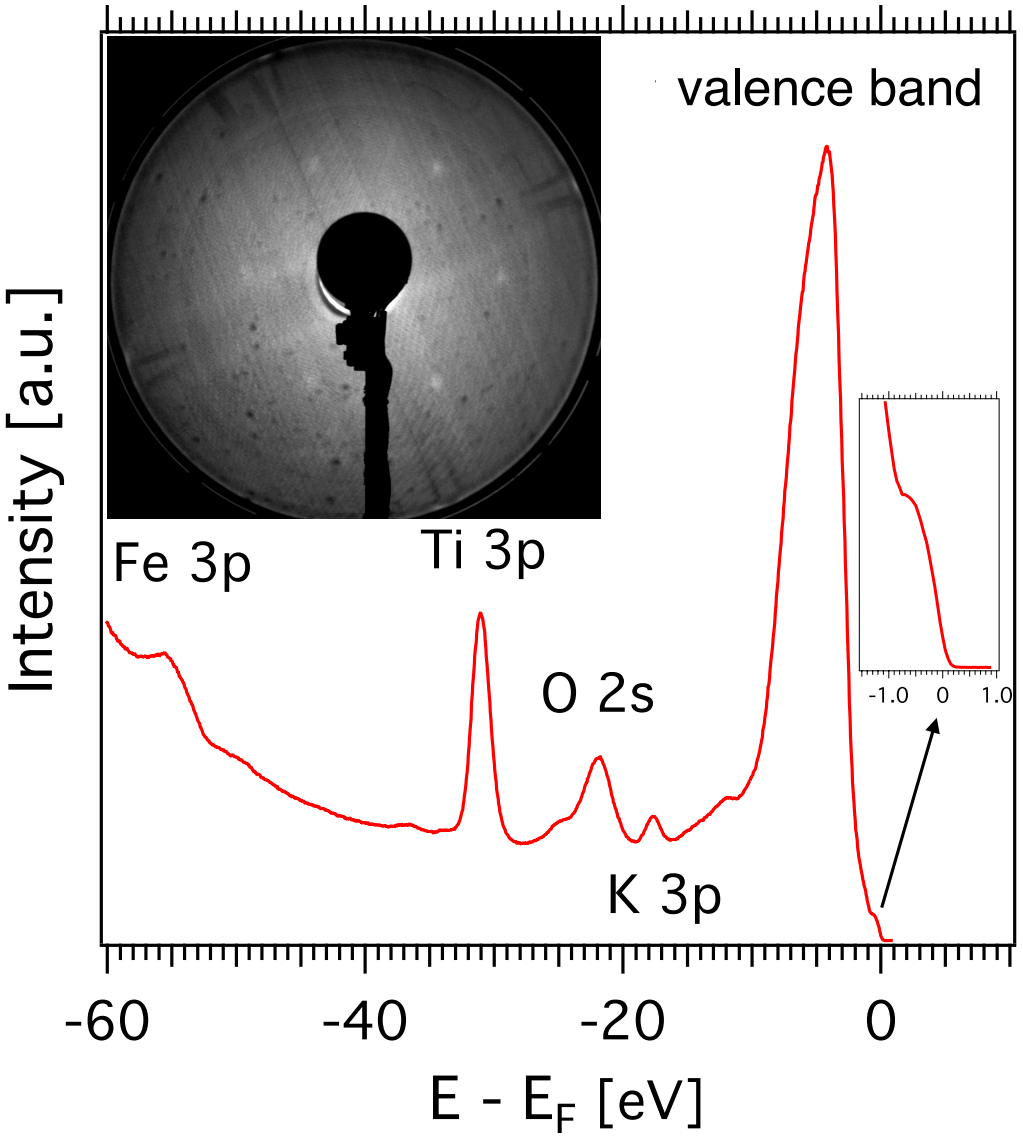

FIGURE 3.19: Core level spectroscopy profile line including the Fe and Ti $3p$ peaks measured with beam energy $h\nu = 94$ eV in LH polarisation. Potassium (K) coming from the bulk as an impurity grew in intensity after longer time annealing. Besides all these core levels, one also observes the valence band, as well as a state close to the Fermi level shown in the in-set, which will be studied and analysed further in the following. The temperature of measurement was 72 K, in the paramagnetic phase. Inset: LEED pattern obtained from the $FeTiO_3$(0001) crystal surface at 42 eV after annealing at 730°C in vacuum (pressure $< 5 \times 10^{-8}$ Torr).

3.2.2 ARPES results

Valence bands

Fig. 3.20(a) and (c) show the valence band measured with LH and LV polarised photons at $h\nu = 94$ eV and $T = 72$ K in the paramagnetic phase. With the 2D curvature treatment, a band at/close to the Fermi level (VB1) is observed, and the rest of the valence band (VB2, a few eV below the Fermi level) is shown to be dispersing indicating that the measured surface is well-ordered. Fig. 3.20(b, d) present a zoom near

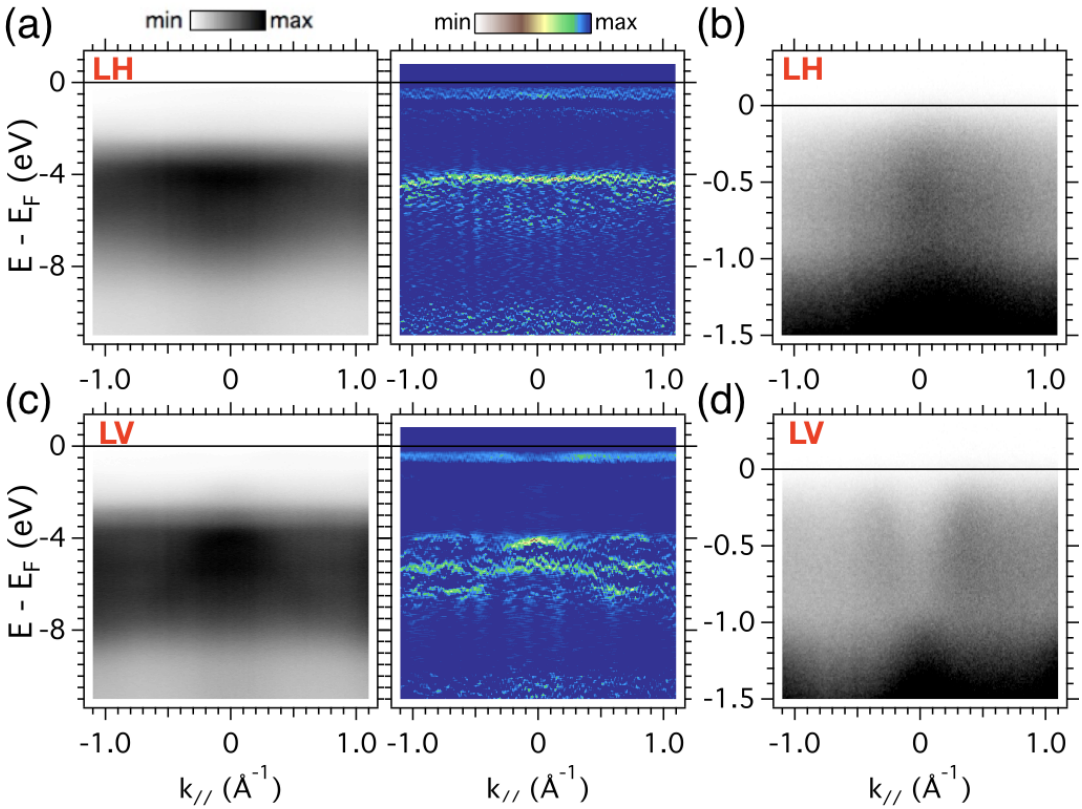

FIGURE 3.20: Energy-momentum dispersions of the valence band measured at normal emission with (a) LH and (c) LV polarised photon at $h\nu = 94$ eV and T = 72 K, together with their 2D curvature spectra. (b) and (d) are the zoom-in of (a) and (c) respectively close to the Fermi level.

the Fermi level of Fig. 3.20(a, c), thus showing distinctly the presence of a dispersing band, especially in LV polarisation (i. e. Fig. 3.20(d)).

Fig. 3.21(a) illustrates the first Brillouin zone (BZ) of $FeTiO_3$. Its reduced 2D BZ is projected on-top of the constant energy maps in Fig. 3.21(c-e). The photon energy $h\nu = 94$ eV locates around the Z point at normal emission, as indicated with a red dashed curve in Fig. 3.21(a).

Fig. 3.21(c) shows the constant energy (binding energy 1.2 eV) map at the very top of VB2, presenting clearly a 3-fold symmetry (a hexagonal pattern). The constant energy (binding energy 0.5 eV) map shown in Fig. 3.21(d) resembles a "rhombus" formed out of two crossing pairs of parallel straight strips. The Fermi surface shown in Fig. 3.21(e) manifests the hexagonal pattern again.

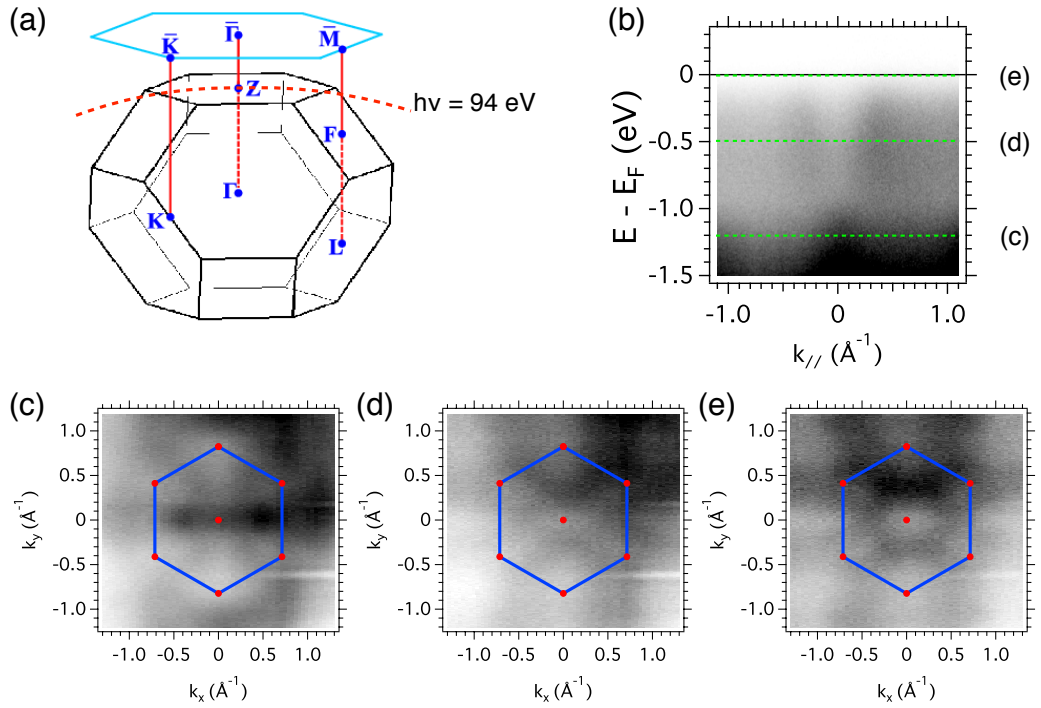

FIGURE 3.21: (a) The first bulk Brillouin zone of $FeTiO_3$ with space group $R\bar{3}$ together with the corresponding reduced 2D Brillouin zone. Notice that the *c*-axis of the bulk Brillouin zone is not in the actual scale for better visualisation. (b) Energy-momentum dispersion of the band at/close to the Fermi level. (c-e) The constant energy maps at binding energy (c) 1.2 eV, (d) 0.5 eV, and (e) at the Fermi level (integrated over $\pm$ 10 meV), as indicated with the three green dashed lines in (b). All data were obtained with LV polarised photons at $h\nu = 94$ eV and $T = 72$ K in the paramagnetic phase.

Magnetic phase transition

Fig. 3.22(a) tracks the integrated photoemission spectra of the dispersing band at/close to the Fermi level (shown as a shoulder in the integrated spectra in Fig. 3.19), across the magnetic phase transition ($T_N = 55$ K).

Concomitantly with the magnetic phase transition, a clear charging effect is present, due to which all the bands are rigidly shifted away from the original Fermi level by a temperature-dependent energy value compared to their original energy at $T = 72$ K, as shown in Fig. 3.22(b). This strong charging effect arises as the system becomes more and more insulating in the magnetic phase, in line with the disappearance of the conduction-band peak in Fig. 3.22(a). Note that though energy shifts inferred from the Ti 3*p* peak and the valence band peak are close in energy and behave almost identical as a function of the temperature, the valence band peak position in binding energy shows a relative change with respect to the Ti 3*p* peak, as shown in Fig. 3.22(c). My understanding to this relative change between Ti 3*p* peak and valence band peak is that the valence band is composed of several dispersing bands, which may vary in energy when approaching the ferrimagnetic phase transition, thus leading to a redistribution of DOS. As a consequence, the valence band peak varies slightly in binding energy.

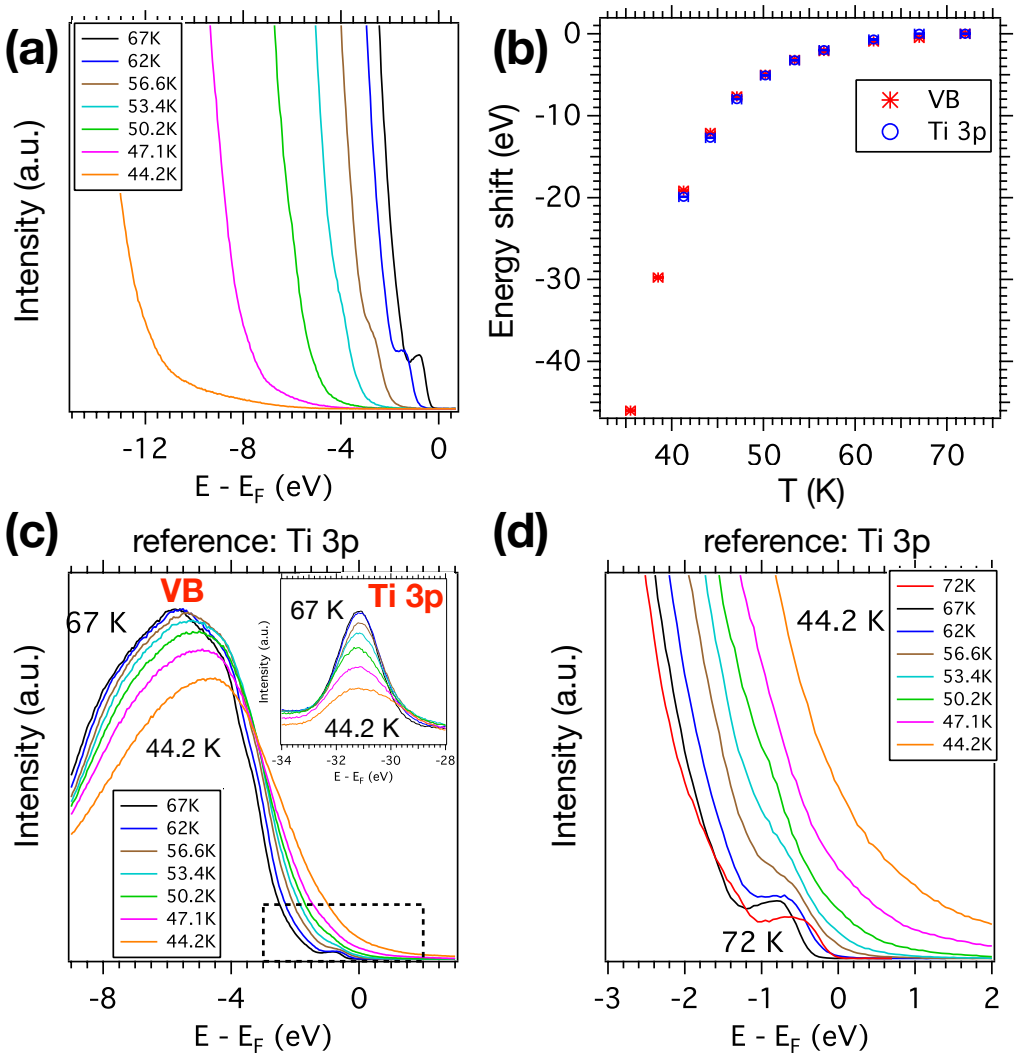

FIGURE 3.22: (a) Integrated photoemission spectra of the dispersing band at/close to the Fermi level measured with LV polarised $h\nu = 94$ eV photons at various temperatures. The Fermi level at $T = 72$ K is used as the global reference for the other temperatures. It is clear that the state around the Fermi level disappears as temperature drops below 50 K, as a consequence of the magnetic transition. On the other hand, the large shift in the energy of the valence band's leading edge is due to the progressive charging of the sample as it becomes insulating in the magnetic state. To prove this point, panel (b) in the right shows the energy shifts of the Ti-3p core level and the valence-band peak compared to their values at $T = 72$ K (see Fig. 3.19). The two shifts have an identical temperature dependence (within our resolution), demonstrating the extrinsic (charging) nature of the valence band shift. (c) The same integrated photoemission spectra of the whole valence band (VB) at various temperatures after using the Ti 3p core level peak as a global reference, as shown in the inset where the Ti 3p peaks are shifted to the same binding energy. (d) Zoom-in to the dispersing band at/close to the Fermi level as indicated with the dashed box in panel (c) using the Ti 3p core level peak as a global reference. The photoemission spectra at 72 K (Fig. 3.19) is specially appended in order to show change of the top of the valence band (the shoulder signal).

Fig. 3.22(c) shows the integrated photoemission spectra of the valence band (including the small shoulder close to the Fermi level) at various temperatures with an energy compensation determined from the Ti $3p$ core level, i. e., taking the Ti $3p$ core level as an intrinsic reference for all measured photoemission spectra as shown in the inset. As one can see, the VB peak moves gradually and slowly towards the Fermi level when the temperature decreases. A zoom-in to the shoulder part (VB1) is present in Fig. 3.22(d). Behaving different from the VB peak (mainly the VB2), this shoulder peak (VB1) moves away from the Fermi level indicating an opening/increasing of a gap, in line with the on-going charging of the sample. Due to the stronger broadening of VB2 and its moving towards the Fermi level, the shoulder's moving away from the Fermi level is covered by the background from the tail of VB2 when the temperature approaching 50 K. It is nevertheless noteworthy that the vanishing of the conduction state peak can be observed.

3.2.3 Discussion and Conclusion

Supposing that $FeTiO_3$ in the paramagnetic phase keeps a similar electronic structure (i. e. similar distribution of DOS with small constant energy shift) as in the 0 K ground state (see Fig. 3.18), we can take advantage of the previously introduced results of DFT calculation to help us to understand our ARPES data. In fact, the most salient difference between the paramagnetic and antiferromagnetic phases is the ordering of the atomic spins. But the spin-spin correlation term $J_{1(2)}s_i \cdot s_j$ (i and j are intralayer (interlayer) nearest neighbouring sites) is a correction small in energy to the Hamiltonian.

The very first thing we can clarify is that the observed dispersing state (i. e. the should in Fig. 3.19 and Fig. 3.22) at/close to the Fermi level corresponds to the top of the valence band (VB1) as shown in Fig. 3.18(b-d), with the conduction band being roughly 2.5 eV above the Fermi level. This top of valence band has extended spectrum weights at/crossing the Fermi level, probably due to the not so low temperature 72 K, in line with its reported semiconducting behavior. The gap between VB1 and VB2 (the rest of the valence band at higher binding energy) is around 0.6 eV (Fig. 3.18(b)), consistent with the different topographies observed in the constant energy maps shown in Fig. 3.21(c-e).

Another analysis that can be done is about the parity of the matrix element of photoemission. According to another DFT calculation for the $Fe_2Ti_3/FeTiO_3$ interface, the emerged top of the valence band has a strong d_{z^2} orbit character [184]. As shown in Fig. 3.23, in our measurement configuration of $FeTiO_3(0001)$, the d_{z^2} has even parity with respect to the mirror plane xz, which crosses the central part of the vertical detector slit. The final state is also required to be even in order to have detectable signals. So for LV light polarisation, which has odd parity with respect to the xz mirror plane, the total matrix element is odd. Thus, there will be a strong intensity suppression around $k_{slit} = 0$, as observed in our experiment: notice the missing intensity at the bottom of the dispersing band at/near E_F. What happened here is similar to the polarisation dependence shown by the two-dimensional electron system of s-orbital character at the surface of SnO_2 (see Fig. 3.6 in Section 3.1.2).

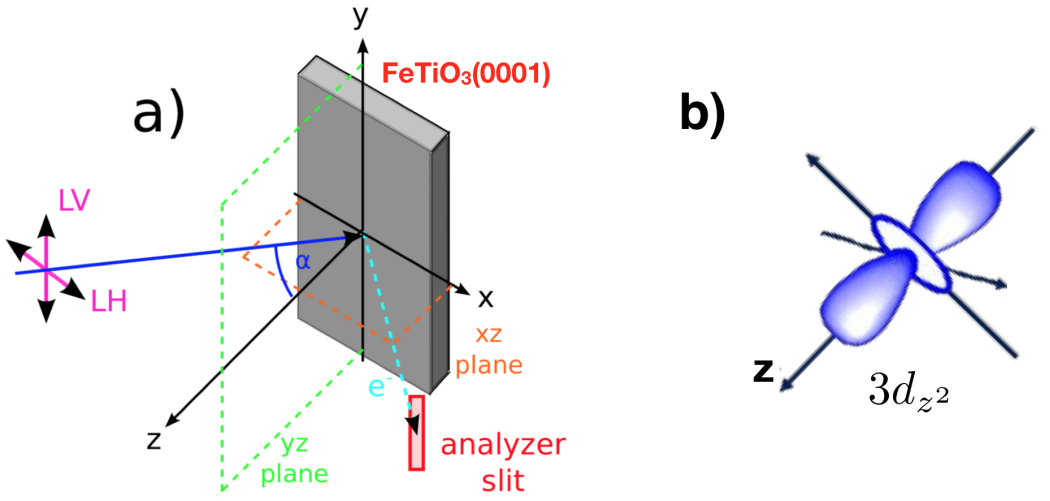

FIGURE 3.23: (a) Sketch showing the ARPES setup including sample, incidence photon & photo-electron beams, detector slit, the xz & yz planes and the direction of linear horizontal and vertical polarisations. Adapted from Ref. [185]. (b) Sketch of the $3d_{z^2}$-orbital state with the z axis along normal direction z in panel (a). The positive and negative wave function phases are indicated as blue and white. Adapted from Ref. [186].

A question related to section 3.1 is what is the role of oxygen vacancies in $FeTiO_3$. Naively thinking, surface oxygen vacancies in $FeTiO_3$ have the same effect as in many other oxides, such as $SrTiO_3$, anatase TiO_2, ZnO and SnO_2, as previously shown in this chapter. However, the surface energy calculated with DFT (Fig. 3.24(a)) and the DOS calculated for the oxidised surface O=Fe-O_3- (Fig. 3.24(b-d)) go against that idea. Firstly, as shown in Fig. 3.24(a), compared to the oxygen deficient surfaces O_1-Fe-Fe- and O_2-Fe-Fe-, and the oxygen abundant surface O=Fe-O_3-, the Fe-O_3-Ti-surface still remains as the energetically most favored surface in vacuum. Therefore, it should be rather difficult to create oxygen vacancies at the surface of $FeTiO_3$. Second, the DOS calculation shown in Fig. 3.24(b-d) suggests that surface oxidation narrows the bandgap, similar to the $Fe_2O_3/FeTiO_3$ interface, which showed p-type ferrimagnetic semiconductor behavior and half-metallic behavior [163,167,184,187], or to $FeTiO_{3+\delta}$ eptaxial thin films (Fig. 3.24(e)) [188]. It seems that in the case of $FeTiO_3$, oxygen abundance instead of the oxygen vacancies helps to increase the conductivity. So even if oxygen vacancies are created, it is unlikely that they can induce mobile carriers. Based on these considerations, our observation of a conducting state at the Fermi level, which is the top of the valence band (VB1), may suggest a surface hole doping (i. e. p-type doping) to the $FeTiO_3$ sample mimicking the $Fe_2O_3/FeTiO_3$ interface.

As a brief conclusion of this section, I successfully measured for the first time, to my knowledge, a conducting state at the (0001) unreconstructed surface of $FeTiO_3$ in the paramagnetic phase at T = 72 K, and characterised its Fermi surface manifesting the 3-fold symmetry ($R\bar{3}$) of the lattice with a hexagonal pattern. This state can be assigned to the top of the valence band of $FeTiO_3$, suggesting a hole doping of this surface resembling the $Fe_2O_3/FeTiO_3$ interface. Furthermore, the opening of a gap at the Fermi level across the magnetic transition has been recorded with ARPES, suggesting a Néel temperature $T_N \approx 52$ K in agreement with previous research works. These ARPES data obtained at the $FeTiO_3$(0001) surface in the paramagnetic

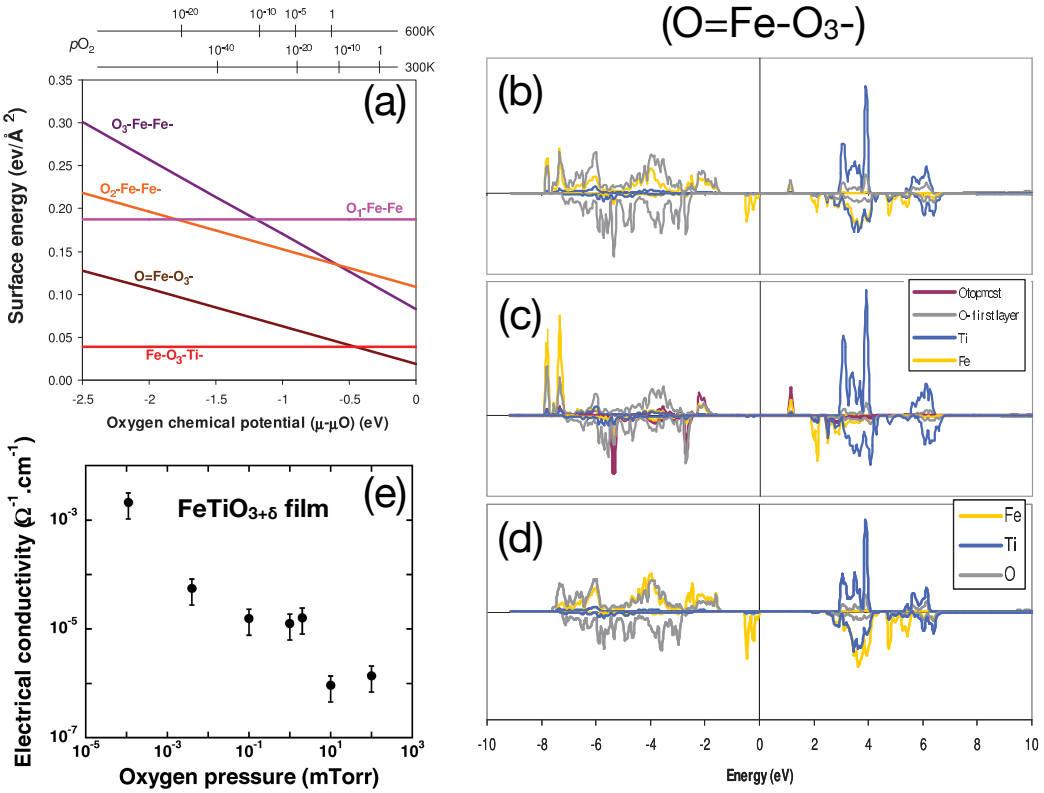

FIGURE 3.24: (a) Surface energy of selected surface terminations plotted as a function of oxygen chemical potential, using Fe_2O_3 as the chemical reservoir for Fe, $FeTiO_3$ for Ti, and O_2 for oxygen. (b-d) Electron DOS for the O=Fe-O_3- surface. Total DOS decomposed to Fe (yellow), Ti (blue), and O (gray) is shown in (b), while (c) shows a decomposition of just the surface Fe, Ti, and O, with (d) showing the decomposition into Fe, Ti, and O of the other layers. Taken from Ref. [173]. (e) Room temperature electrical conductivity of ilmenite $FeTiO_{3\pm\delta}$ films as a function of oxygen pressure. Taken from Ref. [188].

phase provide new and useful insights for understanding the properties of $FeTiO_3$, and will serve as guidance for the future DFT theoretical calculations in the paramagnetic phase.

Future experiments, using spin-resolved PES, could try to determine if a net spin polarisation of the valence band appears across the magnetic transition. One difficulty is that at temperatures well below the transition the sample becomes highly insulating.

Chapter 4

3D topological-metals: $(Ti, Zr, Hf)_2Te_2(P, As)$

This chapter presents my ARPES and SARPES results on the new family of topological metals of the tetradymite family M_2Te_2X (with M = Ti, Zr or Hf, and X = P or As). High quality samples were grown and kindly provided by the team of Dr. Ryan Baumbach (MagLab Tallahassee, Florida State University), who furthermore characterised them by transport and quantum oscillation measurements, and calculated the DFT band structure for comparison with our ARPES data. Part of this data, specifically a comparison between transport, quantum oscillations, DFT and ARPES, has already been published (Ref. [189]). The subsequent results on the spin texture of topological states in these compounds are the subject of a second paper to be submitted soon.

The chapter is divided as follows: the first section will present my ARPES data, which confirms the existence of massless Dirac surface states in a new family of 3D topological metals M_2Te_2X. The ARPES data shows an excellent agreement with slab DFT calculations. Furthermore, in the second section, the data reveals the existence of a Dirac-node arc centred at the $\bar{M}$ points of the surface-projected Brillouin zone and extending along the $\bar{\Gamma} - \bar{M}$ direction. Lastly in the third section, taking advantage of SARPES, the helicity, i.e. the spin texture of the Dirac surface states at $\bar{M}$ points in Ti_2Te_2P and Hf_2Te_2P is experimentally confirmed and determined to be reminiscent of the well-known 3D topological insulator example Bi_2Se_3. Furthermore, the Dirac node arc in Ti_2Te_2P is shown to be also "helical", i.e. every Dirac point forming part of such an arc corresponds to a helical surface state.

4.1 Massless Dirac surface states in $(Ti, Zr, Hf)_2Te_2(P, As)$

A family of exfoliative tetradymite compounds with the formula T_2Ch_2Pn as shown in Fig. 4.1(a), fabricated as a modification to the well-known topological insulator binaries Bi_2Ch_3 (with Ch = Se, Te) by replacing one chalcogen (Ch) with a pnictogen (Pn) and Bi with the tetravalent transition metals T = Ti, Zr, or Hf [189], were cleaved in situ and measured with ARPES at two end-stations, PF in KEK, Japan and CASSIOPEE in SOLEIL, France.

Zr_2Te_2P was the first reported compound of this family by R. J. Cava's group in 2015 [190]. So as a starting point, we repeated part of their experiment for comparison and implemented an energy-dependent ARPES measurement. The next two compounds we measured are Ti_2Te_2P and Hf_2Te_2P synthesised by replacing Zr with Hf and Ti, which have different atomic radii but the same number of valence electrons, with the hope of tuning the strength of SOC, which plays a crucial role in the formation of topological surface states. Let us recall that the SOC originates

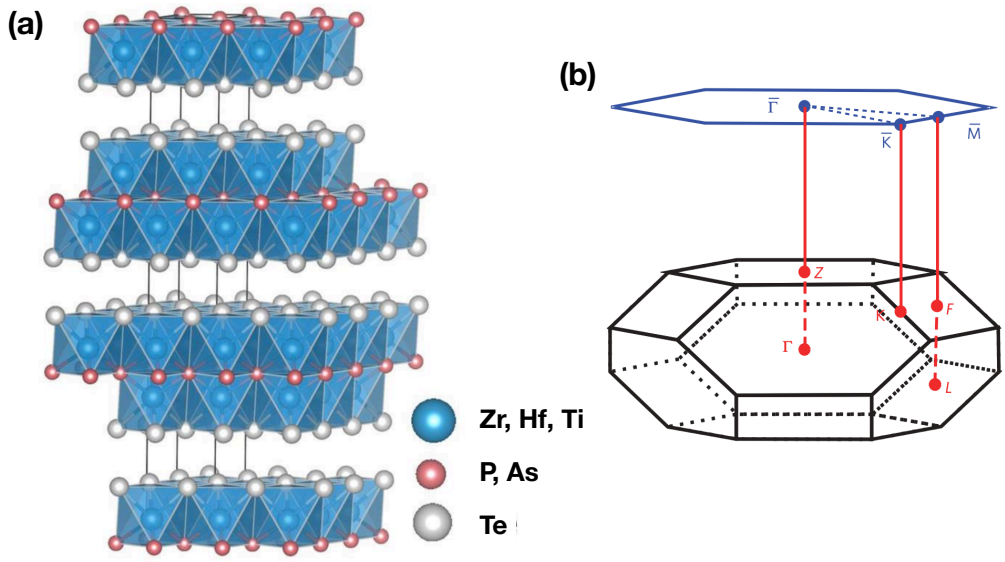

FIGURE 4.1: (a) The crystal structure of M_2Te_2X (with M = Ti, Zr or Hf, and X = P or As). Adapted from Ref. [190]. (b) The rhombohedral Brillouin zone projects onto a hexagonal surface Brillouin zone. All the time-reversal invariant momenta (TRIMs) are labeled.

from an effective magnetic field due to the relativistic motion of the electron in an electric field (section 1.5) [71], which is generated by the periodically arranged positively charged atomic nuclei and surrounding inner shell orbital electrons. Thus, usually the larger the atomic number, i.e. the heavier the atom, the stronger the SOC. Such a SOC strength tuning could be also realised by replacing P with a heavier isoelectronic element As, leading to the fourth compound Zr_2Te_2As we characterised with ARPES.

4.1.1 Fermi surfaces

We first measured the in-plane and out-of-plane Fermi surfaces of the different materials, in order to characterise their similarities and differences, and validate the identification of the surface states -which should not disperse in the out-of-plane direction.

Zr_2Te_2P The obtained in-plane Fermi surface of Zr_2Te_2P, shown in Fig. 4.2(a), is comparable with the reported results [190] indicating these samples' synthesis is successful, and basically demonstrates the 3-fold symmetry of the Brillouin zone shown in Fig. 4.1(b). Fig. 4.2(b) shows that the Fermi surface of states forming the small circle around $\bar{\Gamma}$ has a cylindrical shape, indicating these states are quasi-2D in agreement with the quantum oscillation experiment results [189].

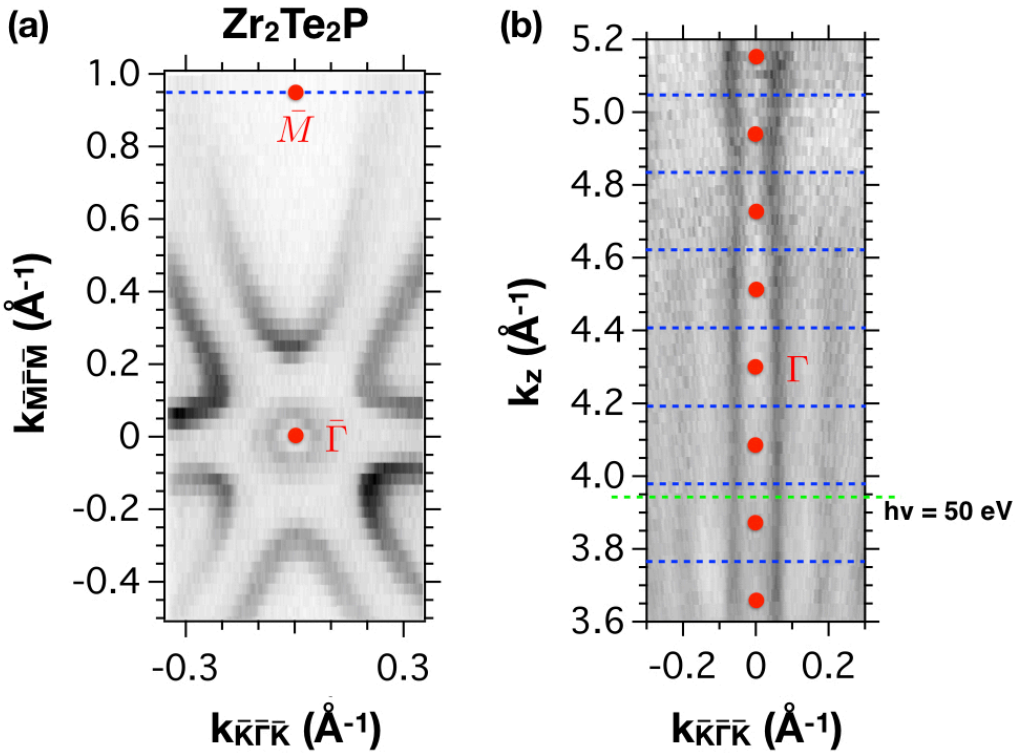

FIGURE 4.2: (a) In-plane Fermi surface of Zr_2Te_2P measured with $h\nu = 50$ eV photons. (b) Out-of-plane Fermi surface of Zr_2Te_2P measured at normal emission by varying the photon energy from 40 eV to 90 eV with a step of 1 eV. All these data were obtained with linear horizontal polarised (LH) photons at a low temperature $T = 20$ K. A $V_0 = 12$ eV inner potential is used in panel (b). In both panels, dashed blue lines represent the Brillouin zone boundaries.

Hf_2Te_2P As a direct comparison, the in-plane Fermi surface of Hf_2Te_2P shown in Fig. 4.3 was measured using the same experimental setups (synchrotron KEK, photon energy, polarisation, resolutions, temperature). The only minor difference is the presence of several surface domains. In fact, we found that Hf_2Te_2P always forms domains after cleaving *in situ*, and gives a signal of poorer quality compared to the other three compounds. As will be discussed later, this could be related to its "weak" topological character. As aforementioned in section 1.5, for 3D weak topological materials, the interlayer interaction is weak such that they are equivalent to a stack of 2D quantum spin Hall systems connected adiabatically [32–34]. This character can lead to a poor 3D crystallisation during the synthesis process, with alternating 2D layers having some misfit. Even if these 3D weak topological materials are well crystallised, they will tend to form interlayer mismatch due to external forces, such as cleaving force.

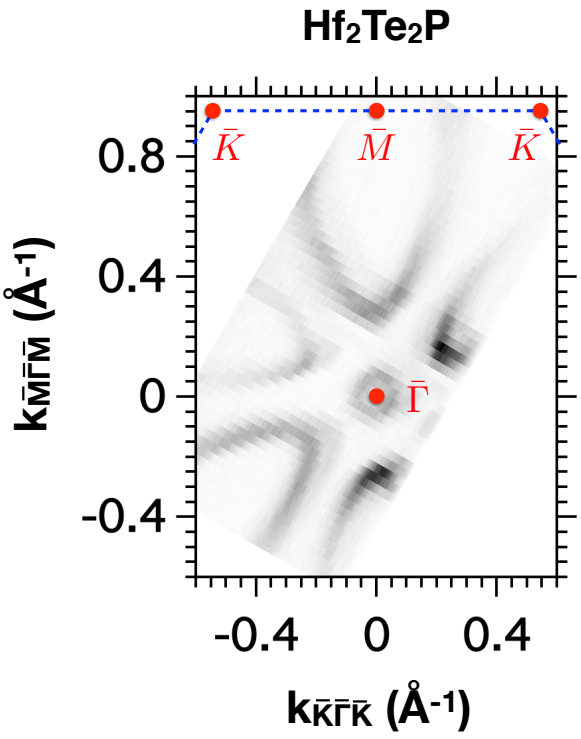

FIGURE 4.3: In-plane Fermi surface of Hf_2Te_2P measured with LH polarised $h\nu = 50$ eV photons at $T = 20$ K. The dashed blue lines represent the Brillouin zone boundaries.

Ti_2Te_2P In Ti_2Te_2P, the strength of SOC is smaller than in Hf_2Te_2P or Zr_2Te_2P. Fig. 4.4(a) shows the in-plane Fermi surface measured with the same conditions for Zr_2Te_2P and Hf_2Te_2P except that Ti_2Te_2P was measured at CASSIOPEE in SOLEIL, France. At $\bar{\Gamma}$, we did not observe the small circle pockets like in Zr_2Te_2P and Hf_2Te_2P but a small point indicating an energy lowering of the corresponding band after the element substitution from Zr, to Hf, and to Ti.

Fig. 4.4(b) is the out-of-plane Fermi surface of Ti_2Te_2P measured along $k_{\bar{M}\bar{\Gamma}\bar{M}}$ such that not only the states around $\bar{\Gamma}$ are included, but also the states at the vertex closer to $\bar{\Gamma}$ of the ellipse centred at $\bar{M}$. This result again demonstrates the quasi-2D character of these bands.

Zr_2Te_2As The SOC is stronger in Zr_2Te_2As with respect to Ti_2Te_2P. Not surprisingly, the in-plane Fermi surface shown in Fig. 4.5(a) is similar to the one measured in Zr_2Te_2P and a better signal-to-noise ratio than Zr_2Te_2P. In order to check the photon polarisation dependence, the same in-plane Fermi surface was measured with LV polarised photons. By checking the intensities of the 6 ellipses centred at the consecutive points $\bar{M}$ and $\bar{M}\prime$, the 3 ellipses centred at $\bar{M}$ are more intense than those at $\bar{M}'$ with LH polarisation and vice-versa with LV polarisation.

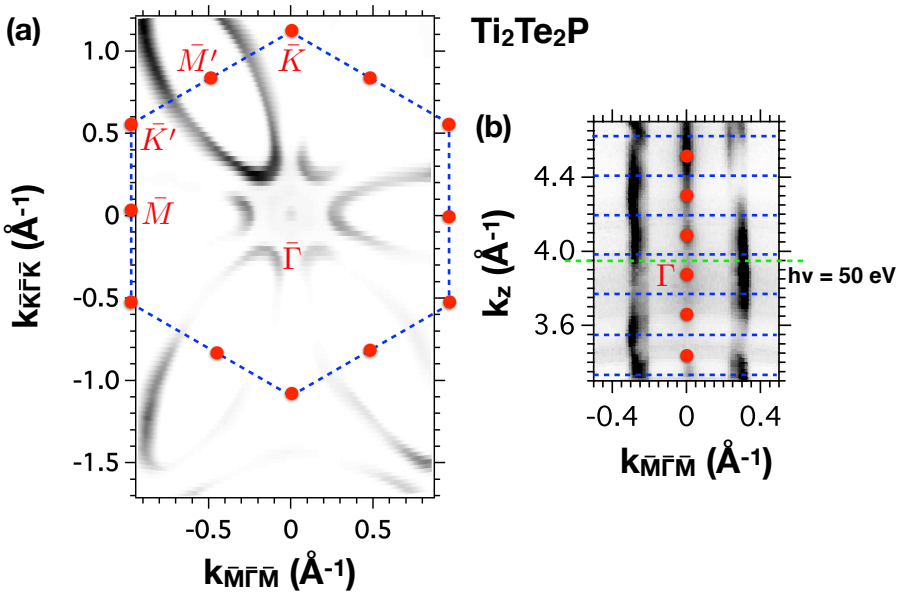

FIGURE 4.4: (a) In-plane Fermi surface of Ti_2Te_2P measured with LH polarised $h\nu = 50$ eV photons. (b) Out-of-plane Fermi surface of Ti_2Te_2P measured at normal emission with linear vertical polarised photons by varying the photon energy from 40 eV to 84.5 eV with a step of 0.5 eV. All these data were obtained at $T = 6$ K. A $V_0 = 12$ eV inner potential is used in panel (b). In both panels, dashed blue lines represent the Brillouin zone boundaries.

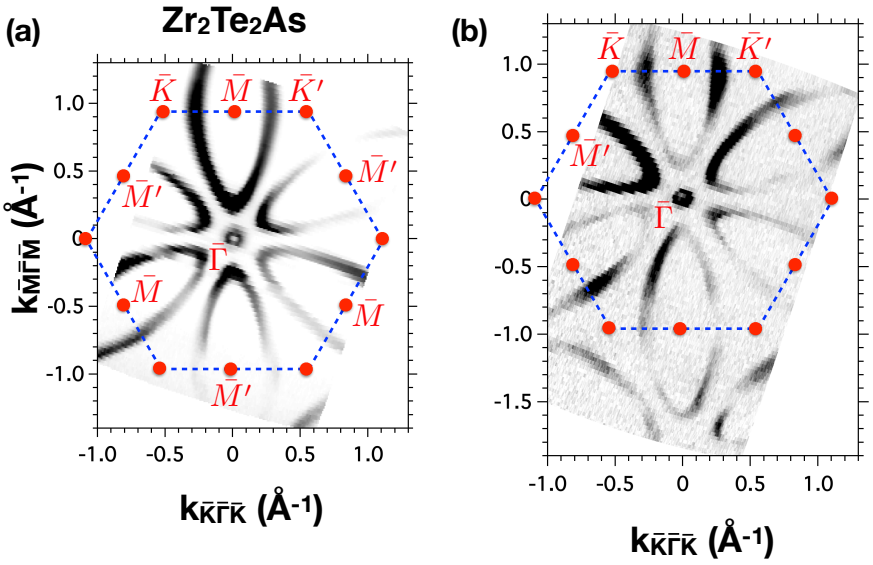

FIGURE 4.5: (a-b) In-plane Fermi surfaces of Zr_2Te_2As measured with (a) LH, and (b) LV polarised $h\nu = 50$ eV photons. All these data were obtained at $T = 6$ K. In both panels, dashed blue lines represent the Brillouin zone boundaries.

4.1.2 E − k dispersions

According to the DFT slab calculations, there should be Dirac-like surface states at $\bar{\Gamma}$ *above* the Fermi level (E_F), in Zr_2Te_2P, Hf_2Te_2P and Zr_2Te_2As, due to a $d-p$ band inversion [189–191]. Notably, Hf_2Te_2P is supposed to have two of such Dirac states [189, 191]. Even though ARPES cannot measure states at energies well above roughly $E - E_F \approx k_B T$, we measured the occupied bands around $\bar{\Gamma}$ to compare with the DFT predictions. On the other hand, all these four compounds are expected to have one topological surface state below E_F at the $\bar{M}$ points, due to the Te p-bands inversion [189–191]. We also measured these states, and will discuss their physics below.

All ARPES data shown in this subsection were acquired with LH polarisation. Zr_2Te_2P and Hf_2Te_2P were measured at KEK, PF, in Japan with a sample temperature $T = 20$ K, while Ti_2Te_2P and Zr_2Te_2As were measured at CASSIOPEE, Synchrotron SOLEIL, in France with a sample temperature $T = 6$ K.

Zr_2Te_2P Fig. 4.6(a) shows the ARPES measured states giving the small closed circle around $\bar{\Gamma}$ in Fig. 4.2(a). The agreement with the DFT calculated bands projected to this momentum direction shown in Fig. 4.6(b) is good, except that there is an overall constant energy shift of around 200 meV. We attribute the origin of such energy shift to surface band bending effects, which are typical in tetradymite topological insulators [192, 193]. The MDC of the two pairs of bands crossing E_F around $\bar{\Gamma}$ can be fitted well with four Lorentzian peaks, as shown in Fig. 4.6(e), and the fitted Fermi momenta of these hole-like states are $k_h^{inner} = (0.070 \pm 0.005)$ Å^{-1} and $k_h^{outer} = (0.111 \pm 0.005)$ Å^{-1}.

In agreement with the previously reported data [190] and the DFT calculations, we observe at the $\bar{M}$ point, a Dirac-like massless surface state in the bulk bandgap, as shown in Fig. 4.6(c), with a similar Fermi level shift compared to the DFT calculated bands in Fig. 4.6(d).

The MDC and its fit in Fig. 4.6(f) suggest that even though the surface state is just next to the bulk bands, they do not merge into each other. Later we will show that with better data quality or/and a larger SOC strength, this feature will be more obvious. The fitted Fermi momenta of these electron-like states at $\bar{M}$ are $k_e^{inner} = (0.291 \pm 0.005)$ Å^{-1} for bulk bands, and $k_e^{outer} = (0.348 \pm 0.005)$ Å^{-1} for surface states.

Fig. 4.6(g) shows the EDC at $\bar{M}$ including the band bottom of the conduction band, the Dirac point, and the band top of the valence band, whose binding energy positions can be extracted from Lorentzian peak fits such that we get the bulk bandgap at $\bar{M}$ $E_{gap} = (0.45 \pm 0.01)$ eV, and the Dirac point binding energy $E_D = (1.01 \pm 0.01)$ eV.

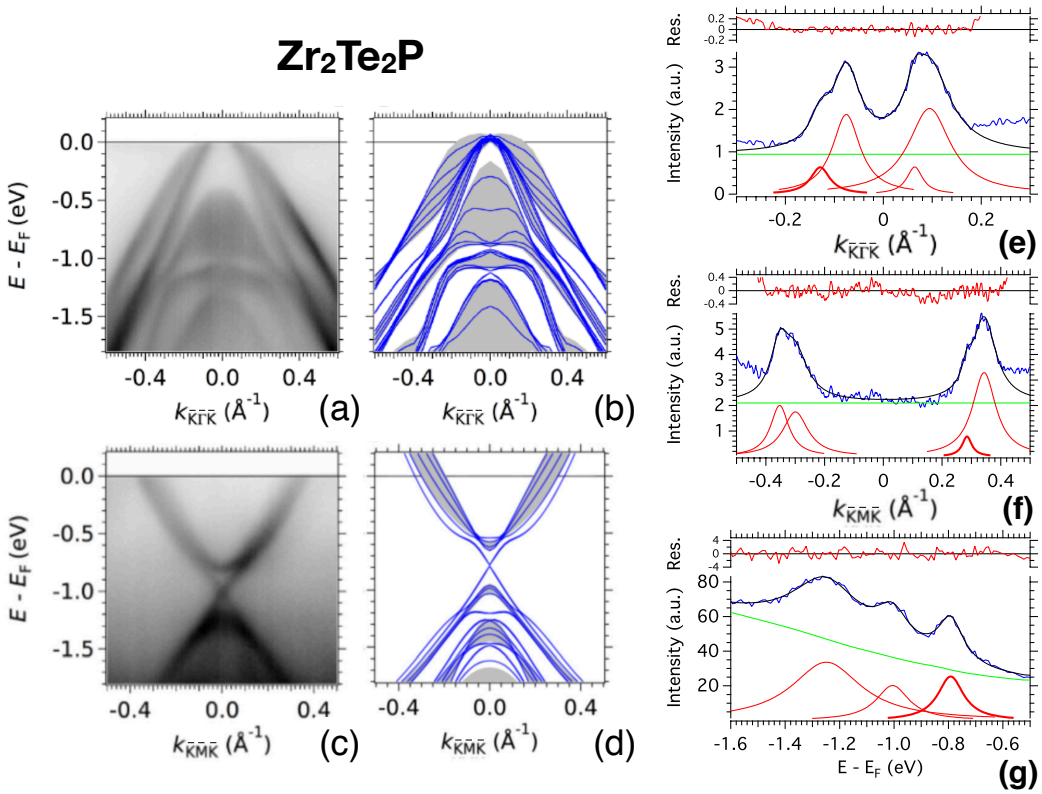

FIGURE 4.6: (a-d) Comparison between ARPES measurements and band structure calculations for Zr_2Te_2P for dispersions along the $\bar{K} - \bar{\Gamma} - \bar{K}$ direction at $\bar{\Gamma}$ (upper panels) and along the $\bar{K} - \bar{M} - \bar{K}$ direction at $\bar{M}$ (lower panels) [189]. (a) and (c) are ARPES determined band dispersions, while (b) and (d) are DFT calculated bands. Fermi level E_F is indicated by the horizontal black line. Blue solid lines are bands obtained from a 5-layer slab calculation and therefore represent surface states. The grey ribbons represent the surface-projected bulk bands. (e) Momentum distribution curve (MDC) at E_F (integrated over ± 10 meV) of states around $\bar{\Gamma}$ in panel (a). (f) Momentum distribution curve (MDC) at E_F (integrated over ± 10 meV) of states around $\bar{M}$ in panel (c). (g) Energy distribution curve (EDC) at $\bar{M}$ (integrated over ± 0.005 Å^{-1}). These MDCs and EDCs (blue curves) are fitted with Lorentzian peaks (red peaks) and a quadratic (MDC) or Shirley (EDC) background (the green curve). The overall fits are the black curves, while the red line in each top inset is the fitting residual. These ARPES data were measured in PF, KEK, Japan with LH polarised photons at $h\nu = 120$ eV and $T = 20$ K.

Hf_2Te_2P Similarly to Fig. 4.6, Fig. 4.7(a-d) shows the comparison between ARPES measurements and band structure calculations for Hf_2Te_2P. The agreement is good and a similar energy shift is observed. The Lorentzian peak fit of the MDC at E_F around $\bar{\Gamma}$ in Fig. 4.7(e) gives: $k_h^{inner} = (0.056 \pm 0.005)$ Å^{-1} and $k_h^{outer} = (0.106 \pm 0.005)$ Å^{-1}. In Fig. 4.7(f), the bulk bands (inner) and the surface state (outer) are well separated at $\bar{M}$ and Lorentzian peak fit gives: $k_e^{inner} = (0.272 \pm 0.005)$ Å^{-1} and $k_e^{outer} = (0.325 \pm 0.005)$ Å^{-1}. The EDC in Fig. 4.7(g) shows that the bandgap is $E_{gap} = (0.48 \pm 0.01)$ eV, and the Dirac point is at $E_D = (1.14 \pm 0.01)$ eV binding energy.

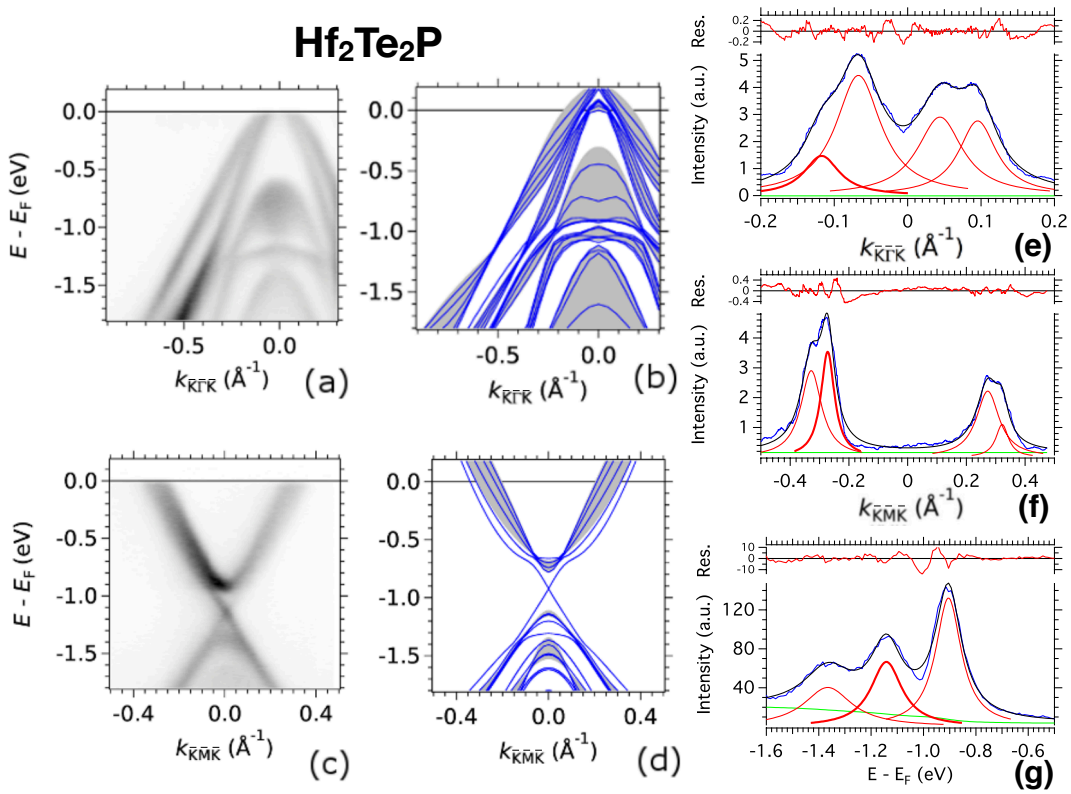

FIGURE 4.7: (a-d) Comparison between ARPES measurements and band structure calculations for Hf_2Te_2P for dispersions along the $\bar{K}-\bar{\Gamma}-\bar{K}$ direction at $\bar{\Gamma}$ (upper panels) and along the $\bar{K}-\bar{M}-\bar{K}$ direction at $\bar{M}$ (lower panels) [189]. (a) and (c) are ARPES determined band dispersions, while (b) and (d) are DFT calculated bands. Fermi level E_F is indicated by the horizontal black line. Blue solid lines are bands obtained from a 5-layer slab calculation and therefore represent surface states. The grey ribbons represent the surface-projected bulk bands. (e) Momentum distribution curve (MDC) at E_F (integrated over ± 10 meV) of states around $\bar{\Gamma}$ in panel (a). (f) Momentum distribution curve (MDC) at E_F (integrated over ± 10 meV) of states around $\bar{M}$ in panel (c). (g) Energy distribution curve (EDC) at $\bar{M}$ (integrated over ± 0.005 Å^{-1}). These MDCs and EDCs (blue curves) are fitted with Lorentzian peaks (red peaks) and a quadratic (MDC) or Shirley (EDC) background (the green curve). The overall fits are the black curves, while the red line in each top inset is the fitting residual. These ARPES data were measured in KEK, PF, Japan with LH polarised photons at $h\nu = 120$ eV and $T = 20$ K.

Ti_2Te_2P As seen in Fig. 4.8(a), in Ti_2Te_2P the top of the parabolic state at $\bar{\Gamma}$ is now close to E_F, meaning that this state has lowered its energy with respect to Zr_2Te_2P. As already noted, this gives rise to a much smaller circular Fermi contour (point-like instead of ring-like) around $\bar{\Gamma}$ in Ti_2Te_2P compared to Zr_2Te_2P. Additionally, the band bottoms of states above the gap leave some fingerprints, for instance the weak hexagonal contour around $\bar{\Gamma}$ in Fig. 4.4(a). Fig. 4.8(e) is the corresponding MDC showing 5 peaks: two from the band bottoms of states above the gap at momentum ± 0.3 Å^{-1}, two from the bulk states below the gap at momentum ± 0.11 Å^{-1}, and one from the top of the cone-like surface state at $\bar{\Gamma}$. Fig. 4.8(c) shows the Dirac surface state around the $\bar{M}$ point in Ti_2Te_2P with the Dirac point at $E_D = (0.85 \pm 0.01)$ eV

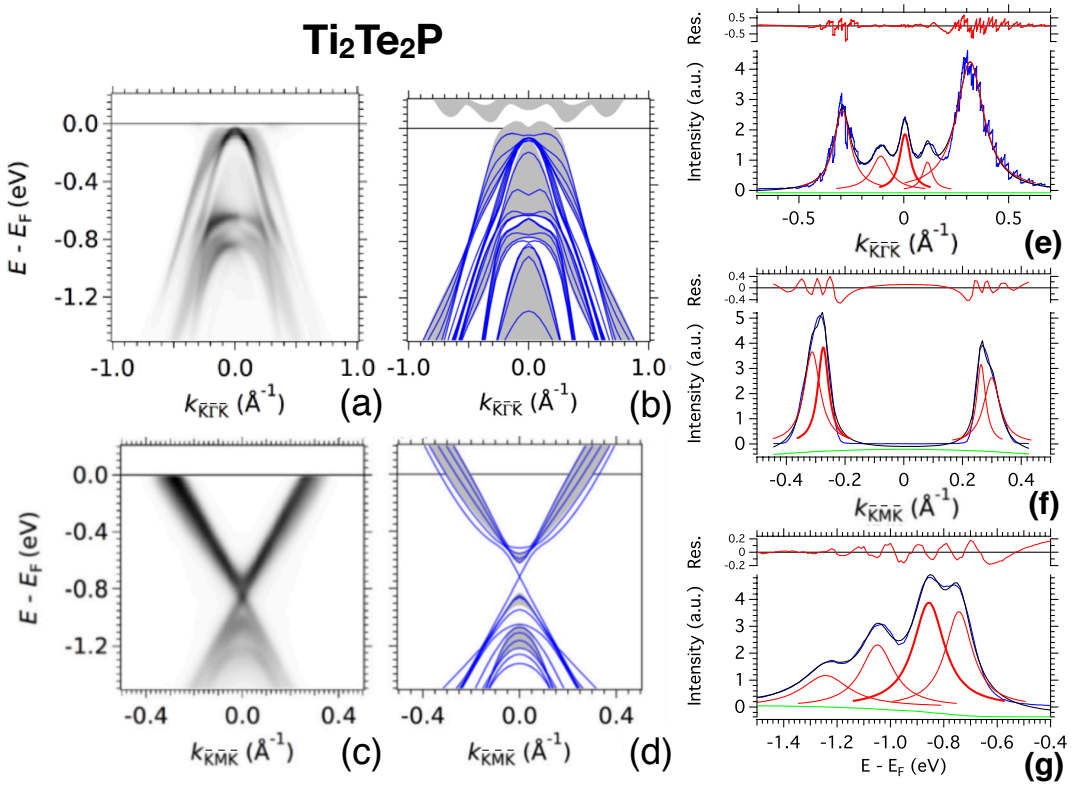

FIGURE 4.8: (a-d) Comparison between ARPES measurements and band structure calculations for Ti_2Te_2P for dispersions along the $\bar{K} - \bar{\Gamma} - \bar{K}$ direction at $\bar{\Gamma}$ (upper panels) and along the $\bar{K} - \bar{M} - \bar{K}$ direction at $\bar{M}$ (lower panels) [189]. (a) and (c) are ARPES determined band dispersions, while (b) and (d) are DFT calculated bands. Fermi level E_F is indicated by the horizontal black line. Blue solid lines are bands obtained from a 5-layer slab calculation and therefore represent surface states. The grey ribbons represent the surface-projected bulk bands. (e) Momentum distribution curve (MDC) at E_F (integrated over ± 10 meV) of states around $\bar{\Gamma}$ in panel (a). (f) Momentum distribution curve (MDC) at E_F (integrated over ± 10 meV) of states around $\bar{M}$ in panel (c). (g) Energy distribution curve (EDC) at $\bar{M}$ (integrated over ± 0.005 Å^{-1}). These MDCs and EDCs (blue curves) are fitted with Lorentzian peaks (red peaks) and a quadratic (MDC) or Shirley (EDC) background (the green curve). The overall fits are the black curves, while the red line in each top inset is the fitting residual. These ARPES data were measured in CASSIOPEE in SOLEIL, France with LH polarised photons at $h\nu = 50$ eV and $T = 6$ K.

binding energy. Compared to the DFT calculation, a roughly 150 meV energy shift is observed, indicating that the size of the constant energy shift is material dependent. The corresponding MDC in Fig. 4.8(f) also indicates a separation of the bulk bands (inner) and the surface state (outer) at $\bar{M}$: $k_e^{inner} = (0.269 \pm 0.005)$ Å^{-1} and $k_e^{outer} = (0.305 \pm 0.005)$ Å^{-1}. The bandgap extracted from the EDC in Fig. 4.8(f) is $E_{gap} = (0.31 \pm 0.01)$ eV.

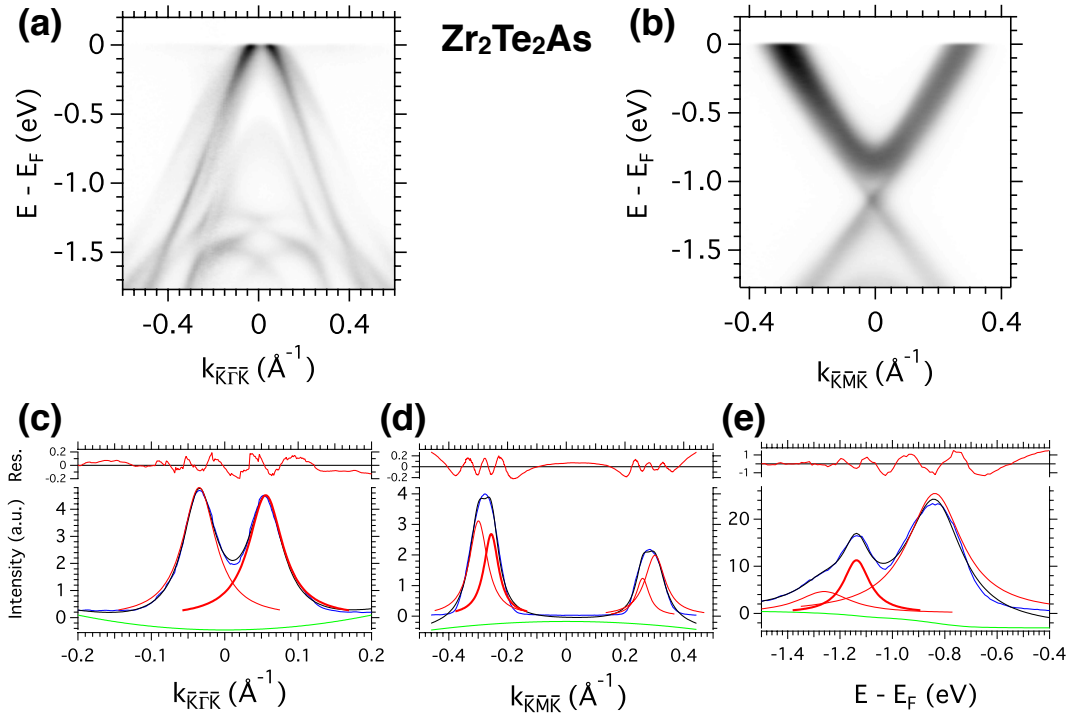

FIGURE 4.9: (a-b) ARPES measurements of Zr_2Te_2As's band dispersions (a) along the $\bar{K}-\bar{\Gamma}-\bar{K}$ direction at $\bar{\Gamma}$ and (b) along the $\bar{K}-\bar{M}-\bar{K}$ direction at $\bar{M}$ [189]. (c) Momentum distribution curve (MDC) at E_F (integrated over ± 10 meV) of states around $\bar{\Gamma}$ in panel (a). (d) Momentum distribution curve (MDC) at E_F (integrated over ± 10 meV) of states around $\bar{M}$ in panel (b). (e) Energy distribution curve (EDC) at $\bar{M}$ (integrated over ± 0.005 Å^{-1}). These MDCs and EDCs (blue curves) are fitted with Lorentzian peaks (red peaks) and a quadratic (MDC) or Shirley (EDC) background (the green curve). The overall fits are the black curves, while the red line in each top inset is the fitting residual. These ARPES data were measured in CASSIOPEE in SOLEIL, France with LH polarised photons at $h\nu = 50$ eV and T = 6 K.

Zr_2Te_2As Fig. 4.9(a-b) presents our ARPES data of the states at $\bar{\Gamma}$ along the $\bar{K}-\bar{\Gamma}-\bar{K}$ direction, and the ones at $\bar{M}$ along the $\bar{K}-\bar{M}-\bar{K}$ direction in Zr_2Te_2As. The hole type states around $\bar{\Gamma}$ are similar to those in Ti_2Te_2P, except that the top of the parabolic state is well above the Fermi level. The parabolic state has a very large ARPES intensity dominating the MDC in Fig. 4.9(c) such that the Lorentzian peak fit cannot resolve the other bulk branches and gives $k_h = (0.045 \pm 0.005)$ Å^{-1}.

Compared to Zr_2Te_2P, Zr_2Te_2As has a stronger SOC strength and better ARPES data quality, such that the peak fit of the MDC at E_F at the $\bar{M}$ point in Fig. 4.9(d) clearly resolves the bulk bands and the Dirac surface state, and gives $k_e^{inner} = (0.258 \pm 0.005)$ Å^{-1} and $k_e^{outer} = (0.300 \pm 0.005)$ Å^{-1}. The EDC in Fig. 4.9(e) shows the bulk bandgap is $E_{gap} = (0.43 \pm 0.01)$ eV, and the Dirac point lies at $E_D = 1.14 \pm 0,01$ eV binding energy.

4.1.3 Tuning the Dirac points by potassium deposition on the surface

For real applications, it would be desirable to have the Dirac point at E_F such that the backscattering in the solid will be strongly suppressed leading to dissipationless transport. Note that, according to the DFT calculations, Hf_2Te_2P has an additional Dirac surface state around 200 meV above the Fermi level at $\bar{\Gamma}$ [189,191] which could even be around 100 meV lower in energy given the observed energy shift between the ARPES data and the calculations. These considerations motivated us to try to tune the Fermi level by potassium (K) deposition at the sample's surface, thus hoping to bring the Dirac point of Hf_2Te_2P within the energy range of the occupied bands.

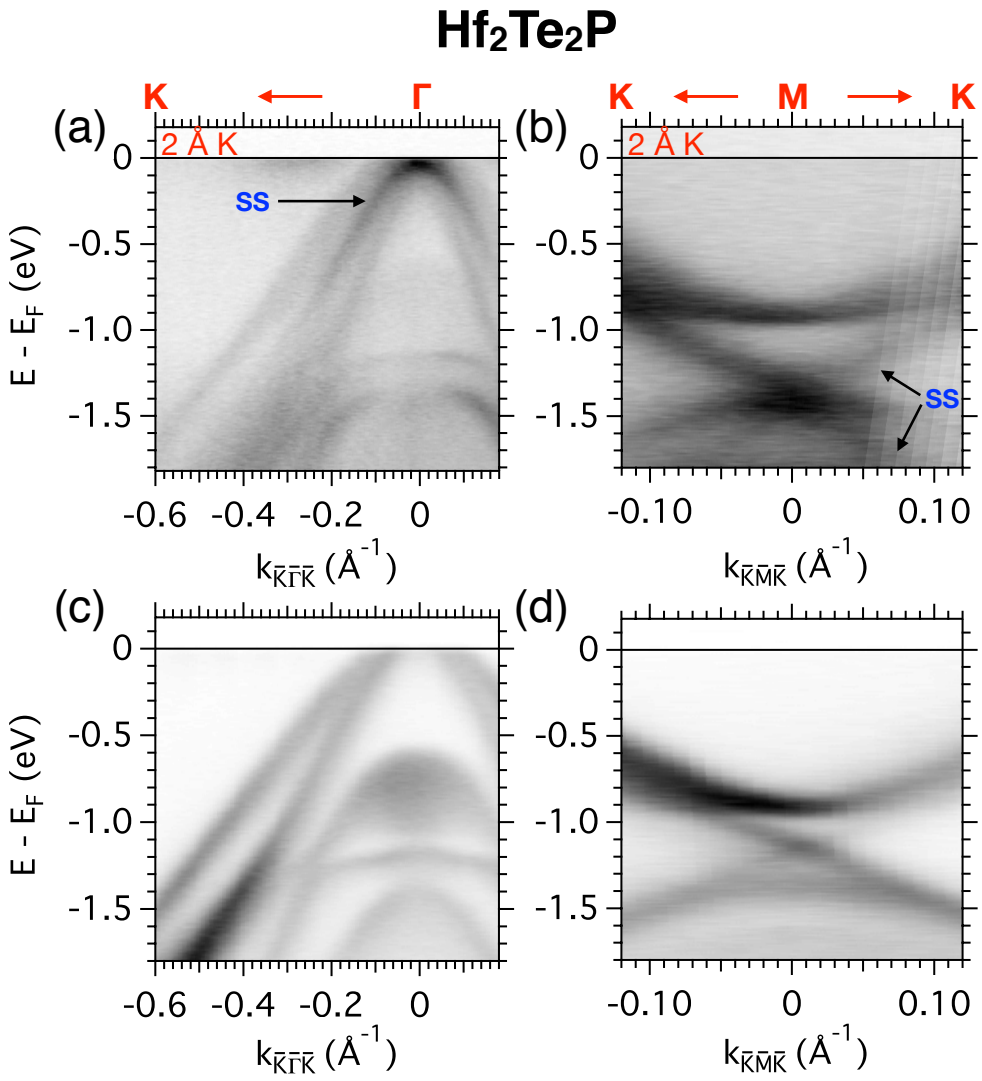

FIGURE 4.10: (a, b) ARPES energy-momentum intensity maps at the surface of Hf_2Te_2P capped with 2 Å of potassium, measured respectively at $\bar{\Gamma}$ along $\bar{K}-\bar{\Gamma}-\bar{K}$ and at $\bar{M}$ along $\bar{K}-\bar{M}-\bar{K}$. (c, d) Analogous measurements at the bare (i.e., non capped) surface of Hf_2Te_2P. All the data were acquired with LH polarised photons at an energy $h\nu = 50$ eV at $T = 20$ K. The surface state (SS) is indicated by the black arrows in panel (b).

Fig. 4.10(a) shows the electronic states at $\bar{\Gamma}$ along $\bar{K}-\bar{\Gamma}-\bar{K}$ measured at the

surface of Hf_2Te_2P capped with 2 Å of potassium. Compared to the bare surface of Hf_2Te_2P in Fig. 4.10(c) (i.e. Fig. 4.7(a)), a new hole-like surface state with its top energy right below the Fermi level, indicated with an arrow, appears around $\bar{\Gamma}$. On the other hand, there are no observable energy shifts of the bulk bands except that the signal-to-noise ratio is much lower due to K capping.

Fig. 4.10(b) shows the electronic states including the Dirac surface state at $\bar{M}$ along $\bar{K}-\bar{M}-\bar{K}$ measured after the K capping at Hf_2Te_2P surface. Compared to Fig. 4.10(d) (i.e. Fig. 4.7(b)), the Dirac crossing point of the surface state (SS) is shifted down by around 200 meV to a binding energy 1.35 eV, while the bulk bands (above and below the gap) remain unchanged. This is an important observation that proves such surface electron doping (K deposition) affects mainly the surface states instead of the bulk states. So we have a reason to believe that the newly appeared state at $\bar{\Gamma}$ shown in Fig. 4.10(a) is a surface state shifted down by around 200 meV. According to the DFT band and parity calculations shown below, this surface state should be the weak topological surface state at $\bar{\Gamma}$ [189, 191].

The K deposition experiment demonstrates that the Dirac crossing points are tunable and can be tuned to the Fermi level by surface electron doping in Hf_2Te_2P.

Notably, similar results have been reported recently [194], in a combined ARPES-STM work to study both surface states at $\bar{\Gamma}$ above E_F.

4.1.4 Parity analysis

For a better understanding of the measured band structures, especially the Dirac surface states at $\bar{M}$ along $\bar{K}-\bar{M}-\bar{K}$ direction, the parity analysis at TRIM points together with the calculated band dispersions, which were done by our collaborators in Florida University, will be reproduced here [189].

With a given time-reversal (TR) invariant Hamiltonian H_{TR}, a Bloch Hamiltonian can be defined as [33, 34]

$$H(\vec{k}) = e^{-i\vec{k}\cdot\vec{r}} H_{TR} e^{+i\vec{k}\cdot\vec{r}} \tag{4.1}$$

with eigenstates being the Bloch wavefunctions $|u_{n,\vec{k}}>$.

For spin 1/2 particles, we have

$$H(-\vec{k}) = \Theta H(\vec{k}) \Theta^{-1} \tag{4.2}$$

with Θ the TR operator.

So at the TRIM points Γ_i where $-\vec{\Gamma}_i = \vec{\Gamma}_i + \vec{G}$ with $\vec{G}$ the reciprocal lattice vector, $H(\vec{\Gamma}_i) = \Theta H(\vec{\Gamma}_i)\Theta^{-1}$, i.e. $[H(\vec{\Gamma}_i), \Theta] = 0$. So the eigenstates $|u_{n,\vec{\Gamma}_i}>$ have a Kramers degeneracy. Then the product of parities of all the Kramers degenerate bands below the band of interest at Γ_i can be calculated based on the calculated Bloch wavefunctions, and labeled as δ_i. In 3-dimensional space, there are $2^3 = 8$ such TRIM points in k space. By multiplying all of these δ_i at the corresponding Γ_i, the main Z_2 topological index ν_0 is defined as

$$(-1)^{\nu_0} = \prod_{i=1}^{8} \delta_i \tag{4.3}$$

In our case, M_2Te_2X (with M = Ti, Zr or Hf, and X = P or As) has a rhombohedral Brillouin zone as shown in Fig. 4.1, where the TRIM points are labeled: Γ, F, L, Z. The other 2 pairs of F and L points, obtained after a 60° rotation, are not indicated. Typical band structures of these family of materials are demonstrated in Fig. 4.11. The bandgap between band 1 and 2 is referred as gap 1, while the gap between band

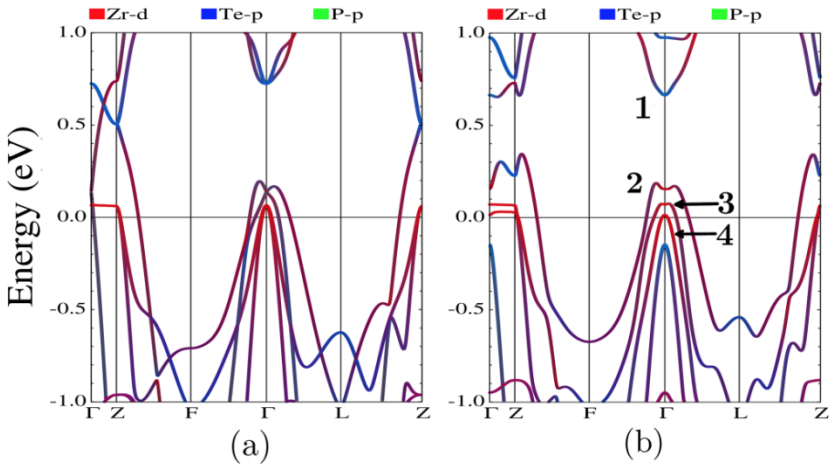

FIGURE 4.11: The Band structures of Zr_2Te_2P in the rhombohedral unit cell along the TRIM points (a) without the inclusion of the spin-orbit coupling (SOC) and (b) with the inclusion of SOC [189]. The colours used indicate the orbital character of the bands: red, blue, and green colours correspond to Zr d, Te p, and P p orbitals, respectively.

2 and 3 is referred as gap2. The parity analysis for these compounds is summarised in Tab. 4.1.

Gap 1 The parity of all the bands below gap 1 was calculated and multiplied together for the 8 TRIM points to determine the corresponding parity products, which are (+), (+), (+) and (-) for Zr_2Te_2P and Hf_2Te_2P, and are all positive for Ti_2Te_2P at the Γ, F, L, Z TRIM points respectively. This gives a Z_2 topological index $\nu_0 = 1$ for Zr_2Te_2P and Hf_2Te_2P, whereas $\nu_0 = 0$ for Ti_2Te_2P. This implies that there is an odd number of topological surface states in gap 1 for Zr_2Te_2P and Hf_2Te_2P, whereas there is an even (or zero) number of topological surface states for Ti_2Te_2P.

Gap 2 Similar analysis was performed to gap 2. From this analysis, we find $\nu_0 = 1$ for Zr_2Te_2P and Ti_2Te_2P, whereas $\nu_0 = 0$ for Hf_2Te_2P. For Zr_2Te_2P and Ti_2Te_2P, the parity product is negative only at L which projects onto $\bar{M}$ point of the hexagonal reduced 2D BZ, whereas for Hf_2Te_2P the parity product is negative at the Z and L. This makes the overall product positive and results in a Z_2 index of 0. Thus we expect that for Zr_2Te_2P and Ti_2Te_2P, there is an odd number of Dirac-like states (three at the L points), and for Hf_2Te_2P, there is an even number of Dirac-like states (one at the $\bar{\Gamma}$ point and three at $\bar{M}$ points). Therefore, for Hf_2Te_2P, the parity analysis shows that the surface Dirac band at the $\bar{M}$ point does not have strong topological character because the parity inversion happens at both the Z and L point as stated above.

$(\nu_0, \Gamma FLZ)$	Zr_2Te_2P	Hf_2Te_2P	Ti_2Te_2P
gap 1	(1, +++-)	(1, +++-)	(0, ++++)
gap 2	(1, +-++)	(0, +-+-)	(1, +-++)

TABLE 4.1: Parity calculation for M_2Te_2X (with M = Ti, Zr or Hf, and X = P or As): ν_0 the main Z_2 index, ΓFLZ TRIM points, + even parity, - odd parity.

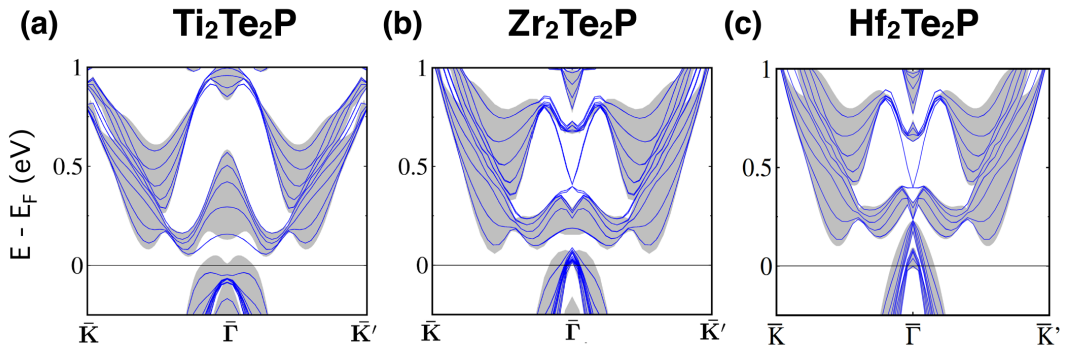

FIGURE 4.12: The superposition of bulk bands (shown as grey ribbons) with bands obtained from a slab of 5 quintuple layers (shown as blue lines) depicting the presence of a Dirac-like surface state at the $\bar{\Gamma}$ is shown for (a) Ti_2Te_2P, (b) Zr_2Te_2P, and (c) Hf_2Te_2P. Taken from Ref. [189]

However, gap 1 at Γ is above the Fermi level in all these 4 compounds, thus the surface states inside this gap are above the Fermi level, such that the topological character of gap 1 will not affect the physical properties of these compounds. So the strong or weak topological character will be determined by the topological character of gap 2, which is well below the Fermi level at $\bar{M}$.

To summarise, at $\bar{M}$ all of them have one topological surface state, while at $\bar{\Gamma}$ Ti_2Te_2P has no Dirac states, Zr_2Te_2P has one, and Hf_2Te_2P has two, as shown in the slab calculations Fig. 4.12 [189]. In recent works of Hf_2Te_2P, the existence of such multiple Dirac states has been reported and discussed. Notably, a surface derived Dirac-node arc (see Fig. 4.13) around $\bar{M}$ protected by in-plane time-reversal invariance has been observed, and claimed to be a signature of weak topological Z_2 invariants [191]. This work in Hf_2Te_2P by M. M. Hosen *et.al*. in 2018 [191] motivated us to explore similar phenomena in other compounds of this family.

4.2 Dirac-node arcs

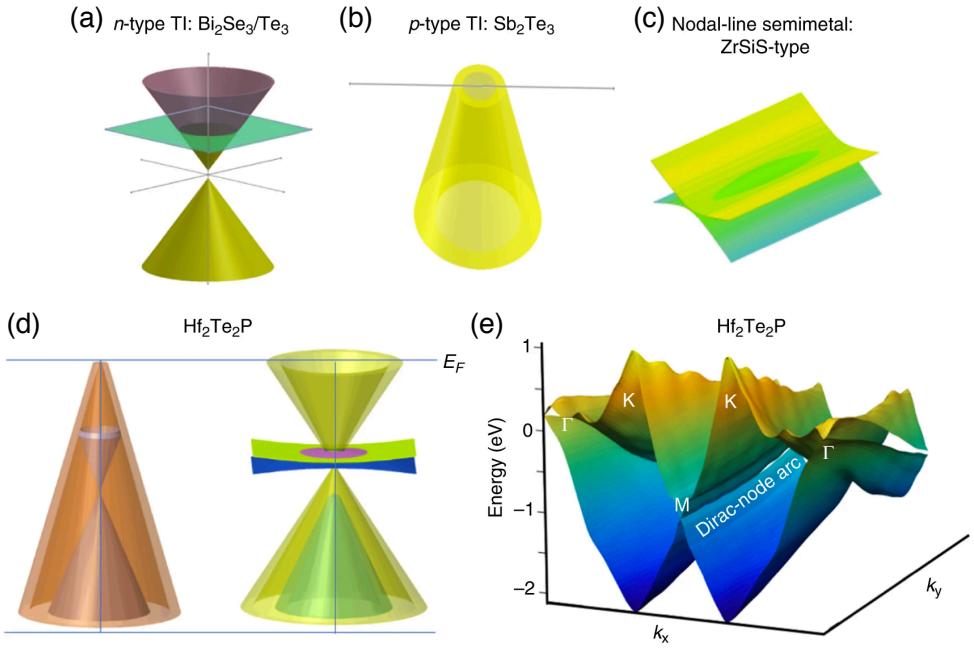

FIGURE 4.13: (a, b) Sketch of electronic surface state dispersion of the *n*-type topological insulator and *p*-type topological insulator, respectively. (c) Dispersion of bulk states in a nodal-line semimetal of ZrSiS-type. (d) Sketch of electronic dispersions of Hf_2Te_2P. This material consists of both n- and *p*-type topological surface states as well as a surface Dirac-node arc phase. (e) View of the calculated surface electronic structure of this material that confirms its weak topological nature, also showing the Dirac-node arc starting at M. The Dirac-node arc is purely surface-derived, in contrast to the nodal-line semimetal phase shown in c, which is bulk-derived. Taken from Ref. [191]

Further detailed analysis of the ARPES data shows that the Dirac surface states at $\bar{M}$ do not behave like a standard single Dirac cone. As an example, this behavior in Ti_2Te_2P is explicitly demonstrated in Fig. 4.14. The constant-energy maps show a strong anisotropy (see Fig. 4.14(a)), forming highly elongated, elliptical (instead of circular) sheets centred at $\bar{M}$ that gradually shrink to a quasi-1D line as the binding energy approaches the Dirac point (at around 850 meV binding energy). In other words, the Dirac point forms a quasi-flat state, instead of a linearly dispersing state, along the $\bar{\Gamma} - \bar{M}$ direction (see Fig. 4.15(g). By cutting perpendicular to this 1D "line" in k space, we found that it is formed out of the Dirac points of a series of parallel Dirac edge states (see Fig. 4.14(b)). After crossing the Dirac point towards lower binding energies, this 1D Dirac-node "line" does not expand back to a closed ellipse but transforms into two almost parallel sheets, like in ZrSiS-type nodal-line semimetals [195].

Similar behavior can also be found in the other 3 compounds, as shown in Fig. 4.15.

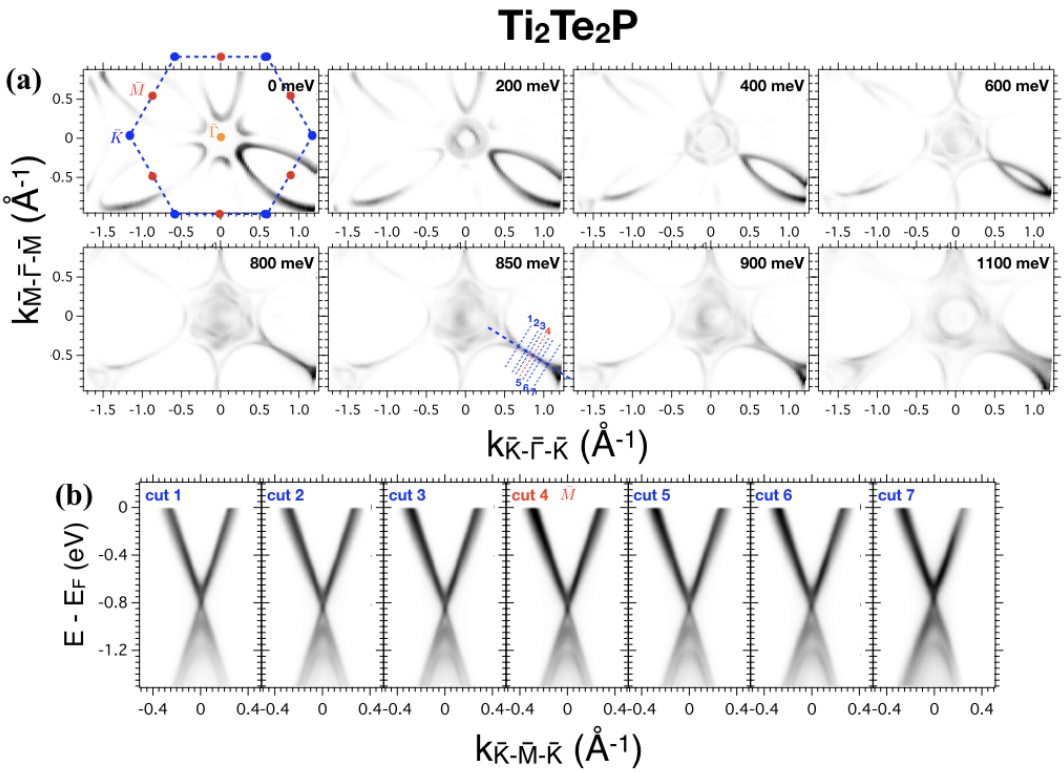

FIGURE 4.14: Experimental observation of the Dirac-node arc in Ti_2Te_2P by normal ARPES. (a) Constant energy mappings at various binding energies. (b) Dispersion maps along the K-M-K direction along the cut directions indicated in the 850 meV constant energy contour panel where the nodal arc is presented. All data were collected at the CASSIOPEE high-resolution ARPES endstation at synchrotron Soleil with LH polarised $h\nu = 50$ eV photons at a temperature of T = 5 K.

4.3 SARPES study on Ti_2Te_2P and Hf_2Te_2P

In the preceding sections we demonstrated how, with the help of DFT calculations, the band structures and topological properties of these 4 compounds are well understood and supported by our ARPES data. However, the standard ARPES alone is not enough to differentiate the topological surface states from the linearly dispersing states in 2D Dirac materials, due to the lack of knowledge about the spin textures of these bands, especially at $\bar{M}$ points in the Brillouin zone (BZ).

Here we used spin-resolved ARPES to study two compounds Ti_2Te_2P and Hf_2Te_2P, and thus reveal the spin information of their electronic bands at $\bar{M}$ points in the 2D hexagonal BZ. Our results prove that the linear Dirac bands found in Ti_2Te_2P and Hf_2Te_2P [189, 191] are indeed spin polarised. Further, all states forming the Dirac-node arc are shown to be also spin polarised.

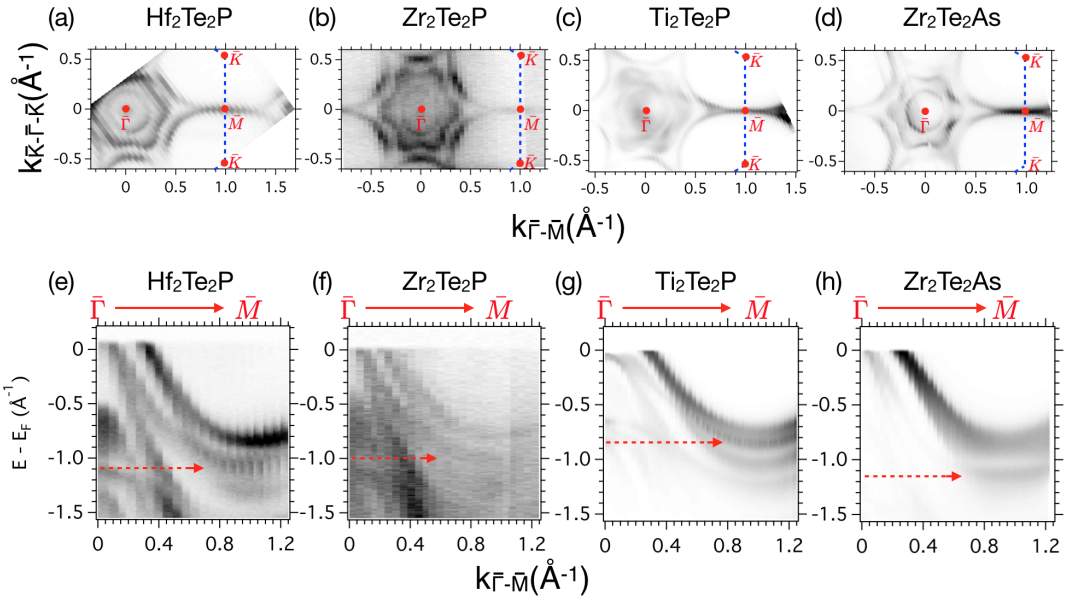

FIGURE 4.15: (a-d) Constant energy maps around the Dirac point of Hf_2Te_2P, Zr_2Te_2P, Ti_2Te_2P and Zr_2Te_2As (hence at binding energies 1.14 eV, 1.00 eV, 0.85 eV and 1.15 eV, respectively), together with the reduced 2D first Brillouin zones (blue dashed lines). (e-h) The electronic dispersions from $\bar{\Gamma}$ to $\bar{M}$. The red arrows indicate the quasi-flat states leading to the corresponding Dirac-node arcs. All the data were acquired with LH polarised photons at temperatures $T = 20$ K (a, b, e, f) and $T = 6$ K (c, d, g, h).

4.3.1 Helical Dirac surface states at $\bar{M}$

Fig. 4.16(a) shows again the in-plane FS map of Ti_2Te_2P together with the corresponding surface-projected Brillouin zone and the TRIM points. At $\bar{M}$ point along $\bar{K} - \bar{M} - \bar{K}$, there is a linearly dispersing surface state in the bulk bandgap as shown in Fig. 4.16(b), in which a clear crossing point is observed at an energy of 0.85 eV below the Fermi level. By measuring the in-plane spin component along $\bar{\Gamma} - \bar{M}$ with spin-resolved ARPES, we obtained the spin-resolved electronic dispersion of this surface state as presented in Fig. 4.16(b), right panel, which clearly shows two spin-polarised (red: pointing towards readers; blue: pointing away from readers) branches proving this surface state is indeed a non-trivial topological Dirac state. Compared to the well-known topological insulators Bi_2Se_3 and Bi_2Te_3 [44], the helicity of the spin texture remains the same in Ti_2Te_2P: left-handed for upper Dirac cone and right-handed for lower Dirac cone when looking from above the surface.

Similar measurements were also carried out on Hf_2Te_2P and results are demonstrated in Fig. 4.16(c-e). Fig. 4.16(c) shows the linearly dispersing surface state with a Dirac point at around 1.1 eV below the Fermi level. Instead of measuring the full spin-resolved electronic dispersion, which is very time consuming, one spin-resolved MDC Fig. 4.16(d) at the binding energy indicated by the green dashed line in Fig. 4.16(c) and two spin-resolved EDCs Fig. 4.16(e) indicated by blue and red dashed lines at the left and right side of the Dirac crossing point in Fig. 4.16(c) were taken.

In Fig. 4.16(d), the two spin components reverse their relative magnitude when passing $\bar{M}$ point along $\bar{K} - \bar{M} - \bar{K}$ direction, such that the spin polarisation is negative for the left branch and positive for the right branch at this binding energy

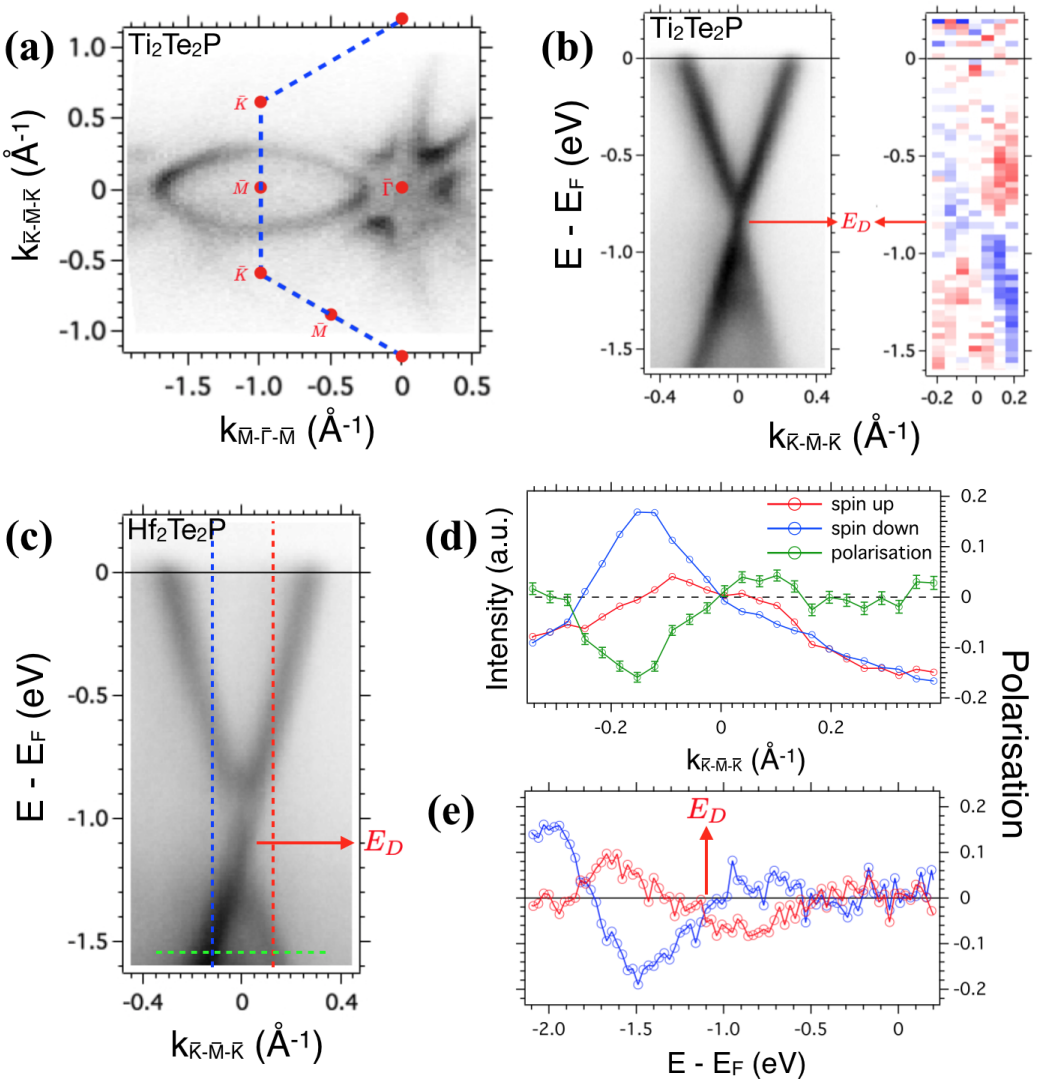

FIGURE 4.16: (a) In-plane Fermi surface map of Ti_2Te_2P showing a 3-fold symmetry. (b) Energy-momentum dispersion of Ti_2Te_2P at $\bar{M}$ point along $\bar{K} - \bar{M} - \bar{K}$ direction showing a Dirac crossing point around 0.85 eV below E_F, and the corresponding spin-resolved energy-momentum dispersion showing a clear spin polarisation of the non-trivial Dirac surface state (red: pointing towards readers; blue: pointing away from readers). (c) The energy-momentum dispersion of states of Hf_2Te_2P at $\bar{M}$ point along $\bar{K} - \bar{M} - \bar{K}$ direction showing a Dirac crossing point around 1.1 eV below E_F. (d) The spin-resolved MDC taken at binding energy indicated by the green dashed line in (c). (e) The spin-resolved EDCs indicated in (c) with the blue and the red dashed lines. All data were collected at the ESPRESSO spin-ARPES endstation in synchrotron HiSOR with LH polarised $h\nu = 55$ eV photons at a temperature of $T = 20$ K. The effective Sherman function used to obtain the spin polarisation is 0.18, as calibrated for $h\nu = 55$ eV with Bi(111) during the beam time in HiSOR in 2017.

$E - E_F = -1.55$ eV. In Fig. 4.16(e), the spin polarisation of each individual EDC reverses above and below the Dirac crossing point, and the two EDCs have opposite polarisations at a given binding energy, while they cross and show a vanishing spin

polarisation exactly at the energy of the Dirac point. At $E - E_F = -1.55$ eV, the blue curve representing the left branch is negative while the red curve representing the right branch is positive. This is exactly what the spin-resolved MDC Fig. 4.16(d) shows. Based on these spin-resolved results, we conclude that this surface state in Hf_2Te_2P is also a spin-polarised Dirac state with a Dirac crossing point 1.1 eV below the Fermi level and the same helicity as Bi_2Se_3 and Bi_2Te_3.

4.3.2 Helical Dirac node arcs

As demonstrated and discussed in the previous sections, Ti_2Te_2P and Hf_2Te_2P have Dirac-node arcs formed by the Dirac crossing point at $\bar{M}$ extending along $\bar{\Gamma} - \bar{M} - \bar{\Gamma}$ direction. This is shown again in Fig. 4.17(a-c) for the case of Ti_2Te_2P. However, in order to prove that this nodal line is a non-trivial topological Dirac node arc, we need to verify that at all points along this arc the surface states are spin-polarised. So we carried out three spin-resolved EDCs, at three different positions along the nodal line as indicated by (1)-(3) green dashed lines in Fig. 4.17(c). Fig. 4.17(d)-(f) are the corresponding results and reveal that all the surface states, whose crossing points are on the node arc, are spin polarised and share a common E_D.

4.4 Discussion and concluding remarks

A new family of topological metals M_2Te_2X (with M = Ti, Zr or Hf, and X = P or As) has been systematically characterised employing both standard and spin-resolved ARPES. With the help of DFT calculations (band calculations and parity analysis) and based on our obtained ARPES data, the electronic structures together with the topological properties of these compounds have been comprehensively understood. Several features make this family of materials stand out from other topological materials:

1. They are intrinsic metals (Strictly speaking, Ti_2Te_2P is classified as a semimetal [196]). The experimental realisation of topological superconductivity has been strongly pursued for both fundamental interests like Majorana fermions and non-Abelian statistics [32, 197], and potential important applications like quantum computation. If M_2Te_2X (with M = Ti, Zr or Hf, and X = P or As) can be tuned to the superconductivity regime by lowering temperature and/or applying external pressure, and the surface states protected by the strong topological character are still present, then the superconducting states and topological states naturally coexist in a single crystal. Notably, the conducting bands in these topological metals are mainly *p*- and *d*- bands such that unconventional superconductivity is possible to realise, such as odd-parity superconductors which are topological superconductors if the Fermi surface encloses an odd number of time-reversal-invariant momenta in the Brillouin zone [198–200].

   Experimentally, many groups have studied the proximity-induced superconductivity on the surface of 3D topological insulators and showed that the superconductivity can indeed be induced in the topological surface states [201–207]. M_2Te_2X (with M = Ti, Zr or Hf, and X = P or As) can serve as a basis for the realisation of superconducting states and also 3D topological surface states. Thus, a large choice for possible interface combinations is available to test, for example, unconventional superconductors or other typical 3D topological materials, hoping to realise the dreamed topological superconductivity.

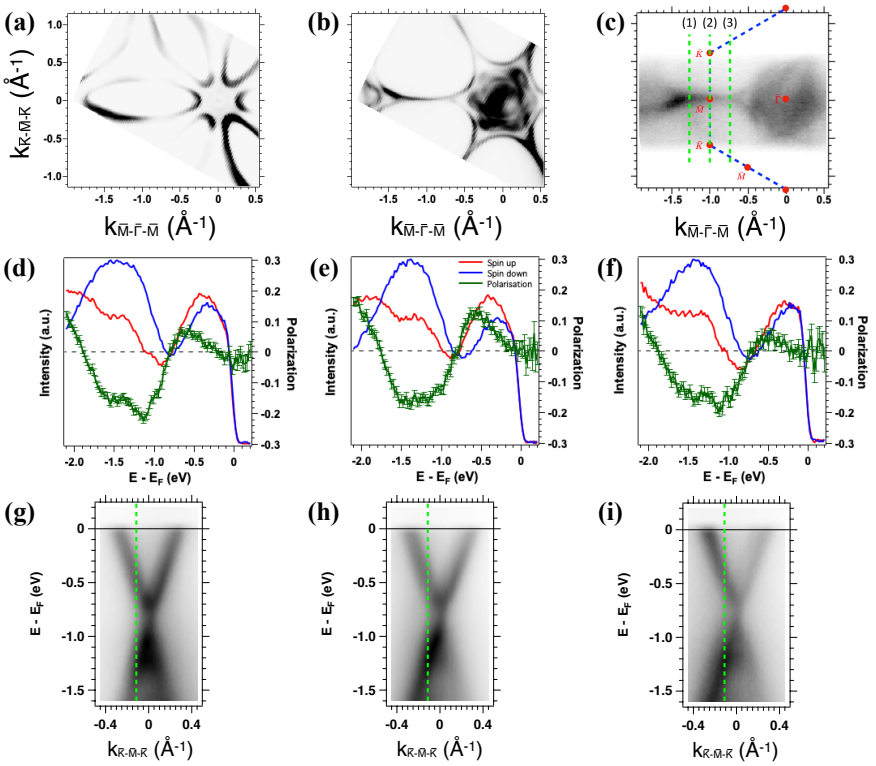

FIGURE 4.17: (a) In-plane Fermi surface map of Ti_2Te_2P showing a complete contour around $\bar{M}$. (b) The constant energy mapping at $E - E_F = 0.85$ eV crossing the Dirac point showing the Dirac node arc. (a-b) are normal ARPES data obtained at the CASSIOPEE endstation at synchrotron Soleil with LH polarised $h\nu = 50$ eV photons at a temperature of $T = 5$ K. (c) The same constant energy map of Ti_2Te_2P but measured with LH photons at $h\nu = 55$ eV at the spin-ARPES endstation at synchrotron HiSOR at $T = 20$ K. (d)-(f) The spin-resolved EDCs measured at (1)-(3) cutting positions respectively along the Dirac node arc shown in Fig. 4.17(c) in the same way as Fig. 4.16(e). The effective Sherman function used to obtain the spin polarisation is 0.25, as calibrated for $h\nu = 55$ eV with Bi(111) during the beam time in HiSOR in 2018. (g-i) The energy-momentum dispersion references of Fig. 4.17(d-f) on top of which the green dashed lines indicate where the spin-resolved EDCs were taken.

2. Multiple types of topological surface states coexist. As aforementioned in the parity analysis, at $\bar{\Gamma}$ all compounds have a surface state with the strong topological character in the bulk bandgap well above the Fermi level, except Ti_2Te_2P due to a weak SOC strength from Ti to drive the $d - p$ band parity inversion at $\bar{\Gamma}$. Additionally, Hf_2Te_2P has one more surface state but with weak topological character in a bulk bandgap below the previous gap but still above the Fermi level at $\bar{\Gamma}$. On the other hand, at $\bar{M}$ all the four compounds have another surface state, with a weak topological character in Hf_2Te_2P and a strong topological character in the other three. These multiple topological surface states features have been reported in previous works. especially Hf_2Te_2P, and open the possibility of topological surface state engineering. Further experiments are needed to explore possible related exotic transport properties.

3. The Dirac cone centred at $\bar{M}$ is highly anisotropic resulting in the formation of a Dirac-node arc along $\bar{\Gamma} - \bar{M}$ direction in the Brillouin zone. This feature was first reported in Hf_2Te_2P [191], and has been demonstrated here in all the other compounds, proving that the Dirac-node arc is not necessarily a signature of the weak topological Z_2 invariants, as the other three in fact have a strong topological character associated to the corresponding topological surface state at $\bar{M}$. The potassium capping experiments in Hf_2Te_2P in this thesis suggests it is easy to dope the topological surface state at $\bar{M}$. In Ti_2Te_2P, the Dirac point is the closest to the Fermi level (around 0.85 eV) compared to the other three compounds, such that Ti_2Te_2P is the most promising compound to tune the Dirac point to the Fermi level (for example hole doping) and to create a highly anisotropic 2D electron system with spin polarised carriers being very massive in one direction while being massless in the perpendicular direction.

Element dependence For the convenience of discussion, the quantities extracted from MDCs and EDCs of the four studied compounds are summarised in the Tab. 4.2.

	Ti_2Te_2P	Zr_2Te_2P	Hf_2Te_2P	Zr_2Te_2As
$k_h \pm 0.005$ (Å^{-1})	0, 0.111	0.070, 0.111	0.056, 0.106	0.045
$k_e \pm 0.005$ (Å^{-1})	0.269, 0.305	0.291, 0.348	0.272, 0.325	0.258, 0.300
$E_D \pm 0.01$ (eV)	0.85	1.01	1.14	1.14
$E_{gap} \pm 0.01$ (eV)	0.31	0.45	0.48	0.43

TABLE 4.2: Typical quantities characterising the electronic structures of M_2Te_2X (with M = Ti, Zr or Hf, and X = P or As), extracted from the MDCs and EDCs quantitative analysis. k_hs are the typical momenta of the (inner, outer) hole-like states at the Fermi level around $\bar{\Gamma}$. In Zr_2Te_2As, the MDC can not resolve the inner and outer bands, such that only one value is shown. k_es are the typical momenta of the (surface, bulk) electron-like states at the Fermi level around $\bar{M}$. E_Ds are the binding energy of the Dirac points at $\bar{M}$. E_{gap}s are the bulk bandgaps at $\bar{M}$.

The strength of the spin-orbit coupling (SOC) is systematically varied by element replacing Ti $\rightarrow$ Zr $\rightarrow$ Hf (increasing the strength), and P $\rightarrow$ As (increasing the strength). Thus, the study of this family of topological metal serves as an example of studying how the strength of SOC affects the electronic properties including the topology of materials. According to the DFT calculation without and with the inclusion of SOC (see Fig. 4.11), the SOC mainly modifies the band structure at $\bar{\Gamma}$ and $\bar{M}$.

At $\bar{\Gamma}$, the SOC splits the bands close to the Fermi level, which are mainly composed of d-bands from Ti, Zr, or Hf, and p-bands from Te. Topologically, this SOC from Ti, Zr, and Hf, induces 0, 1, and 2 topological surface states at $\bar{\Gamma}$. Thus, SOC with a larger strength drives more band inversion and formation of surface states. It would be interesting to study the transition from 0 to 1 by partially replacing Ti with Zr.

The strength of SOC also affects the band splitting energy. As a result of larger strength of SOC from Ti_2Te_2P to Zr_2Te_2P, the hole-like parabolic quasi-2D state is pushed up above the Fermi level forming a small circle in the in-plane Fermi surface with a momentum radius $k_h^{inner} = 0.07$ Å^{-1}. By increasing the coupling strength further from Zr_2Te_2P to Hf_2Te_2P, this energy split should be larger and push the

quasi-2D state farther above the Fermi level leading to a larger k_h^{inner}. In fact, k_h^{inner} becomes smaller in Tab. 4.2 from Zr_2Te_2P to Hf_2Te_2P. The reason is that in Hf_2Te_2P, a new topological surface state forms slightly above the Fermi level and contributes to the ARPES photoemission intensity. So the unexpected reduction of k_h^{inner} is a signature of the topological surface state with weak topological character above the Fermi level at $\bar{\Gamma}$.

At $\bar{M}$, the SOC opens a gap from the original crossing bands mainly composed of Te p-bands, and drives a band inversion producing a topological surface state in the opened gap. These Te p-bands at $\bar{M}$ extend to and connect with those p- and d-bands at $\bar{\Gamma}$. So the gap width E_{gap} and the energy position of the Dirac point of the topological surface states E_D are still varied by replacing Ti $\rightarrow$ Zr $\rightarrow$ Hf, as shown in Tab. 4.2.

As Te is not replaced, the topological surface state at $\bar{M}$ exists in all the four compounds. However, the topological character of this surface state can still be affected by the strength of SOC through the modification of the band structure at $\bar{\Gamma}$. The Z_2 invariant is a global property determined by the overall band structure below a certain bulk bandgap. For instance here, when the coupling strength is tuned to be strong enough from Zr_2Te_2P to Hf_2Te_2P, a new topological surface state forms at $\bar{\Gamma}$ in the aforementioned bandgap, such that there is an even number of topological surface states included in the Brillouin zone, instead of an odd number like in Ti_2Te_2P and Zr_2Te_2P. Then the Z_2 invariant ν_0 is determined to be 0 instead of 1, leading to a weak topological character in Hf_2Te_2P. It would be interesting to study the transition from a strong to a weak topological character by partially replacing Zr with Hf.

Since P p-bands contribute few to the band structure around the Fermi level in Zr_2Te_2P, the element replacement from P to As did not lead to a transition in the topological character or big difference in the electronic structure in Zr_2Te_2As, as shown in the Fermi surface maps and Tab. 4.2.

Z_2 invariants Experimentally, we found Hf_2Te_2P tends to form multiple domains after cleavage in situ while Ti_2Te_2P does not. By comparing the standard ARPES results in Fig. 4.16(b) and (d), we can see that Hf_2Te_2P gives a weaker signal (lower signal-to-noise ratio) than Ti_2Te_2P under the same measurement conditions. These observations suggest that Ti_2Te_2P has stronger interlayer interactions thus being more robust to external cleaving forces, and is better crystallised in bulk than Hf_2Te_2P. As mentioned before, the surface states at $\bar{M}$ in Hf_2Te_2P and Ti_2Te_2P have different Z_2 invariant indexes ν_0, namely 0 for Hf_2Te_2P and 1 for Ti_2Te_2P, even though both are spin-polarised and form similar topologically non-trivial Dirac node arcs. So here we could establish a link between theory and experiment:
$\nu_0 = 0(1) \leftrightarrow$ weak (strong) interlayer interactions $\leftrightarrow$ being sensitive (robust) to external interventions, like cleaving forces $\leftrightarrow$ low (high) ARPES signal-to-noise ratio and a high (low) possibility of observing multiple domains

Spin texture The in-plane spin texture of the topological surface states around $\bar{M}$ in Ti_2Te_2P and Hf_2Te_2P has been fully characterised by means of spin-resolved ARPES. The clear spin polarisation of the surface states undoubtedly indicates non-trivial massless Dirac fermions. Notably, the measured spin polarisation always shows a positive tail and does not converge to 0 in the large binding energy range beyond 1.7 eV. As this observation was reproducible in different experiments and

both compounds, we believe these unexpected signals are valid and indicate possible topological surface states buried inside of the valence bands. Further experiments are needed to understand and explain this observation.

The Dirac-node arc has been shown experimentally to be helical with all the composing surface states spin polarised and thus being non-trivial topological surface states. On the Dirac-node arc but not at $\bar{M}$, the time-reversal invariance is not guaranteed anymore as these momenta points are not TRIM points. A natural following question will be how is the spin texture influenced by the presence of such a Dirac-node arc. Compared to the simple Dirac cone type topological surface states, for example, the ones in Bi_2Te_3, the in-plane spin polarisation results did not show a noticeable difference. Then how about the out-of-plane component of the spin polarisation? A non-zero out-of-plane spin polarisation could be expected in the topological surface states at momentum positions away from TRIM points. This is left as an open question for future experimental explorations.

Chapter 5

One-dimensional heavy fermion material: $YbNi_4P_2$

This chapter will present an ARPES study on the quasi-one-dimensional heavy fermion material $YbNi_4P_2$ (see Fig. 5.1), which is a Kondo lattice system with a Kondo temperature $T_K = 8$ K and orders ferromagnetically (FM) at $T_C \approx 0.15$ K with a small magnetic moment of 0.05 μB aligned within the (a, b) plane [51, 52]. Our samples were synthesised by the team of Prof. Cornelius Krellner at Frankfurt University, our collaborators for this study.

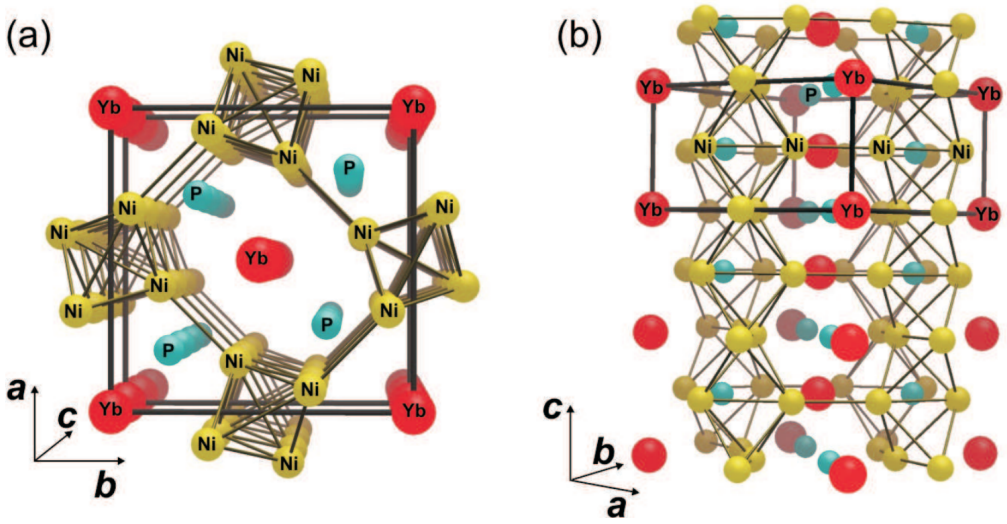

FIGURE 5.1: Tetragonal crystal structure (space group $P4_2/mnm$ (no. 136)) of $YbNi_4P_2$ with lattice parameters: a = b = 7.0565(2) Å, c = 3.5877(1) Å. (a) Stereoscopic view along c with the Yb chains located in the channels between chains of edge-connected Ni tetrahedra. (b) Rotated view, with the c direction along the vertical axis, the Yb chains are well separated from each other in the ab plane. The primitive cell is indicated with black rigid bonds in (a) and (b). Taken from Ref. [208]

The first section will briefly introduce what we already know about $YbNi_4P_2$ from transport measurements and DFT calculations. The second section will present my ARPES measurements on $YbNi_4P_2$. Specifically, the Fermi surface topography demonstrates the existence of quasi-1D electronic states, which according to existing theories are a necessary condition for the occurrence of a ferromagnetic quantum-critical point. Following this, high resolution energy-momentum maps concerning

the states close to the Fermi level (f electrons and conduction bands) will be shown and discussed.

5.1 $YbNi_4P_2$: a heavy fermion system with a ferromagnetic quantum critical point

In this section, I am going to review several features observed in $YbNi_4P_2$ through transport measurements based on Ref. [51,52,208], and theoretically calculated band structure based on Ref. [51,209].

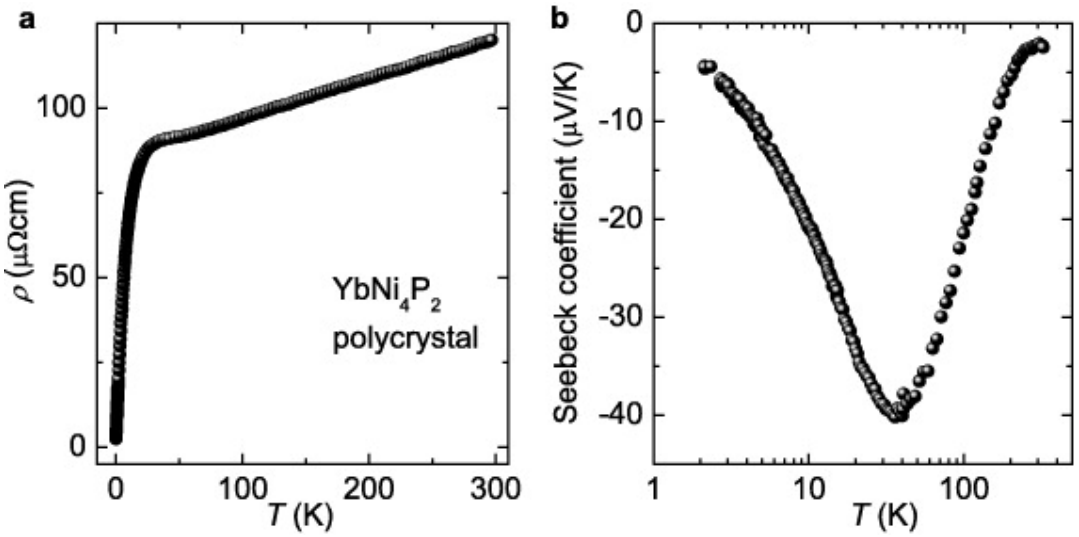

FIGURE 5.2: (a) The temperature dependence of the resistivity with a pronounced drop below 30 K, indicating the onset of coherent Kondo scattering. (b) The temperature dependence of the Seebeck coefficient shows a distinct minimum at 35 K, characteristic of Yb-based Kondo lattices. The large absolute values near this minimum are commonly ascribed to a strongly energy-dependent quasi-particle density of states at the Fermi level. Taken from Ref. [51]

A metallic Kondo lattice Fig. 5.2 presents the temperature dependence of the resistivity, $\rho(T)$, and the Seebeck coefficient, $S(T)$, between $T = 2$ and 300 K, showing that $YbNi_4P_2$ is a Kondo lattice with strong interactions between Yb $4f$ and conduction electrons. $\rho(T)$ decreases linearly down to 50 K before dropping rapidly below 30 K. As introduced in Chapter 1, a single site (magnetic impurity) Kondo scattering increases the resistivity at low temperatures, while the coherence Kondo scattering developed on an "Anderson lattice" leads to a sudden drop of resistivity at low temperatures. Thus, the rapid drop of $\rho(T)$ in Fig. 5.2(a) suggests an onset of coherent Kondo scattering on the Yb-$4f$ electron lattice (Ni is not magnetic in this system as will be discussed later). The presence of strong hybridization between the 4f and the conduction electrons in $YbNi_4P_2$ is further supported by thermopower measurements, as shown in Fig. 5.2(b). $S(T)$ is negative within the whole temperature range investigated, a fact that is well established in Yb-based Kondo lattices [210]. Moreover, $S(T)$ presents a pronounced minimum at 35 K with absolute values as high as 40 μV K^{-1}. Extrema in $\rho(T)$ and $S(T)$ originate from Kondo scattering on the ground and the excited crystal electric field (CEF) levels [51,211]. A reliable estimate of the

Kondo energy scale, T_K (for the lowest-lying CEF Kramers doublet), can be obtained by means of the magnetic entropy calculated from the specific heat data, discussed below. At 4 K, the entropy increases to $0.5R$ ln2 (R is the ideal gas constant), establishing a doublet ground state with $T_K \cong 8$ K.

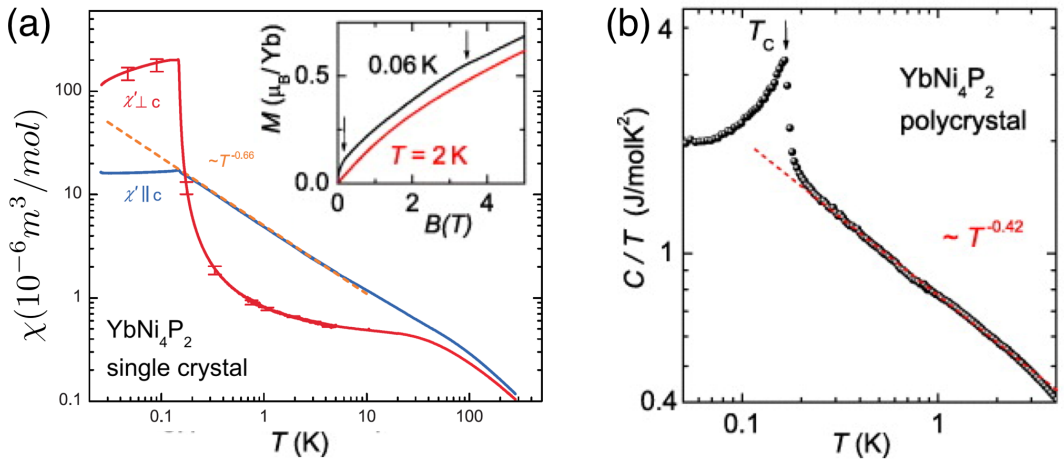

FIGURE 5.3: (a) Real part of the magnetic susceptibility χ' plotted as a function of temperature, measured perpendicular ($\chi'_\perp$) and parallel ($\chi'_\parallel$) to the c axis in a $YbNi_4P_2$ single crystal. The orange dashed line emphasises the $T^{-0.66}$ behavior of $\chi'_\parallel$ versus T below 10 K. Taken from Ref. [52]. Inset: the field dependence of the magnetisation $M(B)$ below (black line) and above (red line) T_C measured in a $YbNi_4P_2$ polycrystal. The arrow on the left-hand side indicates the step-like increase due to the small ordered ferromagnetic moment, $M_{ord} \cong 0.05\ \mu_B$, obtained by extrapolating the linear curve between 0.1 and 0.2 T to zero field. In determining the ordered moment, we assume that in the polycrystal the fully aligned moment dominates the magnetisation at these low fields. The right-hand arrow marks an anomaly at a higher field representing either the rotation of the ferromagnetic moments along the magnetic hard direction or complete suppression of the Kondo screening. (b) The temperature dependence of the zero-field specific heat divided by temperature (C/T) in a double logarithmic representation clearly reveals a power law divergence, $C/T = T^{-0.42}$, indicated by the red dashed line, measured in a $YbNi_4P_2$ polycrystal. At the transition temperature T_c = 0.17 K, this specific heat curve shows a sudden jump resulting in a λ shape indicating a 2nd order phase transition. Taken from Ref. [51].

2nd order ferromagnetic transition The real-part of the ac-susceptibility $\chi'(T)$ as shown in Fig. 5.3(a), measured both with magnetic field $H \parallel c$ ($\chi'_\parallel$) and $H \perp c$ ($\chi'_\perp$), provides strong evidence of the ferromagnetic order at low temperatures. As T is lowered towards $T_C = (0.150 \pm 0.005)$ K, $\chi'_\perp$ increases sharply up to a value of $\approx 200 \times 10^{-6}$ m^3/mol, which is ≈ 3.7 after transformed to the dimensionless volume susceptibility by dividing the molar volume $V_{mol} = 53.8 \times 10^{-6}$ m^3 mol^{-1}. This value is much larger than the typical values of χ for the antiferromagnetism (0 - 0.1), but consistent with the typical values of χ for the ferromagnetism (0.1 - 5×10^3). Both the sharply increasing behavior and the relatively large value of χ suggest a ferromagnetic phase below T_C. On the other hand, $\chi'_\parallel$ increases with decreasing T, following a $T^{-0.66}$ power law below 10 K down to T_C, where it saturates at a value

of $\approx 17 \times 10^{-6}$ m^3/mol (i.e. ≈ 0.3 for the dimensionless volume susceptibility). This anisotropy of the susceptibility suggests that the spins align perpendicularly to the c direction, and $\chi'_{\parallel}$ measures the transversal fluctuations.

Ferromagnetic order can also be inferred by the field dependence of the magnetisation $M(B)$ shown in the inset of Fig. 5.3(a). At $T = 0.06$ K below T_C, a small magnetisation residual $M_{ord} \cong 0.05\ \mu_B$ is obtained by extrapolating the linear curve between 0.1 T and 0.2 T to zero field, while at $T = 2$ K above T_C, $M(B)$ goes to zero when $B \to 0$.

Fig. 5.3(b) shows the temperature dependence of the specific heat divided by temperature (C/T) in a double logarithmic representation giving a slightly larger transition temperature T_c = 0.17 K measured in a $YbNi_4P_2$ polycrystal than in a single crystal. The typical λ shape of C/T v.s. T curve indicates that the phase transition is 2nd order [51]. However, intensive theoretical and experimental investigations on itinerant systems (like d-electron systems) have shown that metallic ferromagnets tend to develop via either a first-order phase transition [57–61, 212], or through the formation of intermediate superconducting [213, 214] or inhomogeneous magnetic phases [215, 216]. Thus, the localised nature of the Yb-4f states together with the Kondo coupling of the 4f-electrons to the conduction electrons must be considered in order to understand this 2nd order ferromagnetic phase transition at low temperatures. This idea is further supported by the volume thermal expansion $\beta(T)$ measurement results and the divergency behavior of the Grüneisen ratio $\Gamma(T) = \beta(T)/C(T)$ [217]. Notably, the power law divergence $C/T = T^{-0.42}$ suggests a non-Fermi liquid behavior, as will be discussed later.

Anisotropy As previously mentioned, $YbNi_4P_2$ single crystal shows an anisotropy in $\chi'(T)$ between c axis and (a, b) plane. Fig. 5.4 shows again this anisotropy in the electrical resistivity ρ and of the C/T.

The electrical resistivity $\rho(T)$ shown in Fig. 5.4(a-c) presents clearly the anisotropy expected from the crystal structure. Above 100 K, the resistivity along c (the Yb chain direction), is a factor of 2 smaller than perpendicular to the chains ($j \parallel a$). In this temperature range, the electrical transport is dominated by phonons, reflected in a linear-in-T dependence for both directions [219]. At 1.8 K (the lowest temperature in Fig. 5.4(a)), the anisotropy ρ_a/ρ_c amounts already to a factor of 5. Furthermore, the temperature dependence below 50 K is strongly dependent on the direction of the current flow. For the easy transport direction ($j \parallel c$), a pronounced drop is observed below $T = 30$ K, characteristic of coherent Kondo scattering. For $j \perp a$, $\rho(T)$ increases below 50 K, presents a well defined maximum at $T = 20$ K and then also strongly decreases towards lower temperatures. Below 0.5 K (Fig. 5.4(b, c)), besides the anisotropy, the electrical resistivity shows interesting non-Fermi liquid (NFL) behavior. Below T_C, $\rho(T)$ follows a T^n power law, with $n_\perp = 2.9$ and $n_\parallel = 2.5$, very likely because of charge-carrier scattering from ferromagnetic magnons [52]. The resistivity is quasi-T-linear just above T_C.

Fig. 5.4(d, e) show the T and B dependences of C/T. At B = 0, a sharp λ-type phase transition in C/T versus T is observed. A magnetic field applied parallel to the c axis shifts the transition temperature to lower T (see Fig. 5.4(d)), whereas for $B \perp c$, the crossover to the polarised state is shifted to higher temperatures (see Fig. 5.4(e)). This magnetic anisotropy indicates an in-plane (perpendicular to c axis) ferromagnetic order in the $YbNi_4P_2$ single crystal.

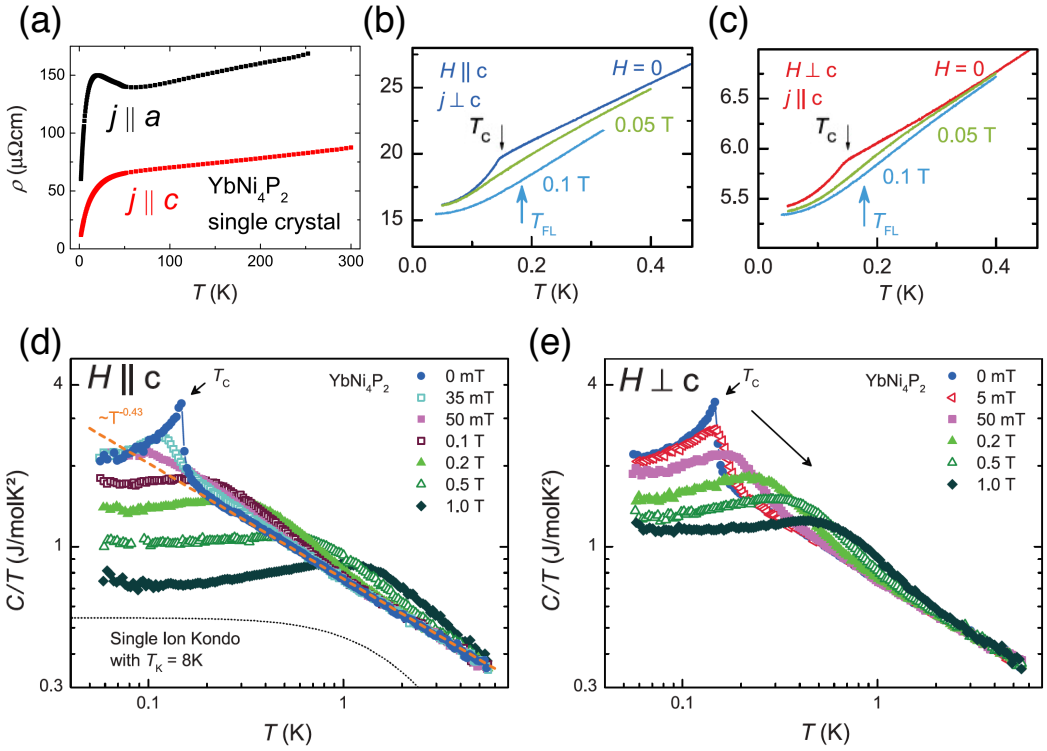

FIGURE 5.4: (a) Temperature dependence (above 1.8 K) of the electrical resistivity ρ with the current along the a (black) and the c (red) direction. The resistivity along c ($j \parallel c$) is distinctively smaller than along a in the whole investigated temperature range. Both directions display a pronounced drop towards lower temperatures due to the onset of coherent Kondo scattering. A pronounced Kondo maximum at $T = 20$ K is visible only for $j \parallel a$. Taken from Ref. [208]. (b, c) Temperature dependence (below 0.5 K) of the electrical resistivity ρ measured with current j (b) perpendicular and (c) parallel to the crystallographic c axis. The kinks at T_C disappear at fields $\mu_0 H \geqslant 0.05$ T in both field directions. At a field of 0.1 T, both resistivities follow a temperature dependence close to T^2 below T_{FL} (arrows). (d,e) C/T versus T of $YbNi_4P_2$ measured at magnetic fields (d) $H \parallel c$ and (e) $H \perp c$. The dashed orange line emphasizes the $T^{-0.43}$ power law behavior observed above 0.2 K up to about 6 K. The dotted black line is the specific-heat contribution calculated within the single ion $S = 1/2$ Kondo model in Ref. [218], with $T_K = 8$ K and C/T scaled by a factor of 0.5 for better visibility. In (d) and (e), the nuclear Schottky contribution has been subtracted from the raw specific-heat data. Taken from Ref. [52].

Non-Fermi liquid behavior The non-Fermi liquid (NFL) character is suggested by the stronger-than-logarithmically diverging Sommerfeld coefficient $\gamma(T) = C(T)/T = T^{-0.42}$ (see Fig. 5.3(b)) and the linear T-dependence of the electrical resistivity $\rho(T)$ (see Fig. 5.4(b, c) and Fig. 5.5) above T_C. Note that in the Fermi liquid regime, $\gamma(T)$ and $\rho(T)$ have the following behavior [220]:

$$\begin{cases} \gamma(T) = \gamma(0) - g_3 T^2 lnT \\ \rho(T) = \rho_0 + AT^2 \end{cases} \tag{5.1}$$

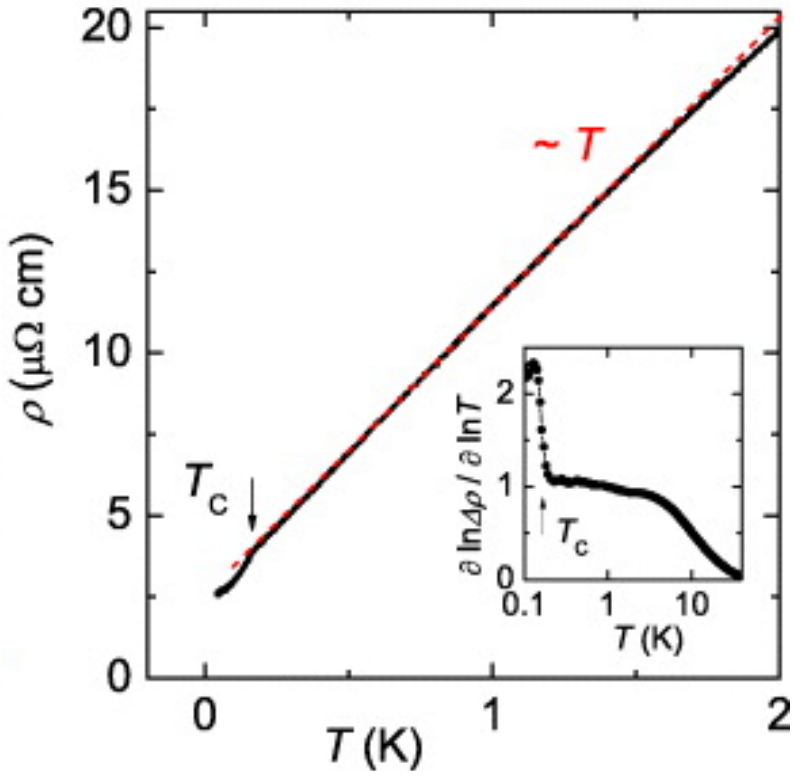

FIGURE 5.5: Linear-in-T resistivity in zero field of a $YbNi_4P_2$ polycrystal. A pronounced drop at T_C precedes a T^2 law within the ordered phase. The temperature dependence of the resistivity exponent, defined as the derivative of $\ln[\Delta\rho(T)] = \ln[\rho(T) - \rho_0]$ with respect to $\ln T$, is presented in the inset. Taken from Ref. [51].

with $\gamma(0)$, g_3, ρ_0 and A being constants.

Such an NFL behaviour, when observed over a sufficiently extended temperature range, is commonly considered as a hallmark of quantum criticality [221–224]. In other words, $YbNi_4P_2$ is located in the close vicinity of a quantum critical point, where $T_C \to 0$ smoothly. Experimentally, the isoelectronic substitution of As for P expands the crystal lattice and causes an increase of T_K and a reduction of T_C in Yb systems [225]. Indeed, it has been found that T_C can be tuned to 0 in $YbNi_4(P_{0.9}As_{0.1})_2$ i. e. at around 10% of such substitution [52].

Electronic band structure calculated by DFT Fig. 5.6 shows the electronic band structure near the Fermi level calculated by DFT with the GGA approximation and assuming frozen Yb $4f$-core electrons. Notably, $4f$ heavy bands close to the Fermi level, related correlations with conduction bands, relativistic effects, and related spin-orbit coupling in Ni and P are not included in the DFT calculation. Even so, a lot of useful informations can be obtained.

First of all, Ni tends to form a non-magnetic ground state, thus it is not likely to be at the origin of the magnetism in $YbNi_4P_2$. Instead, the magnetism in $YbNi_4P_2$ has to be a result of correlated behaviour beyond the scope of the 4f-core calculations in line with the strong signatures of hybridisation of Yb $4f$ moments with conduction electrons suggested by the transport measurements discussed above.

Secondly, at the Fermi level, the 5 intersecting bands as indicated in different colours in Fig. 5.6(a), come essentially from Ni $3d$ states and form 5 individual Fermi

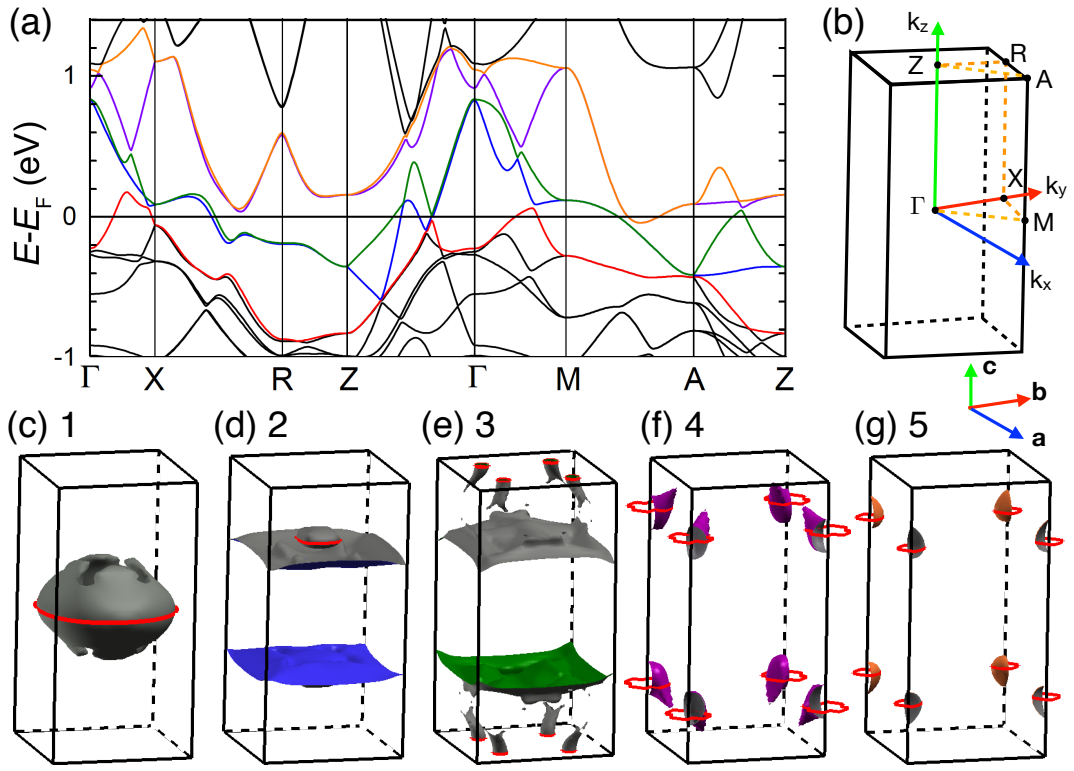

FIGURE 5.6: (a) Bands intersecting the Fermi level highlighted in colour calculated in $YbNi_4P_2$ along selected symmetry lines in the first Brillouin zone. (b) Sketch of the first Brillouin zone of $YbNi_4P_2$ with high symmetry points and lines marked, together with an inset of the lattice coordinates. (c-g) Fermi surfaces (FSs) corresponding to the 5 bands crossing the Fermi level. FS 2 and 3 contain almost flat and parallel FS sheets suggesting the quasi-1D character of the system. The red circle plotted in each FS indicates the FS pocket size potentially detectable by quantum oscillation measurement with the magnetic field parallel to the c axis. Taken from Ref. [209].

surface (FS) contours as demonstrated in Fig. 5.6(c-g) respectively. In particular, FS 2 and 3 contain parallel almost-flat "sheets" indicating a strong quasi-1D electronic structure. In principle, all these sheets contain parts with closed contours that are detectable with quantum oscillation experiments as indicated with red circles in Fig. 5.6(c-g). Assuming the external magnetic field is parallel to the c axis, the corresponding quantum oscillation frequencies and effective masses can be calculated, as listed in Tab. 5.1.

Fig. 5.7 shows the results of Shubnikov-de Haas measurements of a $YbNi_4P_2$ single crystal with the magnetic field parallel to c axis. Panel (a) shows representative traces of the oscillatory part of the resistivity for fields between 20 T and 31 T. Long period oscillations are observed below 1.5 K. The frequency of these oscillations is identified to be $F = 0.21$ kT from the Fourier transformed power spectrum in panel (b). The oscillation amplitudes are damped at increasing temperatures, as shown in the inset panel (c). By fitting the amplitude damping curve with the Lifshitz-Kosevish formula, the effective mass is determined to be $m^*/m_e = 3.5$. However, the measured frequency and effective mass do not match any of the calculated states and FSs. It might be a new state or one of the 5 states but strongly modified by the

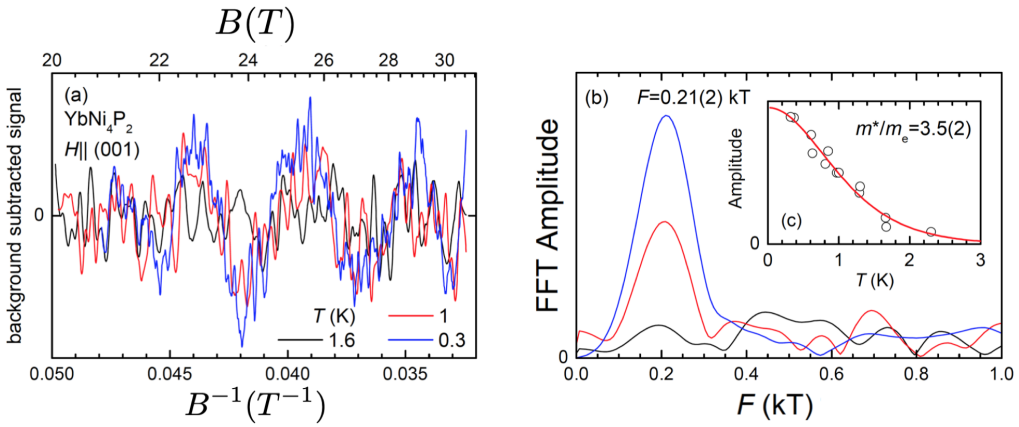

FIGURE 5.7: Shubnikov-de Haas measurements of a $YbNi_4P_2$ single crystal with the magnetic field parallel to the Yb chain direction (c axis). Background subtracted magnetoresistance (a) and Fourier transformed power spectrum (b) at selected temperatures (black: 1.6 K, red: 1 K, blue: 0.3 K). The inset (c) shows the temperature dependence of the oscillation amplitude with the solid line representing a fit of the Lifshitz Kosevich formula to the data with $m^*/m_e = 3.5$. Taken from Ref. [209].

FS	F (kT)	m^*/m_e	k_F (Å^{-1})
1	6.1	1.1	0.43
2	0.6	0.7	0.135
3	0.1	0.3	0.055
4	0.5	0.9	0.123
5	0.2	0.1	0.078
Exp.	0.21	3.5	0.080

TABLE 5.1: DFT Calculated (row 1 to 5) and measured (the last row) quantum oscillation frequencies and effective masses. The last column are the Fermi momenta assuming the cross-sectional area perpendicular to the external magnetic field is circular. Taken from Ref. [209].

correlation with $4f$ heavy bands.

Thus, in order to understand the electronic structure of $YbNi_4P_2$ experimentally, besides additional and more refined quantum oscillation measurements, other experimental techniques, such as ARPES, are needed.

5.2 ARPES studies on $YbNi_4P_2$

$YbNi_4P_2$ shows a second-order quantum critical transition from a ferromagnetic to a paramagnetic phase upon partial substitution of P by approximately 10% As [52]. In two- or three-dimensional metallic systems, theoretical considerations exclude a ferromagnetic quantum critical point (QCP) in clean materials, but point to a first-order ferromagnetic phase transition. Experiments also suggest that the ferromagnetic QCP is preempted either by the formation of superconducting phases [213, 214] or inhomogeneous magnetic phases [215, 216], or by a first-order ferromagnetic phase transition [212]. Thus, probing the dimensionality of the electronic structure of

$YbNi_4P_2$ is essential to understand, from an experimental standpoint, the fundamental microscopic aspects of ferromagnetic quantum criticality.

In order to understand the unexpected power-law exponents in thermodynamic quantities indicating the presence of strong ferromagnetic quantum critical fluctuations, the localized nature of the Yb-4f states, in the presence of very strong spin-orbit coupling and the Kondo coupling of the 4f states to the conduction electrons (i.e. $d-f$ hybridisation) must be considered. Though it is difficult to include these effects in theoretical calculations, the information about them can in principle be extracted from the experimentally measured electronic structures.

ARPES meets these needs for the study of $YbNi_4P_2$, since it can directly measure the FS, whose topography can serve as direct evidence of the dimensionality of the studied system, and band dispersions (including the heavy f-states), which reflect directly band modifications due to spin-orbit coupling or $d-f$ hybridisation.

However, several difficulties need to be surmounted in order to be able to study $YbNi_4P_2$ using ARPES:

- **Single crystalline samples of large sizes**, of the order of $5 \times 5 \times 1$ mm^3, are needed, not only to be able to observe the band dispersions (in principle this is doable, even if challenging, on sub-mm-sized samples if they cleave well), but especially to be able to properly prepare the surface for measurements (see next). The team of Cornelius Krellner at Frankfurt University, our collaborators in this project, recently succeeded in fabricating high-quality single-crystalline samples of $YbNi_4P_2$ meeting those requirements.

- A reproducible way to obtain a **clean crystalline surface**. As introduced in Chapter 1, ARPES is very surface sensitive. However, the crystal structure of $YbNi_4P_2$ is very rigid and extremely difficult to cleave or fracture in UHV. Thus, one needs to prepare the surface directly in-situ by alternate cycles of Argon bombardment and high-temperature annealing. During my Ph.D., I was able to work out a protocol to prepare reliably a clean and crystalline surface of the material. Details will be given later, in the “surface preparation" subsection.

- **Resolution**. As shown later, the emission from the Ni-3d valence band is strong and locates 1-2 eV below the Fermi level, thus its tail gives a strong background extending up to the Fermi level, overlapping with the Yb^{2+} f bands and the conduction electron bands close to the Fermi level. Besides this unwanted background, the gap opened due to the Kondo resonance is typically small (of the order of or smaller than10 meV). Thus, in order to resolve the $d-f$ hybridisation gap, extremely high energy resolution is needed. During the research presented in this thesis, we managed to detect the Yb^{2+} f bands and the conduction electron bands from the Ni 3d valence band background, but were not able to resolve the $d-f$ hybridisation.

Note that all the ARPES measurements presented in this chapter were performed on single crystalline $YbNi_4P_2$(110) oriented samples at $T = 16$ K, well above $T_C = 0.15$ K, hence in the paramagnetic state.

5.2.1 Surface preparation

Prior to ARPES measurements, clean and crystalline (110)-oriented surfaces of $YbNi_4P_2$ were obtained by the following protocol:

- Atomic-scale polishing. The as-grown (110)-oriented crystals were mechanically polished down to a roughness between 0.5° and 1° in the accuracy of surface orientation. The polishing was performed by MaTecK GmbH.
- The first annealing at 500°C-600°C in UHV to clean the surface from unwanted impurities left at the surface by the polishing process.
- Subsequent alternative cycles of bombardment with Ar^+ ions accelerated to 800 eV from an angle of 30° with respect to the sample surface for 20-25 minutes, and annealing in UHV at 500°C-600°C to thoroughly clean and re-crystallise the surface. The recorded pressure during the Argon bombardment was 7.4×10^{-6} mbar.

After these steps, LEED was used to check the quality of the sample surface. If no diffraction points were observed in LEED, we repeated the last step until a good LEED diffraction pattern was observed. Fig. 5.8(a) shows the LEED pattern we obtained for $YbNi_4P_2$ indicating a clean and well crystallised surface. Then the sample can be transferred to the ARPES chamber for further measurements.

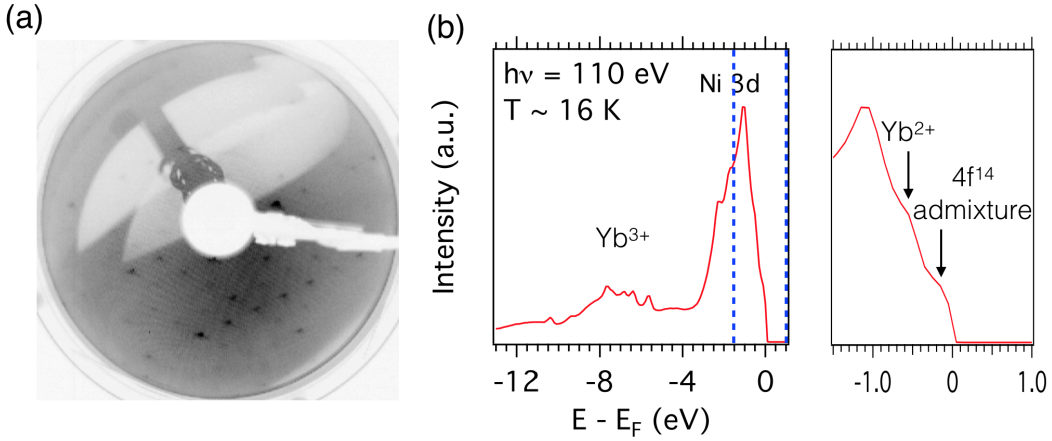

FIGURE 5.8: (a) LEED pattern of $YbNi_4P_2$ after proper surface treatments. The LEED electron energy is 152 eV. (b) Photoemission spectrum of $YbNi_4P_2$ taken at $T = 16$ K with $h\nu = 110$ eV and linear horizontal polarised photons, together with a zoom-in from -1.5 to 1.0 eV indicated by the blue dashed lines.

Fig. 5.8(b) is the angle-integrated photoemission spectrum measured at $T = 16$ K with $h\nu = 110$ eV and linear horizontal polarised photons. Notice that the core electrons ordered in energy from inner to outer are "$\cdots, 5p^6, 6s^2, 4f^{14}$", and in $YbNi_4P_2$, Yb stays in the trivalent ground state with a core electron configuration of "$\cdots, 5p^6, 4f^{13}$". Several features of the photoemission spectrum related to Yb 4f and Ni 3d in the spectrum can be observed:

1. the well-known broad $4f^{12}$ (i.e. Yb^{4+}) final state multiplet lying at binding energy between 5 and 12 eV as expected from photoionisation of a trivalent Yb $4f^{13}$ (i.e. Yb^{3+}) ground state configuration;
2. strong emissions from the Ni 3d valence bands between 0.3 and 3 eV binding energy;
3. a small built up shoulder close to the Fermi level, which is assigned to the $4f^{13}$ final states arising from a $4f^{14}$ admixture to the trivalent bulk ground state.

4. another weak shoulder between 0.5 and 1.0 binding energy, which is the divalent Yb^{2+} signal due to the surface valence instability [226–228].

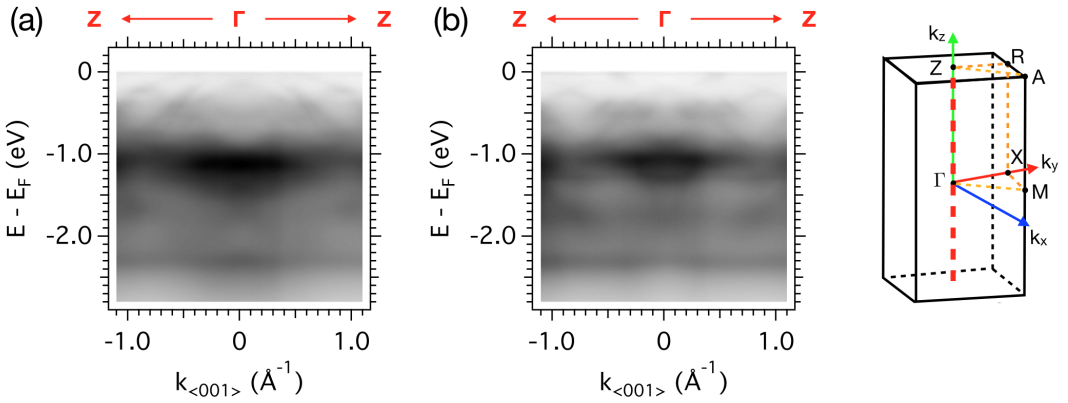

FIGURE 5.9: Dispersing valence and conduction bands and f-levels in $YbNi_4P_2$ measured with (a) linear horizontal and (b) linear vertical polarised photons at $h\nu$ = 90 eV corresponding the Γ point in bulk Brillouin zone. Inset: the first Brillouin zone. The red dashed line indicates the measurement direction Z - Γ - Z.

As shown in Fig. 5.9, the angle-resolved spectra shows rapidly dispersing valence and conduction bands, that we assign to Ni-3d states, demonstrating that a clean and crystalline surface was obtained after following the protocol described before. Thus, we can now use ARPES to characterise the Fermi surface and the low-energy electronic structure of $YbNi_4P_2$.

5.2.2 Quasi-1D Fermi surfaces of $YbNi_4P_2$

Fig. 5.10(a) shows again the crystal structure of $YbNi_4P_2$, with the 1D chains of Yb atoms along the c axis. The corresponding Brillouin zone and high-symmetry points are presented in Fig. 5.10(b), together with the quasi-1D Fermi sheets expected from DFT calculations [51]. Note that, in order to observe the quasi-1D Fermi sheets by ARPES, the <001> direction must be included in the Fermi surface mapping. Thus, by using (110)-oriented crystals, the quasi-1D Fermi sheets can be detected either through in-plane mappings at constant photon energy (measurements in the <001>×<1$\bar{1}$0> plane), or through out-of-plane mappings by varying the photon energy (measurements in the <001>×<110> plane).

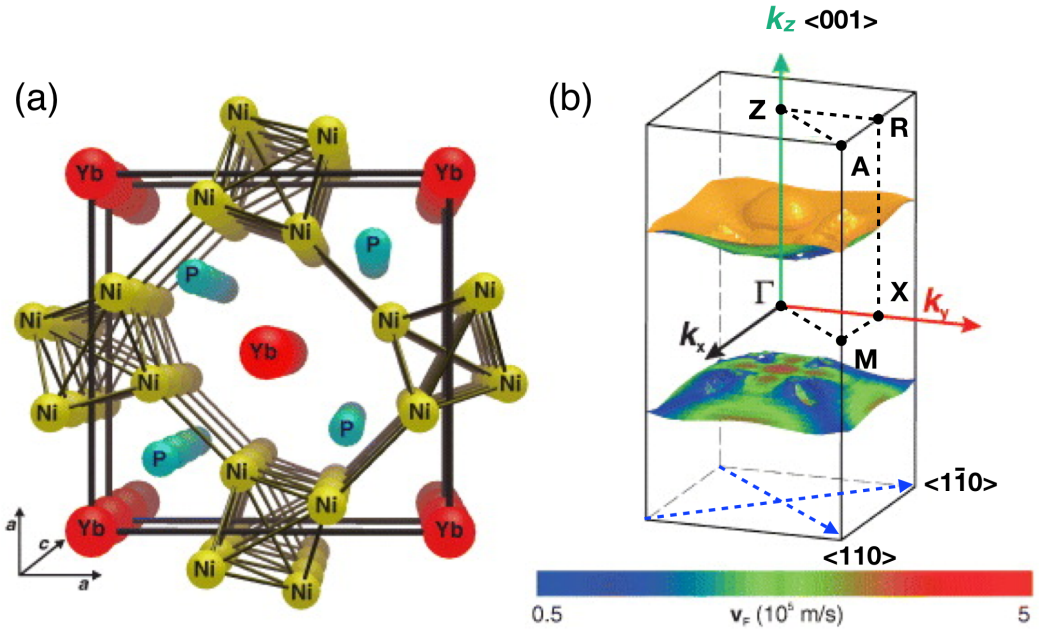

FIGURE 5.10: (a) Stereoscopic view of $YbNi_4P_2$'s tetragonal lattice along c axis with the Yb chains located in the channels between chains of edge-connected Ni tetrahedra. (b) Calculated topography of one of the uncorrelated Fermi surfaces with the most pronounced 1D character manifested in two nearly flat sheets, well separated along kz. The quantity of the Fermi velocity, v_F, of mainly the Ni 3d conducting states dominating the density of states at the Fermi level is colour-scaled as the in-set color bar. Taken from Ref. [51]

In-plane constant energy maps

Detector slit // <1$\bar{1}$0> The measurements presented in Fig.5.11(a-d) correspond to in-plane constant energy (E_F and E_F - 80 meV) maps with the <1$\bar{1}$0> direction along the detector slits, as shown in the schematic first Brillouin zone Fig. 5.11(f). In this configuration, the quasi-1D Fermi sheets are parallel to the slits, and hence are measured at exact specific angles of the sample manipulator, symmetrically positioned with respect to the sample's normal. Probably due to the presence of the $4f$ heavy bands close to the Fermi level and the possible $d-f$ hybridisation, the quasi-1D feature is not very clear in the Fermi surface maps shown in Fig. 5.11(a, c), but manifests itself in the 80 meV binding energy constant energy maps shown in Fig. 5.11(b, d). Moreover, as will be discussed later, the small elliptical pocket centred at Γ and elongated in the $\Gamma - Z$ direction shown in Fig. 5.11(d) is suggested to be responsible for signals detected in the Shubnikov-de Haas measurements.

Notably, the constant energy maps measured with LH polarisation show a strong left-right asymmetry with respect to the normal emission angle (i.e. between positive and negative $k_{<001>}$ regimes) due to geometrical factors (orientation of the light electric field with respect to the surface) in the photoemission matrix elements, usually indicating a very marked orbital character (here in $YbNi_4P_2$, $3d$ orbits) of the electronic structure.

The negative and the positive $k_{<001>}$ regimes of the constant energy (E_F - 80 meV) map shown in Fig.5.11(b) can be symmetrised through a mirror operation, as shown in Fig. 5.12(a) and (b) respectively. Compared with the 5 individual calculated Fermi surfaces (FSs) as shown in Fig. 5.12(c), we conclude that (the assignment of the FS

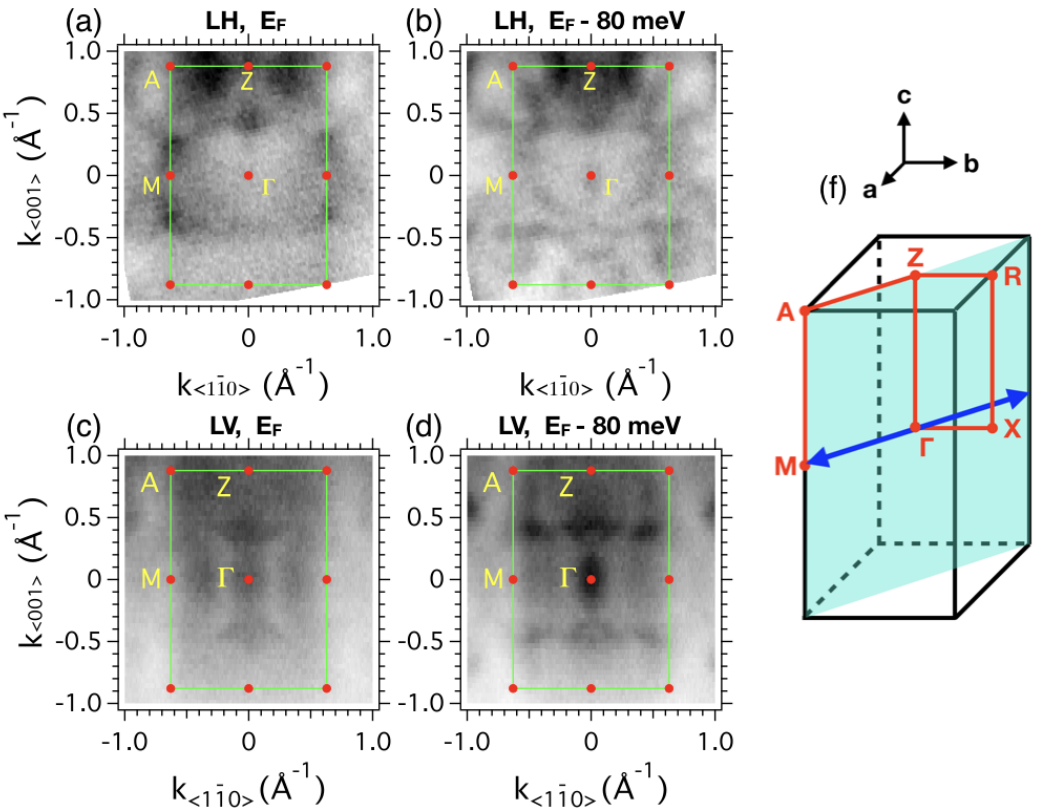

FIGURE 5.11: (a-d) In-plane constant energy (0 and 80 meV binding energy) maps of $YbNi_4P_2$ measured with (a-b) linear horizontal (LH) and (c-d) linear vertical (LV) polarised photons at $h\nu$ = 90 eV corresponding to a Γ point in bulk Brillouin zone. The measurement temperature was $T = 16$ K. The ARPES detector slit was aligned along <1$\bar{1}$0> direction. (f) Sketch of the first Brillouin zone (BZ). The sky-blue plane indicates where the in-plane constant energy maps were taken in the BZ. The blue double arrow line is parallel to the detector slit.

contours is summarised in Fig. 5.13):

1. FS 1 is observed in Fig. 5.12(a). The measured momentum radius of the FS 1 pocket along $\Gamma - M$ direction is ≈ 0.45 Å^{-1}, which matches well the DFT calculated value of 0.43 Å^{-1}.

2. FS 2 is observed in Fig. 5.12(a) and presented as a pair of flat and parallel "stripes" parallel to $k_{<1\bar{1}0>}$ at momenta $k_{<001>} \approx \pm 0.45$ Å^{-1} together with small circular pockets at the center of these stripes, proving the quasi-1D character of the electronic structure. The measured momentum radius of these small pockets at the center of the stripes is ≈ 0.15 Å^{-1}, close to the DFT calculated value of 0.135 Å^{-1}. Additionally, this radius can also be determined, from the constant energy map shown in Fig. 5.11(d), to be ≈ 0.14 Å^{-1}.

3. The almost cylindrical part of FS 3 crossing the $A - Z - R$ plane is observed at $k_{<1\bar{1}0>} \approx \pm 0.3$ Å^{-1} in Fig. 5.12(b), while its quasi-1D part is difficult to identify due to its vicinity to the also quasi-1D FS 2. The fine structure of the almost cylindrical part was not well resolved, and the measured momentum radius of the cross section at the $A - Z - R$ plane is roughly estimated to be

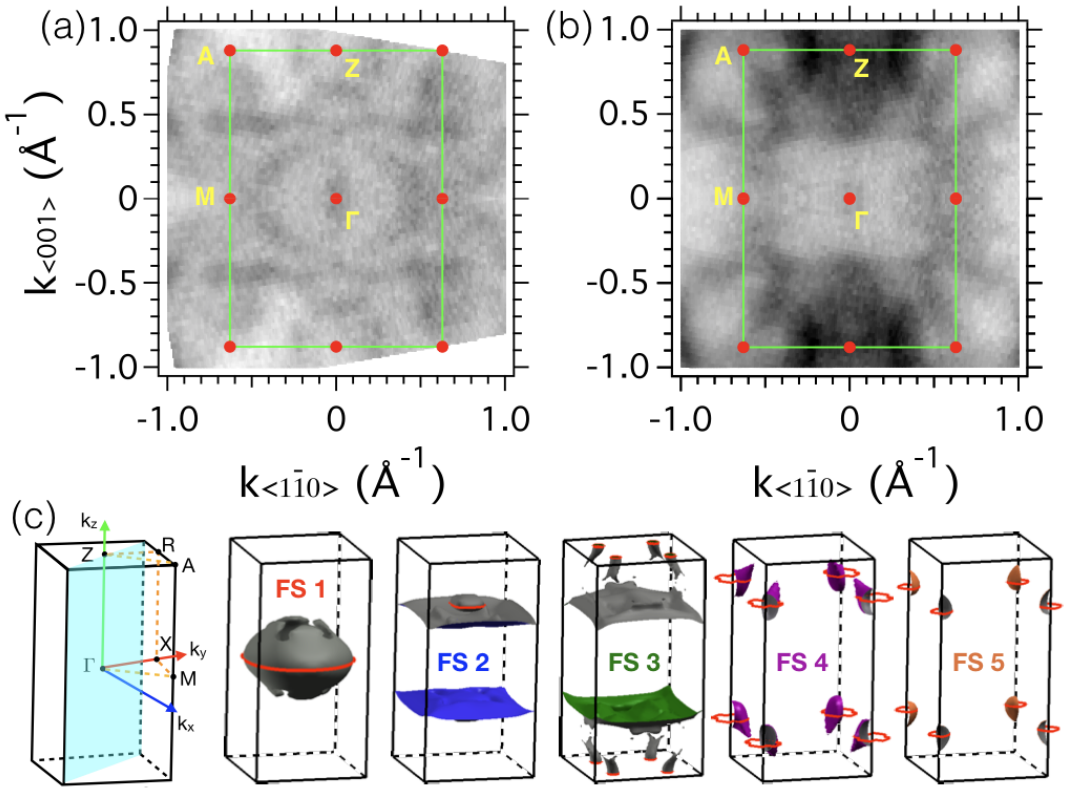

FIGURE 5.12: (a, b) Symmetrised constant energy (E_F - 80 meV) maps of (a) the negative $k_{<001>}$ regime and (b) the positive $k_{<001>}$ regime of Fig.5.11(b) through the mirror operation. (c) Sketches of the first Brillouin zone and the 5 calculated Fermi surfaces [209]. The sky-blue plane indicates where the constant energy maps were taken.

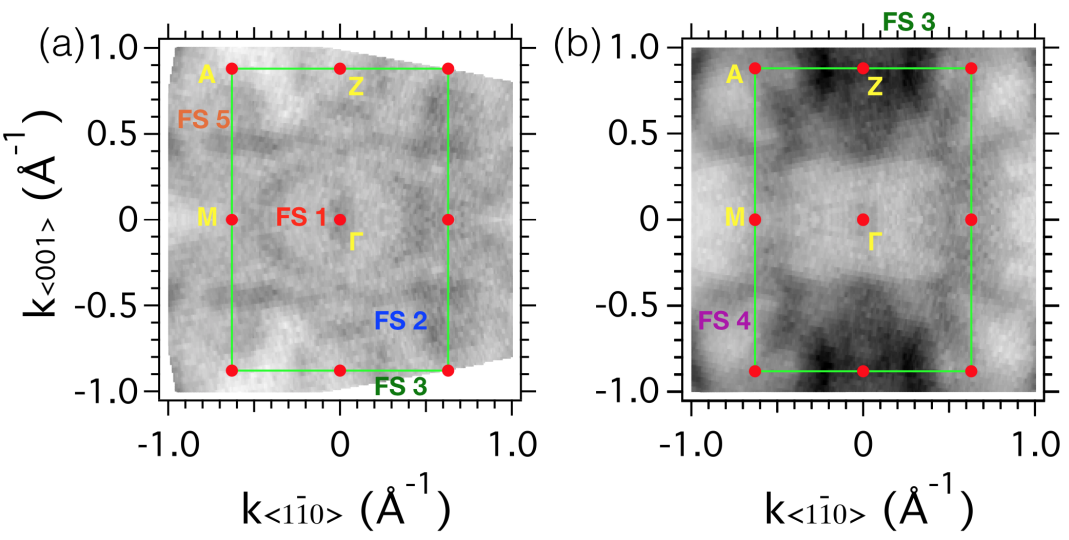

FIGURE 5.13: Reproduction of Fig. 5.12(a, b) but tagged with the corresponding FS names.

0.05 Å^{-1}, close to the DFT calculated value of 0.055 Å^{-1}. Notably, a similar almost cylindrical part was also presented in Fig. 5.12(a) but at smaller momenta $k_{<1\bar{1}0>} \approx \pm 0.2$ Å^{-1}, possibly due to the presence of strong spin-orbit coupling as will be discussed later.

4. Small pockets (though some are not completely closed) are observed at the $A - M$ edges in both Fig. 5.12(a) and (b). In panel (a), the estimated momentum radius is ≈ 0.09 Å^{-1} close to the DFT calculated value 0.078 Å^{-1} for FS 5, while in panel (b), the estimated momentum radius is ≈ 0.15 Å^{-1} close to the DFT calculated value of 0.123 Å^{-1} for FS 4.

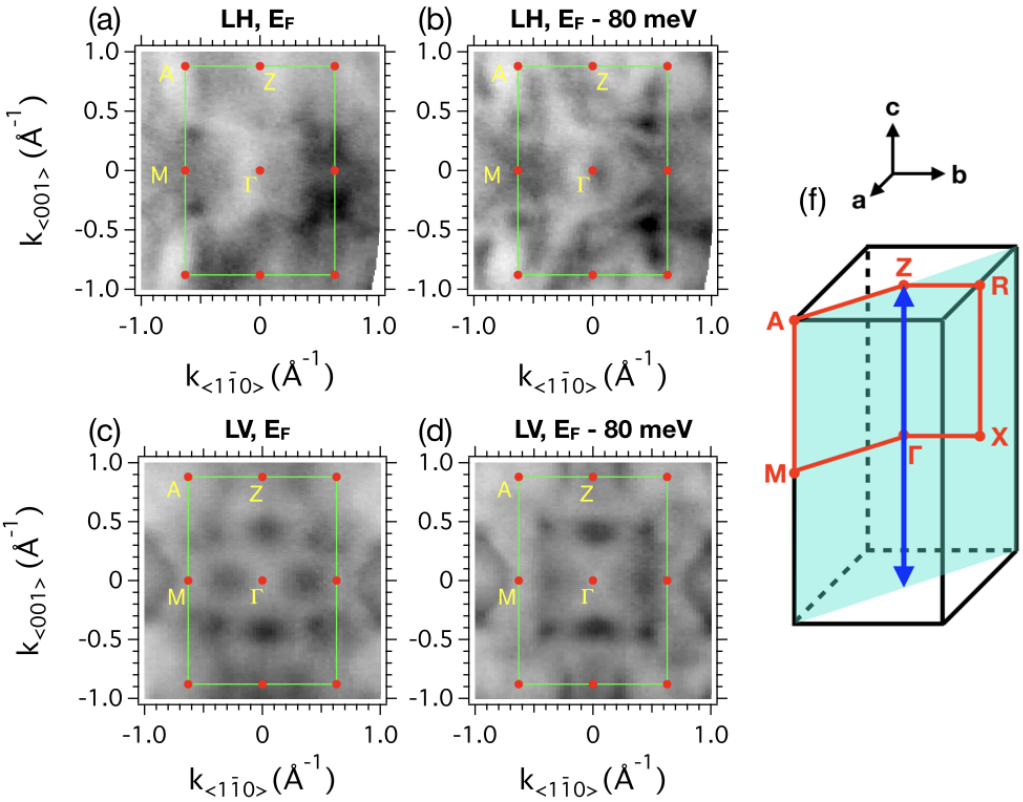

FIGURE 5.14: (a-d) In-plane constant energy (0 and 80 meV binding energy) maps of $YbNi_4P_2$ measured with (a-b) linear horizontal (LH) and (c-d) linear vertical (LV) polarised photons at $h\nu$ = 90 eV corresponding to a Γ point in bulk Brillouin zone. The measurement temperature was T = 16 K. The ARPES detector slit was aligned along <001> direction. (f) Sketch of the first Brillouin zone (BZ). The sky-blue plane indicates the measurement plane. The blue double arrow line indicates orientation of the detector slit.

Detector slit // <001> Fig. 5.14(a-d) show in-plane constant energy (E_F and E_F - 80 meV) maps obtained with the sample rotated in-plane by 90°, i.e., with the <001> direction along the ARPES detector slit. In this configuration, the quasi-1D Fermi sheets are perpendicular to the detector slits, and their Fermi momenta will be measured for virtually all angles of the manipulator. Similar to the detector slit // <1$\bar{1}$0>, the quasi-1D feature best manifests itself below the Fermi level, as shown in Fig. 5.14(b, d). Again, a strong left-right asymmetry between the positive and negative momentum regimes of $k_{<1\bar{1}0>}$ is observed in the LH polarisation case as shown in Fig. 5.14(a, b). Similar mirror symmetrisation was applied to the positive $k_{<1\bar{1}0>}$ regime and the negative $k_{<1\bar{1}0>}$ regime of Fig. 5.14(b), as shown in Fig. 5.15(a-b). On the other hand, the constant energy maps measured with LV polarisation shown in Fig. 5.14(c-d) are completely symmetric in terms of intensity and shape as

the LV polarised electric field is parallel, hence fully projected, on the sample surface, so that its contribution to the photoemission matrix elements is independent of the measurement angle. Even though the quasi-1D Fermi sheets are very hard to observe in this geometry, the small cylindrical pockets (parts of FS 3) crossing $A-Z-A$ and the round pockets (FS 4 and 5) at the $A-M$ Brillouin zone edges can be clearly identified.

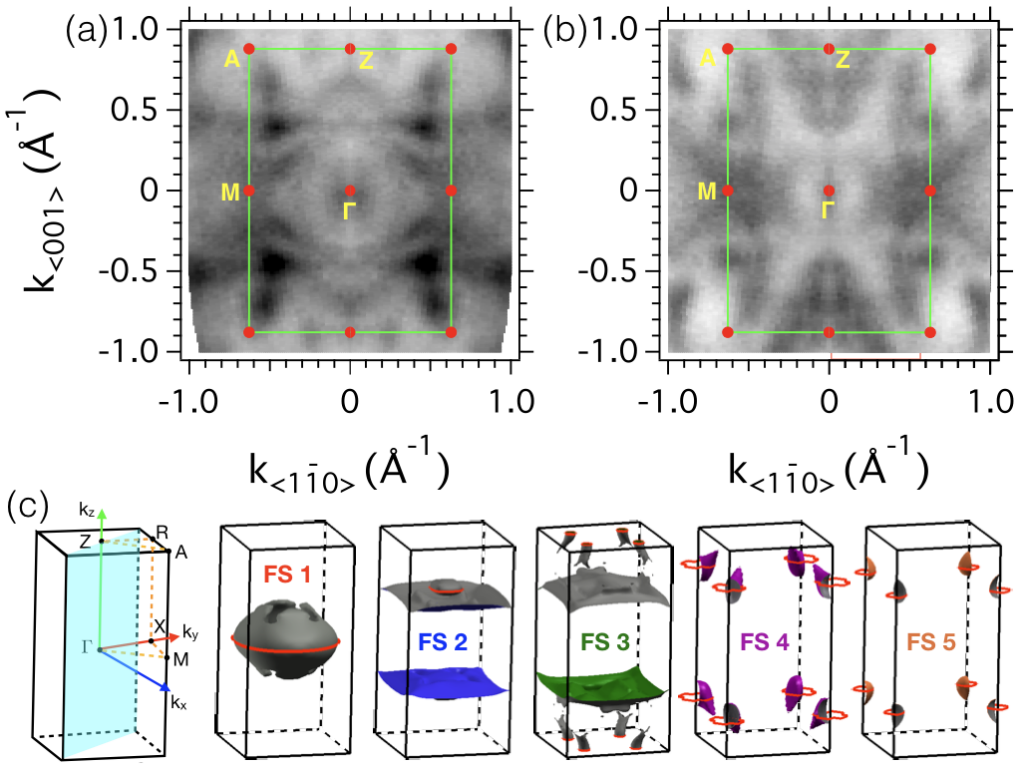

FIGURE 5.15: (a, b) Symmetrised constant energy (E_F - 80 meV) maps of (a) the positive $k_{<1\bar{1}0>}$ regime and (b) the negative $k_{<1\bar{1}0>}$ regime of Fig. 5.14(b) through the mirror operation. (c) Sketches of the first Brillouin zone and the 5 calculated Fermi surfaces [209]. The sky-blue plane indicates where the constant energy maps were taken.

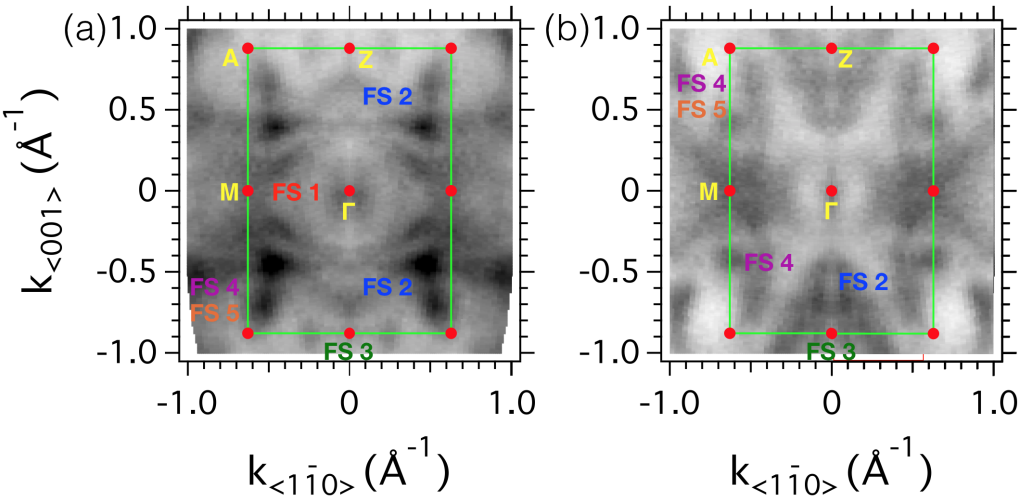

FIGURE 5.16: Reproduction of Fig. 5.15(a, b) but tagged with the corresponding FS names.

Comparing Fig. 5.15(a) and (b), one major difference is notable: The quasi-1D sheets at momenta $k_{<001>} \approx \pm 0.45$ Å^{-1} are clearly presented in Fig. 5.15(a), while they leave no trace in Fig. 5.15(b). The small pockets centred at the quasi-1D strips (FS 2) have a momentum radius ≈ 0.16 Å^{-1} in Fig. 5.15(a), and a momentum radius ≈ 0.10 Å^{-1} in Fig. 5.15(b).

Note also that different electronic states can be visualised in the constant energy maps depending on the orientation of the detector slits. A clear example are the features around Γ enclosed between the quasi-1D sheets: when the slits are parallel to the <1$\bar{1}$0> direction, one observes an ellipse centred at Γ along the <1$\bar{1}$0> direction with a long axis of ± 0.45 Å^{-1} (see Fig. 5.12(a)), but when the slits are along the $<\ 001\ >$ direction, one observes a smaller ellipse along the <1$\bar{1}$0> direction with a long axis ± 0.3 Å^{-1} (see Fig. 5.15(b)) plus a larger incomplete ellipse along the <1$\bar{1}$0> direction crossing the Brillouin zone boundary at the M points, as shown in Fig. 5.15(a).

Other Fermi surfaces (FS 4 and 5) can also be found at the $A - M$ edges of the Brillouin zone, and have similar pocket sizes as those determined in Fig. 5.12. All these identifications of FS contours are summarised in Fig. 5.16.

Notably, the small cylindrical pockets (parts of FS 3) crossing $A - Z - A$ shown in Fig. 5.15(a) show an excellent agreement with the DFT calculation, while those shown in Fig. 5.15(b) tend to be smaller along $k_{<1\bar{1}0>}$ towards to the Γ point, and merge with a pocket centred at $(k_{<001>} \approx 0.6$ Å^{-1}, $k_{<1\bar{1}0>} = 0)$, which is probably a part of FS 2.

In order to confirm that the stripes observed so far in the <1$\bar{1}$0> × <001> plane (see Fig. 5.17(a)) correspond indeed to quasi-1D Fermi sheets in 3D reciprocal space, and not to particular cuts of quasi-2D sheets parallel to their cylindrical axis (see Fig. 5.17(c)), one needs to measure the Fermi surface in two other orthogonal planes (see Fig. 5.17(b)): a cut along the <110> × <001> plane (perpendicular to the crystal surface) should show again the quasi-1D stripes, while a cut along the <110>×<1$\bar{1}$0> plane across Γ should not show any signature of these Fermi sheets.

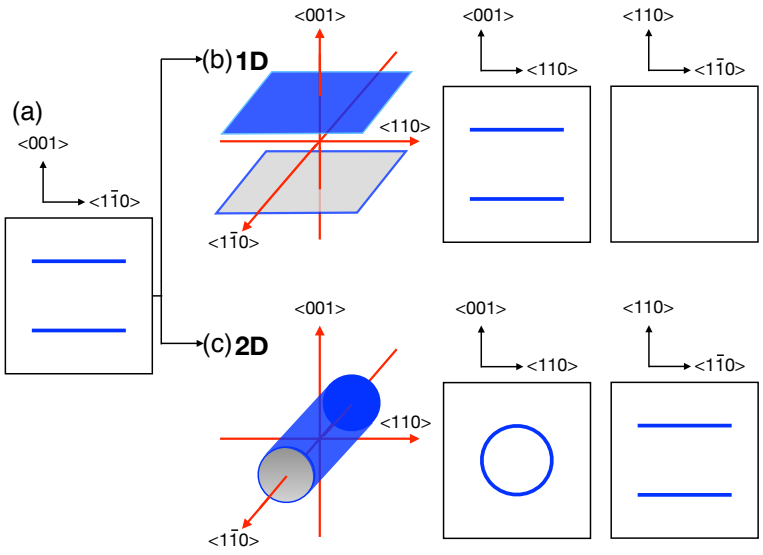

FIGURE 5.17: (a) Sketch of two stripes observed in the <1$\bar{1}$0>×<001> Fermi surface map. (b, c) Respective sketches of the 1D and 2D Fermi surfaces compatible with (a), together with the other two possible cuts, <001>×<110> and <110>×<1$\bar{1}$0> of the whole 1D and 2D Fermi surfaces.

Out-of-plane constant energy maps

In the 3D reciprocal space of $YbNi_4P_2$, the out-of-plane direction <110> is equivalent to the in-plane direction <1$\bar{1}$0>. Thus, the constant energy maps in the <001>×<110> plane should also show the pairs of quasi-1D Fermi sheets, together with other features similar to the ones observed in the maps along the <001>×<1$\bar{1}$0> plane.

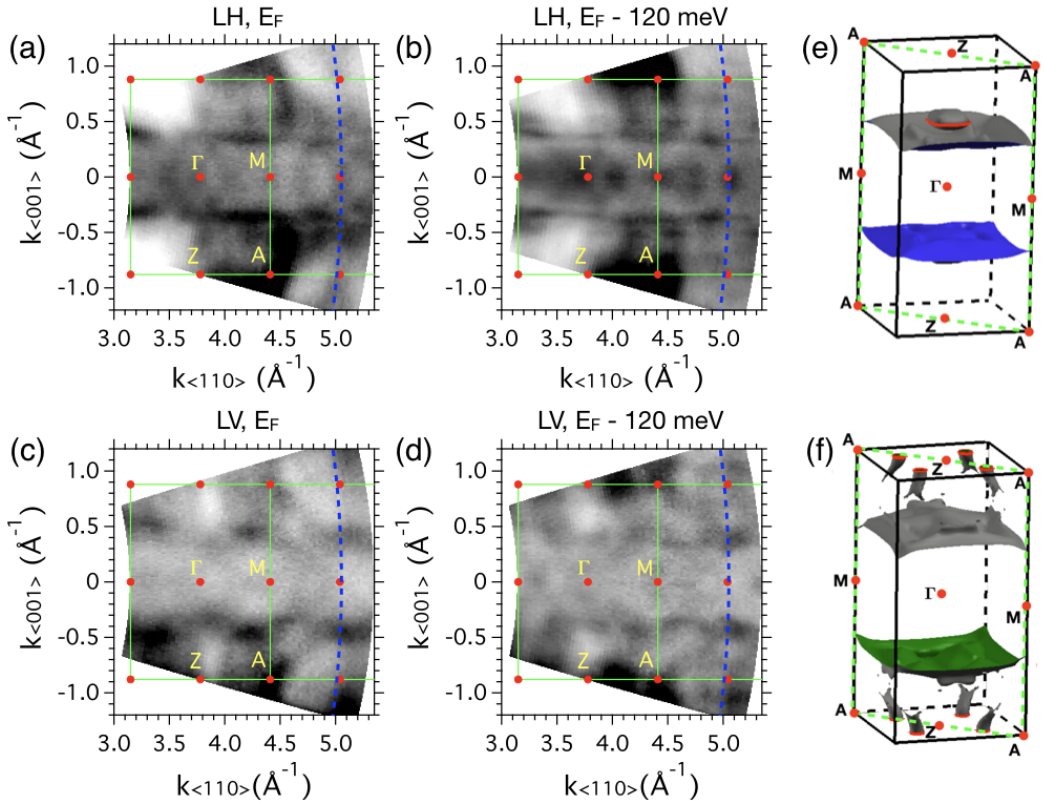

FIGURE 5.18: (a, c) Out-of-plane Fermi surfaces measured with (a) linear horizontal and (c) linear vertical polarised photons by varying the photon energy from 30 to 100 eV with an energy step of 1 eV. (b) and (d) are the respective constant energy maps at binding energy 120 meV. The blue dashed curves indicates where the in-plane Fermi surface maps were taken ($h\nu = 90$ eV). The data was measured at $T = 16$ K. An inner potential $V_0 = 11$ eV was used for the reconstruction of the out-of-plane electron momentum. (e, f) Sketches of the first Brillouin zone together with the two pairs of calculated quasi-1D Fermi surface sheets. The dashed green rectangles indicate where the out-of-plane Fermi surfaces in panels (a) and (c) were taken.

Fig. 5.18(a) shows the out-of-plane Fermi surface cut measured with linear horizontal polarisation. As expected, one clearly observes a pair of quasi-1D stripes, whose signal becomes even sharper at a binding energy of 120 meV, as seen in the constant energy map of Fig. 5.18(b). The use of linear vertical polarisation, Figs. 5.18(c-d), puts in evidence the other pair of zig-zagging sheets that we identify to FS 3 of the DFT calculations.

On the other hand, the constant energy maps in the <110> × <1$\bar{1}$0> plane, presented in Fig. 5.19, show no sign of quasi-1D features, neither at E_F nor at larger binding energy.

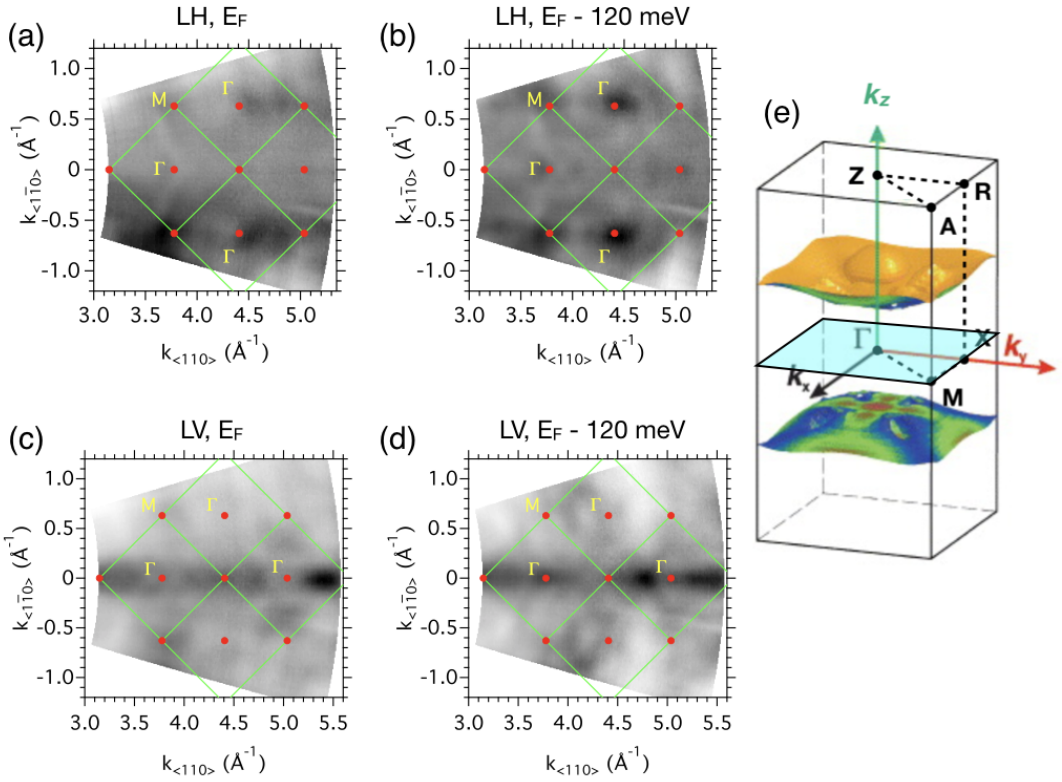

FIGURE 5.19: (a, c) Out-of-plane Fermi surfaces measured with (a) linear horizontal and (c) linear vertical polarised photons by varying the photon energy from 30 to (a) 100 eV and (c) 110 eV with an energy step 0.5 eV. (b) and (d) are constant energy maps of (a) and (c) respectively at binding energy 120 meV. The measurement temperature was $T = 16$ K, and an inner potential $V_0 = 11$ V is assumed. (e) Sketch of the first Brillouin zone together with the calculated Fermi surface sheets showing the most pronounced 1D character. The sky blue plane indicates where the out-of-plane Fermi surfaces in panels (a) and (c) were measured.

Thus, the in-plane and out-of-plane constant energy maps taken together shown in Fig. 5.11, 5.14, 5.18, 5.19 demonstrate the presence of two pairs of quasi-1D Fermi sheets in the 3D electronic structure of $YbNi_4P_2$.

5.2.3 E − k dispersions along high symmetry directions

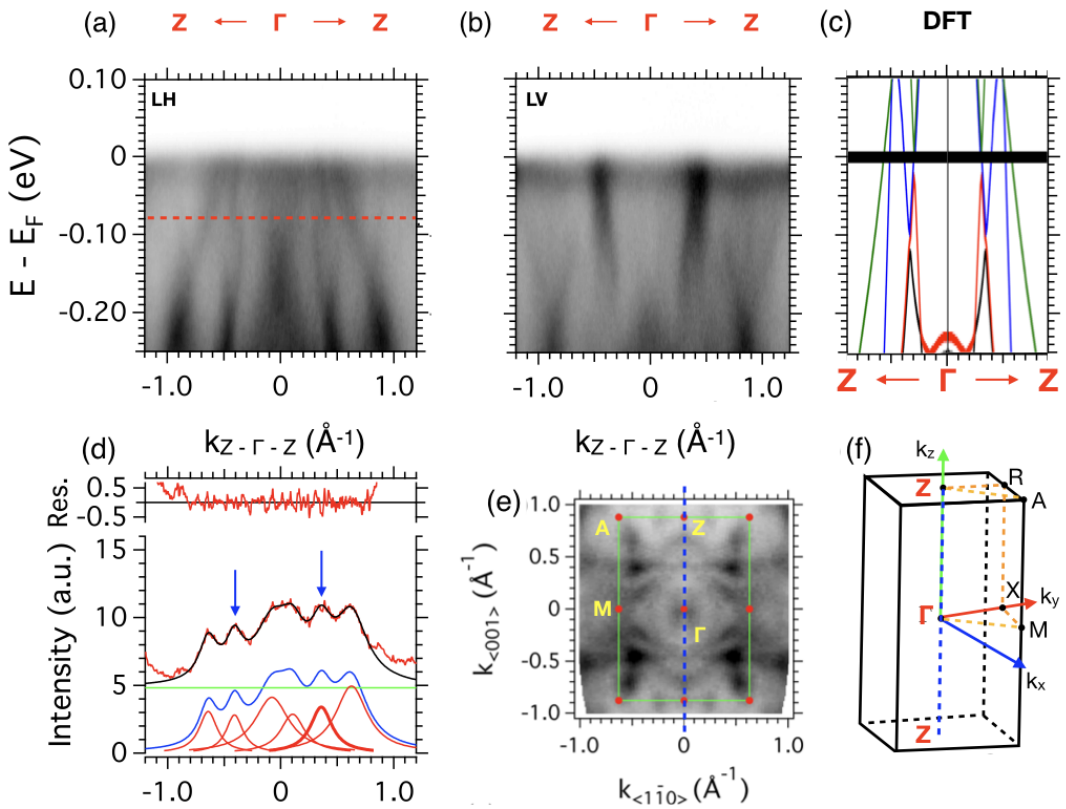

FIGURE 5.20: (a, b) Energy - momentum dispersions along $Z - \Gamma - Z$ measured at $h\nu$ = 90 eV and T = 16 K with (a) linear horizontal and (b) linear vertical polarised photons. The red dashed line in panel (a) indicates where the MDC shown in panel (d) was taken. (c) DFT calculated bands along $Z - \Gamma - Z$. The red band corresponds to FS 1, the 3D ellipsoid centred at Γ. The blue band corresponds to FS 2, the most typical quasi-1D Fermi sheets with small closed pockets slightly above and in the middle of the sheets. So from Γ to Z, there are 3 branches of blue band crossing the Fermi level: first the quasi-1D sheet, then the two boundaries of small closed pockets. The green band corresponds to FS 3, the other quasi-1D Fermi sheet together with small cylindrical Fermi surfaces crossing the $A - Z - R$ planes. (d) An MDC taken at binding energy 80 meV within an integration range ±2 meV. The blue arrows indicate the momentum positions ($\approx \pm 0.4$ Å^{-1}) of the quasi-1D sheets shown in panel (e). (e) Symmetrised in-plane constant energy map at binding energy 80 meV, identical to Fig. 5.14(a), measured with the detector slit aligned along <001> direction, as indicated with the blue dashed line. (f) Sketch of the first Brillouin zone. The blue dashed line indicates the detector slit.

Z-Γ-Z Fig. 5.20(a-b) show the ARPES energy-momentum maps of the conduction band in $YbNi_4P_2$ measured along the $Z - \Gamma - Z$ line, as indicated with blue dashed lines in Fig. 5.20(e-f). According to the DFT calculated bands shown in Fig. 5.20(c), there are 3 types of bands relevant within this energy range, the red, blue, and green bands corresponding to FS 1, 2, and 3 respectively. Experimentally, an additional band crossing the Fermi level around Γ can be observed in Fig. 5.20(a-b), which forms a closed pocket-like Fermi surface contour centred at Γ as shown in

Fig. 5.20(e). It could be a new band not considered in the calculation, or the strongly renormalised red band due to possible SOC and $d-f$ hybridisation.

As mentioned before and presented again in Fig. 5.20(e), FS 2, corresponding to the blue band and manifesting a strongest quasi-1D character, was observed experimentally. The Fermi momenta of the quasi-1D sheets can be inferred from the MDC shown Fig. 5.20(d), and indicated by the blue arrows at $k_{<1\bar{1}0>} = -0.41$ Å^{-1} and 0.36 Å^{-1}, matching with the momenta inferred from the constant energy maps in the previous section. Note that this MDC is not taken at the Fermi level but at binding energy 80 meV, where the quasi-1D Fermi sheets manifests. In this way, the MDC peaks can directly correspond to the the Fermi sheets shown in Fig. 5.20(e). As these states disperse with a very high velocity towards the Fermi level, the momenta inferred from their peak positions can be used to estimate the corresponding Fermi momenta. The unequal values of the extracted Fermi momenta are due to the fact that the measurements of Fig. 5.20(a, b) were not exactly aligned along $Z-\Gamma-Z$ but slightly away from Γ together with an off-set angle around 5° with respect to the blue dashed line $Z-\Gamma-Z$.

The other two outer peaks in Fig. 5.20(d) correspond to the outer boundaries of the small closed pockets in the middle of the quasi-1D sheets (FS 2). In fact, such outer boundaries are very close to the other pair of quasi-1D sheets in FS 3, as shown in the calculated bands (the outer green and blue branches) Fig. 5.20(c).

The non-dispersive feature right below E_F corresponds to the f-states. The resolution of the present experiments, and the minimum temperature reachable at CASSIOPEE (about 15 K), larger than the Kondo temperature $T_K \approx 8$ K of this material, do not allow us at present to resolve the possible $d-f$ hybridisation gap.

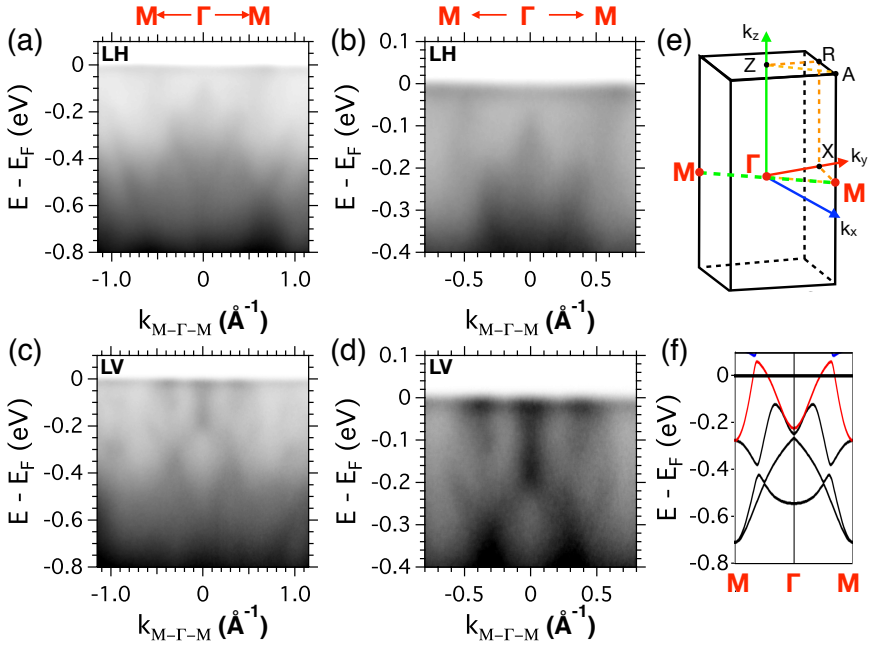

FIGURE 5.21: (a,c) Energy - momentum dispersions along $M-\Gamma-M$ direction measured at $h\nu = 90$ eV and T = 16 K with (a) linear horizontal and (c) linear vertical polarised photons. (b) and (d) are zoom-ins of (a) and (c) respectively over a smaller binding energy range close to E_F. (e) Sketch of the first Brillouin zone. The green dashed line indicates where the Energy - momentum dispersions in panel (a, c) were taken. (f) The DFT calculated bands along $M-\Gamma-M$ [209]. The red band corresponds to FS 1.

M-Γ-M Fig. 5.21(a-d) show the measured ARPES energy-momentum maps along the $M - \Gamma - M$ direction, using linear horizontal and vertical polarisations. Compared to the DFT calculated bands in Fig. 5.21(f), there is an unexpected state around Γ at the Fermi level. Detailed quantitative analysis shown in Fig. 5.22 suggests that this experimentally observed state corresponds to the state detected by the Shubnikov-de Haas quantum oscillation measurements.

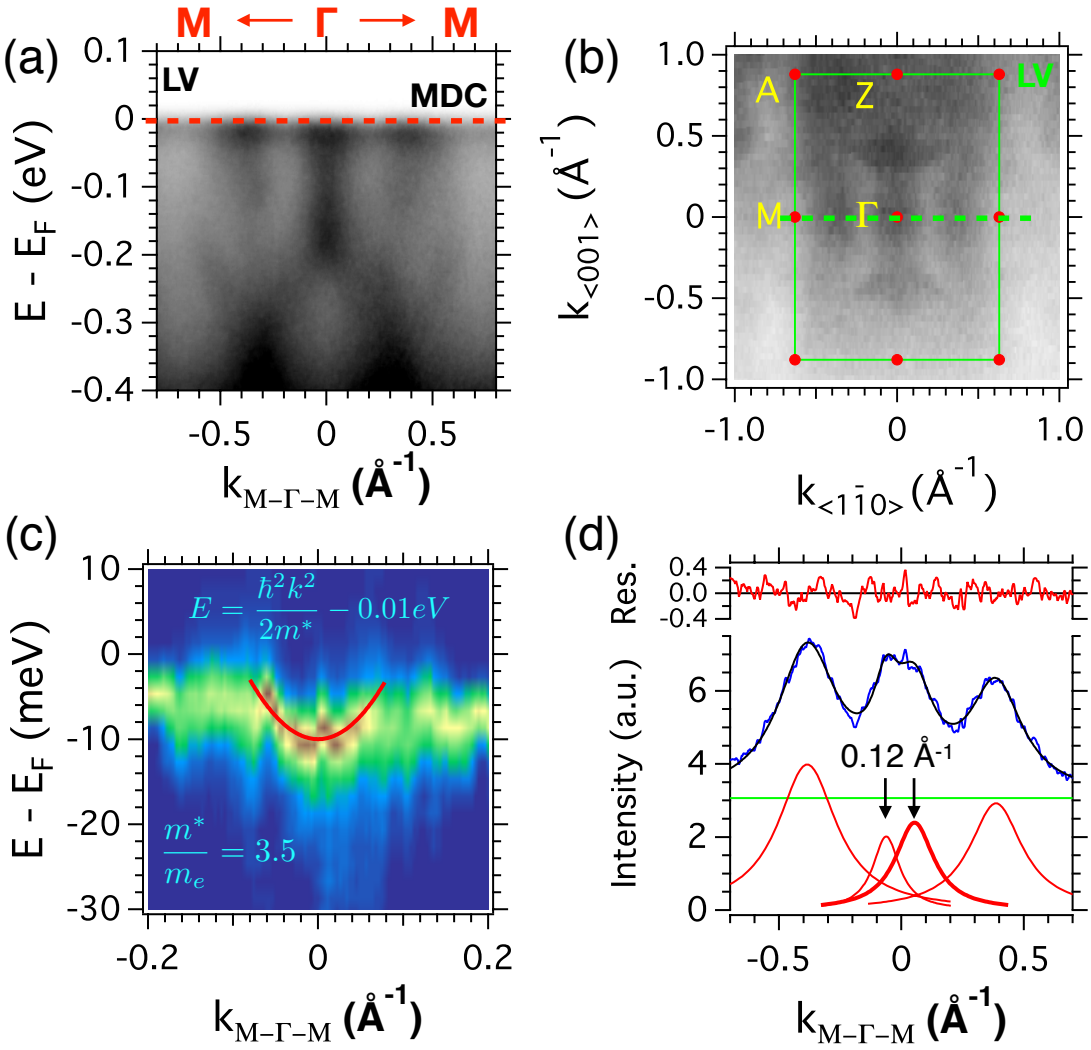

FIGURE 5.22: (a) Energy-momentum dispersion along $M - \Gamma - M$ measured at $h\nu$ = 90 eV and T = 16 K with linear vertical polarised photons. The red dashed line indicates the MDC in panel (d) taken at the Fermi level with an interval ±0.002 eV. (b) The in-plane Fermi surface measured with the same experimental condition as panel (a). The green dashed line indicates where panel (a) was taken. (c) 2D curvature of the state around Γ close to the Fermi level in panel (a). The red curve is a parabolic band with an effective mass $m^* = 3.5m_e$ and the band bottom at binding energy 10 meV. (d) Four Lorentzian peaks (red) and a constant background (green) were used to fit the MDC (blue).

Fig. 5.22 summarises the quantitative analysis of the ARPES state measured around Γ close to the Fermi level as shown in Fig. 5.22(a). First of all, from the in-plane Fermi surface (see Fig. 5.22(b)), we know that the state around Γ forms a small elliptical pocket, such that it is detectable by means of quantum oscillation. Second, the 2D

curvature of this state (see Fig. 5.22(c)) shows a slight dispersion, which can be well approximated with a parabolic function $E = \frac{\hbar^2 k^2}{2m^*} - E_b$ by setting the band bottom binding energy $E_b = 10$ meV and the effective mass $m^* = 3.5m_e$ as determined in the Shubnikov-de Haas quantum oscillation measurements. Third, the four-Lorentzian-peaks fit of the MDC curve (see Fig. 5.22(d)) indicates that the momentum radius along $\Gamma - M$ of the small elliptical pocket is around 0.06 $Å^{-1}$, which is smaller than, but comparable to, the value (0.08 $Å^{-1}$) determined by Shubnikov-de Haas quantum oscillation measurements. Note that close to the Fermi level, the fitted momenta from MDCs tend to be smaller than the real values due to the presence of the Fermi-Dirac distribution and the Gaussian broadening of the measured spectrum. Thus, the overall quantitative analysis suggests that this ARPES measured state around Γ is responsible for the signals measured in the aforementioned Shubnikov-de Haas quantum oscillation measurements.

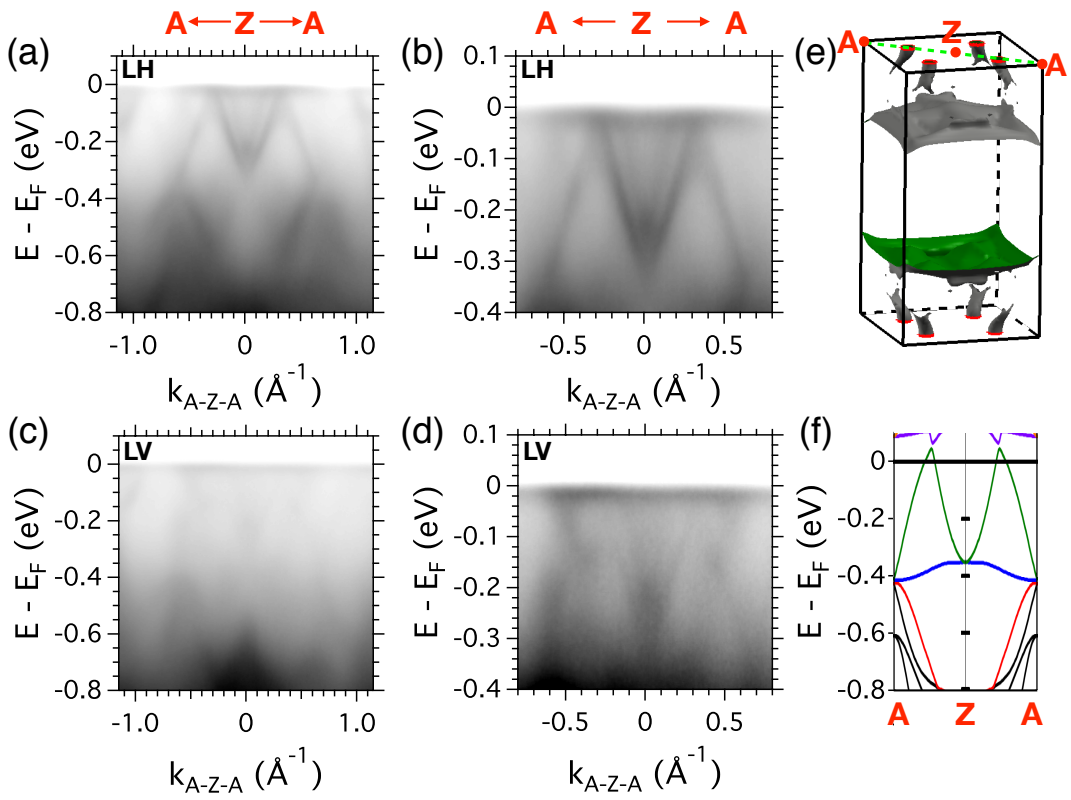

FIGURE 5.23: (a,c) Energy - momentum dispersions along $A - Z - A$ direction measured at $h\nu$ = 90 eV and T = 16 K with (a) linear horizontal and (c) linear vertical polarised photons. (b) and (d) are zoom-ins of (a) and (c) respectively over a smaller binding energy range close to E_F. (e) Sketch of the first Brillouin zone together with the 3rd Fermi surface (FS 3) [209]. The green dashed line indicates where the energy - momentum dispersions were taken. (f) The DFT calculated bands along $A - Z - A$ [209]. The green band corresponds to FS 3 in panel (e) forming small and almost-cylindrical Fermi sheets crossing the $A - Z - R$ top surface of the Brillouin zone perpendicularly.

A - Z - A Fig. 5.23(a-d) show the ARPES energy-momentum map along the $A - Z - A$ line (see Fig. 5.23(e)) for both linear horizontal and vertical polarisations. Compared with the DFT calculated bands in Fig. 5.23(f), the overall qualitative match is

good, except the following differences:

- A localised heavy band right below E_F was observed, presenting increased intensity at the momenta where it crosses the rapidly dispersing bands approaching E_F. This might be an indication of $d-f$ hybridization. Future experiments with higher resolution at lower temperatures should help visualizing the expected Kondo hybridization gap.
- The blue band corresponding to FS 2 in the DFT calculations (see Fig. 5.6(d), or Fig. 5.12(c), or Fig. 5.15(c)), which has a quasi-1D character, was not observed in both LH and LV results.
- The top of the red band corresponding to FS 1 ((see Fig. 5.6(c), or Fig. 5.12(c), or Fig. 5.15(c)) was observed to be at binding energy around 0.35 eV, while it is below 0.4 eV binding energy in the calculated result.
- at the Z points between $k = \pm 0.3$ Å^{-1}, double bands were observed with ARPES, instead of a single band as suggested by the DFT calculation. The unexpected inner bands are most probably due to spin-orbit coupling of Ni 3d-electrons, which was not included in the DFT calculation. Note that the band top of the green states form cylindrical shape Fermi surfaces perpendicular to the $A-Z-R$ plane (see Fig. 5.12(a), Fig. 5.15(a) and Fig. 5.23(e)) suggesting a possible 2D character.

Further quantitative analysis of Fig. 5.23(b), shown in Fig. 5.24(a), was applied by fitting the peaks of a series of EDCs and MDCs as shown in Fig. 5.24(c) and (d). EDCs were taken from -0.17 Å^{-1} to 0.17 Å^{-1} with a step of 0.01 Å^{-1}, and fitted with three Lorentzian peaks plus a Shirley background and a Fermi-Dirac distribution at 16 K. MDCs were taken from binding energy 0.02 eV to 0.22 eV with a step of 0.004 eV, and fitted with four Lorentzian peaks plus a constant background. All the fitted peak positions were plotted in Fig. 5.24(a) as green markers. Note that there is an overlapping interval between EDCs and MDCs, where consistent results were obtained for the two outer branches. These quantitative peak fits capture well the measured band dispersions, and show the double bottom feature, which may suggest the presence of a Rashba spin-orbit coupling of these quasi-2D states.

Assuming that the Rashba spin-orbit coupling comes to play as illustrated in Fig. 5.24(b), the Rashba parameter α can be determined. At a certain momentum k_0, the splitting energy is $2\alpha k_0$, which can be determined from the fit results of the EDC at k_0. For example in Fig. 5.24(c), $k_0 = 0.065$ Å^{-1} and $2\alpha k_0 = 0.109$ eV (the energy difference of the left two peaks), such that $\alpha \approx 0.84$ eV·Å. Similar calculations can be done for other momenta, and the obtained values of α vary between 0.8 and 0.9. Another way to determine α is to divide the energy difference between the band bottoms and the crossing point $\frac{\alpha^2 m^*}{2\hbar^2}$, and the momentum difference between the two band bottoms $\frac{2\alpha m^*}{\hbar^2}$. Based on the overall fit results shown in Fig. 5.24(a), we have $\frac{\alpha^2 m^*}{2\hbar^2} \approx 0.028$ eV and $\frac{2\alpha m^*}{\hbar^2} \approx 0.13$ Å^{-1}. Thus, $\alpha \approx 0.86$ eV·Å, being consistent with the results obtained from EDCs.

The Rashba parameter determined in $YbNi_4P_2$ is much larger than the typical values of most semiconductors, and is around one sixth of the values in giant Rashba effect bulk crystals such as BiTeI [229] or ferroelectric GeTe [230] (about 5 eV·Å^{-1}), suggesting the spin-orbit coupling is sizeable in $YbNi_4P_2$, thus needs to be included in the DFT calculation in order to characterise the electronic structure and understand its unique transport properties.

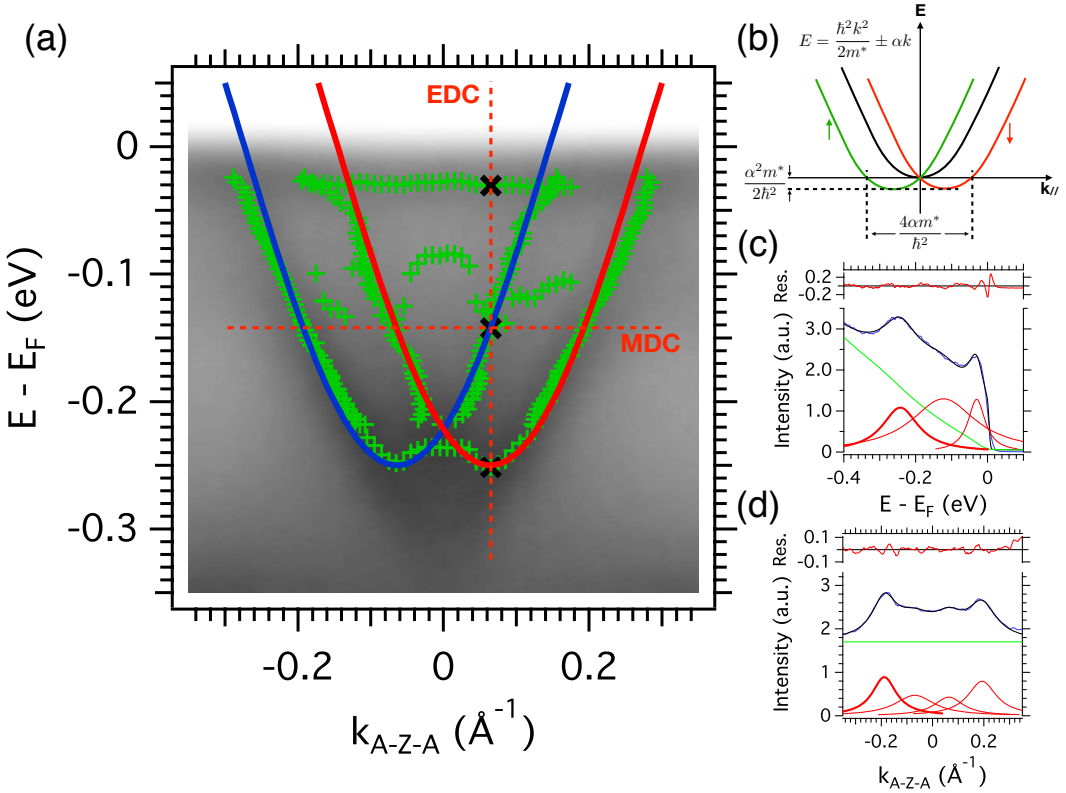

FIGURE 5.24: (a) Energy - momentum dispersions along $A-Z-A$ direction measured at $h\nu$ = 90 eV and T = 16 K with the linear horizontal polarised photons. Green markers indicate peak positions fitted in EDCs and MDCs, as demonstrated in panel (c) and (d). The red and blue curves follow cosine functions $E = -0.25cos[7.5(k \pm 0.064)]$, representing a pair of bands split due to Rashba spin-orbit coupling, as illustrated in panel (b). The dashed lines show where the typical EDC and MDC shown in panel (c) and (d) were taken. (b) An illustration of the band splitting due to a Rashba type spin-orbit coupling with a Rashba parameter α. A parabolic band was used because the bottom of a cosine band can be approximated as a parabolic band. (c) A typical EDC (the integration interval is ± 0.005 Å^{-1}) of panel (a) with a three-Lorentzian-peaks fit in order to extract the band dispersion information quantitatively. Fitted peak positions are plotted in panel (a) as green markers. A Shirley background (the green curve) was used in the fit. (d) A typical MDC (the integration interval is ± 0.002 eV) of panel (a) with a four-Lorentzian-peaks fit in order to extract the band dispersion information quantitatively. Fitted peak positions are plotted in panel (a) as green markers. A constant background (the green curve) was used in the fit.

5.3 Discussion

5.3.1 Fermi surface nesting

The Fermi surface nesting is always present in a 1D system leading to a gap opening at the Fermi level [231,232], which could explain why the quasi-1D Fermi sheets were best observed tens of meV below, instead of exactly at, the Fermi level. However, the $d-f$ hybridisation has a similar effect, opening a gap and pushing down the conducting bands. With the present energy resolution and the data acquired at a

constant temperature, we cannot separate these effects or tell which one is dominant.

5.3.2 Orbital parity analysis

The in-plane constant energy maps measured with LH polarisation (see Fig. 5.11 and Fig. 5.14) showed strong left-right asymmetry respect to the normal emission angle, while the ones measured with LV polarisation were completely symmetric. As aforementioned, this kind of strong geometrical factors (orientation of the light electric field with respect to the surface) in the photoemission matrix elements, usually indicate a very marked orbital character (here in $YbNi_4P_2$, $3d$ orbitals) of the electronic structure. A simple orbital parity analysis without considering the spin degeneracy is given below. However, in most of the cases, these conducting states are not purely of e_g and t_{2g} character. Further information of the orbital characters of the 5 individual Fermi surfaces are needed from the theoretical calculation.

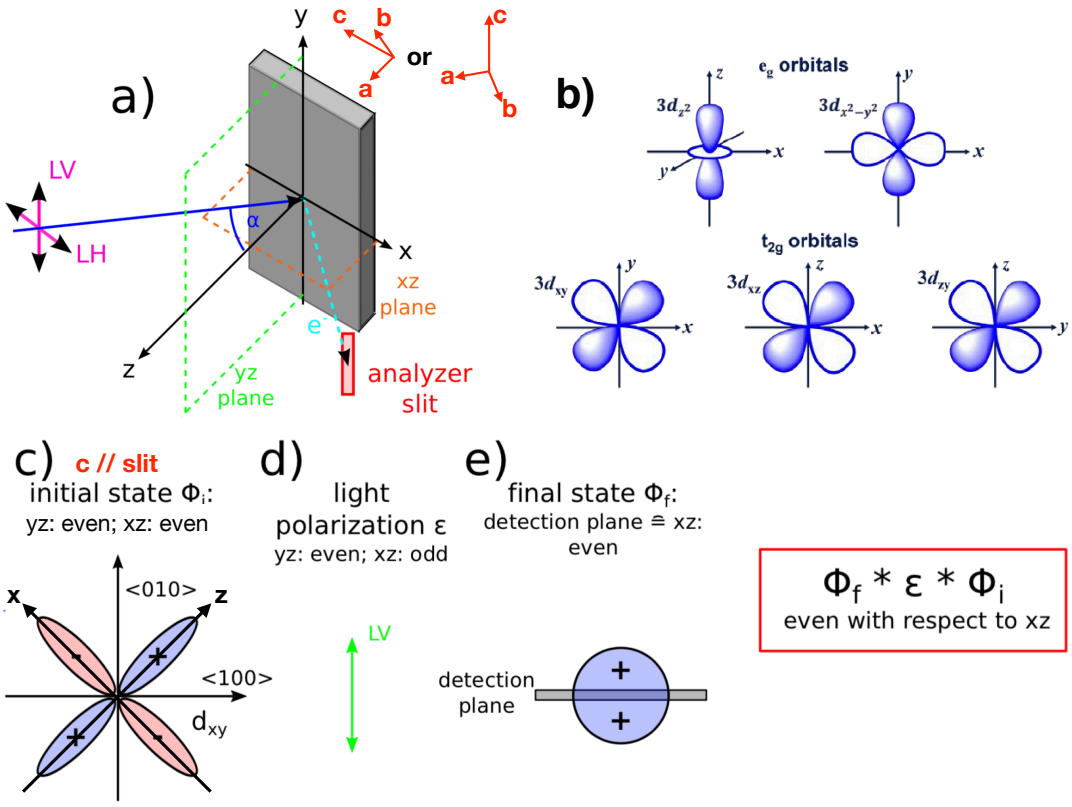

FIGURE 5.25: (a) Sketch showing the ARPES setup including sample, incidence photon & photo-electron beams, detector slit, the xz & yz planes and the direction of linear horizontal and vertical polarisations. Adapted from Ref. [185]. Specifically in our case for $YbNi_4P_2$, the surface direction is (110), and the quasi-1D chain (c axis) can be aligned along y or x, as illustrated by the two red systems of coordinates. (b) Sketch of the 5 d-orbital states. Note that the $x-y-z$ coordinates in panel (b) are identical to the $a-b-c$ lattice coordinates, instead of the $x-y-z$ coordinates shown in panel (a). The positive and negative wave function phases are indicated as blue and white. Adapted from Ref. [186]. (c) Parity of the initial state Φ_i (d_{xy}) with the quasi-1D chain (c axis) parallel to the detector slit (y axis). (d) Parity of the light polarisation $\vec{\epsilon}$ (LV). (e) Parity of the final state with respect to the detection plane. Adapted from Ref. [2].

As introduced in Chapter 2, the photocurrent I depends on the so-called matrix element $|M_{fi}|^2$:

$$I \propto |M_{fi}|^2. \tag{5.2}$$

The matrix element $|M_{fi}|^2$ describes the optical transition of the photoelectron using one electron wave functions and is proportional to

$$|M_{fi}|^2 \propto \int dr^3 \Phi_f(\vec{r}) \vec{\epsilon} \vec{r} \Phi_i(\vec{r}), \tag{5.3}$$

where $\Phi_f(\vec{r})$ is the final-state wave function of the photo-electrons, $\vec{\epsilon}$ is the light polarisation vector, and $\Phi_i(\vec{r})$ is the initial-state wave function of electrons. For a non-zero matrix element, the product $\Phi_f(\vec{r})\ \vec{\epsilon}\ \Phi_i(\vec{r})$ needs to be an even function with respect to mirror planes defined by the crystal lattice of the sample and the geometry of the measurement.

As illustrated in Fig. 5.25(a), two mirror planes xz and yz can be defined. The parity of $\Phi_f(\vec{r})$, $\vec{\epsilon}$ (LH or LV) and $\Phi_i(\vec{r})$ (here the five $3d$-orbital states as shown in Fig. 5.25(b)) can also be determined, as exampled in Fig. 5.25(c-e). If detecting electrons emitted in (or close to) the planes defined by the mirror plane, the final state needs to be even with respect to that mirror plane (otherwise its wave-function would vanish in all points along that plane, and the state cannot be detected). Thus, the initial state is required to have the same parity as the polarisation with respect to the same mirror plane, in order to be detected. Note that at the normal emission position, detectable initial states should have the same parity as the polarisation with respect to both xz and yz mirror planes.

The parity analysis and detectable $3d$ orbital states with each polarisation are listed in Tab. 5.2 with the quasi-1D chain (c axis) aligned along the detector slit direction (y axis), and in Tab. 5.3 with the c axis aligned along the x axis.

	xz	yz
LH_x (xz: even; yz: odd)	d_{z^2}, $d_{x^2-y^2}$, d_{xy} (even)	$d_{x^2-y^2}$ (odd)
LH_z (xz: even; yz: even)	d_{z^2}, $d_{x^2-y^2}$, d_{xy} (even)	d_{z^2}, d_{xy} (even)
LV (xz: odd; yz: even)	d_{xz}, d_{yz} (odd)	d_{z^2}, d_{xy} (even)

TABLE 5.2: The quasi-1D chain (c axis) is aligned parallel to the detector slit direction (y axis). The parity of light polarisations (LH_x, LH_z and LV) with respect to xz and yz mirror planes is given in the first column. Detectable orbital states having the same parity as the polarisation with respect to xz (yz) mirror planes are given in the second (third) column. Note that the subscripts of the $3d$ orbitals x, y and z refer to the crystal coordinate $a-b-c$, instead of the $x-y-z$ coordinate shown in Fig. 5.25(a), which is used for the naming of the mirror planes xz and yz, and LH components LH_x and LH_z.

Relating this parity analysis with the measured Fermi surfaces with different polarisations and orientations of the sample, the possibilities of the orbital character of each Fermi sheet can be limited. For example, the quasi-1D sheets were mainly observed with LH polarisation and were not observable with LV polarisation, suggesting that these quasi-1D sheets are mainly composed of d_{z^2} and/or d_{xy} orbital states. Thus, along the quasi-1D chain, only σ and/or δ binding interactions are possible.

	xz	yz
LH_x (xz: even; yz: odd)	d_{z^2}, d_{xy} (even)	d_{xz}, d_{yz} (odd)
LH_z (xz: even; yz: even)	d_{z^2}, d_{xy} (even)	d_{z^2}, $d_{x^2-y^2}$, d_{xy} (even)
LV (xz: odd; yz: even)	$d_{x^2-y^2}$ (odd)	d_{z^2}, $d_{x^2-y^2}$, d_{xy} (even)

TABLE 5.3: The quasi-1D chain (c axis) is aligned parallel to x axis. The parity of light polarisations (LH_x, LH_z and LV) with respect to xz and yz mirror planes is given in the first column. Detectable orbital states having the same parity as the polarisation with respect to xz (yz) mirror planes are given in the second (third) column. Note that the subscripts of the $3d$ orbitals x, y and z refer to the crystal coordinate $a-b-c$, instead of the $x-y-z$ coordinate shown in Fig. 5.25(a), which is used for the naming of the mirror planes xz and yz, and LH components LH_x and LH_z.

5.4 Conclusion and Perspective

In this chapter, after recalling the transport experimental studies and theoretical calculations on $YbNi_4P_2$, a thorough characterisation of $YbNi_4P_2$'s electronic structure in the paramagnetic phase by means of ARPES, has been presented.

From the ARPES determined topography of the Fermi surfaces (both in-plane and out-of-plane), the quasi-1D character of the electronic structure has been confirmed for the first time in a ferromagnetic quantum-critical material, as expected from its quasi-1D lattice structure. This quasi-1D character is not only important to understand the anisotropic behaviours in transport properties, such as the resistance and the magnetic susceptibility, but also important in the formation of the ferromagnetic quantum criticality, which is not allowed in 2D or 3D systems.

Besides the confirmation of the quasi-1D Fermi sheets (FS 2 and FS 3), quasi-2D (parts of FS 3) or 3D (FS 1, FS 4 and FS 5) Fermi sheets were also clearly observed and characterised. The ARPES determined pocket sizes of these closed contours match quantitatively with the calculated results. Further quantum oscillation experiments are needed to compare with. Additionally, an unexpected (from the DFT calculation) closed small Fermi surface pocket centred at Γ was observed. The further quantitative analysis suggests that it is responsible for the oscillation signals in the Shubnikov-de Haas measurements shown in Ref. [209].

The ARPES measured high-resolution band dispersions along high symmetric directions ($A-Z-A$, $M-\Gamma-M$ and $Z-\Gamma-Z$), confirm the existence of the heavy $4f$ bands close to the Fermi level. On the other hand and more importantly, the quantitative analysis of the deviation from the calculated band dispersions suggests that strong spin-orbit coupling (SOC) and $d-f$ hybridisation are present in $YbNi_4P_2$, and are thus important to understand the properties of $YbNi_4P_2$ as suggested by the previous transport measurements.

Future ARPES experiments should focus on the Kondo hybridisation gap, to reveal if the quasi-1D Fermi sheets have strong f character. Spin-resolved ARPES experiments will also help to clarify the existence of the strong SOC, especially in the dispersion along $A-Z-A$ where the Rashba type SOC seems to be observed.

The protocol used in the study of $YbNi_4P_2$ can be applied to the As doped compounds in order to probe and characterise the evolution of the electronic structure at finite temperature above the ferromagnetic quantum phase transition as the next step in studying by ARPES this heavy Fermion system.

The surface preparation method can also be generalised to many other types of samples that are hard or impossible to cleave, thus opening a new window of opportunities for ARPES measurements in complex materials.

Appendix A

Résumé en français

Dans le cadre de cette thèse, j'ai travaillé dans l'équipe «Systèmes fortement corrélés et nouveaux états électroniques de la matière» au CSNSM à Orsay. Au cours de la préparation de ma thèse, j'ai étudié plusieurs systèmes électroniques de faible dimension, qui composent le corps principal de cette thèse: le systèmes électronique à deux dimensions (2DES) à la surface (110) de SnO_2, les états de surface topologiques dans une famille de Métaux topologiques 3D M_2Te_2X (avec M = Ti, Zr ou Hf et X = P ou As), et le système de Fermions lourds quasi-1D $YbNi_4P_2$ montrant la criticité quantique ferromagnétique. Le principal outil expérimental que j'ai utilisé est la spectroscopie par photoémission résolue en angle (ARPES). La plupart des données présentées dans cette thèse ont été obtenues dans des synchrotrons modernes (station ARPES haute résolution CASSIOPÉE au le synchrotron SOLEIL; ligne de lumière ARPES BL-2A de la Photon Factory dans le Synchrotron KEK à Tsukuba Japon; station ARPES résolue en spin ESPRESSO au Synchrotron HiSOR à Hiroshima).

1. Concepts d'introduction

Dans le premier chapitre, je présente les concepts de base nécessaires à la compréhension du travail expérimental qui en découle.

La section 1.1 passe brièvement en revue l'évolution de l'étude des systèmes électroniques à deux dimensions à la surface/interface des oxydes depuis la découverte du 2DES à l'interface $LaAlO_3/SrTiO_3$. Lors de l'exploration de tels 2DES à la surface d'oxydes de métaux de transition, en particulier de $SrTiO_3$, de nouvelles méthodes de compréhension ont été développées pour la création et le contrôle de 2DES à la surface et / ou à l'interface d'oxydes.

La section 1.2 présente une introduction pédagogique au développement de concepts de topologie en physique de la matière condensée, qui ont finalement conduit au développement et à la découverte de matériaux topologiques en 3D. Les concepts de base, tels que les invariants Z_2 $(\nu_0; \nu_1, \nu_2, \nu_3)$, le moment invariant par inversion du temps (TRIM) et le verrouillage du moment de rotation, sont couverts.

La section 1.3 présente les systèmes de Fermion lourds et les transitions de phase quantiques possibles. Le diagramme de phase des matériaux de Fermion lourds, la résonance Kondo à basse température et la criticité quantique associée à un paramètre

externe à 0 K sont brièvement décrits. De plus, étant donné que le matériau à fermions lourds étudié dans cette thèse, $YbNi_4P_2$, est un système quasi-1D, la relation entre la topographie de la surface de Fermi et la dimensionnalité d'un système électronique donné est présentée à la fin de cette section.

La section 1.4 introduit la théorie de l'interaction électron-phonon, qui est une source d'information importante pour l'analyse de données pertinente. La fonction d'Eiliashberg et le modèle de phonon de Debye sont les outils théoriques que j'ai utilisés pour l'analyse de l'interaction électron-phonon dans les 2DES.

La section 1.5 présente une introduction pédagogique au couplage spin-orbite dans les solides. Deux types typiques de couplage spin-orbite, Dresselhaus et Rashba, sont discutés.

2. Techniques expérimentales

ARPES est le principal outil expérimental que j'ai utilisé tout au long de mon travail de doctorat. Après une brève introduction à l'ARPES basée sur le modèle en 3 étapes (sous-section 2.1.1), je présente deux travaux originaux, l'étude de l'interaction électron-phonon dans le 2DES à la surface du ZnO (sous-section 2.1.2) et l'étude du couplage spin-orbite dans la bande de valence de ZnTe (sous-section 2.1.3), afin de démontrer le pouvoir de l'ARPES pour la résolution des interactions au sein de systèmes électroniques, outre sa capacité à sonder directement les dispersions de bandes. Dans le cas du ZnO, la self-énergie proche du niveau de Fermi est extraite de manière cohérente et comparée à celle d'un modèle de Debye pour l'interaction électron-phonon. Dans le cas ZnTe, le dédoublement de la bande de valence due au couplage spin-orbite est observée avec ARPES et en parfait accord avec les résultats du calcul DFT.

L'ARPES résolu en spin (SARPES) constitue une technique complémentaire importante dans l'étude des textures de spin des états de surface topologiques dans les métaux topologiques 3D Ti_2Te_2P et Hf_2Te_2P. Une brève introduction au SARPES basée sur la machine ESPRESSO du synchrotron HiSOR au Japon, qui utilise le détecteur de diffraction électronique à très basse énergie (VLEED) (une plaque de Fe à surface oxydée), est donnée dans la section 2.2.

La section 2.3 présente d'autres techniques expérimentales supplémentaires, l'épitaxie par jet moléculaires (MBE) et la diffraction électronique à basse énergie (LEED). La MBE sert à déposer des métaux réducteurs, tels que Al et Eu, sur les surfaces des échantillons, tandis que le LEED est utilisé pour contrôler la propreté et la qualité cristalline de la surface préparée.

3. Oxides: SnO_2 et $FeTiO_3$

Dans le troisième chapitre, j'ai étudié deux oxydes à l'aide d'ARPES principalement: SnO_2 (section 3.1) et $FeTiO_3$ (section 3.2).

Pour SnO_2, nous avons découvert un système électronique à deux dimensions (2DES) à sa surface nue (110) et caractérisons ses structures électroniques à $T = 16\,K$ en utilisant ARPES (sous-section 3.1.2). Il s'agit du premier 2DES réalisé dans un oxyde à structure rutile.

Il a été démontré que la densité de porteurs de ce 2DES pouvait être ajustée via une variation de température réversible jusqu'à la température ambiante ou un dopage en surface avec des lacunes en oxygène créées par une réaction rédox avec des métaux réducteurs évaporés à sa surface, tels que Al ou Eu (sous-section 3.1.3). Les expériences avec le recouvrement métallique conduisant à une réaction rédox révèlent également que les lacunes en oxygène à la surface peuvent doper le minimum de la bande de conduction, nous aidant ainsi à comprendre l'origine du 2DES observé et le développement de la conductivité de type n dans SnO_2 (sous-section 3.1.6), qui fait l'objet d'une longue discussion dans les recherches sur SnO_2.

De plus, nous trouvons que ce 2DES est robuste contre la reconstruction de surface 4×1 ou les impuretés de surface (sous-section 3.1.4), car un 2DES similaire peut être observé sur une surface "sale" sans aucun traitement de nettoyage de surface préalable.

Une analyse quantitative, telle que l'ajustement du niveau fondamental, la modélisation de puits quantiques et la modulation d'intensité des surfaces de Fermi hors du plan, est présentée à la sous-section 3.1.5. L'ajustement du niveau fondamental confirme la formation de Sn métallique. La modélisation par puits quantiques suggère que le 2DES se trouve à 2-3 cellules unitaires (environ 18 Å) sous la surface. La modulation d'intensité des surfaces de Fermi hors du plan est liée au confinement potentiel du puits quantique, en parfait accord avec le résultat obtenu à partir de la modélisation du puits quantique.

Pour $FeTiO_3$, nous avons réussi à mesurer pour la première fois la structure électronique (principalement les bandes de valence) dans sa phase paramagnétique à une température $T = 72$ K (sous-section 3.2.2). Plus précisément, le sommet de la bande de valence au niveau/proche du niveau de Fermi a été sondé et utilisé pour caractériser la transition de phase magnétique de la phase paramagnétique à haute température à la phase antiferromagnétique à basse température (sous-section 3.2.2). La température de Néel déterminée par spectroscopie par photoémission est d'environ 52 K, ce qui est en bon accord avec les études de transport précédentes.

4. Métaux topologiques 3D: (Ti, Zr, Hf)$_2$Te$_2$(P, As)

Ces dernières années, le concept d'isolant topologique 3D a été généralisé, des isolants aux semi-métaux, voire aux métaux. M_2Te_2X (avec M = Ti, Zr ou Hf et X = P ou As) est une nouvelle famille de métaux topologiques de la famille des tétradymites avec le couplage spin-orbite systématiquement accordé par un élément remplaçant Ti $\rightarrow$ Zr $\rightarrow$ Hf) et P $\rightarrow$ As (augmentation de la force du couplage spin-orbite).

Après clivage des échantillons, nous avons mesuré les surfaces de Fermi (à la fois dans le plan et hors du plan) et les dispersions de bandes le long de la direction $\bar{K} - \bar{\Gamma} - \bar{K}$ à $\bar{\Gamma}$ et le long de $\bar{K} - \bar{M} - \bar{K}$ à $\bar{M}$, qui confirment l'existence d'états de surface de Dirac sans masse en $\bar{M}$ dans la zone de Brillouin projetée sur la surface, et montrent un excellent accord avec les calculs de la théorie de la densité fonctionnelle (DFT) et l'analyse de parité basée sur les calculs DFT (section 4.1).

Une analyse plus poussée des données de surface de Fermi révèle que les arcs de nœuds de Dirac centrés sur les points $\bar{M}$ de la zone de Brillouin projetée sur la surface et s'étendant dans la direction $\bar{\Gamma} - \bar{M}$ (section 4.2) existent généralement dans les 4 composés (Ti, Zr, Hf)$_2$Te$_2$P et Zr$_2$Te$_2$As, quelle que soit la force du couplage spin-orbite ou les caractères topologiques forts/faibles. D'autre part, la force du couplage spin-orbite modifie la taille des poches de Fermi aux points $\bar{\Gamma}$ de la zone de Brillouin réduite, l'énergie de liaison des points de croisement de Dirac aux points $\bar{M}$ et les largeurs des espaces hébergeant la surface topologique des états aux points $\bar{M}$.

En se concentrant sur l'arc de nœud de Dirac, dans la section 4.3, nous avons utilisé l'ARPES résolue en spin (SARPES), spécifiquement un instrument appelée ESPRESSO basée au centre de rayonnement synchrotron de Hiroshima au Japon, afin de sonder la texture de spin des états de surface topologiques de type Dirac à points $\bar{M}$ dans Ti$_2$Te$_2$P et Hf$_2$Te$_2$P. Nos résultats expérimentaux résolus en spin de ces états de surface topologiques démontrent le verrouillage entre le spin et le vecteur d'onde, rappelant ainsi le fameux 3D exemple d'isolant topologique Bi$_2$Se$_3$.

De plus, nous avons échantillonné les points le long de l'arc de nœud de Dirac dans Ti$_2$Te$_2$P et appliqué les mesures ARPES résolues en spin. Il apparaît alors que l'arc de nœud de Dirac est également «hélicoïdal», c'est-à-dire que chaque point de Dirac faisant partie d'un tel arc correspond à un état de surface topologique hélicoïdal.

La section 4.4 traite de plusieurs aspects liés à cette famille de métaux topologiques 3D. La réalisation possible de la supraconductivité topologique induite par la possible supraconductivité non conventionnelle due à l'inversion de bande de type d-p ou p-p dans ces métaux topologiques fait de ces matériaux une plateforme pour le futur calcul quantique. La propriété de transport particulière possible de l'arc de nœuds de Dirac en raison de son anisotropie particulière, c'est-à-dire en raison de sa dispersion sans masse le long de $\bar{K} - \bar{M}$ mais avec masse le long de $\bar{\Gamma} - \bar{M}$ conduit à un canal conducteur topologique naturel quasi-1D, d'où émergent les fermions de Majorana. Les caractères topologiques faibles et forts accordés par la force du couplage spin-orbite pourraient être liés à la qualité de la cristallisation et à la qualité de la surface après clivage, par le biais d'interactions entre couches faibles et fortes correspondantes. Les états de surface polarisés en spin aux points de moment non symétriques peuvent conduire à des textures de spin complexes, par exemple des polarisations de spin hors du plan.

5. Matériau unidimensionnel à fermions lourds: $YbNi_4P_2$

$YbNi_4P_2$ est un matériau à fermion lourd quasi-unidimensionnel, qui présente une transition criticité quantique ferromagnétique à 0 K par dopage As. Après un bref examen de plusieurs propriétés de transport typiques de $YbNi_4P_2$ (résonance Kondo, transition ferromagnétique du second ordre, anisotropie de la résistance électrique et de la susceptibilité magnétique et du comportement de sa résistance aux basses températures dans un liquide non de Fermi), et des calculs DFT calculs de sa structure électronique sans prendre en compte le couplage spin-orbite et la présence de la bande lourde Yb $5f$ proche du niveau de Fermi (section 5.1), je présente une caractérisation systématique de sa structure électronique au moyen d'ARPES (section 5.2), qui peut être séparé en deux parties.

La première partie de la caractérisation de la structure électronique (sous-section 5.2.2), axée sur les topographies des surfaces de Fermi, démontre explicitement le caractère quasi unidimensionnel de la structure électronique de $YbNi_4P_2$, qui est non seulement importante pour comprendre son fort comportement de transport anisotrope, mais également cruciale pour l'apparition de la transition critique quantique ferromagnétique du deuxième ordre, car dans les systèmes métalliques propres à deux ou trois dimensions, la criticité quantique ferromagnétique sera remplacée par une transition ferromagnétique du premier ordre ou par la formation de phases supraconductrices phases magnétiques non homogènes.

Outre la confirmation d'une paire de feuilles de Fermi plates et parallèles présentant le caractère quasi unidimensionnel, les autres surfaces de Fermi (en bloc ou quasi-deux dimensions) peuvent également être identifiées en comparant les surfaces de Fermi mesurées par ARPES et les surfaces de Fermi calculées par DFT. Les tailles des poches fermées de Fermi extraites des résultats de mesure ARPES sont comparables aux résultats de calcul DFT. Des mesures d'oscillation quantique futures peuvent être appliquées pour sonder ces poches fermées à la surface de Fermi et pour comparer avec les résultats de mesure ARPES.

La deuxième partie de la caractérisation de la structure électronique (sous-section 5.2.3) présente les dispersions énergie-impulsion mesurées le long de directions de symétrie élevées ($Z-\Gamma-Z$, $M-\Gamma-M$ and $A-Z-A$) dans la première zone de Brillouin et leur comparaison avec les bandes correspondantes calculées par DFT. L'analyse quantitative de ces dispersions nous aide à comprendre certaines feuilles de Fermi inattendues à partir de calculs DFT, et suggère surtout les empreintes de l'hybridation $d-f$ et la présence d'un fort couplage spin-orbite, qui sont importants pour comprendre les exposants de loi de puissance inattendus dans quantités thermodynamiques indiquant la présence de fortes fluctuations critiques quantiques ferromagnétiques. L'hybridation $d-f$, malheureusement, ne peut pas être directement sondée avec les expériences ARPES que nous avons utilisés en raison du fait que le gap provoqué par l'hybridation $d-f$ est inférieur à 1 mV bien plus petit que la résolution de nos expériences ARPES. Par contre, le couplage spin-orbite montre une forte influence

sur la dispersion des bandes dans la direction $A - Z - A$, qui contient deux bandes paraboliques observées au lieu d'une seule selon le calcul de la DFT. Un modèle de couplage spin-orbite de type Rashba est ensuite utilisé pour estimer la force du couplage spin-orbite. La valeur déterminée de la force de couplage spin-orbite est d'environ 0.85 eV·Å, ce qui est relativement grand par rapport à la plupart des matériaux existants.

Bibliography

[1] Emmanouil Frantzeskakis, Tobias Chris Rödel, Franck Fortuna, and Andrés Felipe Santander-Syro. 2D surprises at the surface of 3D materials: Confined electron systems in transition metal oxides. *Journal of Electron Spectroscopy and Related Phenomena*, 219:16–28, 2017.

[2] Tobias Rödel. *Two-dimensional electron systems in functional oxides studied by photoemission spectroscopy*. PhD thesis, Université Paris-Sud, 2016.

[3] K. v. Klitzing, Gerhard Dorda, and Michael Pepper. New method for high-accuracy determination of the fine-structure constant based on quantized Hall resistance. *Physical Review Letters*, 45(6):494, 1980.

[4] Robert B. Laughlin. Quantized Hall conductivity in two dimensions. *Physical Review B*, 23(10):5632, 1981.

[5] Daniel C. Tsui, Horst L. Stormer, and Arthur C. Gossard. Two-dimensional magnetotransport in the extreme quantum limit. *Physical Review Letters*, 48(22):1559, 1982.

[6] B. Andrei Bernevig, Taylor L. Hughes, and Shou-Cheng Zhang. Quantum spin hall effect and topological phase transition in HgTe quantum wells. *Science*, 314(5806):1757–1761, 2006.

[7] A. Ohtomo and H. Y. Hwang. A high-mobility electron gas at the $LaAlO_3/SrTiO_3$ heterointerface. *Nature*, 427(6973):423, 2004.

[8] Jochen Mannhart and D. G. Schlom. Oxide interfaces - an opportunity for electronics. *Science*, 327(5973):1607–1611, 2010.

[9] Hidenori Takagi and Harold Y. Hwang. An emergent change of phase for electronics. *Science*, 327(5973):1601–1602, 2010.

[10] Harold Y. Hwang, Yoh Iwasa, Masashi Kawasaki, Bernhard Keimer, Naoto Nagaosa, and Yoshinori Tokura. Emergent phenomena at oxide interfaces. *Nature materials*, 11(2):103, 2012.

[11] A. D. Caviglia, Stefano Gariglio, Nicolas Reyren, Didier Jaccard, T. Schneider, M. Gabay, S. Thiel, G. Hammerl, Jochen Mannhart, and J.-M. Triscone. Electric field control of the $LaAlO_3/SrTiO_3$ interface ground state. *Nature*, 456(7222):624, 2008.

[12] Alexander Brinkman, Mark Huijben, M. Van Zalk, J. Huijben, U. Zeitler, J. C. Maan, Wilfred Gerard van der Wiel, G. J. H. M. Rijnders, David H. A. Blank, and H. Hilgenkamp. Magnetic effects at the interface between non-magnetic oxides. *Nature materials*, 6(7):493, 2007.

[13] D. A. Dikin, M. Mehta, C. W. Bark, C. M. Folkman, C. B. Eom, and Venkat Chandrasekhar. Coexistence of superconductivity and ferromagnetism in two dimensions. *Physical Review Letters*, 107(5):056802, 2011.

[14] Lu Li, Christoph Richter, Jochen Mannhart, and R. C. Ashoori. Coexistence of magnetic order and two-dimensional superconductivity at $LaAlO_3/SrTiO_3$ interfaces. *Nature physics*, 7(10):762, 2011.

[15] Julie A. Bert, Beena Kalisky, Christopher Bell, Minu Kim, Yasuyuki Hikita, Harold Y. Hwang, and Kathryn A. Moler. Direct imaging of the coexistence of ferromagnetism and superconductivity at the $LaAlO_3/SrTiO_3$ interface. *Nature physics*, 7(10):767, 2011.

[16] Stefan Thiel, German Hammerl, A. Schmehl, C. W. Schneider, and Jochen Mannhart. Tunable quasi-two-dimensional electron gases in oxide heterostructures. *Science*, 313(5795):1942–1945, 2006.

[17] Naoyuki Nakagawa, Harold Y. Hwang, and David A. Muller. Why some interfaces cannot be sharp. *Nature materials*, 5(3):204, 2006.

[18] Alexey Kalabukhov, Robert Gunnarsson, Johan Börjesson, Eva Olsson, Tord Claeson, and Dag Winkler. Effect of oxygen vacancies in the $SrTiO_3$ substrate on the electrical properties of the $LaAlO_3$/ $SrTiO_3$ interface. *Physical Review B*, 75(12):121404, 2007.

[19] E. Slooten, Zhicheng Zhong, H. J. A. Molegraaf, P. D. Eerkes, S. De Jong, F. Massee, E. Van Heumen, M. K. Kruize, Sander Wenderich, J. E. Kleibeuker, et al. Hard x-ray photoemission and density functional theory study of the internal electric field in $SrTiO_3/LaAlO_3$ oxide heterostructures. *Physical Review B*, 87(8):085128, 2013.

[20] A. F. Santander-Syro, O. Copie, T. Kondo, F. Fortuna, S. Pailhes, R. Weht, X. G. Qiu, F. Bertran, A. Nicolaou, A. Taleb-Ibrahimi, et al. Two-dimensional electron gas with universal subbands at the surface of $SrTiO_3$. *Nature*, 469(7329):189, 2011.

[21] C. Bareille, F. Fortuna, T. C. Rödel, F. Bertran, M. Gabay, O. Hijano Cubelos, A. Taleb-Ibrahimi, P. Le Fèvre, M. Bibes, A. Barthélémy, et al. Two-dimensional electron gas with six-fold symmetry at the (111) surface of $KTaO_3$. *Scientific reports*, 4:3586, 2014.

[22] S. Moser, Luca Moreschini, J. Jaćimović, O. S. Barišić, Helmuth Berger, Arnaud Magrez, Y. J. Chang, Keun Su Kim, A. Bostwick, E. Rotenberg, et al. Tunable polaronic conduction in anatase TiO_2. *Physical review letters*, 110(19):196403, 2013.

[23] W. Meevasana, P. D. C. King, R. H. He, S. K. Mo, M. Hashimoto, Anna Tamai, P. Songsiriritthigul, Félix Baumberger, and Z. X. Shen. Creation and control of a two-dimensional electron liquid at the bare $SrTiO_3$ surface. *Nature materials*, 10(2):114, 2011.

[24] A. F. Santander-Syro, C. Bareille, F. Fortuna, O. Copie, M. Gabay, F. Bertran, A. Taleb-Ibrahimi, P. Le Fèvre, G. Herranz, N. Reyren, et al. Orbital symmetry reconstruction and strong mass renormalization in the two-dimensional electron gas at the surface of $KTaO_3$. *Physical Review B*, 86(12):121107, 2012.

[25] P. D. C. King, R. H. He, T. Eknapakul, P. Buaphet, S.-K. Mo, Y. Kaneko, S. Harashima, Y. Hikita, M. S. Bahramy, C. Bell, et al. Subband structure of a two-dimensional electron gas formed at the polar surface of the strong spin-orbit perovskite $KTaO_3$. *Physical review letters*, 108(11):117602, 2012.

[26] T. C. Rödel, F. Fortuna, F. Bertran, M. Gabay, M. J. Rozenberg, A. F. Santander-Syro, and P. Le Fèvre. Engineering two-dimensional electron gases at the (001) and (101) surfaces of TiO_2 anatase using light. *Physical Review B*, 92(4):041106, 2015.

[27] S. McKeown Walker, Alberto De La Torre, Flavio Yair Bruno, Anna Tamai, T. K. Kim, M. Hoesch, M. Shi, M. S. Bahramy, P. D. C. King, and Félix Baumberger. Control of a two-dimensional electron gas on $SrTiO_3$ (111) by atomic oxygen. *Physical review letters*, 113(17):177601, 2014.

[28] T. C. Rödel, C. Bareille, F. Fortuna, C. Baumier, F. Bertran, P. Le Fèvre, M. Gabay, O. Hijano Cubelos, M. J. Rozenberg, T. Maroutian, et al. Orientational tuning of the fermi sea of confined electrons at the $SrTiO_3$ (110) and (111) surfaces. *Physical Review Applied*, 1(5):051002, 2014.

[29] Shamashis Sengupta, Emilie Tisserond, Florence Linez, Miguel Monteverde, Anil Murani, Tobias Rödel, Philippe Lecoeur, Thomas Maroutian, Claire Marrache-Kikuchi, Andrés F. Santander-Syro, et al. Gate-tunable superconductivity at $SrTiO_3$ surface realized by Al layer evaporation. *Journal of Applied Physics*, 124(21):213902, 2018.

[30] Tobias Chris Rödel, Franck Fortuna, Shamashis Sengupta, Emmanouil Frantzeskakis, Patrick Le Fèvre, François Bertran, Bernard Mercey, Sylvia Matzen, Guillaume Agnus, Thomas Maroutian, et al. Universal fabrication of 2D electron systems in functional oxides. *Advanced Materials*, 28(10):1976–1980, 2016.

[31] Patrick Lömker, Tobias C. Rödel, Timm Gerber, Franck Fortuna, Emmanouil Frantzeskakis, Patrick Le Fèvre, François Bertran, Martina Müller, and Andrés F Santander-Syro. Two-dimensional electron system at the magnetically tunable $EuO/SrTiO_3$ interface. *Physical Review Materials*, 1(6):062001, 2017.

[32] Xiao-Liang Qi and Shou-Cheng Zhang. Topological insulators and superconductors. *Reviews of Modern Physics*, 83(4):1057, 2011.

[33] Liang Fu and Charles L. Kane. Topological insulators with inversion symmetry. *Physical Review B*, 76(4):045302, 2007.

[34] Liang Fu, Charles L. Kane, and Eugene J. Mele. Topological insulators in three dimensions. *Physical review letters*, 98(10):106803, 2007.

[35] Markus König, Hartmut Buhmann, Laurens W. Molenkamp, Taylor Hughes, Chao-Xing Liu, Xiao-Liang Qi, and Shou-Cheng Zhang. The quantum spin Hall effect: theory and experiment. *Journal of the Physical Society of Japan*, 77(3):031007, 2008.

[36] Joel E. Moore. The birth of topological insulators. *Nature*, 464(7286):194, 2010.

[37] M. Zahid Hasan and Charles L. Kane. Colloquium: topological insulators. *Reviews of modern physics*, 82(4):3045, 2010.

[38] Xiao-Liang Qi and Shou-Cheng Zhang. The quantum spin Hall effect and topological insulators. *Physics Today*, 63(27):33, 2010.

[39] Joel E. Moore and Leon Balents. Topological invariants of time-reversal-invariant band structures. *Physical Review B*, 75(12):121306, 2007.

[40] Xiao-Liang Qi, Taylor L Hughes, and Shou-Cheng Zhang. Topological field theory of time-reversal invariant insulators. *Physical Review B*, 78(19):195424, 2008.

[41] Rahul Roy. Z_2 classification of quantum spin Hall systems: An approach using time-reversal invariance. *Physical Review B*, 79(19):195321, 2009.

[42] Rahul Roy. Topological phases and the quantum spin hall effect in three dimensions. *Physical Review B*, 79(19):195322, 2009.

[43] Koji Miyamoto and Taichi Okuda. High-Efficient Spin- and Angle-Resolved Photoemission Spectroscopy for Bi_2Te_2Se and Bi_2Se_2Te. *Hyomen Kagaku*, 34:374–379, 07 2013.

[44] Haijun Zhang, Chao-Xing Liu, Xiao-Liang Qi, Xi Dai, Zhong Fang, and Shou-Cheng Zhang. Topological insulators in Bi_2Se_3, Bi_2Te_3 and Sb_2Te_3 with a single Dirac cone on the surface. *Nature physics*, 5(6):438, 2009.

[45] Chao-Xing Liu, Xiao-Liang Qi, HaiJun Zhang, Xi Dai, Zhong Fang, and Shou-Cheng Zhang. Model hamiltonian for topological insulators. *Physical Review B*, 82(4):045122, 2010.

[46] Piers Coleman. Heavy fermions: Electrons at the edge of magnetism. *Handbook of Magnetism and Advanced Magnetic Materials*, 2007.

[47] Piers Coleman. Heavy fermions and the Kondo lattice: a 21st century perspective. *arXiv preprint arXiv:1509.05769*, 2015.

[48] Melvin A. Ruderman and Charles Kittel. Indirect exchange coupling of nuclear magnetic moments by conduction electrons. *Physical Review*, 96(1):99, 1954.

[49] Tadao Kasuya. A theory of metallic ferro-and antiferromagnetism on Zener's model. *Progress of theoretical physics*, 16(1):45–57, 1956.

[50] Kei Yosida. Magnetic properties of Cu-Mn alloys. *Physical Review*, 106(5):893, 1957.

[51] Cornelius Krellner, S. Lausberg, A. Steppke, M. Brando, L. Pedrero, H. Pfau, S. Tencé, Helge Rosner, F. Steglich, and C. Geibel. Ferromagnetic quantum criticality in the quasi-one-dimensional heavy fermion metal $YbNi_4P_2$. *New Journal of Physics*, 13(10):103014, 2011.

[52] Alexander Steppke, Robert Küchler, Stefan Lausberg, Edit Lengyel, Lucia Steinke, Robert Borth, Thomas Lühmann, Cornelius Krellner, Michael Nicklas, Christoph Geibel, et al. Ferromagnetic quantum critical point in the heavy-fermion metal $YbNi_4(P_{1-x}As_x)_2$. *Science*, 339(6122):933–936, 2013.

[53] G. R. Stewart. Non-Fermi-liquid behavior in d-and f-electron metals. *Reviews of modern Physics*, 73(4):797, 2001.

[54] Jacques Flouquet, Georg Knebel, Daniel Braithwaite, D Aoki, Jean-Pascal Brison, Frédéric Hardy, Andrew Huxley, Stéphane Raymond, Bernard Salce, and Ilya Sheikin. Magnetism and superconductivity of heavy fermion matter. *Comptes Rendus Physique*, 7(1):22–34, 2006.

[55] J. L. Smith and P. S. Riseborough. Actinides, the narrowest bands. *Journal of magnetism and magnetic materials*, 47:545–548, 1985.

[56] wikipedia: Kondo insulator. https://en.wikipedia.org/wiki/Kondo_insulator#/media/File:Hybridization.png. Accessed: 2019-09-01.

[57] Dietrich Belitz, Theodore R. Kirkpatrick, and Thomas Vojta. First order transitions and multicritical points in weak itinerant ferromagnets. *Physical review letters*, 82(23):4707, 1999.

[58] Andrey V. Chubukov, Catherine Pépin, and Jerome Rech. Instability of the quantum-critical point of itinerant ferromagnets. *Physical review letters*, 92(14):147003, 2004.

[59] D. Belitz, T. R. Kirkpatrick, and Thomas Vojta. How generic scale invariance influences quantum and classical phase transitions. *Reviews of modern physics*, 77(2):579, 2005.

[60] G. J. Conduit, A. G. Green, and B. D. Simons. Inhomogeneous phase formation on the border of itinerant ferromagnetism. *Physical review letters*, 103(20):207201, 2009.

[61] T. R. Kirkpatrick and D. Belitz. Universal low-temperature tricritical point in metallic ferromagnets and ferrimagnets. *Physical Review B*, 85(13):134451, 2012.

[62] Nicolas Reyren, S. Thiel, A. D. Caviglia, L. Fitting Kourkoutis, German Hammerl, Christoph Richter, C. W. Schneider, Thilo Kopp, A. S. Rüetschi, Didier Jaccard, et al. Superconducting interfaces between insulating oxides. *Science*, 317(5842):1196–1199, 2007.

[63] Chaoyu Chen, José Avila, Emmanouil Frantzeskakis, Anna Levy, and Maria C. Asensio. Observation of a two-dimensional liquid of Fröhlich polarons at the bare $SrTiO_3$ surface. *Nature communications*, 6:8585, 2015.

[64] Zhiming Wang, S McKeown Walker, Anna Tamai, Y. Wang, Z. Ristic, Flavio Yair Bruno, Alberto De La Torre, Sara Riccò, N. C. Plumb, M. Shi, et al. Tailoring the nature and strength of electron-phonon interactions in the $SrTiO_3$ (001) 2D electron liquid. *Nature materials*, 15(8):835, 2016.

[65] Carla Verdi, Fabio Caruso, and Feliciano Giustino. Origin of the crossover from polarons to Fermi liquids in transition metal oxides. *Nature communications*, 8:15769, 2017.

[66] Jonathon Mark Riley, F. Caruso, C. Verdi, L. B. Duffy, Matthew David Watson, Lewis Bawden, K. Volckaert, G. van der Laan, T. Hesjedal, M. Hoesch, et al. Crossover from lattice to plasmonic polarons of a spin-polarised electron gas in ferromagnetic Euo. *Nature communications*, 9(1):2305, 2018.

[67] Herbert Fröhlich. Theory of the superconducting state. I. The ground state at the absolute zero of temperature. *Physical Review*, 79(5):845, 1950.

[68] PM Echenique, R Berndt, EV Chulkov, Th Fauster, A Goldmann, and U Höfer. Decay of electronic excitations at metal surfaces. *Surface Science Reports*, 52(7):219–317, 2004.

[69] Ph Hofmann, I Yu Sklyadneva, EDL Rienks, and EV Chulkov. Electron–phonon coupling at surfaces and interfaces. *New Journal of Physics*, 11(12):125005, 2009.

[70] Vladimir N Kostur and Božidar Mitrović. Electron-phonon interaction in two dimensions: Variation of ImΣ (ε p, ω) with increasing ω D/E F. *Physical Review B*, 48(22):16388, 1993.

[71] Binghai Yan. Spin-orbit coupling: a relativistic effect, August 2016.

[72] Dieter Weiss. Magnetism and Spin-Orbit Interaction: Some basics and examples, August 2011.

[73] C 'e dric Bareille. *Effects of a symmetry breaking on the electronic structures of URu_2Si_2 and $KTaO_3$*. PhD thesis, University Paris South Paris XI, 2013.

[74] Andrés Felipe Santander-Syro. Electronic structure of exotic states in correlated-fermion materials, April 2013.

[75] wikipedia: ARPES. https://en.wikipedia.org/wiki/Angle-resolved_photoemission_spectroscopy#/media/File:ARPESgeneral.png. Accessed: 2019-09-01.

[76] Michael Sing. Introduction to Photoemission Spectroscopy, September 2014.

[77] Friedrich Reinert and Stefan Hüfner. Photoemission spectroscopy—from early days to recent applications. *New Journal of Physics*, 7(1):97, 2005.

[78] Carl Neil Berglund and William Edward Spicer. Photoemission studies of copper and silver: theory. *Physical Review*, 136(4A):A1030, 1964.

[79] John Brian Pendry. *Low energy electron diffraction: the theory and its application to determination of surface structure*, volume 2. Academic Press, 1974.

[80] J. B. Pendry. Theory of photoemission. *Surface Science*, 57(2):679–705, 1976.

[81] J. F. L. Hopkinson, J. B. Pendry, and D. J. Titterington. Calculation of photoemission spectra for surfaces of solids. *Computer Physics Communications*, 19(1):69–92, 1980.

[82] T. C. Rödel, J. Dai, F. Fortuna, E. Frantzeskakis, P. Le Fèvre, F. Bertran, M. Kobayashi, R. Yukawa, T. Mitsuhashi, M. Kitamura, et al. High-density two-dimensional electron system induced by oxygen vacancies in ZnO. *Physical Review Materials*, 2(5):051601, 2018.

[83] John S. Toll. Causality and the dispersion relation: logical foundations. *Physical review*, 104(6):1760, 1956.

[84] wikipedia: ZnO. https://en.wikipedia.org/wiki/Zinc_oxide#/media/File:Wurtzite_polyhedra.png. Accessed: 2019-09-01.

[85] Otfried Madelung, W Von der Osten, and U Rössler. *Intrinsic Properties of Group IV Elements and III-V, II-VI and I-VII Compounds/Intrinsische Eigenschaften Von Elementen Der IV. Gruppe und Von III-V-, II-VI-und I-VII-Verbindungen*, volume 22. Springer Science & Business Media, 1986.

[86] Claus F Klingshirn, Andreas Waag, Axel Hoffmann, and Jean Geurts. *Zinc oxide: from fundamental properties towards novel applications*, volume 120. Springer Science & Business Media, 2010.

[87] M. Oshikiri, Y. Imanaka, F. Aryasetiawan, and G. Kido. Comparison of the electron effective mass of the n-type Zno in the wurtzite structure measured by cyclotron resonance and calculated from first principle theory. *Physica B: Condensed Matter*, 298(1):472–476, 2001.

[88] M. Oshikiri, F. Aryasetiawan, Y. Imanaka, and G. Kido. Quasiparticle effective-mass theory in semiconductors. *Physical Review B*, 66(12):125204, 2002.

[89] Gabriele Giuliani and Giovanni Vignale. *Quantum theory of the electron liquid*. Cambridge university press, 2005.

[90] Claus F. Klingshirn, Andreas Waag, Axel Hoffmann, and Jean Geurts. *Zinc oxide: from fundamental properties towards novel applications*, volume 120. Springer Science & Business Media, 2010.

[91] Ü Özgür, Ya I. Alivov, Chunli Liu, A. Teke, M. An Reshchikov, S. Doğan, V.C.S.J. Avrutin, S.-J. Cho, and H. Morkoç. A comprehensive review of Zno materials and devices. *Journal of applied physics*, 98(4):11, 2005.

[92] wikipedia: ZnTe. https://en.wikipedia.org/wiki/Zinc_telluride#/media/File:Zinc-selenide-unit-cell-3D-balls.png. Accessed: 2019-09-01.

[93] H. Qu, J. Kanski, P. O. Nilsson, and U. O. Karlsson. Angle-resolved photoelectron spectroscopy study of the surface electronic structure of ZnTe (110). *Physical Review B*, 43(12):9843, 1991.

[94] William M Haynes. *CRC handbook of chemistry and physics*. CRC press, 2014.

[95] Tooru Tanaka, Katsuhiko Saito, Mitsuhiro Nishio, Qixin Guo, and Hiroshi Ogawa. Enhanced light output from ZnTe light emitting diodes by utilizing thin film structure. *Applied Physics Express*, 2(12):122101, 2009.

[96] Klaus Reimann. Table-top sources of ultrashort THz pulses. *Reports on Progress in Physics*, 70(10):1597, 2007.

[97] Q. Wu, T. D. Hewitt, and X.-C. Zhang. Two-dimensional electro-optic imaging of THz beams. *Applied Physics Letters*, 69(8):1026–1028, 1996.

[98] G. Karczewski, S. Maćkowski, M. Kutrowski, T. Wojtowicz, and J. Kossut. Photoluminescence study of CdTe/ZnTe self-assembled quantum dots. *Applied physics letters*, 74(20):3011–3013, 1999.

[99] Jiyong Fu and J Carlos Egues. Spin-orbit interaction in GaAs wells: From one to two subbands. *Physical Review B*, 91(7):075408, 2015.

[100] C. S. Knox, L. H. Li, M. C. Rosamond, E. H. Linfield, and C. H. Marrows. Deconvolution of Rashba and Dresselhaus spin-orbit coupling by crystal axis dependent measurements of coupled InAs/GaSb quantum wells. *Physical Review B*, 98(15):155323, 2018.

[101] Taichi Okuda, Yasuo Takeichi, Yuuki Maeda, Ayumi Harasawa, Iwao Matsuda, Toyohiko Kinoshita, and Akito Kakizaki. A new spin-polarized photoemission spectrometer with very high efficiency and energy resolution. *Review of Scientific Instruments*, 79(12):123117, 2008.

[102] Taichi Okuda, Koji Miyamaoto, Hirokazu Miyahara, Kenta Kuroda, Akio Kimura, Hirofumi Namatame, and Masaki Taniguchi. Efficient spin resolved spectroscopy observation machine at Hiroshima Synchrotron Radiation Center. *Review of Scientific Instruments*, 82(10):103302, 2011.

[103] A. Y. Cho and J. R. Arthur. Molecular beam epitaxy. *Progress in solid state chemistry*, 10:157–191, 1975.

[104] Kenjiro Oura, V. G. Lifshits, A. A. Saranin, A. V. Zotov, and M. Katayama. *Surface science: an introduction*. Springer Science & Business Media, 2013.

[105] T. C. Rödel, Manali Vivek, Franck Fortuna, Patrick Le Fèvre, François Bertran, Rubén Weht, Jacek Goniakowski, Marc Gabay, and Andrés F Santander-Syro. Two-dimensional electron systems in $ATiO_3$ perovskites (A= Ca, Ba, Sr): control of orbital hybridization and order. *arXiv preprint arXiv:1705.10755*, 2017.

[106] Matthias Batzill and Ulrike Diebold. Surface studies of gas sensing metal oxides. *Physical Chemistry Chemical Physics*, 9(19):2307–2318, 2007.

[107] Matthias Batzill, Khabibulakh Katsiev, and Ulrike Diebold. Surface morphologies of Sno_2 (110). *Surface science*, 529(3):295–311, 2003.

[108] Lindsay R. Merte, Mathias S. Jørgensen, Katariina Pussi, Johan Gustafson, Mikhail Shipilin, Andreas Schaefer, Chu Zhang, Jonathan Rawle, Chris Nicklin, Geoff Thornton, et al. Structure of the SnO_2 (110)-(4×1) surface. *Physical review letters*, 119(9):096102, 2017.

[109] *Catalysis and Chemical Processes*. Eds. R. Pearce and W. R. Patterson, 1981.

[110] M. Sinner-Hettenbach, Mats Göthelid, T. Weiß, N. Barsan, U. Weimar, H. von Schenck, L. Giovanelli, and G. Le Lay. Electronic structure of SnO_2 (110)-4×1 and sputtered SnO_2 (110) revealed by resonant photoemission. *Surface science*, 499(1):85–93, 2002.

[111] S. Semancik and D. F. Cox. Fundamental characterization of clean and gas-dosed tin oxide. *Sensors and Actuators*, 12(2):101–106, 1987.

[112] Joseph Watson. The tin oxide gas sensor and its applications. *Sensors and Actuators*, 5(1):29–42, 1984.

[113] David F. Cox, Teresa B. Fryberger, and Steve Semancik. Surface reconstructions of oxygen deficient SnO_2 (110). *Surface Science*, 224(1-3):121–142, 1989.

[114] Matthias Batzill and Ulrike Diebold. The surface and materials science of tin oxide. *Progress in surface science*, 79(2-4):47–154, 2005.

[115] F. H. Jones, R. Dixon, J. S. Foord, R. G. Egdell, and J. B. Pethica. The surface structure of SnO_2 (110)(4×1) revealed by scanning tunneling microscopy. *Surface science*, 376(1-3):367–373, 1997.

[116] Frank J. Berry. Tin-antimony oxide catalysts. In *Advances in catalysis*, volume 30, pages 97–131. Elsevier, 1981.

[117] Matthias Batzill, Khabibulakh Katsiev, James M. Burst, Ulrike Diebold, Anne M. Chaka, and Bernard Delley. Gas-phase-dependent properties of SnO_2 (110), (100), and (101) single-crystal surfaces: Structure, composition, and electronic properties. *Physical Review B*, 72(16):165414, 2005.

[118] Philip G. Harrison, Craig Bailey, and Wan Azelee. Modified Tin (IV) Oxide (M/SnO_2 M= Cr, La, Pr, Nd, Sm, Gd) Catalysts for the Oxidation of Carbon Monoxide and Propane. *Journal of Catalysis*, 186(1):147–159, 1999.

[119] Frigyes Solymosi and János Kiss. Adsorption and reduction of NO on tin (IV) oxide catalysts. *Journal of Catalysis*, 41(2):202–211, 1976.

[120] M. J. Fuller and M. E. Warwick. The catalytic oxidation of carbon monoxide on tin (IV) oxide. *Journal of Catalysis*, 29(3):441–450, 1973.

[121] Matti A. Mäki-Jaskari and Tapio T. Rantala. Band structure and optical parameters of the SnO_2 (110) surface. *Physical Review B*, 64(7):075407, 2001.

[122] R. G. Egdell, J. Rebane, T. J. Walker, and D. S. L. Law. Competition between initial-and final-state effects in valence-and core-level x-ray photoemission of sb-doped SnO_2. *Physical Review B*, 59(3):1792, 1999.

[123] J. Haines and J. M. Léger. X-ray diffraction study of the phase transitions and structural evolution of tin dioxide at high pressure: ffrelationships between structure types and implications for other rutile-type dioxides. *Physical Review B*, 55(17):11144, 1997.

[124] K. Reimann and M. Steube. Experimental determination of the electronic band structure of SnO_2. *Solid State Communications*, 105(10):649–652, 1998.

[125] J Robertson. Electronic structure of SnO_2, GeO_2, PbO_2, TeO_2 and MgF_2. *Journal of Physics C: Solid State Physics*, 12(22):4767, 1979.

[126] S. Munnix and M. Schmeits. Electronic structure of tin dioxide surfaces. *Physical Review B*, 27(12):7624, 1983.

[127] David F. Cox, Teresa B. Fryberger, and Steve Semancik. Oxygen vacancies and defect electronic states on the SnO_2 (110)-1×1 surface. *Physical Review B*, 38(3):2072, 1988.

[128] R. G. Egdell, S. Eriksen, and W. R. Flavell. Oxygen deficient SnO_2 (110) and TiO_2 (110): A comparative study by photoemission. *Solid state communications*, 60(10):835–838, 1986.

[129] P. A. Cox, R. G. Egdell, C. Harding, W. R. Patterson, and P. J. Tavener. Surface properties of antimony doped tin (IV) oxide: a study by electron spectroscopy. *Surface Science*, 123(2-3):179–203, 1982.

[130] Jean Marc Themlin, Robert Sporken, J. Darville, R. Caudano, J. M. Gilles, and R. L. Johnson. Resonant-photoemission study of SnO_2: cationic origin of the defect band-gap states. *Physical Review B*, 42(18):11914, 1990.

[131] P. A. Cox, R. G. Egdell, C. Harding, A. F. Orchard, W. R. Patterson, and P. J. Tavener. Free-electron behaviour of carriers in antimony-doped tin (IV) oxide: A study by electron spectroscopy. *Solid State Communications*, 44(6):837–839, 1982.

[132] R. G. Egdell, S. Eriksen, and W. R. Flavell. A spectroscopic study of electron and ion beam reduction of SnO_2 (110). *Surface science*, 192(1):265–274, 1987.

[133] P. C. Hollamby, P. S. Aldridge, G. Moretti, R. G. Egdell, and W. R. Flavell. The influence of oxygen deficiency and Sb doping on inverse photoemission spectra of SnO_2. *Surface science*, 280(3):393–397, 1993.

[134] J. Oviedo and M. J. Gillan. The energetics and structure of oxygen vacancies on the SnO_2 (110) surface. *Surface science*, 467(1-3):35–48, 2000.

[135] J. A. Marley and R. C. Dockerty. Electrical properties of stannic oxide single crystals. *Physical Review*, 140(1A):A304, 1965.

[136] K. H. L. Zhang, R. G. Egdell, F. Offi, S. Iacobucci, L. Petaccia, S. Gorovikov, and P. D. C. King. Microscopic origin of electron accumulation in In_2O_3. *Physical review letters*, 110(5):056803, 2013.

[137] L. F. J. Piper, Leyla Colakerol, P. D. C. King, Andre Schleife, J. Zúñiga-Pérez, Per-Anders Glans, Tim Learmonth, A. Federov, T. D. Veal, F. Fuchs, et al. Observation of quantized subband states and evidence for surface electron accumulation in CdO from angle-resolved photoemission spectroscopy. *Physical Review B*, 78(16):165127, 2008.

[138] R. Yukawa, K. Ozawa, S. Yamamoto, H. Iwasawa, K. Shimada, Eike F. Schwier, K. Yoshimatsu, H. Kumigashira, H. Namatame, M. Taniguchi, et al. Phonon-dressed two-dimensional carriers on the ZnO surface. *Physical Review B*, 94(16):165313, 2016.

[139] Robert Joseph Cava, Huiwen Ji, Michael K Fuccillo, Quinn D. Gibson, and Yew San Hor. Crystal structure and chemistry of topological insulators. *Journal of Materials Chemistry C*, 1(19):3176–3189, 2013.

[140] Nathan P. Guisinger, Tiffany S. Santos, Jeffrey R. Guest, Te-Yu Chien, Anand Bhattacharya, John W. Freeland, and Matthias Bode. Nanometer-scale striped surface terminations on fractured $SrTiO_3$ surfaces. *ACS nano*, 3(12):4132–4136, 2009.

[141] Kyle M. Shen and J.C. Seamus Davis. Cuprate high-T_c superconductors. *Materials Today*, 11(9):14 – 21, 2008.

[142] Alex M. Ganose and David O. Scanlon. Band gap and work function tailoring of SnO_2 for improved transparent conducting ability in photovoltaics. *Journal of Materials Chemistry C*, 4(7):1467–1475, 2016.

[143] Zhiming Wang, Zhicheng Zhong, Xianfeng Hao, Stefan Gerhold, Bernhard Stöger, Michael Schmid, Jaime Sánchez-Barriga, Andrei Varykhalov, Cesare

Franchini, Karsten Held, et al. Anisotropic two-dimensional electron gas at $SrTiO_3$ (110). *Proceedings of the National Academy of Sciences*, 111(11):3933–3937, 2014.

[144] Siobhan McKeown Walker, Flavio Yair Bruno, Zhiming Wang, Alberto De La Torre, Sara Riccó, Anna Tamai, Timur K. Kim, Moritz Hoesch, Ming Shi, Mohammad Saeed Bahramy, et al. Carrier-Density Control of the $SrTiO_3$ (001) Surface 2D Electron Gas studied by ARPES. *Advanced Materials*, 27(26):3894–3899, 2015.

[145] Simon Moser. An experimentalist's guide to the matrix element in angle resolved photoemission. *Journal of Electron Spectroscopy and Related Phenomena*, 214:29–52, 2017.

[146] R. Yukawa, K. Ozawa, S. Yamamoto, R.-Y. Liu, and I. Matsuda. Anisotropic effective mass approximation model to calculate multiple subband structures at wide-gap semiconductor surfaces: Application to accumulation layers of $SrTiO_3$ and ZnO. *Surface Science*, 641:224–230, 2015.

[147] http://chemistry-reference.com/standard%20thermodynamic%20values.pdf. Accessed: 2019-06-04.

[148] J. A. Dean. *Lange's handbook of chemistry*. McGraw-Hill, New York, 11th edition, 1979.

[149] D. R. Lide. *CRC handbook*. CRC Press, Boca Raton, Florida, 84th edition, 2003.

[150] S. Backes, T. C. Rödel, F. Fortuna, E. Frantzeskakis, P. Le Fèvre, F. Bertran, M. Kobayashi, R. Yukawa, T. Mitsuhashi, M. Kitamura, et al. Hubbard band versus oxygen vacancy states in the correlated electron metal $SrVO_3$. *Physical Review B*, 94(24):241110, 2016.

[151] P. De Padova, M. Fanfoni, R. Larciprete, M. Mangiantini, S. Priori, and P. Perfetti. A synchrotron radiation photoemission study of the oxidation of tin. *Surface science*, 313(3):379–391, 1994.

[152] Peng Zhang, P. Richard, T. Qian, Y.-M. Xu, X. Dai, and H. Ding. A precise method for visualizing dispersive features in image plots. *Review of Scientific Instruments*, 82(4):043712, 2011.

[153] S. Moser, V. Jovic, R. Koch, L. Moreschini, J.-S. Oh, C. Jozwiak, A. Bostwick, and E. Rotenberg. How to extract the surface potential profile from the arpes signature of a 2deg. *Journal of Electron Spectroscopy and Related Phenomena*, 225:16–22, 2018.

[154] P. S. Peercy and B. Morosin. Pressure and Temperature Dependences of the Raman-Active Phonons in SnO_2. *Physical Review B*, 7(6):2779, 1973.

[155] A. Dieguez, A. Romano-Rodrıguez, A. Vila, and J. R. Morante. The complete Raman spectrum of nanometric SnO_2 particles. *Journal of Applied Physics*, 90(3):1550–1557, 2001.

[156] P. Sangeetha, V. Sasirekha, and V. Ramakrishnan. Micro-raman investigation of tin dioxide nanostructured material based on annealing effect. *Journal of Raman Spectroscopy*, 42(8):1634–1639, 2011.

[157] Y. Aiura, I. Hase, H. Bando, T. Yasue, T. Saitoh, and D.S. Dessau. Photoemission study of the metallic state of lightly electron-doped $SrTiO_3$. *Surface Science*, 515(1):61–74, 2002.

[158] P. D. C. King and Tim D. Veal. Conductivity in transparent oxide semiconductors. *Journal of Physics: Condensed Matter*, 23(33):334214, 2011.

[159] J. Oviedo and M. J. Gillan. Reconstructions of strongly reduced SnO_2 (110) studied by first-principles methods. *Surface science*, 513(1):26–36, 2002.

[160] Heinz Sibum, Volker Güther, Oskar Roidl, Fathi Habashi, Hans Uwe Wolf, and Carsten Siemers. Titanium, titanium alloys, and titanium compounds. *Ullmann's encyclopedia of industrial chemistry*, pages 1–35, 2000.

[161] Stephen E. Haggerty and Violaine Sautter. Ultradeep (greater than 300 kilometers), ultramafic upper mantle xenoliths. *Science*, 248(4958):993–996, 1990.

[162] S. S. Sunkara and R. K. Pandey. Ilmenite–a wide band gap semiconductor for novel electronic applications. *Ceramic Transactions,*, 60:83–93, 1995.

[163] Tatsuo Fujii, Masakazu Kayano, Yusuke Takada, Makoto Nakanishi, and Jun Takada. Ilmenite–hematite solid solution films for novel electronic devices. *Solid State Ionics*, 172(1-4):289–292, 2004.

[164] Zhongning Dai, Peiran Zhu, Shunya Yamamoto, Atsumi Miyashita, Kazumasa Narum, and Hiroshi Naramoto. Pulsed laser deposition of ilmenite $FeTiO_3$ epitaxial thin film onto sapphire substrate. *Thin solid films*, 339(1-2):114–116, 1999.

[165] Feng Zhou, Sushma Kotru, and Raghvendra K. Pandey. Nonlinear current–voltage characteristics of ilmenite–hematite ceramic. *Materials Letters*, 57(13-14):2104–2109, 2003.

[166] Tomasz Dietl and Hideo Ohno. Ferromagnetic III–V and II–VI Semiconductors. *MRS bulletin*, 28(10):714–719, 2003.

[167] Yoshikazu Ishikawa and Syun-iti Akimoto. Magnetic properties of the $FeTiO_3$-Fe_2O_3 solid solution series. *Journal of the Physical Society of Japan*, 12(10):1083–1098, 1957.

[168] A. T. Raghavender, Nguyen Hoa Hong, Kyu Joon Lee, Myung-Hwa Jung, Z. Skoko, Mikhail Vasilevskiy, M. F. Cerqueira, and A. P. Samantilleke. Nanoilmenite $FeTiO_3$: Synthesis and characterization. *Journal of magnetism and magnetic materials*, 331:129–132, 2013.

[169] Anil B. Gambhire, Machhindra K. Lande, Sandip B. Rathod, Balasaheb R. Arbad, Kaluram N. Vidhate, Ramakrishna S. Gholap, and Kashinath R. Patil. Synthesis and characterization of $FeTiO_3$ ceramics. *Arabian Journal of Chemistry*, 9:S429–S432, 2016.

[170] Xin Tang and Ke-ao Hu. The formation of ilmenite $FeTiO_3$ powders by a novel liquid mix and H_2/H_2O reduction process. *Journal of materials science*, 41(23):8025–8028, 2006.

[171] Fuxing Ye and Akira Ohmori. The photocatalytic activity and photoabsorption of plasma sprayed TiO_2–Fe_3O_4 binary oxide coatings. *Surface and Coatings Technology*, 160(1):62–67, 2002.

[172] R. A. P. Ribeiro, A. Camilo Jr., and S. R. De Lazaro. Electronic structure and magnetism of new ilmenite compounds for spintronic devices: $FeBO_3$ (B= Ti, Hf, Zr, Si, Ge, Sn). *Journal of Magnetism and Magnetic Materials*, 394:463–469, 2015.

[173] Nicholas C. Wilson and Salvy P. Russo. Ilmenite (0001) surface investigated using hybrid density functional theory. *Physical Review B*, 84(7):075310, 2011.

[174] Tatsuo Fujii, Masakazu Kayano, Yusuke Takada, Makoto Nakanishi, and Jun Takada. Preparation and characterization of epitaxial $FeTiO_{3+\delta}$ films. *Journal of magnetism and magnetic materials*, 272:2010–2011, 2004.

[175] R. A. P. Ribeiro and S. R. de Lazaro. Structural, electronic and elastic properties of $FeBO_3$ (B= Ti, Sn, Si, Zr) ilmenite: a density functional theory study. *Rsc Advances*, 4(104):59839–59846, 2014.

[176] V. Yu Galkin, W. A. Ortiz, and Eric Fawcett. A new magnetic phase in the SDW alloy Cr+ 3.2% Co: effect of doping with V. *Journal of Physics: Condensed Matter*, 9(44):L577, 1997.

[177] Axel D. Becke. A new mixing of Hartree–Fock and local density-functional theories. *The Journal of chemical physics*, 98(2):1372–1377, 1993.

[178] Yen-Hua Chen. Synthesis, characterization and dye adsorption of ilmenite nanoparticles. *Journal of Non-Crystalline Solids*, 357(1):136–139, 2011.

[179] R. A. Fellows, A. R. Lennie, D. J. Vaughan, and G. Thornton. A LEED study of the $FeTiO_3$ (0001) surface following annealing in O_2 partial pressures. *Surface science*, 383(1):50–56, 1997.

[180] Robert A. Fellows, Alistair R. Lennie, Andreas W. Munz, David J. Vaughan, and Geoff Thornton. Structures of $FeTiO_3$ (0001) surfaces observed by scanning tunneling microscopy. *American Mineralogist*, 84(9):1384–1391, 1999.

[181] Karsten Reuter and Matthias Scheffler. Composition, structure, and stability of RuO_2 (110) as a function of oxygen pressure. *Physical Review B*, 65(3):035406, 2001.

[182] N. C. Wilson, J. Muscat, D. Mkhonto, P. E. Ngoepe, and N. M. Harrison. Structure and properties of ilmenite from first principles. *Physical Review B*, 71(7):075202, 2005.

[183] Varoujan Chakarian, David K. Shuh, Jory A. Yarmoff, Hui-Shu Tao, Ulrike Diebold, Brian L. Maschhoff, Theodore E Madey, and Neal D. Shinn. The influence of preadsorbed K on the adsorption of PF_3 on Ru (0001) studied by soft x-ray photoelectron spectroscopy. *The Journal of chemical physics*, 100(7):5301–5313, 1994.

[184] Rossitza Pentcheva and Hasan Sadat Nabi. Interface magnetism in $Fe_2O_3/FeTiO_3$ heterostructures. *Physical Review B*, 77(17):172405, 2008.

[185] R. Yukawa, S. Yamamoto, K. Ozawa, Marie D'Angelo, M. Ogawa, M. G. Silly, F. Sirotti, and I. Matsuda. Electronic structure of the hydrogen-adsorbed $SrTiO_3$ (001) surface studied by polarization-dependent photoemission spectroscopy. *Physical Review B*, 87(11):115314, 2013.

[186] Abhijit Biswas, Ki-Seok Kim, and Yoon Hee Jeong. Metal–Insulator Transitions and Non-Fermi Liquid Behaviors in 5d Perovskite Iridates. In *Perovskite Materials-Synthesis, Characterisation, Properties, and Applications*. InTech Croat, 2016.

[187] Hajime Hojo, Koji Fujita, Katsuhisa Tanaka, and Kazuyuki Hirao. Fabrication of p-type ferrimagnetic semiconductor thin films based on $FeTiO_3$–Fe_2O_3 solid solution. *Journal of Magnetism and Magnetic Materials*, 310(2):2105–2107, 2007.

[188] E. Popova, B. Warot-Fonrose, H. Ndilimabaka, M. Bibes, N. Keller, B. Berini, K. Bouzehouane, and Y. Dumont. Systematic investigation of the growth and structural properties of $FeTiO_{3\pm\delta}$ epitaxial thin films. *Journal of Applied Physics*, 103(9):093909, 2008.

[189] K.-W. Chen, N. Aryal, J. Dai, D. Graf, S. Zhang, S. Das, P. Le Fèvre, F. Bertran, R. Yukawa, K. Horiba, et al. Converting topological insulators into topological metals within the tetradymite family. *Physical Review B*, 97(16):165112, 2018.

[190] Huiwen Ji, I. Pletikosić, Q. D. Gibson, Girija Sahasrabudhe, T. Valla, and Robert Joseph Cava. Strong topological metal material with multiple Dirac cones. *Physical Review B*, 93(4):045315, 2016.

[191] M. Mofazzel Hosen, Klauss Dimitri, Ashis K. Nandy, Alex Aperis, Raman Sankar, Gyanendra Dhakal, Pablo Maldonado, Firoza Kabir, Christopher Sims, Fangcheng Chou, et al. Distinct multiple fermionic states in a single topological metal. *Nature communications*, 9(1):3002, 2018.

[192] Marco Bianchi, Dandan Guan, Shining Bao, Jianli Mi, Bo Brummerstedt Iversen, Philip DC King, and Philip Hofmann. Coexistence of the topological state and a two-dimensional electron gas on the surface of Bi_2Se_3. *Nature communications*, 1:128, 2010.

[193] E. Frantzeskakis, N. De Jong, B. Zwartsenberg, T. V. Bay, Y. K. Huang, S. V. Ramankutty, A. Tytarenko, D. Wu, Y. Pan, S. Hollanders, et al. Dirac states with knobs on: Interplay of external parameters and the surface electronic properties of three-dimensional topological insulators. *Physical Review B*, 91(20):205134, 2015.

[194] T. J. Boyle, A. Rossi, M. Walker, P. Carlson, M. K. Miller, J. Zhao, P. Klavins, C. Jozwiak, A. Bostwick, E. Rotenberg, et al. Topological surface states above the Fermi level in Hf_2Te_2P. *Physical Review B*, 100(8):081105, 2019.

[195] Jin Hu, Zhijie Tang, Jinyu Liu, Xue Liu, Yanglin Zhu, David Graf, Kevin Myhro, Son Tran, Chun Ning Lau, Jiang Wei, et al. Evidence of topological nodal-line fermions in ZrSiSe and ZrSiTe. *Physical review letters*, 117(1):016602, 2016.

[196] topological material zoo: Ti_2Te_2P. https://topologicalquantumchemistry.com/#/detail/418978. Accessed: 2019-09-01.

[197] Masatoshi Sato and Yoichi Ando. Topological superconductors: a review. *Reports on Progress in Physics*, 80(7):076501, 2017.

[198] Masatoshi Sato. Topological properties of spin-triplet superconductors and Fermi surface topology in the normal state. *Physical Review B*, 79(21):214526, 2009.

[199] Masatoshi Sato. Topological odd-parity superconductors. *Physical Review B*, 81(22):220504, 2010.

[200] Liang Fu and Erez Berg. Odd-parity topological superconductors: theory and application to $Cu_xBi_2Se_3$. *Physical review letters*, 105(9):097001, 2010.

[201] J. R. Williams, A. J. Bestwick, P. Gallagher, Seung Sae Hong, Y. Cui, Andrew S. Bleich, J. G. Analytis, I. R. Fisher, and D. Goldhaber-Gordon. Unconventional josephson effect in hybrid superconductor-topological insulator devices. *Physical review letters*, 109(5):056803, 2012.

[202] Mei-Xiao Wang, Canhua Liu, Jin-Peng Xu, Fang Yang, Lin Miao, Meng-Yu Yao, C. L. Gao, Chenyi Shen, Xucun Ma, X Chen, et al. The coexistence of superconductivity and topological order in the Bi_2Se_3 thin films. *Science*, 336(6077):52–55, 2012.

[203] Fan Yang, Fanming Qu, Jie Shen, Yue Ding, Jun Chen, Zhongqing Ji, Guangtong Liu, Jie Fan, Changli Yang, Liang Fu, et al. Proximity-effect-induced superconducting phase in the topological insulator Bi_2Se_3. *Physical Review B*, 86(13):134504, 2012.

[204] M. Snelder, C. G. Molenaar, Yu Pan, D. Wu, Y. K. Huang, A. de Visser, A. A. Golubov, W. G. van der Wiel, H. Hilgenkamp, M. S. Golden, et al. Josephson supercurrent in a topological insulator without a bulk shunt. *Superconductor science and technology*, 27(10):104001, 2014.

[205] Eryin Wang, Hao Ding, Alexei V. Fedorov, Wei Yao, Zhi Li, Yan-Feng Lv, Kun Zhao, Li-Guo Zhang, Zhijun Xu, John Schneeloch, et al. Fully gapped topological surface states in Bi_2Se_3 films induced by a d-wave high-temperature superconductor. *Nature physics*, 9(10):621, 2013.

[206] A. D. K. Finck, Cihan Kurter, Yew San Hor, and Dale J. Van Harlingen. Phase coherence and Andreev reflection in topological insulator devices. *Physical Review X*, 4(4):041022, 2014.

[207] Jeroen B Oostinga, Luis Maier, Peter Schüffelgen, Daniel Knott, Christopher Ames, Christoph Brüne, Grigory Tkachov, Hartmut Buhmann, and Laurens W. Molenkamp. Josephson supercurrent through the topological surface states of strained bulk HgTe. *Physical Review X*, 3(2):021007, 2013.

[208] Cornelius Krellner and Christoph Geibel. Magnetic anisotropy of $YbNi_4P_2$. In *Journal of Physics Conference Series*, volume 391, pages 1–4, 2012.

[209] Sven Friedemann. Electronic Structure investigations in Yb-based heavy fermion materials, November 2012.

[210] Yinglu Tang, Sinn-wen Chen, and G. Jeffrey Snyder. Temperature dependent solubility of Yb in Yb–$CoSb_3$ skutterudite and its effect on preparation, optimization and lifetime of thermoelectrics. *Journal of Materiomics*, 1(1):75–84, 2015.

[211] U. Köhler, N. Oeschler, F. Steglich, S. Maquilon, and Z. Fisk. Energy scales of $Lu_{1-x}Yb_xRh_2Si_2$ by means of thermopower investigations. *Physical Review B*, 77(10):104412, 2008.

[212] D. Belitz and T. R. Kirkpatrick. A compilation of metallic systems that show a quantum ferromagnetic transition. *arXiv preprint arXiv:1204.0873*, 2012.

[213] Elena Hassinger, Dai Aoki, Georg Knebel, and Jacques Flouquet. Pressure–temperature phase diagram of polycrystalline UCoGe studied by resistivity measurement. *Journal of the Physical Society of Japan*, 77(7):073703–073703, 2008.

[214] S. S. Saxena, P. Agarwal, K. Ahilan, F. M. Grosche, R. K. W. Haselwimmer, M. J. Steiner, E. Pugh, I. R. Walker, S. R. Julian, P. Monthoux, et al. Superconductivity on the border of itinerant-electron ferromagnetism in UGe_2. *Nature*, 406(6796):587, 2000.

[215] M. Brando, W. J. Duncan, D. Moroni-Klementowicz, C. Albrecht, D. Grüner, Rafik Ballou, and F. M. Grosche. Logarithmic fermi-liquid breakdown in $NbFe_2$. *Physical review letters*, 101(2):026401, 2008.

[216] T. Westerkamp, M. Deppe, R. Küchler, M. Brando, C. Geibel, P. Gegenwart, A. P. Pikul, and F. Steglich. Kondo-cluster-glass state near a ferromagnetic quantum phase transition. *Physical review letters*, 102(20):206404, 2009.

[217] Lijun Zhu, Markus Garst, Achim Rosch, and Qimiao Si. Universally diverging Grüneisen parameter and the magnetocaloric effect close to quantum critical points. *Physical Review Letters*, 91(6):066404, 2003.

[218] K. D. Schotte and U. Schotte. Interpretation of Kondo experiments in a magnetic field. *Physics Letters A*, 55(1):38–40, 1975.

[219] R. P. Huebener. Effect of phonon drag on the electrical resistivity of metals. *Physical Review*, 146(2):502, 1966.

[220] Thomas Pruschke. Landau's Fermi Liquid concept to the extreme: The physics of Heavy Fermions. In *American Institute of Physics Conference Series*, volume 1485, pages 78–134, 2012.

[221] Piers Coleman and Andrew J. Schofield. Quantum criticality. *Nature*, 433(7023):226, 2005.

[222] Hilbert Löhneysen, Achim Rosch, Matthias Vojta, and Peter Wölfle. Fermi-liquid instabilities at magnetic quantum phase transitions. *Reviews of Modern Physics*, 79(3):1015, 2007.

[223] Philipp Gegenwart, Qimiao Si, and Frank Steglich. Quantum criticality in heavy-fermion metals. *nature physics*, 4(3):186, 2008.

[224] Qimiao Si and Frank Steglich. Heavy fermions and quantum phase transitions. *Science*, 329(5996):1161–1166, 2010.

[225] A. L. Cornelius, J. S. Schilling, D. Mandrus, and J. D. Thompson. Anomalous hydrostatic pressure dependence of the Curie temperature of the Kondo-lattice compound YbNiSn to 38 GPa. *Physical Review B*, 52(22):R15699, 1995.

[226] K. Kummer, Yu Kucherenko, S. Danzenbächer, C. Krellner, C. Geibel, M. G. Holder, L. V. Bekenov, T. Muro, Y. Kato, T. Kinoshita, et al. Intermediate valence in Yb compounds probed by $4f$ photoemission and resonant inelastic x-ray scattering. *Physical Review B*, 84(24):245114, 2011.

[227] L. H. Tjeng, S.-J. Oh, E.-J. Cho, H.-J. Lin, C. T. Chen, G.-H. Gweon, J.-H. Park, J. W. Allen, T. Suzuki, M. S. Makivić, et al. Temperature dependence of the kondo resonance in $YbAl_3$. *Physical review letters*, 71(9):1419, 1993.

[228] Alexander Generalov, D. A. Sokolov, Alla Chikina, Yu Kucherenko, V. N. Antonov, L. V. Bekenov, S. Patil, A. D. Huxley, J. W. Allen, K. Matho, et al. Insight into the temperature dependent properties of the ferromagnetic kondo lattice ybnisn. *Physical Review B*, 95(18):184433, 2017.

[229] K. Ishizaka, M. S. Bahramy, H. Murakawa, M. Sakano, T. Shimojima, T. Sonobe, K. Koizumi, S. Shin, H. Miyahara, A. Kimura, et al. Giant Rashba-type spin splitting in bulk BiTeI. *Nature materials*, 10(7):521, 2011.

[230] Domenico Di Sante, Paolo Barone, Riccardo Bertacco, and Silvia Picozzi. Electric control of the giant rashba effect in bulk GeTe. *Advanced Materials*, 25(4):509–513, 2013.

[231] Rudolf Peierls. *More surprises in theoretical physics*, volume 19. Princeton University Press, 1991.

[232] George Gruner. *Density waves in solids*. CRC Press, 2018.

université PARIS-SACLAY
ÉCOLE DOCTORALE
Physique en Île-de-France (EDPIF)

Titre : Systèmes électroniques de basse dimensionnalité étudiés par spectroscopie de photoémission résolue en angle et en spin

Mots clés : systèmes électroniques bidimensionnels; électrons corrélés; oxydes fonctionnels; métaux topologiques; matériaux à fermions lourds; spectroscopie de photoémission résolue en angle.

Résumé : Les matériaux dans lesquels des interactions à plusieurs particules, un confinement de faible dimension et/ou un fort couplage spin-orbite sont présents témoignent d'une grande variété de phénomènes, mais sont encore mal compris. Des informations essentielles sur l'origine de tels phénomènes peuvent être obtenues en mesurant leur structure électronique. Cette thèse présente une étude expérimentale de la structure électronique de matériaux de faible dimension et/ou fortement corrélés présentant un intérêt fondamental actuel, en utilisant la spectroscopie par photoémission résolue en angle et en spin (ARPES et SARPES).
Dans la partie introductive, je présente mon travail sur deux exemples de type "livre de texte", mais innovants, montrant comment les interactions affectent la structure de bande d'un matériau : le couplage des électrons avec des phonons dans une distribution de Debye dans un système électronique à deux dimensions (2DES) dans ZnO, semi-conducteur à oxyde à bande interdite large utilisé dans les applications photovoltaïques, et le dédoublement induit par un fort couplage spin-orbite (SOC) dans la bande de valence du ZnTe, un autre semi-conducteur important utilisé dans les dispositifs optoélectroniques. Ensuite, dans la suite de cette thèse, je discute de mes résultats originaux dans trois systèmes différents de basse dimensionnalité et d'intérêt actuel en recherche :

1. La réalisation d'un 2DES à la surface (110) de SnO_2, le premier du genre dans une structure rutile. L'ajustabilité de la densité de ses porteurs au moyen de la température ou du dépôt d'Eu, et la robustesse vis-à-vis les reconstructions de surface et l'exposition aux conditions ambiantes rendent ce 2DES prometteur pour les applications. Au moyen d'un simple réaction redox à la surface, ces travaux ont prouvé que les lacunes en oxygène pouvaient doper la bande de conduction à la surface de SnO_2, résolvant ainsi un problème longtemps débattu concernant le rôle desdites lacunes dans le dopage de type n dans SnO_2.
2. L'étude des états de surface topologiques dans M_2Te_2X (avec M = Hf, Zr ou Ti ; et X = P ou As), une nouvelle famille de métaux topologiques en trois dimensions, provenant du SOC et étant protégés par la symétrie du renversement du temps. Leur structure électronique et leur texture de spin, étudiées par ARPES et SARPES, révèlent la présence de fermions de Dirac sans masse donnant naissance à des arcs de noeuds de Dirac.
3. L'étude du matériau $YbNi_4P_2$ à fermions lourds quasi unidimensionnel, qui présente une transition de phase quantique de second ordre d'une phase ferromagnétique à une phase paramagnétique de liquide de Fermi lors de la substitution partielle du phosphore par l'arséniure. Une telle transition ne devrait se produire que dans les systèmes zéro ou unidimensionnels, mais la mesure directe de la structure électronique des matériaux ferromagnétiques quantiques critiques faisait jusqu'à présent défaut. Grâce à une préparation et nettoyage méticuleux in situ de la surface des monocristaux $YbNi_4P_2$, qui sont impossibles à cliver, leur structure électronique a été mesurée avec succès au moyen de l'ARPES, dévoilant ainsi le caractère quasi-1D, nécessaire à la compréhension de la criticité quantique ferromagnétique, dans $YbNi_4P_2$. Le protocole utilisé pour rendre ce matériau accessible à l'ARPES peut être facilement généralisé à d'autres matériaux exotiques dépourvus de plan de clivage.

Université Paris-Saclay
Espace Technologique / Immeuble Discovery
Route de l'Orme aux Merisiers RD 128 / 91190 Saint-Aubin, France

université PARIS-SACLAY
ÉCOLE DOCTORALE
Physique en île-de-France (EDPIF)

Title : Low-dimensional electron systems studied by angle- and spin-resolved photoemission spectroscopy

Keywords : two-dimensional electron systems; correlated-electrons; functional oxides; topological metals; heavy-fermion materials; angle-resolved photoemission spectroscopy.

Abstract : Materials in which many-body interactions, low-dimensional confinement, and/or strong spin-orbit coupling are present show a rich variety of phenomena, but are still poorly understood. Essential information about the origin of such phenomena can be obtained by measuring their electronic structure. This thesis presents an experimental study of the electronic structure of some low-dimensional and/or strongly correlated materials of current fundamental interest, using angle- and spin-resolved photoemission spectroscopy (ARPES and SARPES).
In the introductory part, I present my work on two innovative textbook examples showing how interactions affect the band structure of a material : the coupling of electrons with phonons in a Debye distribution in a two-dimensional electron system (2DES) in ZnO, a wide-band-gap oxide semiconductor used in photovoltaic applications, and the splitting induced by strong spin-orbit coupling (SOC) in the bulk valence band of ZnTe, another important semiconductor used in optoelectronic devices. Then, in the rest of this thesis, I discuss my original results in three different low-dimensional systems of current interest :

1. The realisation of a 2DES at the (110) surface of SnO_2, the first of its kind in a rutile structure. Tunability of its carrier density by means of temperature or Eu deposition and robustness against surface reconstructions and exposure to ambient conditions make this 2DES promising for applications. By means of a simple redox reaction on the surface, this work has proven that oxygen vacancies can dope the conduction band minimum at the surface of SnO_2, solving a long-debated issue about their role in n-type doping in SnO_2.
2. The study of topological surface states in M_2Te_2X (with M = Hf, Zr, or Ti ; and X = P or As), a new family of three-dimensional topological metals, originating from SOC and being protected by time-reversal symmetry. Their electronic structure and spin texture, studied by ARPES and SARPES, reveal the presence of massless Dirac fermions giving rise to Dirac-node arcs.
3. The investigation of the quasi-one-dimensional heavy-fermion material $YbNi_4P_2$, which presents a second-order quantum phase transition from a ferromagnetic to a paramagnetic phase upon partial substitution of phosphorous by arsenide. Such a transition is expected to occur only in zero- or one-dimensional systems, but a direct measurement of the electronic structure of ferromagnetic quantum-critical materials was missing so far. By careful in-situ preparation and cleaning of the surface of $YbNi_4P_2$ single crystals, which are impossible to cleave, their electronic structure has been successfully measured by ARPES, thus effectively unveiling the quasi-one-dimensionality of $YbNi_4P_2$. Moreover, the protocol used to make this material accessible to ARPES can be readily generalised to other exotic materials lacking a cleavage plane.

Université Paris-Saclay
Espace Technologique / Immeuble Discovery
Route de l'Orme aux Merisiers RD 128 / 91190 Saint-Aubin, France